Forward modelling and inversion of streaming potential for the interpretation of hydraulic conditions from self-potential data

by

Megan Rae Sheffer

B.Sc., Queen's University, 1995
M.A.Sc., University of British Columbia, 2002

A THESIS SUBMITTED IN PARTIAL FULFILMENT OF
THE REQUIREMENTS FOR THE DEGREE OF

Doctor of Philosophy

in

The Faculty of Graduate Studies

(Geological Engineering)

The University Of British Columbia

December, 2007

Abstract

The self-potential method responds to the electrokinetic phenomenon of streaming potential and has been applied in hydrogeologic and engineering investigations to aid in the evaluation of subsurface hydraulic conditions. Of specific interest is the application of the method to embankment dam seepage monitoring and detection. This demands a quantitative interpretation of seepage conditions from the geophysical data.

To enable the study of variably saturated flow problems of complicated geometry, a three-dimensional finite volume algorithm is developed to evaluate the self-potential distribution resulting from subsurface fluid flow. The algorithm explicitly calculates the distribution of streaming current sources and solves for the self-potential given a model of hydraulic head and prescribed distributions of the streaming current cross-coupling conductivity and electrical resistivity. A new laboratory apparatus is developed to measure the streaming potential coupling coefficient and resistivity in unconsolidated soil samples. Measuring both of these parameters on the same sample under the same conditions enables us to properly characterize the streaming current cross-coupling conductivity coefficient. I present the results of a laboratory investigation to study the influence of soil and fluid parameters on the cross-coupling coefficient, and characterize this property for representative well-graded embankment soils. The streaming potential signals associated with preferential seepage through the core of a synthetic embankment dam model are studied using the forward modelling algorithm and measured electrical properties to assess the sensitivity of the self-potential method in detecting internal erosion. Maximum self-potential anomalies are shown to be linked to large localized hydraulic gradients that develop in response to piping, prior to any detectable increase in seepage flow through the dam. A linear inversion algorithm is developed to evaluate the three-dimensional distribution of hydraulic head from self-potential data, given a known distribution of the cross-coupling coefficient and

electrical resistivity. The inverse problem is solved by minimizing an objective function, which consists of a data misfit that accounts for measurement error and a model objective function that incorporates a priori information. The algorithm is suitable for saturated flow problems or where the position of the phreatic surface is known.

Table of Contents

Appendices

List of Tables

List of Figures

Acknowledgements

The research work presented in this thesis was supported by the Natural Sciences and Engineering Research Council of Canada and the Canadian Electricity Association Technologies Inc. Dam Safety Interest Group. Their funding is greatly appreciated.

I extend thanks to BC Hydro and Powertech Labs for releasing the field and laboratory data sets for use in the forward modelling study. I am grateful to Eldad Haber for his pearls of wisdom, and thank both him and Roman Shekhtman for their significant contributions to the forward modelling code. I also thank Ross Penner for willingly conducting the cut-off wall experiment as his undergraduate research project.

The laboratory investigation could not have been completed without the expert guidance of Phil Reppert, the continuous support of John Howie, the tireless efforts of Bill Leung in fabricating the test cell, the help of Scott Jackson with the electronics, and the assistance of Roger Middleton. I extend thanks to the geotechnical group in the Department of Civil Engineering for their support during this project.

My involvement with BC Hydro and the Dam Safety Interest Group has fostered many professional relationships that have turned into friendships. I extend gratitude to Ken Lum for facilitating the research sponsored by the Dam Safety Interest Group, and for his support and respect. Many thanks to Bob Corwin and Rich Markiewicz for our fruitful discussions on SP, and to Sam Johansson, Torleif Dahlin and Pontus Sjödahl for graciously hosting visits to Sweden.

I extend immense gratitude to Doug Oldenburg for his support and encouragement, and for creating a friendly and dynamic research group environment. I am also grateful to Roger Beckie for his support and open door policy. Special thanks to Garry Clarke and John Howie for their helpful contributions as members of my supervisory committee. It would have been a long and painful road without the help and company of fellow UBC-GIF

members, EOS-East residents and Rock Dogs, both past and present. In particular, I would like to thank Len and Peter for patiently fielding and answering my many questions.

I am eternally grateful to Mike for his patience, encouragement, love and unflagging support, and to Anna for allowing me to complete my thesis before her first birthday.

Dedication

In memory of Bob Corwin

Statement of Co-Authorship

I was responsible for writing all five manuscripts, which were reviewed by my co-authors. Prof. Douglas Oldenburg supervised the numerical modelling research presented in Chapters 2, 5 and 6. I acted as principal investigator for the laboratory research presented in Chapters 3 and 4. The scope of work was defined with input from Prof. John Howie, who served in a supervisory role. Dr. Philip Reppert collaborated on the design and development of the apparatus.

Chapter 1

Introduction

The self-potential (SP) method is a passive geophysical technique that responds to naturally-occurring potentials in the subsurface. Since its inception in the early 19th century [*Fox*, 1830], the method has been applied to mineral exploration, oil well logging, geothermal exploration and more recently hydrogeologic, environmental and engineering investigations.

Self-potential data are voltage differences measured using a pair or an array of non-polarizing electrodes and a high input-impedance measurement device. Despite the relative simplicity of the method, its use has been hindered in part by a lack of understanding of the underlying mechanisms that give rise to an SP response. All source mechanisms generate an accumulation of electrical charge in the subsurface. A physical understanding of these source mechanisms is required to enable an effective interpretation of self-potential data to recover practical information about the subsurface.

Mineralization potentials are the signal of interest in mineral exploration. These are associated primarily with sulphide ore bodies and have been explained using an electrochemical mechanism [*Sato and Mooney*, 1960] or related to oxidation potential [*Corry*, 1985]. The amplitude of anomalies encountered over mineralized targets can range in the hundreds of milliVolts, such that other naturally-occurring potentials are typically ignored and considered noise. A number of these "background" potentials are the signals of interest in most other applications of the method. These source mechanisms may be described using coupled flow theory.

Coupled flow phenomena describe the flux of some quantity induced by a driving force other than the primary force typically associated with the flow. An example is thermal diffusion, where a temperature gradient induces the flow of ions in a liquid. When flows are small (viscous laminar) and forces vary slowly, linear flow laws may be used to describe a flux as the product of a potential gradient and a conductivity term. Table 1.1 lists primary

and coupled flow phenomena and illustrates the interdependence of fluid, temperature, electrical and ionic systems. Primary flow laws are listed as diagonal terms in the table, and coupled flow phenomena are listed as off-diagonal terms. Chapter 2 presents a mathematical description of the electrokinetic streaming potential source mechanism. More detail on the general theory can be found in *de Groot* [1951], *Onsager* [1931] and *Mitchell* [1991].

	Gradient			
Flow	*Hydraulic Potential*	*Temperature*	*Electrical Potential*	*Chemical Concentration*
Fluid	**Darcy's Law** (hydraulic conduction)	Thermo-osmosis	Electro-osmosis	Chemical osmosis
Heat	Isothermal heat transfer	**Fourier's Law** (thermal conduction)	Peltier Effect	Dufour Effect
Electrical current	Streaming current (electrokinetic streaming potential)	Seebeck Effect (thermo-electric)	**Ohm's Law** (electrical conduction)	Diffusion and membrane potentials (electrochemical)
Ionic (chemical)	Streaming current	Soret Effect (thermal diffusion)	Electrophoresis	**Fick's Law** (chemical diffusion)

Table 1.1: Primary and coupled flow phenomena. Primary flows are listed as diagonal terms, and coupled flows are listed as off-diagonal terms. (adapted from *Mitchell* [1991]).

Thermoelectric, electrochemical and electrokinetic source mechanisms all give rise to electrical conduction current flow that can be characterized using the self-potential method. Geothermal exploration and the study of volcanic systems relies on both thermoelectric and electrokinetic sources, where fluid flow is driven both by advection and thermal convection [*Corwin and Hoover*, 1979; *Di Maio and Patella*, 1994; *Revil et al.*, 1999b]. Environmental

applications of the SP method include the study of electrochemical signals associated with the migration of concentration fronts [*Maineult et al.*, 2005]. An emerging area is the mapping of reduction-oxidation (redox) potential for the delineation of contaminant plumes and monitoring of remediation strategies. The source mechanism in this application is a current topic of investigation [*Naudet et al.*, 2003, 2004; *Naudet and Revil*, 2005; *Linde and Revil*, 2007].

The electrokinetic phenomenon of streaming potential is the main mechanism of interest for the study of fluid flow in porous media. Figure 1.1 presents a conceptual pore-scale model of streaming potential. An electrical double layer forms at the solid-fluid interface, which consists of an adsorbed layer of tightly bound positive ions and a more loosely bound diffuse outer layer. Under static conditions, the saturated medium is electrically neutral with adsorbed ions from the fluid completely balancing the negative surface charge of the solid particles. The onset of fluid flow pulls positive ions from the diffuse layer in the direction of flow, which generates a streaming current. A charge imbalance results from the movement of ions in the direction of flow, which induces an opposing conduction current. Although the streaming current is strictly limited to the saturated pore channels, the conduction current permeates the entire medium and may be quantified with self-potential measurements. Chapter 4 gives some insight on the properties of the electrical double layer. A more detailed treatment with reference to electrokinetic phenomena is given in *Ishido and Mizutani* [1981], *Morgan et al.* [1989], *Revil et al.* [1999a] and *Sheffer* [2002].

The self-potential method is the only geophysical technique that responds directly to fluid flow. Consequently, the method has been applied to a wide range of problems in an effort to interpret characteristics of the hydraulic regime from the measured electrical potential distribution. Examples include earthquake prediction from fluid flow into a dilatant zone preceding an earthquake [*Mizutani et al.*, 1976; *Corwin and Morrison*, 1977; *Jouniaux and Pozzi*, 1995], hydraulic fracturing in rocks for hydrocarbon recovery [*Moore and Glaser*, 2007], and the study of subglacial flow systems [*Blake and Clarke*, 1999; *Kulessa et al.*, 2003].

A significant body of work exists in the application of SP to the study of groundwater. SP field data have been analysed in the study of flow into pumping wells [*Bogoslovsky and*

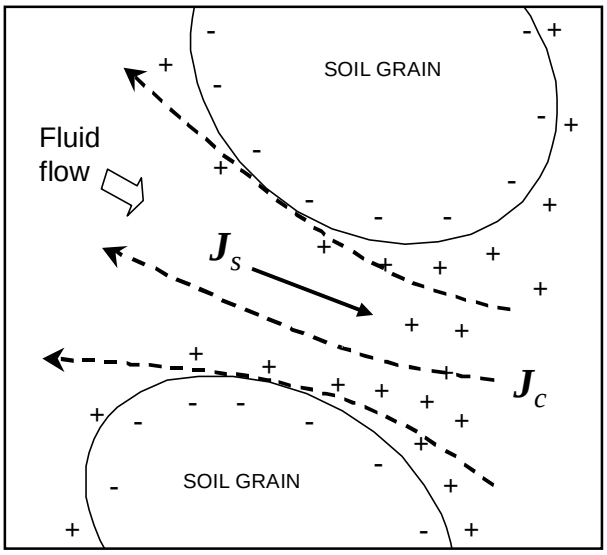

Figure 1.1: Conceptual model of streaming potential, showing streaming current $\boldsymbol{J}_S$ and conduction current $\boldsymbol{J}_C$ flow paths in the pore space of a saturated soil.

Ogilvy, 1973; *Rizzo et al.*, 2004; *Titov et al.*, 2005b], fluid flow in the vadose zone [*Sailhac et al.*, 2004; *Darnet and Marquis*, 2004], brine-contamination in an aquifer [*Titov et al.*, 2005a], and spring flow [*Schiavone and Quarto*, 1984]. Other studies involve delineating and monitoring fluctuations in the position of the water table [*Revil et al.*, 2004; *Suski et al.*, 2006], locating sinkholes [*Jardani et al.*, 2006a, b] and subsurface cavities [*Jardani et al.*, 2006c] from vertical inflow in karstic terrain, assessing the performance of granular drainage systems [*Bogoslovsky and Ogilvy*, 1973], and delineating buried paleochannels [*Revil et al.*, 2005].

One key application of the SP technique is the monitoring of seepage flow through earth dams. This has prompted research involving SP measurements on experimental lab-scale [*Armbruster et al.*, 1989] and field-scale [*Merkler et al.*, 1989; *Wurmstich et al.*, 1991] embankments, as well as on existing dams [e.g. *Ogilvy et al.*, 1969; *Bogoslovsky and Ogilvy*, 1970; *Johansson et al.*, 2005].

Embankment dams are constructed of permeable materials and are designed to allow limited amounts of seepage flow from the impounded reservoir. Internal erosion, or the loss of fine-grained material due to seepage forces, is one of the most prevalent failure modes

in embankment dams [*ICOLD*, 1995; *Sherard et al.*, 1963]. Deviations from expected flow rates through an embankment may be indicative of "piping" or preferential seepage zones through the core or foundation material, which can severely compromise the stability of the structure.

Dam safety surveillance typically consists of visual inspections supported with instrumentation readings. Standard instrumentation is used to monitor seepage flow from the dam drainage system, displacements, and pore water pressure within the dam body at discrete measurement points. These systems may be installed at the time of construction, but their existence and efficiency is dependent on the design and age of the dam. Internal problems can become quite advanced before instrumentation alerts to a problem or visual signs of damage appear. This has sparked interest in the use of geophysical techniques to augment standard monitoring methods.

The SP method has been used to successfully delineate anomalous zones that correspond with areas of preferential seepage in embankments [*Ogilvy et al.*, 1969; *Bogoslovsky and Ogilvy*, 1970; *Black and Corwin*, 1984; *Butler et al.*, 1989; *Corwin*, 1991]. Practical data acquisition techniques have been developed for one-time surveys and simple monitoring arrays [*Corwin*, 1990, 2005]. However, the current state of practice in SP data interpretation for dam seepage studies is limited to qualitative and simple quantitative techniques that estimate the depth and location of possible seepage paths using point source modelling [e.g. *Panthulu et al.*, 2001; *Rozycki et al.*, 2006; *Corwin*, 2007]. As discussed in Section 1.1, these methods do not provide an adequate physical representation of the underlying hydraulic regime to enable a quantitative interpretation of hydraulic parameters that are of interest.

The research presented in this thesis is aimed at advancing the current state of practice in self-potential data interpretation, with a focus on the application to seepage monitoring in embankment dams. The following sections discuss past developments in the quantitative interpretation of SP data, and outline the current research in the context of this work.

1.1 Quantitative interpretation of SP data

Self-potential data may be interpreted using geometric source techniques, imaging methods, forward modelling and inversion. Although these techniques vary in complexity, past developments can be grouped according to the level of knowledge of the underlying source mechanism.

When the source mechanism is unknown or poorly understood, we can employ geometric source, source imaging and inversion methods to infer the probable locations of current sources that give rise to the SP data. Data interpretation consists of relating the calculated distribution of current sources to possible geologic features or target locations. We cannot interpret any additional information about the physical parameters that characterize the underlying source mechanism since none is assumed.

Geometric source techniques were originally developed to interpret SP anomalies associated with distinct ore bodies. The general assumption is that the mineralized body may be approximated by a polarized model of simple geometry, such as a sphere, infinite cylinder or sheet, which are independent of the polarization mechanism. Curve-matching [*de Witte*, 1948; *Yüngül*, 1950; *Meiser*, 1962], parametric curve [*Paul*, 1965; *Bhattacharya and Roy*, 1981; *Atchuta Rao and Ram Babu*, 1983; *Ram Babu and Atchuta Rao*, 1988], and least-squares inversion methods [*Abdelrahman and Sharafeldin*, 1997; *Abdelrahman et al.*, 2003] have been used to estimate source parameters such as surface location, dip or polarization angle, and depth of the body. *Fitterman and Corwin* [1982] used a least-squares inversion technique to recover the depth, geometry and source intensity of a polarized sheet model of a geothermal fault zone. In cases where the source geometry is poorly constrained, a derivative analysis method [*Abdelrahman et al.*, 1998, 2003] has been applied to estimate the depth and a shape factor of the source.

A common requirement of geometric source techniques is that the SP data must exhibit a discrete anomalous feature that can be attributed to a single polarized body or zone. Regional effects and signals resulting from other sources or source mechanisms must be removed from the data or assumed to have minimal influence. As mentioned above, this type of approach has been applied to interpret discrete anomalous features observed in SP data at embankment sites. The calculated source locations are inferred to correspond to

the location of preferential seepage paths. However, the analysis requires an assumption of source geometry and does not enable an interpretation of seepage-related properties.

Source imaging methods have been used to reconstruct a tomographic map of the distribution of electrical source strength from which the probable location of discrete sources can be estimated. These methods assume that measured SP data at the surface result from the superposition of sources in the subsurface, and consequently must employ some form of normalization to enable a comparison of sources located at different depths. *Di Maio and Patella* [1994] performed a 2-D image reconstruction by cross-correlating a single horizontal component of the measured electric field E_x at surface with a scanning function, which is an analytical representation of E_x generated by a point source of unit strength. They applied their method to interpret SP data collected over a volcanic fracture system. *Patella* [1997] addressed the influence of heterogeneous subsurface resistivity distribution on the imaged source distribution and extended the point source analysis to 3-D. *Jardani et al.* [2006c] used a similar approach to image the depth to the roof of a subsurface cavity. *Hämmann et al.* [1997] built on the work of *Di Maio and Patella* [1994] by cross-correlating the measured electrical field with a scanner function, which corresponds to a unit line source of charge that extends infinitely in the direction perpendicular to the surface data profile. They found that they could only resolve distinct source locations separated by distances five times greater than their depth. Their method was applied to the interpretation of SP profile data collected across a complex hydrogeologic system, which was thought to exhibit electrokinetic and electrochemical behaviour.

The inversion of SP data using an inverse source formulation provides a more rigorous means of interpreting a subsurface distribution of current sources. *Shi* [1998] developed a regularized inversion routine to evaluate a 3-D current source distribution. Her method requires significant a priori information to constrain the depth and amplitude of the sources. Given the inherent non-uniqueness of the problem, *Minsley et al.* [2007a] further developed this routine by introducing sensitivity scaling (similar to depth weighting) and constraints to encourage source compactness. They performed an inversion of SP data to delineate the extents of a contaminant plume where redox processes are occurring [*Minsley et al.*, 2007b].

Source imaging and inverse source methods are beneficial in problems where we have

limited prior knowledge of the source mechanism, or where multiple source mechanisms are at work. However, these approaches do not enable a direct interpretation of subsurface parameters that are linked to a specific source mechanism. This requires the incorporation of a source model into the numerical analysis.

When the source mechanism is known, we can employ forward modelling, imaging and inversion methods to interpret relevant characteristics of the underlying source mechanism from the SP data. The interpretation of hydraulic conditions from self-potential data relies on the assumption of an electrokinetic source mechanism.

Discrete forward modelling methods have been developed to predict the self-potential response to a primary fluid flow field. These methods are based on a coupled flow model that describes the electrokinetic source mechanism. Consequently, they require some knowledge of the relevant physical properties to effectively calculate the distribution of sources and resulting electrical potential in the subsurface. A total potential approach to the coupled flow problem [*Nourbehecht*, 1963] was used to forward model electrokinetic behaviour preceding earthquakes [*Fitterman*, 1978], and thermoelectric effects associated with geothermal areas [*Fitterman*, 1983]. However, this approach is impractical for the study of streaming potential, as suggested by *Sill* [1983].

The convection current approach to the coupled flow problem proposed by *Sill* [1983] has been widely accepted and implemented in most forward modelling studies of streaming potential performed to date. *Sill and Killpack* [1982] developed the first algorithm to use this approach using a 2.5-D solution, which was adapted by *Wilt and Butler* [1990] and applied to evaluate the streaming potential signal at an embankment site [*Wilt and Corwin*, 1989]. *Ishido and Pritchett* [1999] studied electrokinetic behaviour in geothermal reservoir simulations using a finite difference post-processor. *Revil et al.* [1999b] considered both advective and convective fluid flow in a finite element study of a geothermal system. *Wurmstich et al.* [1991] used a 2-D finite element model to evaluate the SP response to seepage in an embankment. They compared their numerical result to measured data obtained over the surface of a field-scale laboratory embankment model. *Berube* [2004] developed a finite element code to study streaming potential signals in dams. *Wurmstich and Morgan* [1994] developed a 3-D finite difference algorithm to study streaming potential

signals generated by radial flow to an oil well in a fluid-saturated halfspace. *Saunders et al.* [2006] performed 3-D finite element modelling of the SP response to oil-well pumping in a two-phase (oil-water) system. *Titov et al.* [2002, 2005b] developed and applied a 2-D finite difference algorithm to evaluate streaming potential signals in groundwater flow problems. *Jardani et al.* [2006a] performed 3-D finite element modelling to study the SP response to vertical infiltration in a karstic environment. *Darnet and Marquis* [2004] performed a synthetic 1-D modelling study of streaming potentials in the vadose zone. Most recently, *Linde et al.* [2007] performed 1-D modelling of the SP response to unsaturated flow in a controlled drainage experiment using a formulation where streaming current is expressed as a function of pore fluid velocity, porosity and excess charge [*Revil and Linde*, 2006].

Although significant work has been done in developing forward models of streaming potential, there is a lack of three-dimensional forward modelling methods that are capable of solving variably saturated flow problems. This type of model is required to solve embankment seepage problems of complicated geometry.

Imaging and parametric inversion methods have been developed to extract hydraulic parameters from SP data. However, these methods are limited to specific groundwater flow problems. Examples include work presented by *Sailhac and Marquis* [2001], who used a 2-D wavelet-based method to invert for electrokinetic source parameters assuming a homogeneous electrical conductivity distribution. *Darnet et al.* [2003] used a weighted least-squares approach to invert for the hydraulic conductivity, cross-coupling conductivity and thickness of a homogeneous aquifer subject to flow from a pumping well. Electrokinetic sources are directly related to the extraction rate of fluid from the well, and the electrical conductivity contrast between the aquifer and well casing is accounted for in their solution.

Other work has focused on determining the position of the water table. Examples include an imaging method presented by *Birch* [1998], who employed a similar approach as *Hämmann et al.* [1997] using line sources of charge. The basis for his approach was first proposed by *Fournier* [1989], who developed an equation for electrical potential at the earth's surface using a total potential formulation of the coupled flow problem [*Nourbehecht*, 1963] for specific application to unconfined groundwater problems. *Fournier* [1989] stated that all electrokinetic sources in a homogeneous medium can be represented by a dipolar sheet

of charge at the position of the water table. This model is assumed in the formulation of the source strength term, which consists of a streaming potential coupling coefficient (C) multiplied by the height of the water table. The position of the water table is interpreted from a zone of constant C on the tomographic image of C. *Revil et al.* [2003] improved the method proposed by *Birch* [1998] by normalizing the function to consider only a vertical orientation of dipoles at the phreatic surface. *Revil et al.* [2003] developed a 2-D weighted least-squares inversion technique based on the formulation presented by *Fournier* [1989] to recover the depth to the water table. *Revil et al.* [2004] improved this routine by incorporating the effect of an electrical conductivity contrast between saturated and unsaturated zones. This routine has been applied in a number of studies to recover the shape of the water table [e.g., *Jardani et al.*, 2006b; *Linde and Revil*, 2007].

Although the imaging and parametric inversion methods listed above are useful in delineating the location of the water table, they consider that all electrokinetic charge accumulates at this boundary. This precludes the investigation of other sources that may arise due to heterogeneities in the saturated zone. For embankment seepage monitoring applications, we are interested in studying zones of preferential flow that develop beneath the phreatic surface. These zones may not have a significant influence on the position of the phreatic surface.

We require a numerical modelling method based on a distributed set of parameters to study complex flow problems. Discrete forward modelling methods can be used to predict the self-potential distribution that results from a given hydraulic regime. However, an inverse methodology facilitates the practical interpretation of measured SP data to extract pertinent hydraulic information. To date, the under-determined problem of inverting self-potential data has only been solved using an inverse source formulation.

Successful application of discrete numerical modelling methods is limited by our knowledge of the physical properties of the subsurface. Realistic estimates of the relevant properties are required to effectively model streaming potential in a discretized framework. While significant effort has been devoted to studying and characterizing hydraulic and electrical properties for different materials, a similar collection of data on coupled flow properties has not been compiled.

Previous laboratory investigations of streaming potential have focused on measuring the streaming potential coupling coefficient C to examine properties of the soil-fluid interface [*Ishido and Mizutani*, 1981; *Morgan et al.*, 1989; *Lorne et al.*, 1999; *Revil et al.*, 1999b; *Reppert and Morgan*, 2003], or to examine the link between C and hydraulic properties such as permeability and saturation [*Jouniaux and Pozzi*, 1995; *Pengra et al.*, 1999; *Guichet et al.*, 2003; *Revil and Cerepi*, 2004]. There is a lack of experimental data reported for soils typical of embankments, particularly those that exhibit a range of grain sizes. Most experimental investigations report measured values of C along with the saturating fluid properties, but do not include values of electrical resistivity ρ measured under the same sample conditions. These two properties are required to calculate the streaming current cross-coupling coefficient $L = -C/\rho$ and are fundamental to any quantitative analysis of streaming potential.

1.2 Thesis objective and outline

The main objective of the research presented in this thesis is to identify what useful information about hydraulic parameters and embankment integrity can be garnered from self-potential data, when streaming potential is the dominant mechanism. I seek to answer this question through the development and application of forward and inverse modelling techniques, and a laboratory investigation of the physical properties that govern the phenomenon.

Figure 1.2 identifies the three key elements of the thesis research and illustrates how they contribute to a quantitative interpretation of hydraulic conditions from self-potential data. A 3-D forward model enables us to predict the self-potential response to a given seepage regime and enables us to study the streaming potential phenomenon in complex problems. The inverse problem makes use of the forward model and enables a direct interpretation of hydraulic head from self-potential data. Realistic estimates of the relevant electrical properties are required as input to the numerical methods to effectively interpret the measured self-potential.

The main body of the thesis consists of five chapters, each of which has been prepared

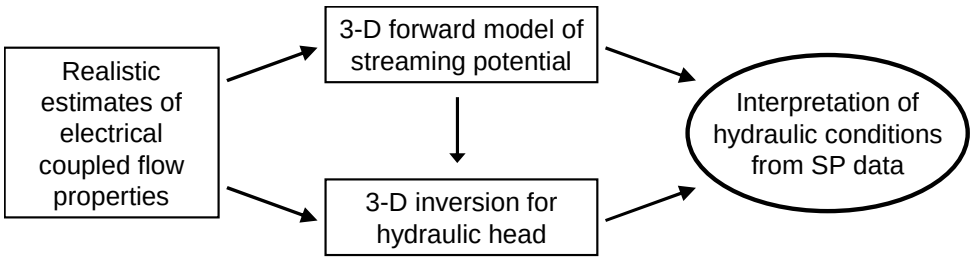

Figure 1.2: Key elements contributing to the quantitative interpretation of hydraulic conditions from SP data.

as a separate manuscript.

Chapter 2 presents a 3-D finite volume algorithm for calculating the self-potential distribution resulting from fluid flow in a porous medium. The algorithm was developed to enable the study of variably saturated flow problems of complex geometry for application to engineering and hydrogeological investigations. This work builds on research first presented in [*Sheffer*, 2002]. The chapter presents a coupled flow model of streaming potential, the governing equations that describe the hydraulic and electrical flow problems, and the solution of these equations using the finite volume method. A series of examples compares predicted and measured self-potential data, shows the importance of proper representation of heterogeneous physical property distributions, and illustrates the need for 3-D models to tackle complex flow problems.

Chapter 3 introduces a laboratory apparatus designed to measure the streaming potential coupling coefficient C and electrical resistivity ρ of saturated soil specimens. These properties are measured on the same sample in order to characterize the streaming current cross-coupling coefficient L, which is a fundamental parameter required for numerical modelling. This chapter details the construction and calibration of the apparatus, which was designed to study well-graded (poorly sorted) soil samples typical of embankments. It is the first of its kind to implement the oscillatory flow method for streaming potential measurements on well-graded samples, and is unique in its design to measure both C and ρ on the same soil specimen. The chapter includes a description of streaming potential and resistivity measurement techniques and a comparison of data acquired using the different

methods.

Chapter 4 presents the results of laboratory measurements performed using the apparatus described in Chapter 3. The objectives of the study were two-fold: to investigate the influence of soil and fluid parameters on the streaming current cross-coupling coefficient, and to characterize this property for representative embankment soils. This chapter presents experimental data acquired on a series of glass bead and embankment soil samples, and discusses the influence of sample density, sample gradation and fluid conductivity on the measured electrical properties. The analysis of glass bead samples includes a comparison with theoretical estimates of the electrical properties and illustrates the major influence of sample equilibration on the measured electrical properties. The analysis of embankment soil data includes a comparison with published values of the streaming current cross-coupling coefficient.

Evaluating the sensitivity of the SP method to detect the onset of internal erosion in the core of a dam is of key importance in determining the suitability of the method for seepage monitoring investigations. Chapter 5 applies the forward modelling algorithm described in Chapter 2 using the electrical properties reported in Chapter 4 to study the SP response to seepage in a synthetic 2-zone field-scale embankment. A series of models are examined to evaluate the residual SP distributions that result from preferential flow through defects within the core. Detection of the predicted SP anomalies is discussed in terms of practical detection limits for the method, and predicted variations in hydraulic head and flow rate in response to the defects.

Chapter 6 presents an inversion algorithm that recovers a 3-D distribution of hydraulic head from self-potential data where streaming potential is the dominant mechanism. The forward model described in Chapter 2 provides a basis for the inverse problem. This chapter describes the formulation and solution of the inverse problem, and is the first time such an approach has been documented. SP data collected in a laboratory-scale model of seepage under a cut-off wall are inverted to recover a hydraulic head distribution that is compared with observed head measurements. This example also serves to demonstrate how prior information about the hydraulic and electrical flow systems can be used to help constrain the solution.

Chapter 7 summarizes the key findings of the research, discusses the practical contributions, and comments on areas of future work. A derivation of the discrete approximation of the coupled electrical flow equation presented in Chapter 2 is included as Appendix A.

1.3 References

Abdelrahman, E. M., and S. M. Sharafeldin, A least-squares approach to depth determination from self-potential anomalies caused by horizontal cylinders and spheres, *Geophysics*, *62*(1), 44–48, 1997.

Abdelrahman, E. M., A. A. B. Ammar, H. I. Hassanein, and M. A. Hafez, Derivative analysis of SP anomalies, *Geophysics*, *63*(3), 890–897, 1998.

Abdelrahman, E. M., H. M. El-Araby, A. G. Hassaneen, and M. A. Hafez, New methods for shape and depth determinations from SP data, *Geophysics*, *68*(4), 1202–1210, 2003.

Armbruster, H., J. Brauns, W. Mazur, and G. P. Merkler, Effect of leaks in dams and trials to detect leakages by geophysical means, in *Detection of Subsurface Flow Phenomena*, *Lecture Notes in Earth Sciences*, vol. 27, edited by G. P. Merkler, H. Militzer, H. Hötzl, H. Armbruster, and J. Brauns, pp. 3–18, Springer-Verlag, Berlin, 1989.

Atchuta Rao, D., and H. V. Ram Babu, Quantitative interpretation of self-potential anomalies due to two-dimensional sheet-like bodies, *Geophysics*, *48*(12), 1659–1664, 1983.

Berube, A. P., Investigating the streaming potential phenomenon using electric measurements and numerical modelling with special reference to seepage monitoring in embankment dams, Ph.D. thesis, Luleå University of Technology, Sweden, 2004.

Bhattacharya, B. B., and N. Roy, A note on the use of a nomogram for self-potential anomalies, *Geophysical Prospecting*, *29*, 102–107, 1981.

Birch, F. S., Imaging the water table by filtering self-potential profiles, *Ground Water*, *36*(5), 779–782, 1998.

Black, W. E., and R. F. Corwin, Application of self-potential measurements to the delineation of groundwater seepage in earth-fill embankments, *Society of Exploration Geophysicists Technical Program Expanded Abstracts*, *3*, 162–164, doi:10.1190/1.1894185, 1984.

Blake, E., and G. Clarke, Subglacial electrical phenomena, *Journal of Geophysical Research*, *104*(B4), 7481–7495, 1999.

Bogoslovsky, V. A., and A. A. Ogilvy, Application of geophysical methods for studying the technical status of earth dams, *Geophysical Prospecting*, *18*, 758–773, 1970.

Bogoslovsky, V. V., and A. A. Ogilvy, Deformations of natural electric fields near drainage structures, *Geophysical Prospecting*, *21*, 716–723, 1973.

Butler, D. K., J. L. Llopis, and C. M. Deaver, Comprehensive geophysical investigation of an existing dam foundation, *The Leading Edge*, *8*(8), 10–18, 1989.

Corry, C. E., Spontaneous polarization associated with porphyry sulfide mineralization, *Geophysics*, *50*(6), 1020–1034, 1985.

Corwin, R. F., The self-potential method for environmental and engineering applications, in *Geotechnical and Environmental Geophysics*, vol. 1, edited by S. H. Ward, pp. 127–145, Society of Exploration Geophysicists, Tulsa, 1990.

Corwin, R. F., Evaluation of effects of cutoff wall construction on seepage flow using self-potential data: East Embankment Wells Dam, *Tech. rep.*, Douglas County Public Utility District no. 1, Washington, 1991.

Corwin, R. F., Investigation of geophysical methods for assessing seepage and internal erosion in embankment dams: Self-potential field data acquisition manual, *Tech. rep.*, Canadian Electricity Association Technologies Inc. (CEATI), Report T992700-0205B/1, Montreal, 2005.

Corwin, R. F., Investigation of geophysical methods for assessing seepage and internal erosion in embankment dams: Interpretation of self-potential data for dam seepage investigations, *Tech. rep.*, Canadian Electricity Association Technologies Inc. (CEATI), Report T992700-0205B/3, Montreal, 2007.

Corwin, R. F., and D. B. Hoover, The self-potential method in geothermal exploration, *Geophysics*, *44*(2), 226–245, 1979.

Corwin, R. F., and H. F. Morrison, Self-potential variations preceding earthquakes in central California, *Geophysical Research Letters*, *4*(4), 171–174, 1977.

Darnet, M., and G. Marquis, Modelling streaming potential (SP) signals induced by water movement in the vadose zone, *Journal of Hydrology*, *285*, 114–124, 2004.

Darnet, M., G. Marquis, and P. Sailhac, Estimating aquifer hydraulic properties from the inversion of surface Streaming Potential (SP) anomalies, *Geophysical Research Letters*, *30*(13), 1679, doi:10.1029/2003GL017631, 2003.

de Groot, S. R., *Thermodynamics of irreversible processes*, *Selected Topics in Modern Physics*, vol. 3, North Holland Publishing Company, Amsterdam, 1951.

de Witte, L., A new method of interpretation of self-potential field data, *Geophysics*, *13*(4), 600–608, 1948.

Di Maio, R., and D. Patella, Self-potential anomaly in volcanic areas: The Mt. Etna case history, *Acta Vulcanologica*, *4*, 119–124, 1994.

Fitterman, D. V., Electrokinetic and magnetic anomalies associated with dilatant regions in a layered earth, *Journal of Geophysical Research*, *83*(B12), 5923–5928, 1978.

Fitterman, D. V., Modeling of self-potential anomalies near vertical dikes, *Geophysics*, *48*(2), 171–180, 1983.

Fitterman, D. V., and R. F. Corwin, Inversion of self-potential data from the Cerro Prieto geothermal field, Mexico, *Geophysics*, *47*(6), 938–945, 1982.

Fournier, C., Spontaneous potentials and resistivity surveys applied to hydrogeology in a volcanic area: Case history of the Chaîne des Puys (Puy-de-Dôme, France), *Geophysical Prospecting*, *37*, 647–668, 1989.

Fox, R. W., On the electro-magnetic properties of metalliferous veins in the mines of Cornwall, *Philosophical Transactions of the Royal Society of London*, *120*, 399–414, 1830.

Guichet, X., L. Jouniaux, and J. P. Pozzi, Streaming potential of a sand column in partial saturation conditions, *Journal of Geophysical Research*, *108*(B3), 2141, doi: 10.1029/2001JB001517, 2003.

Hämmann, M., H. R. Maurer, A. G. Green, and H. Horstmeyer, Self-potential image reconstruction: Capabilities and limitations, *Journal of Environmental and Engineering Geophysics*, *2*(1), 21–35, 1997.

ICOLD, Dam failures: Statistical analysis, in *Bulletin no. 99*, International Commission on Large Dams, 1995.

Ishido, T., and H. Mizutani, Experimental and theoretical basis of electrokinetic phenomena in rock-water systems and its application to geophysics, *Journal of Geophysical Research*, *86*(B3), 1763–1775, 1981.

Ishido, T., and J. W. Pritchett, Numerical simulation of electrokinetic potentials associated with subsurface fluid flow, *Journal of Geophysical Research*, *104*(B7), 15,247–15,259, 1999.

Jardani, A., J. P. Dupont, and A. Revil, Self-potential signals associated with preferential groundwater flow pathways in sinkholes, *Journal of Geophysical Research*, *111*, B09204, doi:10.1029/2005JB004231, 2006a.

Jardani, A., J. P. Dupont, and A. Revil, Least-squares inversion of self-potential (SP) data and application to the shallow flow of ground water in sinkholes, *Geophysical Research Letters*, *33*, L19306, doi:10.1029/2006GL027458, 2006b.

Jardani, A., A. Revil, and J. P. Dupont, Self-potential tomography applied to the determination of cavities, *Geophysical Research Letters*, *33*, L13401, doi:10.1029/2006GL026028, 2006c.

Johansson, S., J. Friborg, T. Dahlin, and P. Sjödahl, Long term resistivity and self potential monitoring of embankment dams: Experiences from Hällby and Sädva dams, Sweden, *Tech. rep.*, Elforsk/Canadian Electricity Association Dam Safety Interest Group, Report 05:15, Stockholm, 2005.

Jouniaux, L., and J. P. Pozzi, Streaming potential and permeability of saturated sandstones under triaxial stress: Consequences for electrotelluric anomalies prior to earthquakes, *Journal of Geophysical Research*, *100*(B6), 10,197–10,209, 1995.

Kulessa, B., B. Hubbard, and G. H. Brown, Cross-coupled flow modeling of coincident streaming and electrochemical potentials and application to sub-glacial self-potential data, *Journal of Geophysical Research*, *108*(B8), 2381, doi:10.1029/2001JB001167, 2003.

Linde, N., and A. Revil, Inverting self-potential data for redox potentials of contaminant plumes, *Geophysical Research Letters*, *34*, L14302, doi:10.1029/2007GL030084, 2007.

Linde, N., D. Jougnot, A. Revil, S. K. Matthäi, T. Arora, and D. Renard, Streaming current generation in two-phase flow conditions, *Geophysical Research Letters*, *34*, L03306, doi:10.1029/2006GL028878, 2007.

Lorne, B., F. Perrier, and J. P. Avouac, Streaming potential measurements 1. Properties of the electrical double layer from crushed rock samples, *Journal of Geophysical Research*, *104*(B8), 17,857–17,877, 1999.

Maineult, A., Y. Bernabé, and P. Ackerer, Detection of advected concentration and pH fronts from self-potential measurements, *Journal of Geophysical Research*, *110*, B11205, doi:10.1029/2005JB003824, 2005.

Meiser, P., A method of quantitative interpretation of self-potential measurements, *Geophysical Prospecting*, *10*, 203–218, 1962.

Merkler, G. P., H. Armbruster, H. Hötzl, P. Marschall, A. Kassel, and E. Ungar, Modelling of streaming potentials and thermoelectrical measurements at a big laboratory channel, in *Detection of Subsurface Flow Phenomena*, *Lecture Notes in Earth Sciences*, vol. 27, edited by G. P. Merkler, H. Militzer, H. Hötzl, H. Armbruster, and J. Brauns, pp. 223–249, Springer-Verlag, Berlin, 1989.

Minsley, B. J., J. Sogade, and F. D. Morgan, Three-dimensional source inversion of self-potential data, *Journal of Geophysical Research*, *112*, B02202, doi:10.1029/2006JB004262, 2007a.

Minsley, B. J., J. Sogade, and F. D. Morgan, Three-dimensional self-potential inversion for subsurface DNAPL contaminant detection at the Savannah River Site, South Carolina, *Water Resources Research*, *43*, W04429, doi:10.1029/2005WR003996, 2007b.

Mitchell, J. K., Conduction phenomena: From theory to geotechnical practice, *Geotechnique*, *43*(3), 299–340, 1991.

Mizutani, H., T. Ishido, T. Yokokura, and S. Ohnishi, Electrokinetic phenomena associated with earthquakes, *Geophysical Research Letters*, *3*, 365–368, 1976.

Moore, J. R., and S. D. Glaser, Self-potential observations during hydraulic fracturing, *Journal of Geophysical Research*, *112*, B02204, doi:10.1029/2006JB004373, 2007.

Morgan, F. D., E. R. Williams, and T. R. Madden, Streaming potential properties of Westerly granite with applications, *Journal of Geophysical Research*, *94*(B9), 12,449–12,461, 1989.

Naudet, V., and A. Revil, A sandbox experiment to investigate bacteria-mediated redox processes on self-potential signals, *Geophysical Research Letters*, *32*, L11405, doi:10.1029/2005GL022735, 2005.

Naudet, V., A. Revil, and J. Y. Bottero, Relationship between self-potential (SP) signals and redox conditions in contaminated groundwater, *Geophysical Research Letters*, *30*, 21,2091, doi:10.1029/2003GL018096, 2003.

Naudet, V., A. Revil, E. Rizzo, J. Y. Bottero, and P. Bégassat, Groundwater redox conditions and conductivity in a contaminant plume from geoelectrical investigations, *Hydrology and Earth System Sciences*, *8*(1), 8–22, 2004.

Nourbehecht, B., Irreversible thermodynamic effects in inhomogeneous media and their applications in certain geoelectric problems, Ph.D. thesis, Massachusetts Institute of Technology, Cambridge, 1963.

Ogilvy, A. A., M. A. Ayed, and V. A. Bogoslovsky, Geophysical studies of water leakages from reservoirs, *Geophysical Prospecting*, *17*, 36–62, 1969.

Onsager, L., Reciprocal relations in irreversible processes, I, *Physical Review*, *37*, 405–426, 1931.

Panthulu, T. V., C. Krishnaiah, and J. M. Shirke, Detection of seepage paths in earth dams using self-potential and electrical resistivity methods, *Engineering Geology*, *59*, 281–295, 2001.

Patella, D., Introduction to ground surface self-potential tomography, *Geophysical Prospecting*, *45*(4), 653–681, 1997.

Paul, M. K., Direct interpretation of self-potential anomalies caused by inclined sheets of infinite horizontal extensions, *Geophysics*, *30*(3), 418–423, 1965.

Pengra, D. B., S. X. Li, and P. Wong, Determination of rock properties by low-frequency AC electrokinetics, *Journal of Geophysical Research*, *104*(B12), 29,485–29,508, 1999.

Ram Babu, H. V., and D. Atchuta Rao, Short note: A rapid graphical method for the interpretation of the self-potential anomaly over a two-dimensional inclined sheet of finite depth extent, *Geophysics*, *53*(8), 1126–1128, 1988.

Reppert, P. M., and F. D. Morgan, Temperature-dependent streaming potentials: 2. Laboratory, *Journal of Geophysical Research*, *108*(B11), 2547, doi:10.1029/2002JB001755, 2003.

Revil, A., and A. Cerepi, Streaming potentials in two-phase flow conditions, *Geophysical Research Letters*, *31*, L11605, doi:10.1029/2004GL020140, 2004.

Revil, A., and N. Linde, Chemico-electromechanical coupling in microporous media, *Journal of Colloid and Interface Science*, *302*, 682–694, 2006.

Revil, A., P. A. Pezard, and P. W. J. Glover, Streaming potential in porous media: 1. Theory of the zeta potential, *Journal of Geophysical Research*, *104*(B9), 20,021–20,031, 1999a.

Revil, A., H. Schwaeger, L. M. Cathles III, and P. D. Manhardt, Streaming potential in porous media: 2. Theory and application to geothermal systems, *Journal of Geophysical Research*, *104*(B9), 20,033–20,048, 1999b.

Revil, A., V. Naudet, J. Nouzaret, and M. Pessel, Principles of electrography applied to self-potential electrokinetic sources and hydrogeological applications, *Water Resources Research*, *39*(5), 1114, doi:10.1029/2001WR000916, 2003.

Revil, A., V. Naudet, and J. D. Meunier, The hydroelectric problem of porous rocks: Inversion of the position of the water table from self-potential data, *Geophysical Journal International*, *159*, 435–444, 2004.

Revil, A., L. Cary, Q. Fan, A. Finizola, and F. Trolard, Self-potential signals associated with preferential ground water flow pathways in a buried paleo-channel, *Geophysical Research Letters*, *32*, L07401, 2005.

Rizzo, E., B. Suski, A. Revil, S. Straface, and S. Troisi, Self-potential signals associated with pumping tests experiments, *Journal of Geophysical Research*, *109*, B10203, doi:10.1029/2004JB003049, 2004.

Rozycki, A., J. M. Ruiz Fonticiella, and A. Cuadra, Detection and evaluation of horizontal fractures in earth dams using the self-potential method, *Engineering Geology*, *82*, 145–153, doi:10.1016/j.enggeo.2005.09.013, 2006.

Sailhac, P., and G. Marquis, Analytic potentials for the forward and inverse modeling of SP anomalies caused by subsurface flow, *Geophysical Research Letters*, *28*(9), 1851–1854, 2001.

Sailhac, P., M. Darnet, and G. Marquis, Electrical streaming potential measured at the ground surface: Forward modeling and inversion issues for monitoring infiltration and characterizing the vadose zone, *Vadose Zone Journal*, *3*, 1200–1206, 2004.

Sato, M., and H. M. Mooney, The electrochemical mechanism of sulfide self-potentials, *Geophysics*, *25*(1), 226–249, 1960.

Saunders, J. H., M. D. Jackson, and C. C. Pain, A new numerical model of electrokinetic potential response during hydrocarbon recovery, *Geophysical Research Letters*, *33*, L15316, doi:10.1029/2006GL026835, 2006.

Schiavone, D., and R. Quarto, Self-potential prospecting in the study of water movements, *Geoexploration*, *22*, 47–58, 1984.

Sheffer, M. R., Response of the self-potential method to changing seepage conditions in embankment dams, M.A.Sc. thesis, University of British Columbia, Vancouver, 2002.

Sherard, J. L., R. J. Woodward, S. F. Gizienski, and W. A. Clevenger, *Earth and earth-rock dams*, John Wiley and Sons, New York, 1963.

Shi, W., Advanced modeling and inversion techniques for three-dimensional geoelectrical surveys, Ph.D. thesis, Massachusetts Institute of Technology, Cambridge, 1998.

Sill, W. R., Self-potential modeling from primary flows, *Geophysics*, *48*(1), 76–86, 1983.

Sill, W. R., and T. J. Killpack, SPXCPL - Two-dimensional modeling program of self-potential effects from cross-coupled fluid and heat flow: User's guide and documentation for Version 1.0, *Tech. rep.*, Earth Science Laboratory, University of Utah Research Institute, Salt Lake City, 1982.

Suski, B., A. Revil, K. Titov, P. Konosavsky, M. Voltz, C. Dagès, and O. Huttel, Monitoring of an infiltration experiment using the self-potential method, *Water Resources Research*, *42*, W08418, doi:10.1029/2005WR004840, 2006.

Titov, K., Y. Ilyin, P. Konosavski, and A. Levitski, Electrokinetic spontaneous polarization in porous media: Petrophysics and numerical modelling, *Journal of Hydrology*, *267*, 207–216, 2002.

Titov, K., A. Levitski, P. K. Konosavski, A. V. Tarasov, Y. T. Ilyin, and M. A. Bues, Combined application of surface geoelectrical methods for groundwater-flow modeling: A case history, *Geophysics*, *70*(5), H21–H31, 2005a.

Titov, K., A. Revil, P. Konosavsky, S. Straface, and S. Troisi, Numerical modelling of self-potential signals associated with a pumping test experiment, *Geophysical Journal International*, *162*, 641–650, 2005b.

Wilt, M. J., and D. K. Butler, Numerical modeling of SP anomalies: Documentation of program SPPC and applications, Report 4, in *Geotechnical Applications of the Self-Potential Method, Technical Report REMR-GT-6*, Department of the Army, U.S. Army Corps of Engineers, Washington, 1990.

Wilt, M. J., and R. F. Corwin, Numerical modeling of self-potential anomalies due to leaky dams: Model and field examples, in *Detection of Subsurface Flow Phenomena*, *Lec-*

ture Notes in Earth Sciences, vol. 27, edited by G. P. Merkler, H. Militzer, H. Hötzl, H. Armbruster, and J. Brauns, pp. 73–89, Springer-Verlag, Berlin, 1989.

Wurmstich, B., and F. D. Morgan, Modeling of streaming potential responses caused by oil well pumping, *Geophysics*, *59*(1), 46–56, 1994.

Wurmstich, B., F. D. Morgan, G. P. Merkler, and R. L. Lytton, Finite-element modeling of streaming potentials due to seepage: Study of a dam, *Society of Exploration Geophysicists Technical Program Expanded Abstracts*, *10*, 542–544, 1991.

Yüngül, S., Interpretation of spontaneous polarization anomalies caused by spheroidal orebodies, *Geophysics*, *15*(2), 237–246, 1950.

Chapter 2

Three-dimensional forward modelling of streaming potential [1]

2.1 Introduction

Fluid flow through porous media generates electrical current flow, which can be characterized through a series of electrode measurements to produce a map of potential. This electrokinetic phenomenon of streaming potential is one of several coupled flow mechanisms, such as thermoelectric and electrochemical effects, that can be measured using the self-potential (SP) method.

Streaming potential is the common if not dominant driving mechanism for the SP signal in geothermal exploration [*Corwin and Hoover*, 1979; *Ishido and Pritchett*, 1999], earthquake prediction [*Mizutani et al.*, 1976; *Corwin and Morrison*, 1977; *Fitterman*, 1978], groundwater studies [*Titov et al.*, 2005a], and engineering and environmental investigations [*Bogoslovsky and Ogilvy*, 1973; *Corwin*, 1990].

Given the analogous behaviour of hydraulic and electrical flow systems and the principles of coupled flow, the self-potential distribution can be studied to evaluate characteristics of the hydraulic regime. A coupled flow model is required to explain the interaction of the hydraulic and electrical flow systems, and the convection current approach proposed by *Sill* [1983] has been the elemental theory implemented in most numerical investigations of streaming potential. *Wurmstich et al.* [1991] used a 2-D finite element code to analyze seepage and the streaming potential response in a model embankment. *Wurmstich and Morgan* [1994] developed a 3-D finite difference algorithm to study streaming potential

[1] A version of this chapter has been published. Sheffer, M.R. and Oldenburg, D.W. (2007) Three-dimensional modelling of streaming potential, Geophysical Journal International, 169:839-848

signals caused by oil well pumping in a fluid-saturated halfspace. *Ishido and Pritchett* [1999] studied the streaming potential response in geothermal reservoir simulations using a finite difference post-processor. *Revil et al.* [1999] used a finite element model to evaluate the streaming potential response over a geothermal field driven by both advective and convective fluid flow. *Titov et al.* [2002, 2005b] developed a 2-D finite difference program to evaluate streaming potential responses in groundwater flow problems.

In this paper we present a 3-D finite volume algorithm for calculating the self-potential distribution resulting from fluid flow in a porous medium. The algorithm was developed to enable the study of variably saturated flow problems of complex geometry for application to engineering and hydrogeological investigations. The equations that describe the hydraulic and electrical flow problems are developed in Section 2.2. Section 2.3 describes the forward modelling methodology and the finite volume solution for self-potential. The numerical solution of a simple flow problem is compared with an analytical solution as a means of verifying the algorithm.

A quantitative study of streaming potential relies on realistic estimates of the relevant physical properties. Section 2.4 discusses the assignment of streaming current cross-coupling conductivity and electrical conductivity distributions for different hydraulic systems. The unconfined flow problem of seepage through a homogeneous embankment is studied as an example. Section 2.5 develops an equation that describes primary and secondary sources of charge that contribute to the self-potential response. An example of a pumping well is used to illustrate how heterogeneous physical property distributions give rise to secondary sources of charge, which can contribute significantly to the SP response.

Finally, a field data example of seepage through an earth embankment and foundation is described in Section 2.6. This example clearly illustrates the need for 3-D modelling capability to correctly capture the flow regime in a problem of complex geometry.

2.2 Theory

2.2.1 Primary flow

Fluid flow through a fully-saturated porous medium is described using the mass conservation equation stated in terms of hydraulic head h [m]:

$$\nabla \cdot \boldsymbol{q} = -S_s \frac{\partial h}{\partial t} + Q_v \, \delta(r - r_s) \, , \tag{2.1}$$

where $\boldsymbol{q}$ is the volumetric flux [$\mathrm{m^3\,s^{-1}\,m^{-2}}$], Q_v is an additional term used to represent any external point sources of fluid flow imposed on the volume [$\mathrm{m^3\,s^{-1}\,m^{-3}}$], and r_s denotes the source location. The specific storage of the volume, S_s [$\mathrm{m^3\,m^{-1}\,m^{-3}}$] takes the form

$$S_s = \rho_f g(\alpha + n\beta) \, , \tag{2.2}$$

where ρ_f is fluid density [$\mathrm{kg\,m^{-3}}$], α is the compressibility of the solid matrix [$\mathrm{m^3\,Pa^{-1}\,m^{-3}}$], n is porosity [$\mathrm{m^3\,m^{-3}}$], β is the fluid compressibility [$\mathrm{m^3\,Pa^{-1}\,m^{-3}}$], and g is gravitational acceleration.

Phenomenological laws have been shown empirically to describe irreversible flow as a linear relation between flux and the gradient of a scalar potential. Fluid flux under laminar flow conditions may be described using a form of Darcy's law:

$$\boldsymbol{q} = -K \nabla h, \tag{2.3}$$

where K is the hydraulic conductivity [$\mathrm{m\,s^{-1}}$] of the volume under study.

The conservation of charge equation is used to describe electrical current flow:

$$\nabla \cdot (\rho_e \boldsymbol{v}) = -\frac{\partial \rho_e}{\partial t} \, , \tag{2.4}$$

where $\boldsymbol{v}$ is the volumetric flux [$\mathrm{m^3\,s^{-1}\,m^{-2}}$] and ρ_e is the volumetric charge density [$\mathrm{C\,m^{-3}}$]. The charge flux term $\rho_e \boldsymbol{v}$ may be written instead as a volumetric current density $\boldsymbol{J}$ [$\mathrm{A\,m^{-2}}$], by considering the definition of electric current. Equation (2.4) now takes the form

$$\nabla \cdot \boldsymbol{J} = -\frac{\partial \rho_e}{\partial t} + I_v \, \delta(r - r_s) \, , \tag{2.5}$$

where I_v [$\mathrm{A\,m^{-3}}$] is the current flow of any external source imposed on the volume. Conduction current density is described using Ohm's law:

$$\boldsymbol{J} = -\sigma \nabla \phi \, , \tag{2.6}$$

where ϕ [V] is the electrical potential and σ [$\mathrm{S\,m^{-1}}$] is the electrical conductivity.

2.2.2 Coupled flow

The interdependence of fluid, temperature, electrical and chemical flow systems can be defined using the theory of coupled flow, which describes the flux of a given quantity in terms of the sum of primary and secondary gradients. A generalized constitutive relation that includes both primary and coupled flow terms is

$$\mathbf{\Gamma}_i = -\sum_{j=i}^{n} L_{ij} \nabla \Phi_j \ , \tag{2.7}$$

where $\mathbf{\Gamma}_i$ is the flux of the quantity i under study, Φ_j is the scalar potential, and L_{ij} is the conductivity term, which is an averaged macroscopic property representative of the volume under study.

The importance of each term on the total flux is dependent on the relative magnitude of the gradient and the corresponding conductivity coefficient such that, for sufficiently slow processes, flow may result from not only the primary gradient, but also from the secondary gradients. In the absence of significant chemical or temperature gradients the coupled flow equations that describe electrokinetic phenomena are

$$\mathbf{\Gamma}_f = -L_{ff} \nabla \Phi_f - L_{fe} \nabla \Phi_e \tag{2.8a}$$

and

$$\mathbf{\Gamma}_e = -L_{ee} \nabla \Phi_e - L_{ef} \nabla \Phi_f \ . \tag{2.8b}$$

The cross-coupling conductivity coefficients link the secondary gradients to the primary flow terms such that $L_{fe} \nabla \Phi_e$ describes fluid flow due to electro-osmosis and $L_{ef} \nabla \Phi_f$ describes streaming current flow. These phenomena are connected through the Onsager reciprocal relations that state $L_{fe} = L_{ef}$, provided the flux and gradient terms are formulated properly, and that flow can be adequately represented by linear constitutive equations in a given system [*Onsager*, 1931].

The gradient terms are considered thermodynamic forces and must be formulated to uphold the principles of nonequilibrium thermodynamics [*de Groot*, 1951]. Consequently,

potential must be expressed in terms of energy per unit quantity i. We define the hydraulic potential Φ_f [$\mathrm{J\,kg^{-1}}$ or $\mathrm{m^2\,s^{-2}}$], which may be described using Bernoulli's equation and related to hydraulic head through the relation $\Phi_f = gh$. Accordingly, $\Gamma_f = \rho_f \boldsymbol{q}_T$ represents the total mass flux, and the primary conductivity term can be defined as $L_{ff} = \rho_f K/g$. Substituting these relations into (2.8a) gives

$$\rho_f \boldsymbol{q}_T = -\frac{\rho_f K}{g}\nabla gh - L_{fe}\nabla\phi \,. \tag{2.9}$$

In a similar fashion, $\Phi_e = \phi$ is the electric potential [$\mathrm{J\,C^{-1}}$ or V], $\Gamma_e = \boldsymbol{J}_T$ represents the total charge flux [$\mathrm{C\,s^{-1}\,m^{-2}}$ or $\mathrm{A\,m^{-2}}$], and $L_{ee} = \sigma$ is the electrical conductivity. Equation (2.8b) now becomes

$$\boldsymbol{J}_T = -\sigma\nabla\phi - L_{ef}\nabla gh \,. \tag{2.10}$$

The cross-coupling coefficients L_{fe} and L_{ef} in (2.9) and (2.10) are equal and have units of [$\mathrm{A\,s^2\,m^{-3}}$]. Re-arranging terms simplifies the equations to

$$\boldsymbol{q}_T = -K\nabla h - k_e\nabla\phi \tag{2.11a}$$

and

$$\boldsymbol{J}_T = -\sigma\nabla\phi - L\nabla h \,, \tag{2.11b}$$

where $k_e = L_{fe}/\rho_f$ is the coefficient of electro-osmotic permeability [$\mathrm{m^2\,s^{-1}\,V^{-1}}$] and $L = gL_{ef}$ is the streaming current cross-coupling conductivity coefficient [$\mathrm{A\,m^{-2}}$].

2.2.3 Governing equations

The constitutive relations defined in (2.11) are now combined with the continuity equations to define the hydraulic and electrical flow problems.

In the study of streaming potentials, the hydraulic gradient is the driving force and the second term in (2.11a) can be neglected. This is supported by *Mitchell* [1991], who reported negligible contribution of the electro-osmotic flow term in materials with $K > 10^{-9}\,\mathrm{m/s}$.

We recognize this uncoupled flow equation as a form of Darcy's law, which is combined with (2.1) to define the saturated hydraulic flow equation:

$$\nabla \cdot K\nabla h = S_s \frac{\partial h}{\partial t} - Q_v\, \delta(r - r_s) \; . \tag{2.12}$$

Variably saturated flow problems require the use of both (2.12) and an unsaturated flow equation, such as

$$\nabla \cdot K(S_w)\nabla h = n\frac{\partial S_w}{\partial t} - Q_v\, \delta(r - r_s) \; , \tag{2.13}$$

where K is now a function of fluid saturation S_w. Steady-state or transient forms of the fluid flow equation may be used to solve the hydraulic problem, depending on the temporal nature of the boundary conditions.

Once we have solved the hydraulic problem for the distribution of hydraulic head h, the subsequent problem is to solve for the self-potential distribution. Since hydraulic relaxation times are orders of magnitude larger than electrical relaxation times, electrical conduction current flow is treated as a steady-state process regardless of the nature of the hydraulic process. This suggests that "snapshots" of the fluid flow regime over time may be analysed as a DC problem. Substitution of (2.11b) into the steady-state form of (2.5) results in the coupled electrical flow equation:

$$\nabla \cdot \sigma\nabla\phi = -\nabla \cdot L\nabla h \; , \tag{2.14}$$

when there are no imposed external sources of current flow.

2.3 Forward modelling methodology

The fluid and electrical flow equations are similar in form and hence one could envisage using the same algorithm [e.g., *Wurmstich and Morgan*, 1994]. However, we choose to use established programs to solve the hydraulic problem to facilitate both mixed boundary conditions and model calibration, as well as the solution of variably saturated flow problems.

Fluid flow modelling is performed using the 3-D finite difference codes MODFLOW, developed by the US Geological Survey [*Harbaugh et al.*, 2000], for saturated flow and MODFLOW-Surfact [*HydroGeoLogic Inc.*, 1996] for variably saturated flow problems.

The electrical equation (2.14) is solved using a finite volume approach and our code is independent of the solution of the hydraulic problem. All that is required is to be able to import values of the hydraulic head. In the following sections we outline the numerical details that pertain to our solution.

2.3.1 Finite volume solution for self-potential

The flow domain constitutes a three-dimensional volume, which consists of a homogeneous or heterogeneous earth model and in some cases surface water, as indicated in Figure 2.1. We recognize electrical property distributions to be discontinuous at interfaces between different materials in the subsurface (e.g. between units 1 and 2 in Figure 2.1), as well as at the earth's surface, where a large conductivity contrast exists. Consequently, we do not wish to evaluate the derivative of σ and instead restate (2.14) as two first-order equations with unknown variables $\boldsymbol{J}$ and ϕ:

$$\nabla \cdot \boldsymbol{J} = f \tag{2.15a}$$

and

$$\sigma^{-1}\boldsymbol{J} - \nabla\phi = 0 \,, \tag{2.15b}$$

where $\boldsymbol{J}$ is the conduction current density. The source term f describes sources of streaming current:

$$f = -\nabla \cdot L\nabla h \,. \tag{2.15c}$$

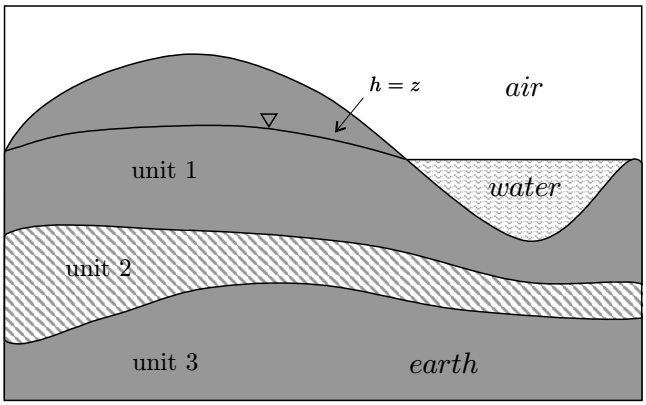

Figure 2.1: Schematic of the spatial flow domain.

The differential equations (2.15a) and (2.15b) are expressed in their weak forms and discretized using a finite volume method [*Haber et al.*, 2000]. The chosen arrangement of (2.15b) is a consequence of the fact that while $\boldsymbol{J}$ is a continuous function, σ and $\nabla\phi$ are discontinuous across an interface separating regions of different conductivity. Integrating these discontinuous variables separately adds accuracy to the solution for ϕ.

The study region is represented by a rectilinear mesh of grid cells. The discrete equations are solved on a staggered grid, with normal components of $\boldsymbol{J}$ located at cell faces and values of potential located at cell centres, as shown in Figure 2.2. Each grid cell is assigned an electrical conductivity σ and a cross-coupling conductivity L. These properties are treated as a constant for each cell, but are considered to be piecewise constant in the domain and can vary significantly from one cell to the next.

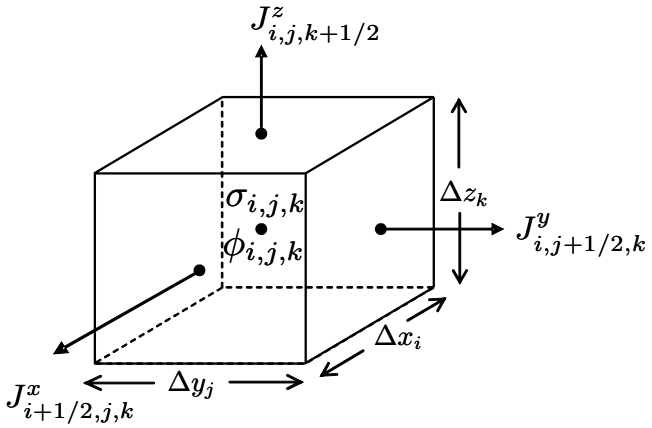

Figure 2.2: Discrete grid cell showing cell dimensions, location of components of current density $\boldsymbol{J}$ at cell faces, and location of potential ϕ and conductivity σ at the cell centre.

The equations in (2.15) must be supplied with boundary conditions. In our implementation we define the outer surface of the domain $\partial\Omega$ as a Neumann no-flow boundary:

$$\boldsymbol{J} \cdot \hat{\mathbf{n}}|_{\partial\Omega} = 0 \; . \tag{2.16}$$

This condition requires that the outer edge of the domain be positioned far from convective sources to remove the influence of the boundary on the solution in the region of interest. To achieve this, the mesh is expanded beyond the physical extents of the study region by successively increasing cell dimensions in each direction.

The electrical conductivity and cross-coupling conductivity models are defined on the expanded mesh, which is generally much larger than the volume studied in hydraulic modelling. The cross-coupling coefficients in this expanded region are set to zero, but a serious effort should be made to estimate reasonable values of electrical conductivity. A more detailed treatment of electrical property models is given in Section 2.4.

Applying the finite volume technique to the equations in (2.15) yields the discrete system:

$$\mathbf{DSG}\boldsymbol{\phi} = -\mathbf{DLGh}, \tag{2.17}$$

where matrix $\mathbf{D}$ is the divergence operator, $\mathbf{G}$ is the gradient operator and the physical property matrices $\mathbf{S}$ and $\mathbf{L}$ respectively contain the harmonic averages of electrical conductivity σ and cross-coupling coefficient L. Vectors $\boldsymbol{\phi}$ and $\mathbf{h}$ respectively contain values of electrical potential and hydraulic head. The no-flow boundary condition in (2.16) is imposed by the divergence matrix $\mathbf{D}$. Equation 2.17 represents a non-unique solution for ϕ. This non-uniqueness is removed by specifying a constant value of ϕ at a single corner of the grid.

The matrix system in (2.17) is solved using the biconjugate gradient stabilized method (BiCGSTAB) [*Van der Vorst*, 1992] with preconditioning [*Barrett et al.*, 1994]. For preconditioning we use either symmetric successive over relaxation (SSOR) or incomplete LU (ILU).

Once (2.17) has been solved, potential or potential difference data are evaluated as:

$$\mathbf{d} = \mathbf{Q}\boldsymbol{\phi}, \tag{2.18}$$

where matrix $\mathbf{Q}$ performs a tri-linear interpolation of ϕ using the eight nearest cell values. In a practical SP survey configuration, data are potential differences that are acquired with respect to a reference electrode. The reference electrode can be located at an arbitrary coordinate in the grid.

2.3.2 Example: Injection well in a homogeneous halfspace

A single point source of fluid flow in a homogeneous, saturated halfspace is a straightforward flow problem that is useful to illustrate the SP response to a primary source of streaming

current, and to verify the numerical algorithm against an analytical solution.

The hydraulic problem represents an injection well that is screened over a finite portion of its length, as illustrated in Figure 2.3. The semi-infinite homogeneous halfspace was modelled as a single isotropic geologic unit 500m-thick extending 10 km in both x and y directions. Halfspace properties are $K_o = 1 \times 10^{-4}$ m/s, $L_o = 1 \times 10^{-5}$ A/m^2, and $\sigma_o = 1 \times 10^{-3}$ S/m . The well screen is centred at a depth of 25 m, and fluid is injected at a constant flow rate of 10,000 m^3/day.

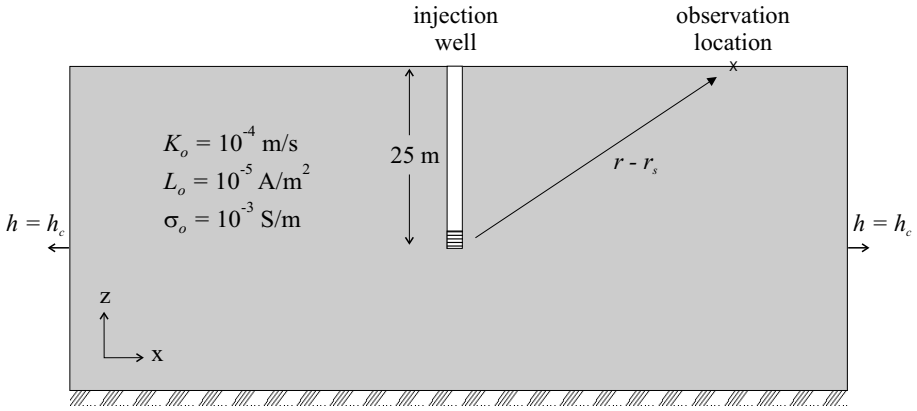

Figure 2.3: Homogeneous halfspace model with injection well showing hydraulic boundary conditions and physical properties of aquifer.

2.3.2.1 Numerical solution

Hydraulic head was resolved on a 190 × 190 × 35 non-uniform mesh. Cell lengths in the x and y directions ranged from 3.3 m at the centre of the mesh to 100 m at the edges. Cell heights ranged from 3.3 m at the well screen to 20 m at depth. A constant head boundary of 500 m was defined at the x and y limits of the mesh. This discretization was chosen to facilitate an accurate solution of head in the vicinity of the well. The self-potential distribution was resolved on a 212 × 212 × 52 mesh in which cell size was progressively expanded by a factor of 1.3. Potential data are referenced to a surface point at the edge of the study region, 5 km from the well. Figure 2.4 shows the predicted hydraulic head distribution in the xz plane of the well. Results are presented as a surface profile in Figure 2.4(a), and in

cross-section in Figure 2.4(b). Similarly, the predicted self-potential distribution is presented in Figure 2.5. Although they are of opposite polarity, a strong similarity is evident between the SP and head equipotential distributions.

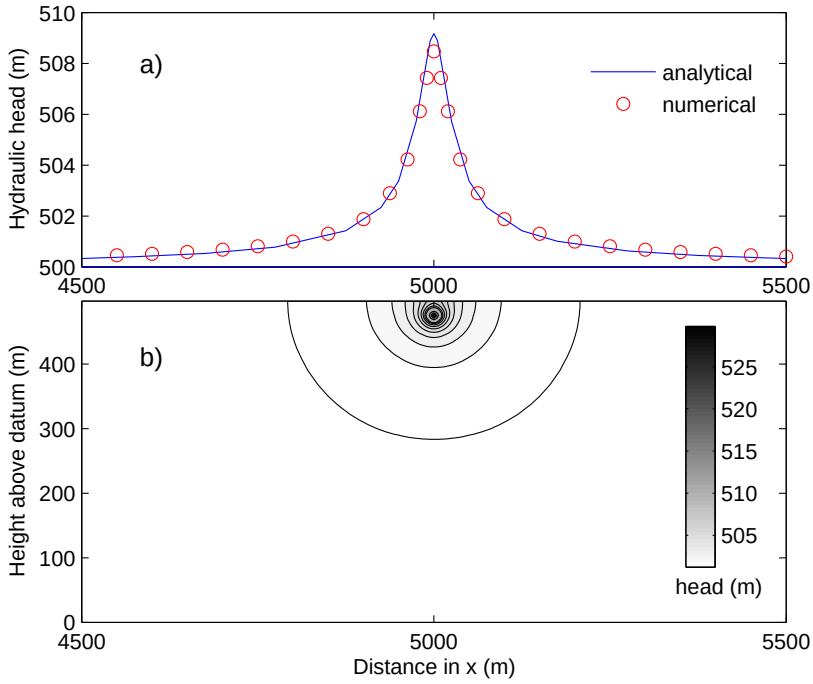

Figure 2.4: Hydraulic head distribution resulting from a point injection well in a homogeneous halfspace: a) analytical and numerical solutions at surface; b) predicted head contours (1 m interval).

2.3.2.2 Analytical solution

To facilitate an analytical solution the equations governing hydraulic and electrical flow are stated as Poisson's equations. The hydraulic equation that defines this problem is the steady-state form of (2.12):

$$\nabla^2 h = -\frac{1}{K} Q_v \, \delta(r - r_s). \tag{2.19}$$

Similarly, substitution of (2.19) into (2.14) reduces the electrical flow equation to:

$$\nabla^2 \phi = \frac{L}{\sigma K} Q_v \, \delta(r - r_s). \tag{2.20}$$

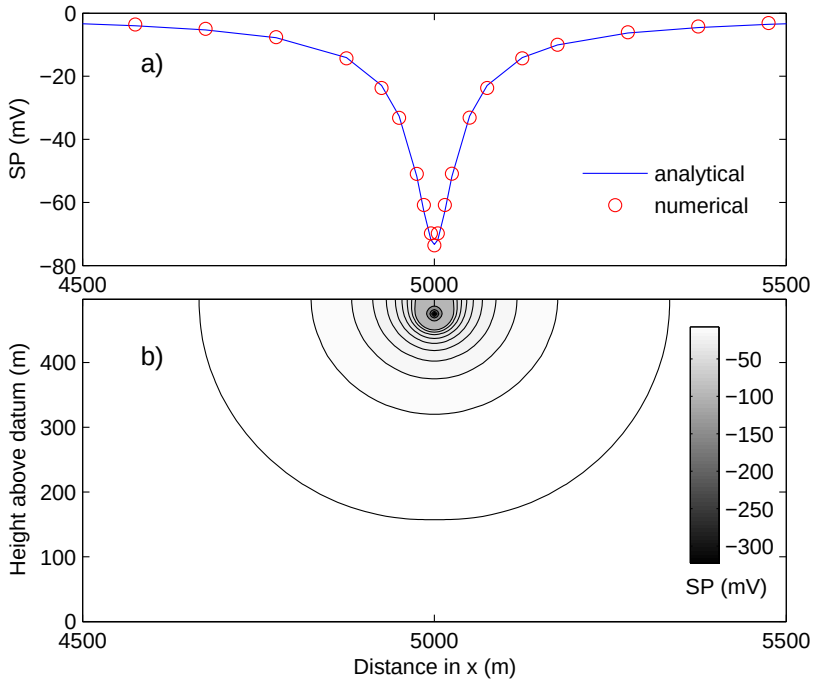

Figure 2.5: Self-potential distribution resulting from a point injection well in a homogeneous halfspace: a) analytical and numerical solutions at surface; b) predicted SP contours (5 mV interval).

The method of images is used to solve the problem analytically, to account for perturbations in the potential fields caused by the presence of the ground surface. When observations are made at surface, the solutions to (2.19) and (2.20) reduce to:

$$h(x, y, 500) = -\frac{Q(r_s)}{2\pi K|r - r_s|} \tag{2.21}$$

and

$$\phi(x, y, 500) = \frac{LQ(r_s)}{2\pi\sigma K|r - r_s|}, \tag{2.22}$$

respectively, where $Q(r_s)$ is the volumetric flow rate of the source $[\,\mathrm{m}^3\,\mathrm{s}^{-1}\,]$ and $|r - r_s|$ denotes the distance between the source and observation location. The analytical solutions for h and ϕ at the ground surface show excellent agreement with the numerical results, as illustrated in the profile plots of Figures 2.4 and 2.5.

2.4 Physical properties

2.4.1 The cross-coupling conductivity coefficient

By applying the divergence theorem, the coupled electrical flow equation (2.14) can be expressed as

$$\int_s \sigma \nabla \phi \cdot d\mathbf{s} = -\int_s L \nabla h \cdot d\mathbf{s} \; . \tag{2.23}$$

In a homogeneous medium,

$$\sigma \int_s \nabla \phi \cdot \hat{\mathbf{n}} \, ds = -L \int_s \nabla h \cdot \hat{\mathbf{n}} \, ds \; , \tag{2.24}$$

where L and σ are macroscopic properties. If we consider a 1-D flow experiment in a porous medium of length Δx and cross-sectional area A, in which flow occurs along the length of the medium, (2.24) is evaluated to give

$$\sigma \frac{\Delta \phi}{\Delta x} A = -L \frac{\Delta h}{\Delta x} A \; . \tag{2.25}$$

Equation (2.25) may be further simplified and rearranged to define the cross-coupling conductivity:

$$L = -\sigma C \; , \tag{2.26}$$

where

$$C = \frac{\Delta \phi}{\Delta h}. \tag{2.27}$$

The streaming potential coupling coefficient C, which is often reported in terms of fluid pressure, may be characterized through laboratory measurements and is typically a negative quantity [e.g., *Ishido and Mizutani*, 1981; *Morgan et al.*, 1989; *Jouniaux and Pozzi*, 1995; *Pengra et al.*, 1999]. The above definition of C is consistent with our formulation of the coupled flow equations in terms of hydraulic head, as shown in (2.11).

2.4.2 Defining σ and L property distributions

Representative values of the cross-coupling conductivity and electrical conductivity must be prescribed for all porous media in the model domain, and can be assigned using measured or theoretical estimates. Electrical conductivity can be measured in the field or laboratory

using geophysical techniques such as the DC resistivity method, or estimated in certain cases using an empirical relation such as Archie's Law [*Archie*, 1942], which can be adjusted to account for varying degrees of saturation [e.g., *Bear*, 1972]. The streaming potential coupling coefficient can be measured in the laboratory as noted in the section above, or estimated using a form of the Helmholtz-Smoluchowski equation [*Overbeek*, 1952], which shows that C is a function of fluid conductivity. Since both σ and C vary with the electrical conductivity of the saturating fluid, appropriate corresponding values must be used to calculate L using (2.26).

As illustrated in Figure 2.1, the flow domain comprises an earth model and may also include surface water. The earth model can consist of a number of distinct units, where each unit is characterized by representative values of L and σ. Since streaming current flow is limited only to porous media, air and water bodies are assigned a null cross-coupling conductivity to impose a no-flow boundary at the physical limits of the porous medium. However, surface water is assigned representative values of fluid conductivity σ_f to permit conduction current flow. Air is typically assigned a null electrical conductivity.

In a confined fluid flow problem, the earth model under study is in a completely saturated state. Consequently, saturated material properties are used to describe each unit, i.e. $L = L^{sat}$ and $\sigma = \sigma^{sat}$. In an unconfined fluid flow problem, a phreatic surface delineates the boundary between saturated and unsaturated zones. The position of this boundary is defined where pore fluid pressure is atmospheric (i.e., $h = z$), as indicated in Figure 2.1. If the phreatic surface intersects a given earth model unit, representative properties must be assigned to both saturated and unsaturated zones within the unit.

There are two approaches to determining a hydraulic solution to an unconfined flow problem. In a saturated or free-surface approach, fluid flow is assumed to dominate below the phreatic surface and is not considered in the unsaturated zone. The position of the phreatic surface, and consequently the size of the saturated model domain, is not known a-priori and is determined through the hydraulic flow analysis. In a variably saturated approach, fluid flow is evaluated within both the saturated and unsaturated zones. This latter approach generates a more realistic hydraulic solution in problems with steeply-dipping interfaces, and is necessary for transient simulations [*Freeze*, 1971]. The delineation

between saturated and unsaturated zones is determined by the condition $h = z$.

The behaviour of streaming current flow in the unsaturated zone is not addressed here. We consider streaming current flow to be limited to the saturated zone, such that the phreatic surface acts as a no-flow boundary. This condition is imposed by specifying $L^{unsat} = 0$. However, the conduction current permeates both saturated and unsaturated zones, and a representative σ^{unsat} is chosen to reflect the unsaturated or partially saturated conditions of the material. For simplicity, we assume a constant value of σ^{unsat} for each unit, which does not vary with the decline in saturation above the phreatic surface. The next example illustrates the assignment of physical properties in an unconfined flow problem.

2.4.3 Example: Homogeneous lab-scale embankment

The SP response to steady-state seepage through a laboratory-scale embankment is examined as an example of an unconfined flow problem, and provides a means of verifying the SP algorithm with measured data.

The homogeneous embankment under study was constructed of Ottawa sand in an acrylic tank and measures 140 cm in length, 10 cm in width and 31 cm in height. The dam was subjected to steady-state flow from constant reservoir heights of 18 cm and 22.5 cm. The hydraulic conductivity and electrical properties of the sand were derived from laboratory testing and are represented in the model as: $K = 4.5 \times 10^{-4}$ m/s, $L^{sat} = 2.5 \times 10^{-4}$ A/m^2, $\sigma^{sat} = 2.5 \times 10^{-3}$ S/m and $\sigma^{unsat} = 1.5 \times 10^{-3}$ S/m. The electrical conductivity of the reservoir water σ_f was measured as 2.8×10^{-3} S/m. Figure 2.6 illustrates a schematic of the electrical property distribution in the study region.

The embankment was modelled using a $70 \times 5 \times 16$ mesh with a uniform cell dimension of 2 cm. The self-potential distribution was resolved on a padded grid, in which padding cells were assigned an electrical conductivity of 1×10^{-8} S/m to represent air. The predicted hydraulic head distribution and SP response at the surface of the embankment are shown for each reservoir level in Figures 2.7 and 2.8. The SP data are referenced to a point centred at the surface of the crest. Predicted and measured SP data at each reservoir level are compared in Figures 2.7(a) and 2.8(a) and show good agreement. The increase in SP amplitude with reservoir level is a direct consequence of the increase in hydraulic gradient

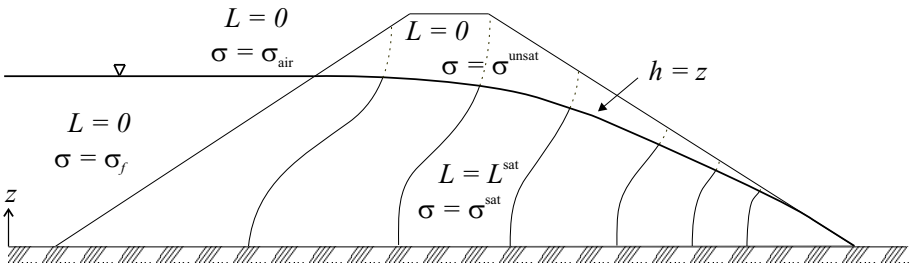

Figure 2.6: Schematic cross-section of a homogeneous earth embankment, illustrating the distribution of electrical properties. Hydraulic head equipotential lines are indicated in the figure, with dotted lines representing hydraulic head in the unsaturated zone. Superscripts *sat* and *unsat* refer to representative properties of the saturated and unsaturated zones, respectively. The value σ_f represents the electrical conductivity of the impounded water. The value σ_{air} is typically chosen as 1×10^{-8} S/m.

across the embankment.

The chosen L and σ property distributions influence how electrical current flows in the subsurface. Figure 2.9 displays fluid, streaming current and conduction current flux patterns for the 22.5 cm reservoir model described in Figure 2.8. Figure 2.9(a) shows vectors of fluid flux $\boldsymbol{q}$ within the saturated zone below the phreatic surface. Figure 2.9(b) displays streaming current flow, which is limited to the saturated zone since the electrical problem is solved using a saturated flow assumption ($L^{unsat} = 0$). Streaming current and fluid flow vector fields appear very similar since both processes are driven by hydraulic gradients in the saturated zone. Figure 2.9(c) illustrates vectors of conduction current flow $\boldsymbol{J}$, which is not confined to the saturated zone and is governed by the electrical conductivity distribution.

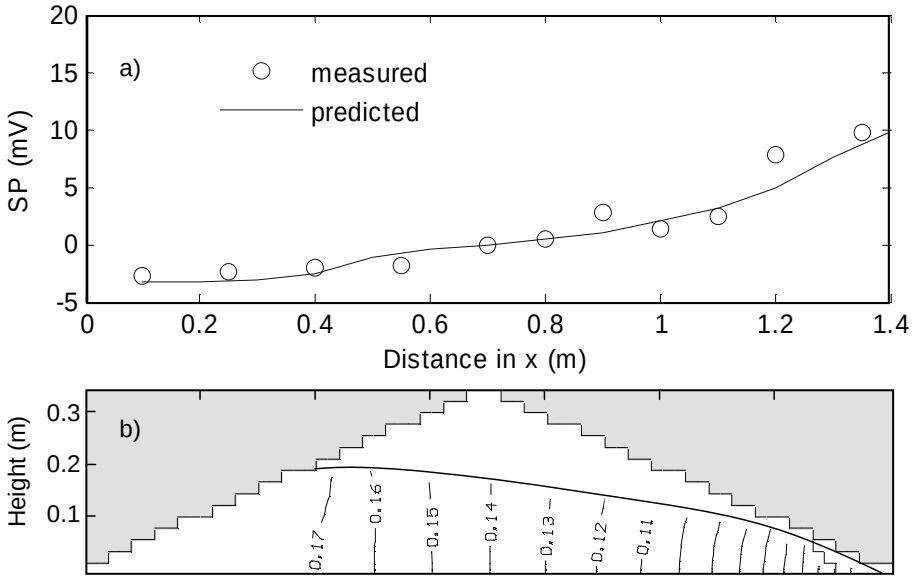

Figure 2.7: Homogeneous embankment subject to steady-state seepage from an 18 cm reservoir: a) Measured and predicted SP data at surface; b) predicted hydraulic head distribution (m).

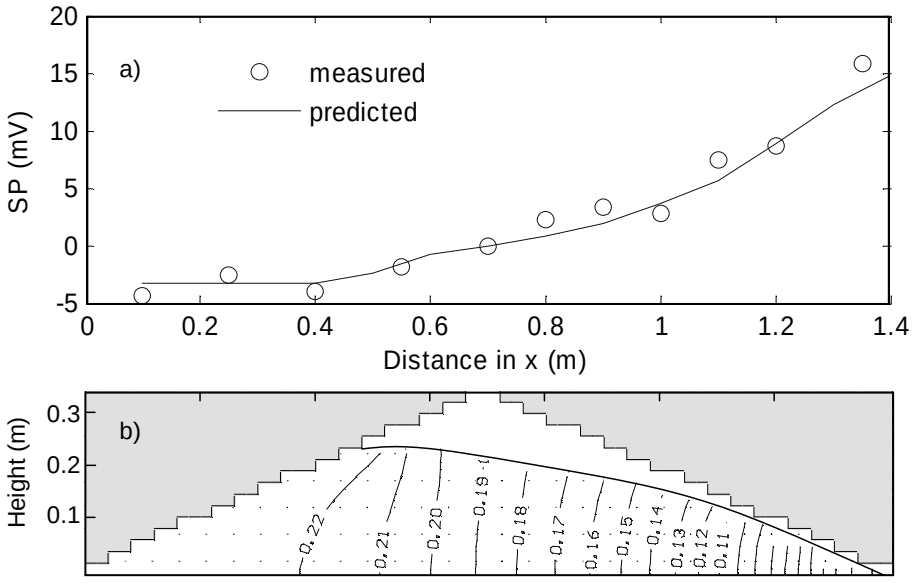

Figure 2.8: Homogeneous embankment subject to steady-state seepage from a 22.5 cm reservoir: a) Measured and predicted SP data at surface; b) predicted hydraulic head distribution (m).

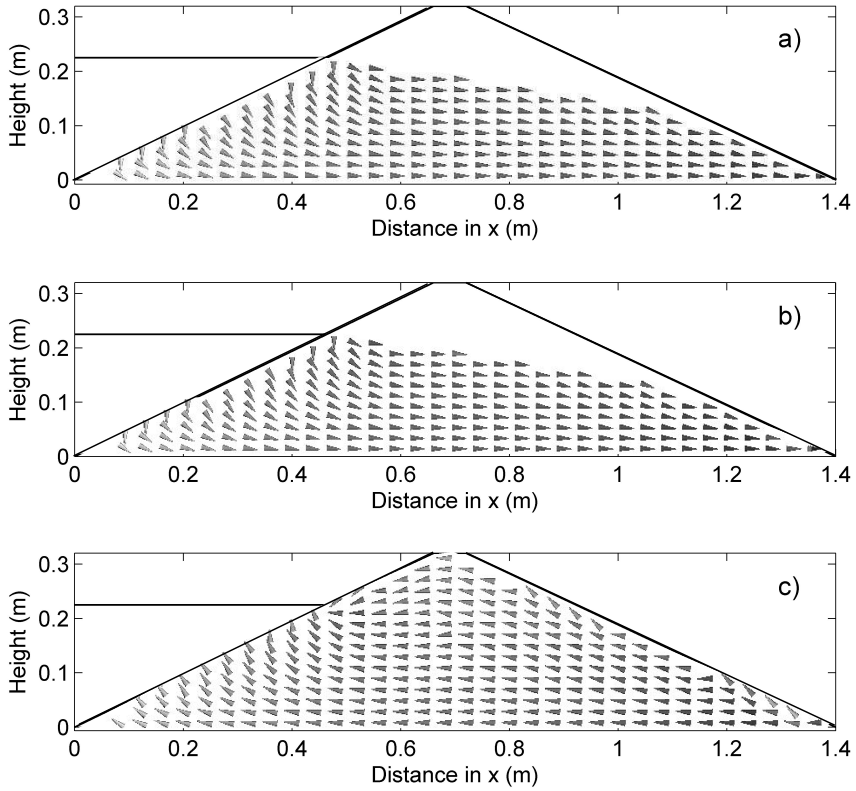

Figure 2.9: Homogeneous embankment subject to steady-state seepage from a 22.5 cm reservoir: a) fluid flux $\boldsymbol{q}$; b) streaming current; c) conduction current $\boldsymbol{J}$.

2.5 Sources of charge contributing to the self-potential

Conduction current flow and the corresponding self-potential field is governed by the distribution of streaming current sources and electrical conductivity in the subsurface. To enable an intuitive understanding of the potential response, (2.14) is expressed as a Poisson equation and restated in terms of charge density. This equation clearly defines the physical conditions that dictate the magnitude and sign of current sources in the subsurface. All properties are assumed isotropic for the sake of discussion.

The source function f defined in (2.15) describes all sources of streaming current in the study region. The nature of these convective sources may be examined by expanding (2.15a) to:

$$\nabla \cdot \boldsymbol{J} = -L\nabla^2 h - \nabla L \cdot \nabla h \; . \tag{2.28}$$

The steady-state form of (2.12) is expanded and re-arranged to give:

$$\nabla^2 h = -\frac{1}{K} Q_v \, \delta(r - r_s) - \frac{1}{K} \nabla K \cdot \nabla h \; . \tag{2.29}$$

Substitution of (2.29) into (2.28) results in:

$$\nabla \cdot \boldsymbol{J} = \frac{L}{K} Q_v \, \delta(r - r_s) + \frac{L}{K} \nabla K \cdot \nabla h - \nabla L \cdot \nabla h \; . \tag{2.30}$$

Here we see an explicit definition of streaming current sources, which may be grouped into two distinct types: 1) "primary" sources due to the injection or withdrawal of fluid from the system, as described by the fluid flow source term Q_v; and 2) "secondary" sources that are generated by gradients in the physical properties K and L in the presence of a hydraulic gradient.

Heterogeneities in σ will perturb the potential field generated by the streaming current source distribution, such that boundaries between regions of different σ may also be considered as secondary sources. Invoking Ohm's law, (2.30) is expanded and re-stated as Poisson's equation for potential ϕ:

$$\nabla^2 \phi = \frac{L}{\sigma K} Q_v \, \delta(r - r_s) + \frac{L}{\sigma K} \nabla K \cdot \nabla h - \frac{1}{\sigma} \nabla L \cdot \nabla h - \frac{1}{\sigma} \nabla \sigma \cdot \nabla \phi \; , \tag{2.31}$$

where the right hand side is the source function that describes all sources that contribute to ϕ. Finally, (2.31) is expressed in terms of volumetric charge density ρ_e [$\mathrm{C\,m^{-3}}$] using

Gauss' law:

$$\rho_e = \epsilon_o \left\{ -\frac{L}{\sigma K} Q_v \, \delta(r - r_s) - \frac{L}{\sigma K} \nabla K \cdot \nabla h + \frac{1}{\sigma} \nabla L \cdot \nabla h + \frac{1}{\sigma} \nabla \sigma \cdot \nabla \phi \right\} . \tag{2.32}$$

The self-potential ϕ is the sum of all potential fields generated by primary and secondary sources of charge within the system, according to the superposition principle. The potential decays with the inverse radial distance $|r - r_s|$ from each source of charge defined by $\rho_e(r_s)$, which may be evaluated through the integral solution:

$$\phi(r) = \frac{1}{4\pi\epsilon_o} \int_V \frac{\rho_e(r_s)}{|r - r_s|} \, dV . \tag{2.33}$$

Equations (2.32) and (2.33) provide a basis for an intuitive understanding of the distribution of electrical charge in the subsurface, and the resulting potential response. The first term on the right hand side of (2.32) describes primary sources of charge. Primary sources typically manifest as injection or pumping wells in an aquifer. As was illustrated in the example shown in Section 2.3.2, a positive injection of fluid into the system results in a concentration of negative charge and consequently a negative SP response. The magnitude of this primary source is controlled by the fluid flow rate and conductivity values at the source.

The remaining three terms on the right hand side of (2.32) describe the secondary sources generated between regions of different conductivity. These are the only sources that contribute to the self-potential in systems where no primary flow sources exist, such as the earth dam example of Section 2.4.3. In a discontinuous conductivity model of the earth, secondary sources appear at an interface between different materials or between different saturation states within a given material. The sign of the accumulated charge depends on the sign of the conductivity and potential gradients at the interface.

Transient hydraulic conditions can give rise to a variable charge distribution, which can be evaluated through (2.32) using time-dependent variables. The release of water from storage in a transient saturated hydraulic analysis manifests as changes in the hydraulic head field with time. Since the conduction current responds instantaneously to hydraulic conditions, as discussed in Section 2.2.3, the charge distribution and corresponding self-potential reflects the head distribution at a given point in time. Similarly, transient fluid saturation resulting from a variably saturated flow analysis can give rise to sources of charge,

which manifest as changes in the hydraulic head and physical property distributions with time.

In any analysis, the magnitude of secondary charge can be significant and can cause difficulty when the SP interpretation is done in terms of a primary source only. The following example illustrates this.

2.5.1 Example: Pumping well in a heterogeneous halfspace

A pumping well model is used to illustrate the effect of heterogeneous physical property distributions on the SP response to a primary flow source. This example serves to show that a heterogeneous hydraulic conductivity distribution can greatly influence the character of the self-potential distribution, whose magnitude is influenced by the electrical properties of the subsurface.

Figure 2.10 displays a schematic of the heterogeneous halfspace model, which represents a pervious sand lens buried within a silty sand deposit. The chosen hydraulic conductivity and electrical properties of the sand aquifer are $K = 1 \times 10^{-4}$ m/s, $L^{sat} = 3 \times 10^{-5}$ A/m^2 and $\sigma^{sat} = 2 \times 10^{-3}$ S/m. The silty sand halfspace properties are $K = 1 \times 10^{-6}$ m/s, $L^{sat} = 1 \times 10^{-5}$ A/m^2 and $\sigma^{sat} = 5 \times 10^{-3}$ S/m. In this example we assume $\sigma^{unsat} = \sigma^{sat}$ for simplicity. The well penetrates the sand aquifer and is pumped at a constant rate of 500 m^3/day. Steady-state hydraulic conditions are simulated and the water table is assumed to be at ground surface a distance from the well. The study region was modelled using a non-uniform $99 \times 99 \times 22$ cell mesh, extending 100 m in depth and 1000 m in x and y directions. The pumping rate is averaged over the total volume of the two cells used to represent the well screen, such that the pumping rate per unit volume is $Q_v = -1.3 \times 10^{-5}$ m^{3}s^{-1}m^{-3}.

Figure 2.11 illustrates the hydraulic head contours in a vertical xz plane centred on the well. Since the confined sand aquifer is more permeable to fluid flow relative to the silty sand halfspace, water is drawn into the aquifer from the surrounding medium. Pumping causes a drawdown in the water table to a height of 78 m at the well, as shown in Figure 2.11(a). Figure 2.11(b) shows the hydraulic head contours for the same pumping well in a homogeneous aquifer ($K = 1 \times 10^{-4}$ m/s) for comparison. Although the well is pumped at the same rate, there is no drawdown in the water table.

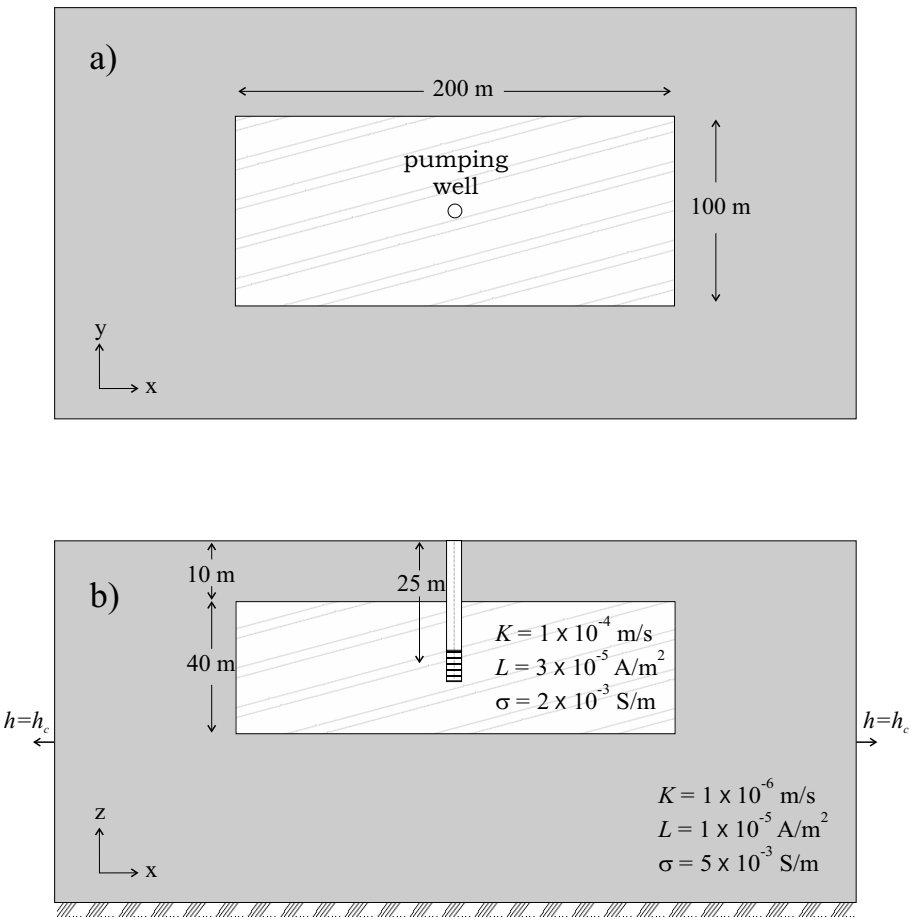

Figure 2.10: Heterogeneous halfspace with pumping well: a) model in plan view, showing outline of subsurface aquifer; b) model in cross-section, showing hydraulic boundary conditions and physical properties of aquifer and halfspace. Well screen length is 10 m.

The chosen pumping rate and physical property distributions dictate the sign and magnitude of streaming current sources in the subsurface. Figure 2.12(a) shows the primary source associated with the pumping well in a homogeneous halfspace model of the aquifer. The pumping well equates to a primary source of positive charge. The total magnitude of this primary current source is equal to 1.74×10^{-3} A (3.9×10^{-6} A/m^3 in each grid cell representing the well screen), which is consistent with that predicted using the first term of (2.30) and the pumping rate noted above. The corresponding self-potential distribution at surface is shown in Figure 2.13(a), which shows a positive SP anomaly centred on the well.

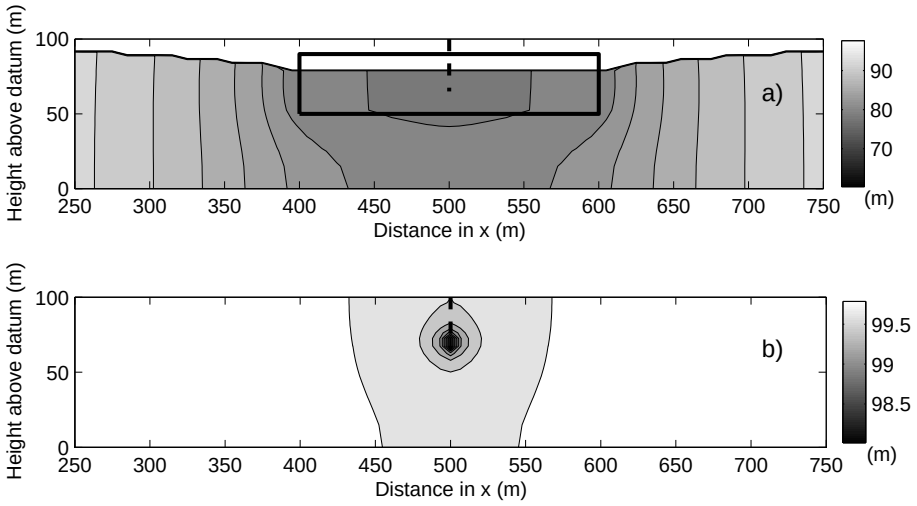

Figure 2.11: Vertical cross-section of hydraulic head in the plane of the pumping well: a) heterogeneous halfspace model; b) homogeneous halfspace ($K = 1 \times 10^{-4}$ m/s) for comparison.

The relative influence of each secondary source term is examined by progressively increasing the level of heterogeneity in the model. The chosen heterogeneous hydraulic conductivity distribution causes positive charge to accumulate at the interface between the aquifer and surrounding halfspace, as shown in Figure 2.12(b). This model assumes that K varies but that L and σ of the halfspace are equal to that of the aquifer. The secondary sources are of smaller magnitude than the primary source, but collectively they contribute significantly to the self-potential response at the ground surface, as shown in Figure 2.13(b). Here we see that the SP contour pattern roughly delineates the shape of the aquifer. Introducing a heterogeneous L distribution in addition to the heterogeneous K model decreases the magnitude of the secondary streaming current sources, as indicated in Figure 2.12(c), since the chosen L values result in the accumulation of negative charge at the interface. However, the net SP response remains positive, as shown in Figure 2.13(c). The chosen heterogeneous distribution of σ results in a further decrease in the magnitude of secondary sources at the aquifer interface, as illustrated by the surface SP pattern shown in Figure 2.13(d). Figure 2.14 illustrates the surface SP data in profile form, along a line at $y = 500$ m. The secondary sources caused by heterogeneous K, L and σ distributions result in a

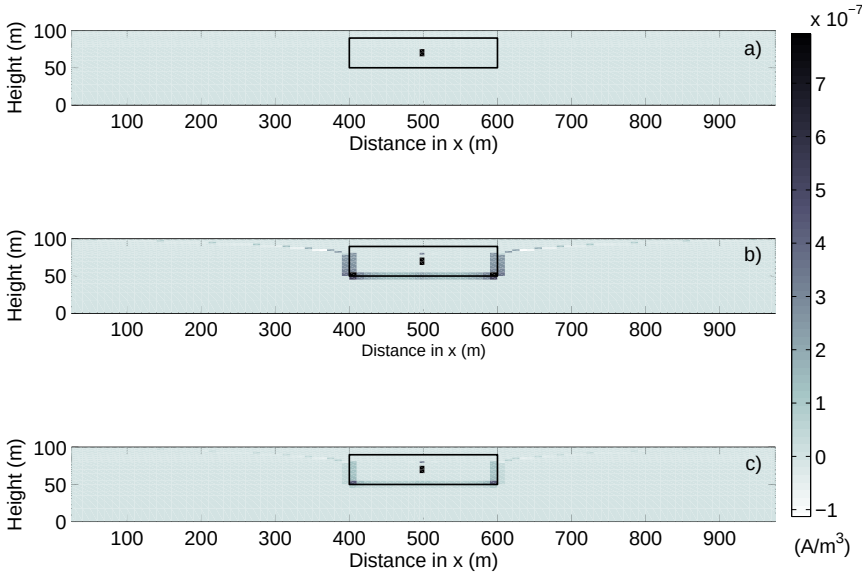

Figure 2.12: Vertical cross-section of streaming current source density in the plane of the pumping well: a) homogeneous halfspace; b) heterogeneous K halfspace; c) heterogeneous K and L halfspace. The total magnitude of primary streaming current sources at the well screen is 7.8×10^{-6} A/m^3.

SP signature of much different amplitude and shape to that predicted using a homogeneous halfspace model.

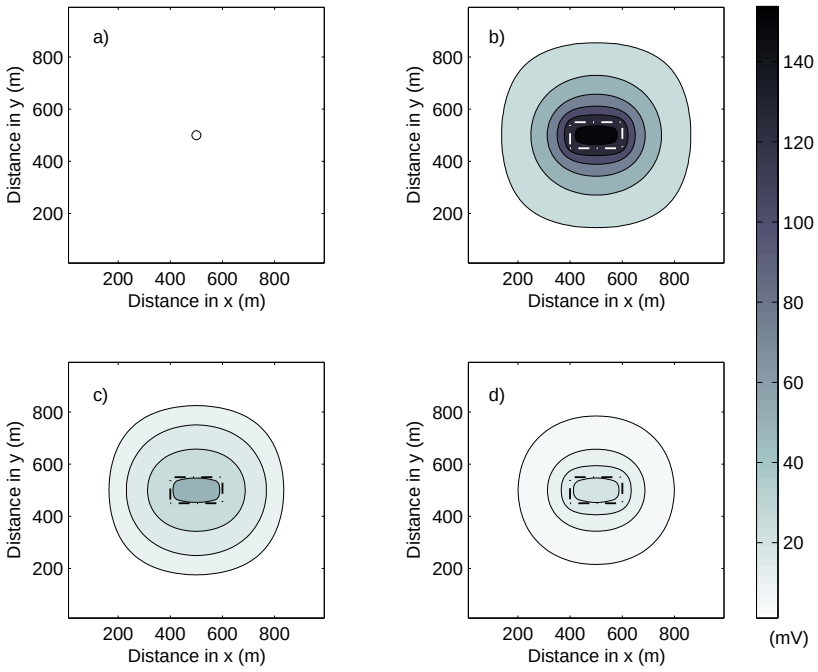

Figure 2.13: Surface plan map of self-potential: a) homogeneous halfspace; b) heterogeneous K halfspace (dashed outline indicates location of subsurface aquifer); c) heterogeneous K and L halfspace; d) heterogeneous K, L and σ halfspace.

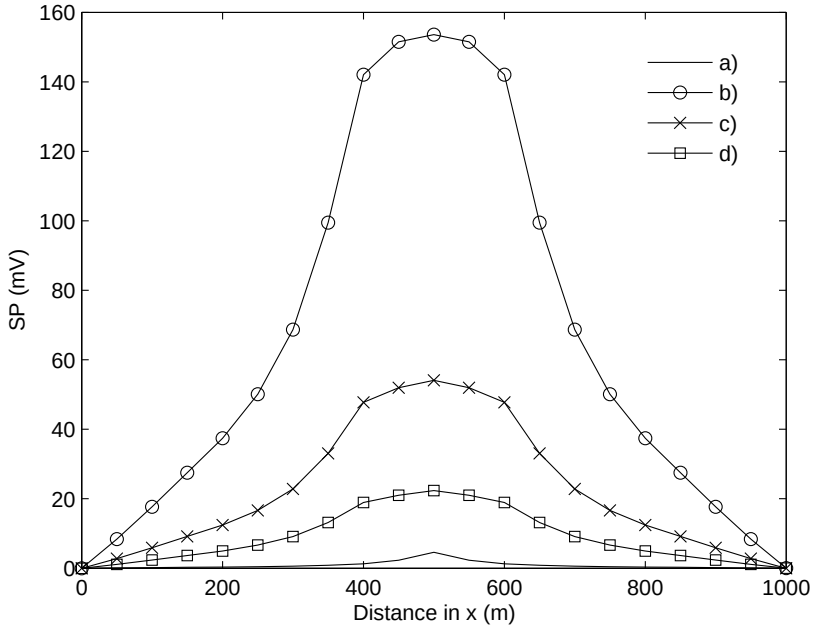

Figure 2.14: Surface profiles of self-potential at $y = 500$ m: a) homogeneous halfspace; b) heterogeneous K halfspace; c) heterogeneous K and L halfspace; d) heterogeneous K, L and σ halfspace.

2.6 Field example

One of the principal motivations for undertaking this research is the interpretation of self-potential data collected during embankment dam seepage investigations. Flow through an embankment and foundation is a problem of complicated geometry that requires a three-dimensional model to properly characterize the hydraulic head and corresponding self-potential distributions across the structure.

Self-potential surveys were performed at a dam site in British Columbia to aid in the assessment of overall seepage conditions, and to investigate the integrity of certain components of the site, which are discussed below. The surveys took place in May and August 2001 to respectively capture representative high and low pool conditions. Data were collected over the surface of the embankment and reservoir using $CuSO_4$ electrodes with a fixed-base electrode configuration, and were corrected for telluric variations. Preliminary modelling was undertaken to aid in the interpretation of self-potential data collected at the site. Our goal was to generate a preliminary 3-D simulation of the self-potential distribution using best estimates of the physical properties K, L and σ.

The key features of the site are highlighted in the plan map shown in Figure 2.15 and a conductivity model shown in Figure 2.16. The main dam is a zoned earthfill dam, which is underlain by alluvial deposits and situated within a granite bedrock valley. A pre-existing diversion dam is located at the upstream toe of this main dam. A clay blanket lines the upstream face of the main dam and keys into the central impervious core of the diversion dam. The foundation materials consist of pervious upper and lower aquifers, which are separated by a thick clay layer. A sheet-pile cut-off wall coincides with the crest of the diversion dam and extends vertically through the upper aquifer into the clay layer to prevent seepage through this zone. A deep grout cut-off is located further upstream and controls seepage through the lower aquifer. The clay blanket, diversion dam core, sheet-pile cut-off and grout curtain form a continuous impervious barrier to flow through the dam and foundation.

Fourteen distinct soil and geologic units are defined in the model of the site. Values of K, L and σ were assigned to each zone in the model. Hydraulic conductivity values were derived from published estimates [*Terzaghi and Lacroix*, 1964]. Values of cross-coupling

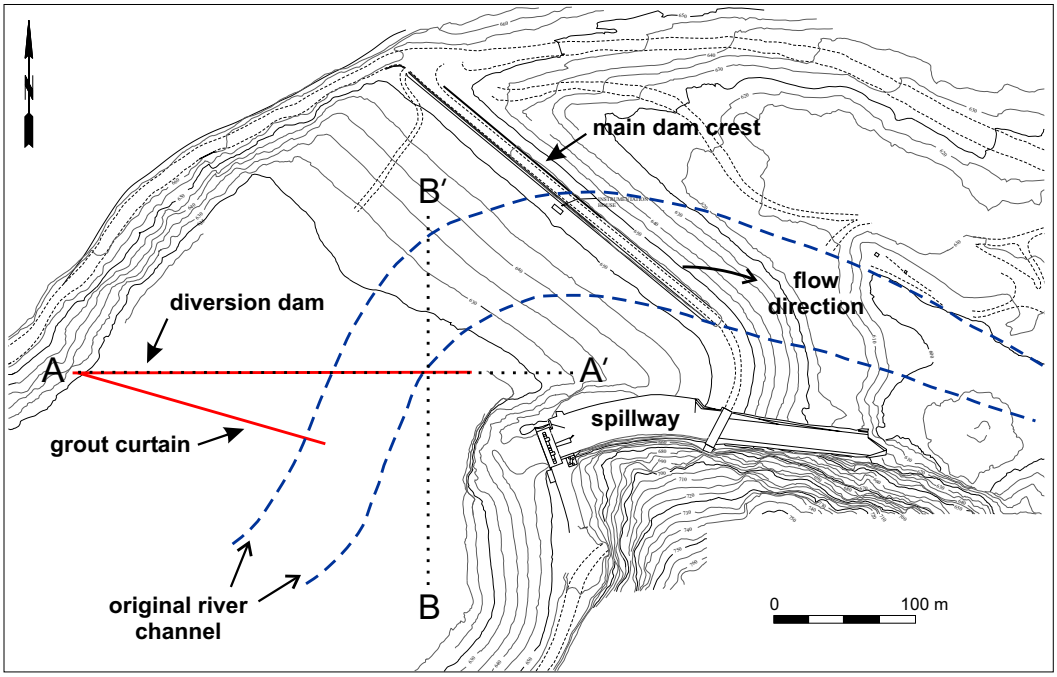

Figure 2.15: Plan map of the embankment dam site, indicating key structural features and survey lines A-A' and B-B'.

conductivity and electrical conductivity were assigned based on published and theoretical estimates for typical soil and rock types found at site, using average reservoir water conductivity values measured during the course of SP surveys performed at the site. These physical property distributions were assigned as a first approximation, and all units were each represented by uniform property distributions.

Figure 2.17 compares measured and predicted data taken along two perpendicular lines at the surface of the reservoir corresponding to the high pool survey. Figure 2.17(a) shows data along the diversion dam crest, and Figure 2.17(b) shows data in a N-S direction across the grout curtain. Measured and predicted data compare well, and show general agreement of trends and range of amplitude. This gives us confidence in both the modelling results and our initial estimates of the physical property distributions. The data clearly show the three-dimensional nature of the self-potential distribution at the site. Effective interpretation will require further work and the development of an inverse methodology.

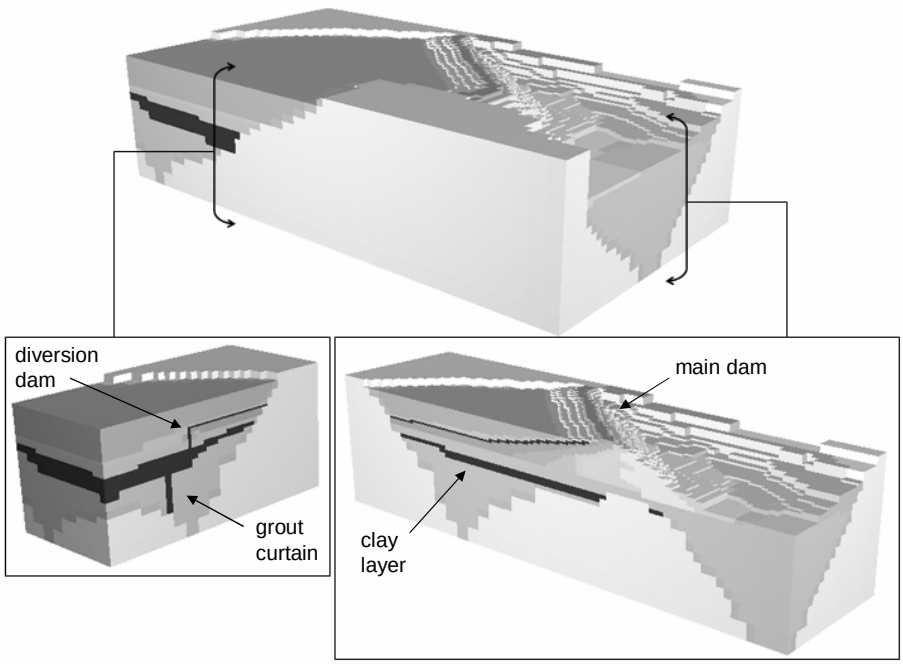

Figure 2.16: Model of the embankment dam and foundation.

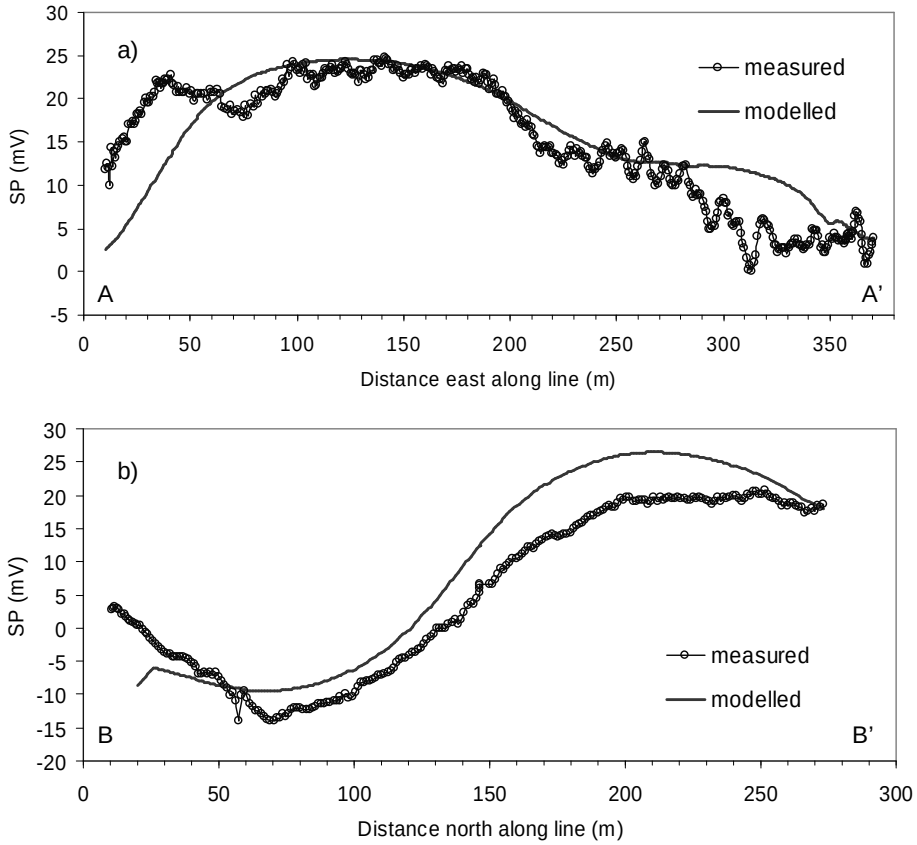

Figure 2.17: Embankment subject to seepage from the reservoir at high pool: a) Measured and predicted SP data at the surface of the reservoir above the diversion dam (survey line A-A'); b) Measured and predicted SP data at the surface of the reservoir in a N-S direction across the grout curtain (survey line B-B').

2.7 Conclusion

We have developed a 3-D forward modelling algorithm that calculates the self-potential field induced by fluid flow in the subsurface, based on the theory of coupled flow. The algorithm was developed using a finite volume discretization on a staggered grid, and explicitly calculates all streaming current sources based on known distributions of hydraulic head and physical properties, namely the streaming current cross-coupling conductivity and electrical conductivity.

The algorithm was used to successfully reproduce an analytical point source solution and approximate the measured SP response to seepage through a homogeneous earth dam. A synthetic pumping well example illustrated that heterogeneous physical property distributions result in an accumulation of charge at physical boundaries. The sign and magnitude of this charge is determined by the physical property and potential gradients at the boundary, and can contribute significantly to the self-potential signal resulting from a primary source. Preliminary modelling of the SP response to seepage at an embankment dam site illustrated the need for a three-dimensional model to characterize the self-potential distribution at a complicated site. These four examples clearly demonstrate the link between the self-potential and hydraulic head distributions. This suggests that information about the hydraulic system may be inferred from the self-potential data, given some knowledge of the electrical property distribution in the subsurface.

2.8 References

Archie, G. E., The electrical resistivity log as an aid in determining some reservoir characteristics, *Transactions of the Society of Petroleum Engineers of the American Institute of Mining, Metallurgical and Petroleum Engineers (AIME)*, *146*, 54–67, 1942.

Barrett, R., et al., *Templates for the Solution of Linear Systems: Building Blocks for Iterative Methods*, Society for Industrial and Applied Mathematics (SIAM), Philadelphia, 1994.

Bear, J., *Dynamics of Fluids in Porous Media*, Dover Publications Inc., New York, 1972.

Bogoslovsky, V. V., and A. A. Ogilvy, Deformations of natural electric fields near drainage structures, *Geophysical Prospecting*, *21*, 716–723, 1973.

Corwin, R. F., The self-potential method for environmental and engineering applications, in *Geotechnical and Environmental Geophysics*, vol. 1, edited by S. H. Ward, pp. 127–145, Society of Exploration Geophysicists, Tulsa, 1990.

Corwin, R. F., and D. B. Hoover, The self-potential method in geothermal exploration, *Geophysics*, *44*(2), 226–245, 1979.

Corwin, R. F., and H. F. Morrison, Self-potential variations preceding earthquakes in central California, *Geophysical Research Letters*, *4*(4), 171–174, 1977.

de Groot, S. R., *Thermodynamics of irreversible processes*, *Selected Topics in Modern Physics*, vol. 3, North Holland Publishing Company, Amsterdam, 1951.

Fitterman, D. V., Electrokinetic and magnetic anomalies associated with dilatant regions in a layered earth, *Journal of Geophysical Research*, *83*(B12), 5923–5928, 1978.

Freeze, R. A., Influence of the unsaturated flow domain on seepage through earth dams, *Water Resources Research*, *7*(4), 929–941, 1971.

Haber, E., U. M. Ascher, D. A. Aruliah, and D. W. Oldenburg, Fast simulation of 3D electromagnetic problems using potentials, *Journal of Computational Physics*, *163*(1), 150–171, 2000.

Harbaugh, A. W., E. R. Banta, M. C. Hill, and M. G. McDonald, Modflow-2000, the U.S. Geological Survey Modular Ground-Water Model - User Guide to Modularization Concepts and the Ground-Water Flow Process, *Tech. rep.*, United States Geological Survey, Open-File Report 00-92, Washington, 2000.

HydroGeoLogic Inc., *MODFLOW-SURFACT Version 2.2 Documentation*, HydroGeoLogic Inc., Herndon, 1996.

Ishido, T., and H. Mizutani, Experimental and theoretical basis of electrokinetic phenomena in rock-water systems and its application to geophysics, *Journal of Geophysical Research*, *86*(B3), 1763–1775, 1981.

Ishido, T., and J. W. Pritchett, Numerical simulation of electrokinetic potentials associated with subsurface fluid flow, *Journal of Geophysical Research*, *104*(B7), 15,247–15,259, 1999.

Jouniaux, L., and J. P. Pozzi, Streaming potential and permeability of saturated sandstones under triaxial stress: Consequences for electrotelluric anomalies prior to earthquakes, *Journal of Geophysical Research*, *100*(B6), 10,197–10,209, 1995.

Mitchell, J. K., Conduction phenomena: From theory to geotechnical practice, *Geotechnique*, *43*(3), 299–340, 1991.

Mizutani, H., T. Ishido, T. Yokokura, and S. Ohnishi, Electrokinetic phenomena associated with earthquakes, *Geophysical Research Letters*, *3*, 365–368, 1976.

Morgan, F. D., E. R. Williams, and T. R. Madden, Streaming potential properties of Westerly granite with applications, *Journal of Geophysical Research*, *94*(B9), 12,449–12,461, 1989.

Onsager, L., Reciprocal relations in irreversible processes, I, *Physical Review*, *37*, 405–426, 1931.

Overbeek, J. T. G., Electrokinetic phenomena, in *Colloid Science*, *Irreversible Systems*, vol. 1, edited by H. R. Kruyt, Elsevier Publishing Company, Amsterdam, 1952.

Pengra, D. B., S. X. Li, and P. Wong, Determination of rock properties by low-frequency AC electrokinetics, *Journal of Geophysical Research*, *104*(B12), 29,485–29,508, 1999.

Revil, A., H. Schwaeger, L. M. Cathles III, and P. D. Manhardt, Streaming potential in porous media: 2. Theory and application to geothermal systems, *Journal of Geophysical Research*, *104*(B9), 20,033–20,048, 1999.

Sill, W. R., Self-potential modeling from primary flows, *Geophysics*, *48*(1), 76–86, 1983.

Terzaghi, K., and Y. Lacroix, Mission dam: An earth and rockfill dam on a highly compressible foundation, *Geotechnique*, *14*(1), 14–50, 1964.

Titov, K., Y. Ilyin, P. Konosavski, and A. Levitski, Electrokinetic spontaneous polarization in porous media: Petrophysics and numerical modelling, *Journal of Hydrology*, *267*, 207–216, 2002.

Titov, K., A. Levitski, P. K. Konosavski, A. V. Tarasov, Y. T. Ilyin, and M. A. Bues, Combined application of surface geoelectrical methods for groundwater-flow modeling: A case history, *Geophysics*, *70*(5), H21–H31, 2005a.

Titov, K., A. Revil, P. Konosavsky, S. Straface, and S. Troisi, Numerical modelling of self-potential signals associated with a pumping test experiment, *Geophysical Journal International*, *162*, 641–650, 2005b.

Van der Vorst, H. A., Bicgstab: A fast and smoothly converging variant of the Bi-CG for the solution of nonsymmetric linear systems, *Journal on Scientific and Statistical Computing*, *13*, 631–644, 1992.

Wurmstich, B., and F. D. Morgan, Modeling of streaming potential responses caused by oil well pumping, *Geophysics*, *59*(1), 46–56, 1994.

Wurmstich, B., F. D. Morgan, G. P. Merkler, and R. L. Lytton, Finite-element modeling of streaming potentials due to seepage: Study of a dam, *Society of Exploration Geophysicists Technical Program Expanded Abstracts*, *10*, 542–544, 1991.

Chapter 3

A laboratory apparatus for streaming potential and resistivity measurements on soil samples [2]

3.1 Introduction

The self-potential (SP) method is a geophysical technique that is used to measure the electrokinetic process of streaming potential, in which electrical current flow is generated by the flow of fluid through a porous medium [*Overbeek*, 1952]. Streaming potential measurements have been performed in engineering and groundwater [*Corwin*, 1990; *Ogilvy et al.*, 1969], oil reservoir [*Wurmstich and Morgan*, 1994], and geothermal investigations [*Ishido and Mizutani*, 1981; *Revil et al.*, 1999] to help infer characteristics of the hydraulic regime.

Practical numerical analysis and interpretation of streaming potential survey data requires estimates of the physical properties that describe the electrical response to fluid flow through a porous medium. Streaming potential measurements have been collected on rock and uniform sand samples [e.g., *Morgan et al.*, 1989; *Pengra et al.*, 1999; *Ahmad*, 1964], but very few data exist for natural unconsolidated sediments. The present investigation is focused on the development of an apparatus to measure the relevant electrical and sample properties of soils over a range of particle sizes.

Streaming potential is a function of the properties of the solid-fluid interface. An electrical double layer forms at the surface of a solid in contact with an electrolyte. This double

[2] A version of this chapter has been published. Sheffer, M.R., Reppert, P.M. and Howie, J.A. (2007) A laboratory apparatus for streaming potential and resistivity measurements on soil samples, Review of Scientific Instruments, 78:094502

layer consists of a tightly adsorbed inner layer and a weakly-bound diffuse outer layer of ions, which act together to balance the surface charge of the solid. A streaming current is generated within the pore space by the fluid flow, which drags ions from the diffuse layer in the direction of flow. The streaming current may be described using a linear flow law [*de Groot*, 1951]:

$$\boldsymbol{J}_S = -L\nabla h, \tag{3.1}$$

where L is the streaming current cross-coupling coefficient and h is hydraulic head. The movement of ions causes a charge imbalance within the pore space in the direction of flow, which drives an opposing conduction current $\boldsymbol{J}_C$. This conduction current permeates the porous medium and is described using Ohm's law:

$$\boldsymbol{J}_C = -\frac{1}{\rho}\nabla\phi, \tag{3.2}$$

where ρ is the electrical resistivity of the saturated porous medium and ϕ is the electrical potential. If no temperature or chemical/ionic concentration gradients exist in the system, the total current $\boldsymbol{J}$ is described using coupled flow theory as the sum of streaming and conduction currents:

$$\boldsymbol{J} = \boldsymbol{J}_C + \boldsymbol{J}_S. \tag{3.3}$$

If we consider one-dimensional flow in a homogeneous porous medium of length l and cross-sectional area A, Equations 3.1 to 3.3 can be shown to reduce to

$$\frac{1}{\rho}\frac{\Delta\phi}{l}A = -L\frac{\Delta h}{l}A\ , \tag{3.4}$$

which may be further simplified and rearranged to define the streaming current cross-coupling conductivity:

$$L = -\frac{C}{\rho}\ , \tag{3.5}$$

where the streaming potential coupling coefficient

$$C = \frac{\Delta\phi}{\Delta h}. \tag{3.6}$$

Laboratory measurements of hydraulic head may be reported in terms of pressure, such that

$$C = \frac{\Delta\phi}{\Delta P}, \tag{3.7}$$

where $P = \gamma_f h$ and γ_f is the product of fluid density and gravitational acceleration.

The purpose of the present study was to develop an apparatus to measure C and ρ for a given material. Of particular importance was the ability to measure these parameters on the same unconsolidated soil specimen in order to characterize L.

The streaming potential coupling coefficient C is typically measured using either the unidirectional flow method or the oscillatory flow method [*Reppert and Morgan*, 2001b]. Although oscillatory flow methods have been implemented in previous studies of streaming potential on glass capillaries and rock samples [*Packard*, 1953; *Sears and Groves*, 1978; *Pengra et al.*, 1999; *Reppert and Morgan*, 2001a], the oscillatory method had previously not been tested on well-graded (poorly sorted) soil samples. Consequently, we adopted a parallel design approach to enable a comparison of the two methods in application to soils testing. Laboratory measurements of DC resistivity are typically performed using 2- or 4-electrode array configurations. The apparatus was designed to measure resistivity using the 2-electrode technique, and the 4-electrode configuration was tested for comparison.

The streaming potential measurements performed in this study consist of a low voltage measurement (0.1 to 1 milliVolt range) across a saturated soil column, which acts as a high impedance current source (typically 1 to 30 kΩ). As a result, the collection of streaming potential data is considered a low voltage-high impedance electrical measurement, and requires unique attention to sources of error in the electronics and environment that are typically ignored in most other laboratory measurement systems.

This article explains the design of the apparatus, and the development of calibration and measurement techniques. We compare the results from unidirectional and oscillatory flow measurements of the streaming potential coupling coefficient, and 2- and 4-electrode measurements of resistivity.

3.2 Experimental apparatus

3.2.1 Overview

A schematic of the experimental apparatus is shown in Figure 3.1. The test cell houses a soil specimen, a pair of non-polarizing electrodes, a pair of stainless steel electrodes and a

pair of gauge pressure transducers to enable measurements of the electrical potential and fluid pressure differences across the sample. An external loading assembly is used to apply a vertical seating load to the top of the soil sample.

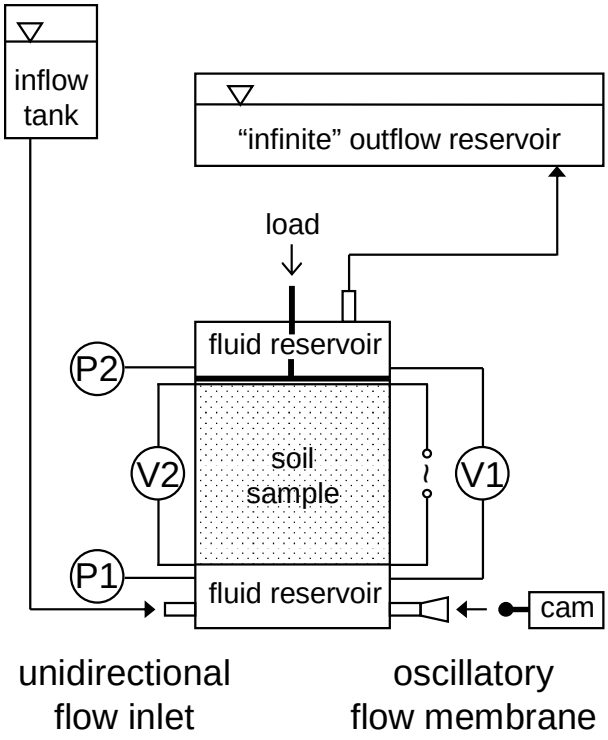

Figure 3.1: Schematic of apparatus.

An "infinite" reservoir imposes a constant hydraulic head boundary to the top of the soil specimen for the purposes of both unidirectional and oscillatory flow testing. In the case of unidirectional flow testing, a constant head reservoir is connected to the base of the test cell to impose a hydraulic gradient that drives fluid flow upwards through the sample. A sealed rubber membrane is connected to the base of the test cell for the purposes of oscillatory flow testing. An oscillating pressure gradient is induced by deflecting the membrane with a mechanical actuator, which generates flow through the sample.

Streaming potential measurements (V1 in Figure 3.1) are made using the non-polarizing electrodes positioned within fluid reservoirs immediately above and below the sample. Pressure measurements (P1 and P2 in Figure 3.1) are made at the same position. Pervious plate

electrodes in contact with both ends of the soil specimen (V2 in Figure 3.1) are used to apply current and measure the resultant voltage drop across the sample for resistivity measurements, which are performed as a separate experiment. An automated data acquisition and control system is used to perform all measurements related to streaming potential and resistivity testing. Specific details about each component of the apparatus are outlined in the sections that follow.

The electrical potential measured across the soil sample must be purely a function of the applied hydraulic gradient to accurately characterize the streaming potential coupling coefficient. Any secondary currents induced by temperature or ionic gradients in the sample, or stray currents from the instrumentation can result in an inaccurate measurement of the streaming potential. Consequently, insulating materials were used to construct the cell, and grounded shielding surrounded the entire apparatus to reduce the effects of 60 Hz noise from ambient sources. The experiments were conducted at constant temperature and diffusion potential effects were avoided by allowing time for the soil sample to reach chemical equilibrium with the saturating fluid.

3.2.2 Test cell and loading assembly

The test cell consists of a sample holder and two cell reservoirs, which are fixed above and below the soil specimen, as indicated in Figure 3.1. Figure 3.2 shows a detailed drawing of the test cell in cross-section.

The sample holder was oriented vertically to allow preparation of fully-saturated, homogeneous soil samples. The cylindrical sample holder was designed as a separate piece to accommodate different sample lengths as required in testing. The sample height had to be short enough to ensure homogeneity, and long enough to apply small hydraulic gradients ($\leq$ 0.1 m of H_2O/m) as well as measure sufficient streaming potential signal across the sample. All experiments discussed in this paper were performed using a 10 cm-long sample holder.

To enable testing of well-graded samples, the diameter of the sample had to be large enough to accommodate a wide range of grain sizes. The inner diameter of the sample holder is 10 cm, which enables testing of samples exhibiting a maximum particle size of

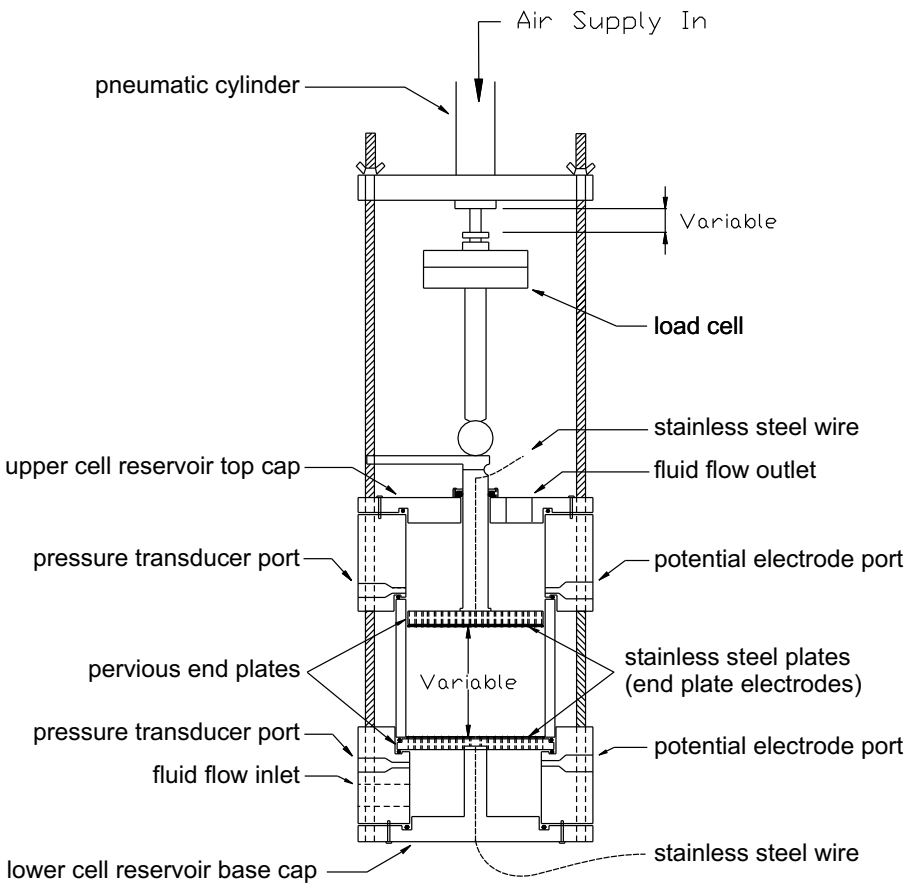

Figure 3.2: Cross-sectional view of the test cell.

9.5 mm [*ASTM*, 1991]. The upper and lower cell reservoir assemblies have the same inner diameter as the sample, and house the pressure transducers and SP electrodes in side ports away from the primary fluid flow path [*Morgan*, 1989].

The cell reservoirs are separated from the sample by pervious top and base plates. The base plate is fixed as part of the lower cell reservoir assembly. The top plate is a separate piece fitted with an acrylic loading ram, to enable the application of a vertical seating load to the top of the prepared sample. This plate and ram assembly was designed to withstand a nominal load of 25 kPa, to prevent the migration of finer soil particles and instabilities in the soil matrix caused by upward fluid flow through the sample. The test cell and loading apparatus were designed as a freestanding unit, such that the cell assembly itself acts as a

loading frame. The vertical seating load is applied to the sample using a pneumatic piston fitted with a ball in contact with the loading ram.

Filter screens are used to retain the soil sample between the top and base plates. The cell reservoirs are enclosed with top and base caps, and the entire cell and loading assembly secured with three stainless steel rods. All cell components in contact with the sample and fluid are acrylic, with the exception of the corrosion-resistant stainless steel current electrodes and filter screens.

3.2.3 Instrumentation

To characterize the streaming potential coupling coefficient using Equation (3.6), the apparatus had to allow testing of samples subject to laminar flow conditions, with equivalent geometry of fluid (streaming current) and conduction current flow path geometry [*Morgan*, 1989]. Consequently, a unique design approach was implemented in the placement of the streaming potential electrodes and pressure transducers. Measurement points were positioned immediately above and below the soil sample, instead of along the side of the sample. This design enables the average flow across the entire cross-sectional area of the sample to be characterized, and implies that the fluid and current flow path lengths are equal to the physical length of the soil specimen. This same principle was applied in designing the electrode configuration for resistivity measurements. Current electrodes were placed in contact with the entire cross-sectional area of the ends of the sample to ensure that current was applied uniformly through the entire soil volume.

Non-polarizing silver-silver chloride electrodes were installed within the upper and lower cell reservoirs for streaming potential measurements. These electrodes are positioned in side ports removed from the fluid flow path to ensure that electromotive effects, attributed to the flow of water across the tip of the electrode, would not influence the streaming potential measurements. Silver-silver chloride electrodes were selected for their particular suitability in laboratory testing and to avoid polarization effects, particularly in unidirectional flow testing [*Morgan*, 1989].

Gauge pressure transducers were installed within the upper and lower cell reservoirs, at the same vertical position as the streaming potential electrodes, to monitor the pressure

difference across the sample. Independent gauge transducers were chosen over a differential transducer to avoid a parallel low-impedance connection bridging the ends of the sample. The transducers are constructed with a plastic housing and a silicon membrane and are powered by isolated 10V DC power supplies.

Two stainless steel plate electrodes were installed directly onto the pervious top and base plates used to support the soil specimen for the purposes of resistivity testing. These current electrodes were machined to coincide with the drilled surface of the end plates in order to have maximum surface area in contact with the ends of the soil specimen, without impeding fluid flow through the sample. All components of the current electrodes were designed of stainless steel exhibiting a high corrosion resistance, to avoid the risk of spurious currents arising from corrosion or contact between different types of metals within the test cell.

A regulator is used to control the pressure applied to the top of the sample from the pneumatic piston, and the applied force is measured with a load cell. The length of the soil specimen is calculated from the referenced height of the loading ram, which is measured using a dial gauge.

3.2.4 Fluid flow system

External fluid reservoirs include a constant head inflow tank used in unidirectional flow testing, and an "infinite" constant head outflow reservoir of large surface area.

The cell was designed to initiate flow from the base of the sample. The inflow constant head reservoir is connected to a port opening in the base cell reservoir via a plastic ball valve. The height of this reservoir may be adjusted to impose a range of hydraulic gradients across the sample for unidirectional flow testing. Typical hydraulic gradients used in testing ranged from 0.02 up to 2.5 m of H_2O/m for pervious samples. The fluid level in the inflow reservoir is maintained using an overflow tube and gravity-driven flow from an isolated plastic supply tank.

A second port and ball valve connects the base cell reservoir to a fixed inlet tube sealed with a rubber membrane. A piston powered by a motorized cam is used to deflect the membrane, which induces an oscillatory pressure pulse at the base of the sample for the purposes of oscillatory flow testing. The cell was designed for upward flow in part to

facilitate the rebound deflection of this membrane.

The infinite reservoir is connected directly to a port opening in the top cap of the upper cell reservoir and is used to apply a constant hydraulic head to the top of the sample. The fluid level is maintained during unidirectional flow testing using an overflow tube. The large surface area of the reservoir is required to ensure that a constant pressure is maintained at the top of the sample during oscillatory flow testing.

3.2.5 Data acquisition and control

The digital data acquisition and control (DAC) system consists of a 200 kHz 16-bit A/D card with differential inputs and 100 GΩ input impedance. The high input impedance of the device is necessary to ensure that the streaming potential is accurately measured across resistive samples. Four input channels are configured to sample data from the Ag-AgCl electrode pair, the upper pressure transducer, the lower pressure transducer, and the load cell, respectively. A grounded channel is sampled prior to each streaming potential measurement to avoid channel cross-talk caused by parasitic capacitance in the multiplexer. One output channel is configured to supply a voltage waveform via a voltage-to-current converter to the current electrode pair for resistivity testing. The resulting potential differences across the Ag-AgCl electrode pair and stainless steel electrode pair are sampled using two input channels.

Sample length and fluid properties are recorded manually. Sample length is calculated from dial gauge measurements of the height of the loading ram with respect to the base of the cell. Fluid properties (electrical conductivity, temperature and pH) are measured in the external reservoirs using portable conductivity and pH meters once the fluid and sample are at equilibrium.

Software programs were developed to collect and process self-potential, pressure and load cell data from unidirectional and oscillatory flow testing, as well as electrical potential and current data from resistivity testing. Details of data acquisition and processing methods are discussed in Sections 3.3 and 3.4.

3.2.6 Sample preparation

The apparatus was designed to enable cell assembly and sample preparation without trapping air in the system, which could adversely affect both streaming potential and resistivity measurements. Cell assembly involves the use of a saturation bath and removable top-cap overflow reservoir to enable air-free assembly of the system. Sample preparation methods were chosen to ensure fully saturated conditions and homogeneous samples. The water pluviation technique is used for uniformly graded samples. A modified slurry deposition technique is used for well-graded samples [*Kuerbis and Vaid*, 1988].

The soil and saturating fluid must be allowed to reach a state of ionic equilibrium to reflect natural conditions and to ensure that diffusion potential effects do not contribute to the measured streaming potential. Ionic transfer between the fluid and solid matrix gives rise to changes in fluid chemistry that can influence the measured electrical properties. A state of sample equilibrium is marked by stable measured parameters that are repeatable over time, and synchronized streaming potential and pressure responses to the onset of fluid flow in streaming potential measurements.

3.3 Streaming potential measurements

3.3.1 Methodology

The unidirectional fluid flow measurement technique involves measuring the streaming potential response to an applied pressure difference across the soil sample for a range of hydraulic gradients under steady-state flow conditions. Figure 3.3 shows streaming potential and pressure time series data acquired using the unidirectional flow method on a sample of glass beads. The static DC offset is removed from the measured potential difference and the hydrostatic pressure is removed from the measured pressure difference prior to plotting these data versus each other, as shown in Figure 3.4. The streaming potential coupling coefficient is calculated from the linear fit between the measured potential and pressure differences. The corrected potential and pressure difference data respectively exhibited average measurement uncertainties of ± 0.1 mV and ± 0.04 kPa in unidirectional flow testing performed using the apparatus.

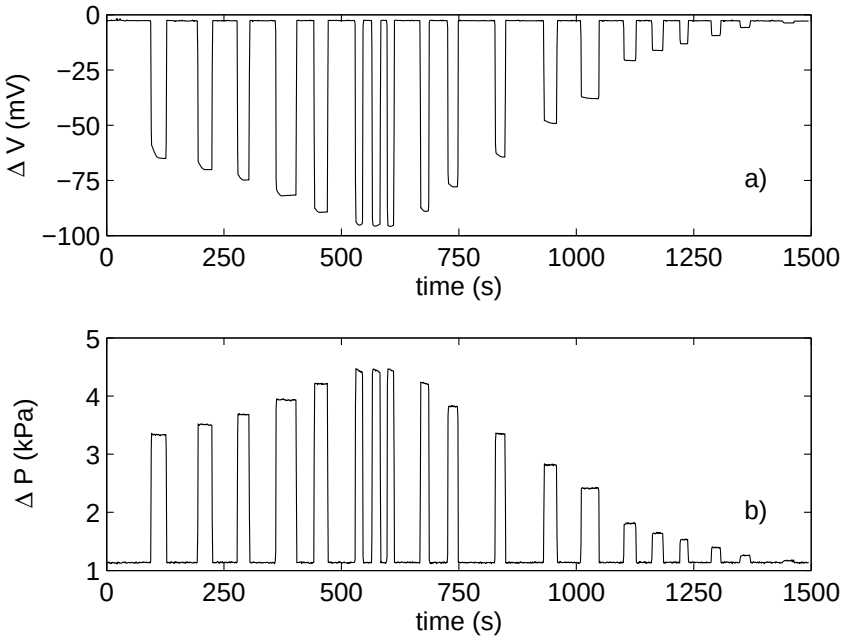

Figure 3.3: Time series data acquired using the unidirectional flow test method: a) streaming potential, b) pressure difference ($\Delta P = P1 - P2$).

Although this technique is seemingly straightforward, the fluid entering the system must be in equilibrium with the soil and pore fluid in the cell to ensure that no ionic gradients exist across the sample. This is one of the main practical limitations of this method, as significant time and effort is required to equilibrate the large amount of fluid. Other limitations include the possibility of electrode drift in the measurements and electrode polarization, as well as limited sensitivity in the streaming potential and pressure data channels due to ambient noise. Recording static streaming potential readings in between applied gradients enables drift corrections, and electrode polarization effects can be eliminated through the use of non-polarizing electrodes. Noise levels, particularly from 60 Hz sources, are minimized through electrical shielding of the apparatus and data filtering.

The oscillatory flow measurement technique does not necessitate equilibrium with external fluid sources. It is also less time-consuming to execute for a given sample as a single test records the response to a sinusoidally-varying imposed gradient. Figure 3.5 shows streaming

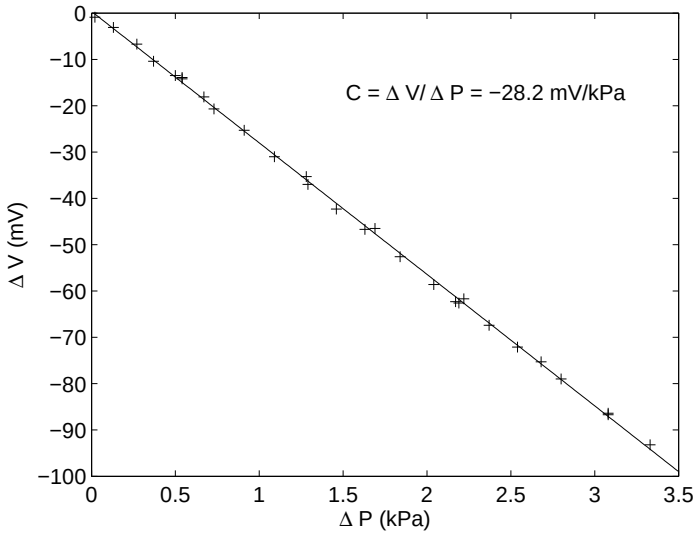

Figure 3.4: Calculation of the streaming potential coupling coefficient (C) from unidirectional flow test data. Measurement error is within the limits of the marker used to identify discrete data points.

potential and pressure difference time series data acquired on a sample of glass beads using the oscillatory flow method. The streaming potential data shown in Figure 3.5 have been corrected for a static offset of 2 mV, and pressure data are plotted as a pressure difference with the hydrostatic pressure removed.

The oscillatory flow technique requires somewhat more advanced data collection and processing tools. Several methods exist to calculate the streaming potential coupling coefficient using this technique [*Reppert and Morgan*, 2001b]. The approach used here is a spectral analysis of the measured signals. The coupling coefficient is determined by stacking the amplitude spectra of the SP and pressure signals, and calculating their ratio at the pulsation frequency:

$$C = \sum_{i=1}^{n} \Delta V_i^{rms} \Big/ \sum_{i=1}^{n} \Delta P_i^{rms}. \tag{3.8}$$

This averaging process minimizes random noise in the data and increases the signal to noise ratio. Figure 3.6 illustrates the analysis procedure. Oscillatory flow test data collected at a pulsation frequency of 0.1 Hz respectively exhibited average uncertainties of ±0.001 mV

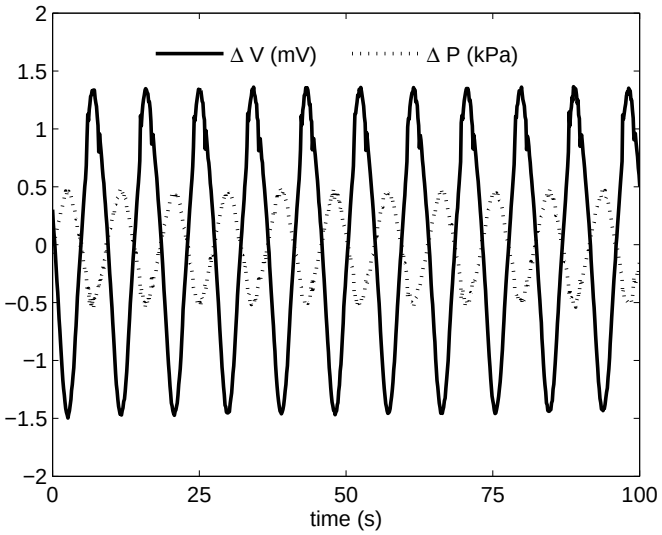

Figure 3.5: Streaming potential and pressure time series data acquired using the oscillatory flow test method.

and ±0.002 kPa for this apparatus.

3.3.2 Calibration and test design

Streaming potential measurements were carried out using the test cell filled entirely with water (no solid matrix) to ensure that no streaming potentials were generated across the pervious filter screens or end plates. The frequency spectrum of the measured background streaming potential under static flow conditions was evaluated to determine appropriate sampling rates and digital filter criteria, and to confirm no significant noise source in the range from zero (DC) to 0.5 Hz, which is the frequency range of interest for all flow testing performed using the apparatus.

The optimum frequency for oscillatory flow testing was determined to be 0.1 Hz based on the results of preliminary testing. The frequency of oscillation must be low enough to prevent inertial flow effects. The amplitude of the pressure pulse must be small enough to prevent liquefaction of the sample, but large enough to generate a discernible response in the streaming potential and pressure.

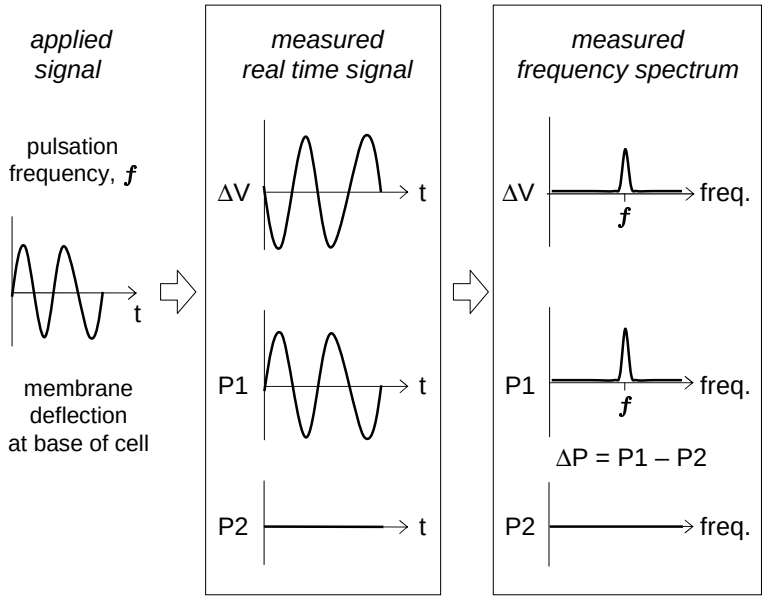

Figure 3.6: Spectral analysis of streaming potential and pressure data acquired using the oscillatory flow test method.

All flow test data were acquired using a digital low-pass filter with a cut-off frequency of 20Hz. Unidirectional flow test data were sampled at an average rate of 256 samples per second and frame size of 256 samples. Each frame of data was filtered and averaged to produce one point of data per second. Oscillatory flow test data were acquired at an average scan rate of 328 samples per second and frame size of 32,768 samples to resolve frequencies down to 0.01 Hz. Several frames of data were averaged to improve the signal to noise ratio.

3.3.3 Comparison of unidirectional and oscillatory flow test methods

The validity of the oscillatory measurement technique was confirmed through a comparison of C values derived from unidirectional and oscillatory flow testing performed on glass bead and soil samples. Figure 3.7 illustrates the results of unidirectional and subsequent oscillatory flow tests performed on each sample. The oscillatory flow tests were performed immediately following each unidirectional flow test in an attempt to capture similar sample conditions, which in most cases did not correspond to complete equilibrium conditions. Ev-

ident in Figure 3.7 is a strong agreement between C values derived from corresponding flow tests. Three data points corresponding to samples *gb_a, gb_b* and *gbnc_a* deviate notably from this trend. These samples exhibited a very rapid change in the measured properties upon termination of steady unidirectional fluid flow. Consequently, the results of unidirectional and oscillatory flow tests represent different sample conditions prior to equilibrium. This is confirmed by measured resistivity values, which dropped respectively by 7%, 10% and 13% in each sample between unidirectional and oscillatory flow tests. The lower sample resistivity translates to a smaller magnitude of C, which is evident in the data shown in Figure 3.7.

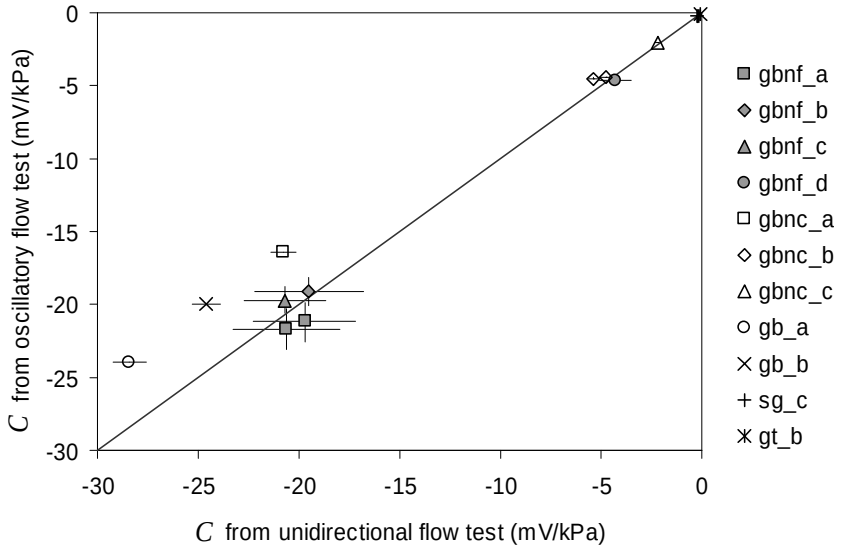

Figure 3.7: Comparison of streaming potential coupling coefficient (C) values measured using unidirectional and oscillatory flow test methods. Soil samples are labelled according to material type (gb: glass beads, s: sand and gravel c: glacial till), changes to the gradation (nf: fines removed, nc: coarse fraction removed) and the sample identifier (e.g., _a). Measurement error exceeding marker size is indicated by error bars.

3.4 Resistivity measurements

3.4.1 Methodology

The DC resistivity method consists of measuring the electrical potential response to current flow generated by a DC or low frequency AC source. An AC current source is typically used to prevent error introduced by polarization of the current electrodes. At low source frequencies, the measured resistivity is equivalent to the DC limit [*Telford et al.*, 1990]. The resistance R (ratio of the measured voltage and current) is converted to resistivity using the relation:

$$\rho = kR, \tag{3.9}$$

where k is a geometric factor specific to the experiment.

Field surveys typically employ a 4-electrode configuration, where one pair of electrodes is used to inject current and a second pair of electrodes is used to measure the potential difference. The subsurface resistivity may be derived using a factor specific to the electrode configuration and geometry. The confined geometry of a laboratory experiment makes it possible to use either a 2- or 4-electrode configuration. Current is applied across the sample by means of two plate or ring electrodes, and the resulting potential difference is measured using the same or a separate pair of electrodes.

The apparatus consists of two stainless steel end-cap plate electrodes in contact with the top and bottom cross-sectional area of the soil specimen. These are used to apply a low frequency AC source current to the sample. The apparatus was designed to measure resistivity using the 2-electrode method, but potential difference measurements were also made using the Ag-AgCl electrode pair (4-electrode method) for comparison.

3.4.2 Calibration and test design

Contact resistance measurements were made to calculate the amplitude of the source voltage waveform required to apply sufficient current across the sample. A peak source amplitude of 0.3 V was chosen to accommodate large sample resistances ($\sim$30 kΩ) and the 10 V output limit of the voltage-to-current converter. The influence of the source waveform type on the measured resistance was assessed over a range of 50 Hz to 1000 Hz, and a sinusoidal

waveform was chosen as the optimal signal type. The source voltage was generated by the DAC board and was converted to a 0.117 mA rms current source.

Measurements were made across a range of frequencies to determine a suitable source frequency. Figure 3.8 shows the effect of source frequency on the measured resistance using 2- and 4-electrode techniques on two samples of glass beads. The 2-electrode measurements are effectively constant at frequencies above 50 Hz, but deviate significantly at lower frequencies. This is attributed to polarization effects at the current electrodes. The 4-electrode measurements fall off from the DC resistivity limit at frequencies above 100 Hz. This behaviour is attributed to the complex impedance of the sample [*Olhoeft*, 1985]. These data suggest an optimum source frequency of 100 Hz to enable a comparison of the two methods.

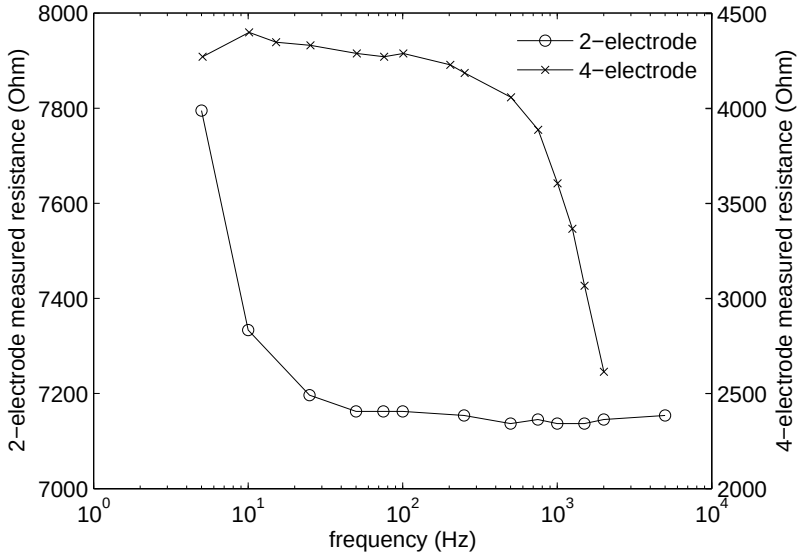

Figure 3.8: Frequency dependence of the resistance of glass bead samples measured using 2- and 4-electrode DC resistivity methods. Note that 2- and 4-electrode data series were collected at different stages of sample equilibration. Measurement error is within the limits of the marker used to identify discrete data points.

The confined sample geometry and chosen electrode configuration enable us to calculate the sample resistivity using a geometric factor A/l:

$$\rho = \frac{A}{l} R, \tag{3.10}$$

where A is the cross-sectional area of the sample and l is the sample length. To confirm this relation, resistivity measurements were performed on the test cell filled with fluids of known conductivity for current electrode separations ranging from 7 cm to a maximum sample length of 10 cm. Fluid conductivity was controlled by varying the concentration of sodium sulphate in de-aired distilled water, and was measured using a portable conductivity meter. Figure 3.9 compares the resistivity derived using (3.10) from 2-electrode measurements to the resistivity of the fluid contained in the cell. The near unity match confirms the validity of (3.10) to calculate sample resistivity.

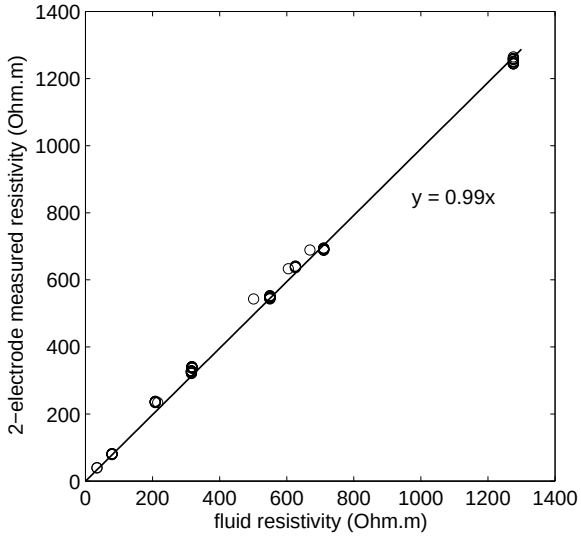

Figure 3.9: Comparison of resistivity measured using the 2-electrode method to the known resistivity of fluid filling the test cell. Resistivity is calculated from the measured resistance using a geometric factor k, which is calculated as a function of sample volume defined in (3.10). Measurement error is within the limits of the marker used to identify discrete data points.

DC resistivity data were collected at a similar scan rate and frame size as the oscillatory flow test data, but no digital filtering was applied due to the high amplitude of the measured signals.

3.4.3 Comparison of 2- and 4-electrode methods

The potential difference measured using the Ag-AgCl electrode pair is representative of the true potential difference across the sample if the sample resistance (R_s) is significantly greater than the resistance of the fluid column between the electrodes and the ends of the sample (R_f). This assumption does not hold in the case of a fluid-filled cell, as shown by the data in Figure 3.10. The measured 4-electrode resistance derived using (3.10) is 34% smaller than the known resistivity of the fluid, which is in contrast to the near unity match for the 2-electrode case shown in Figure 3.9. This suggests that there is net potential drop between the ends of the sample and the Ag-AgCl electrodes, which results in a smaller potential difference measured using the 4-electrode technique.

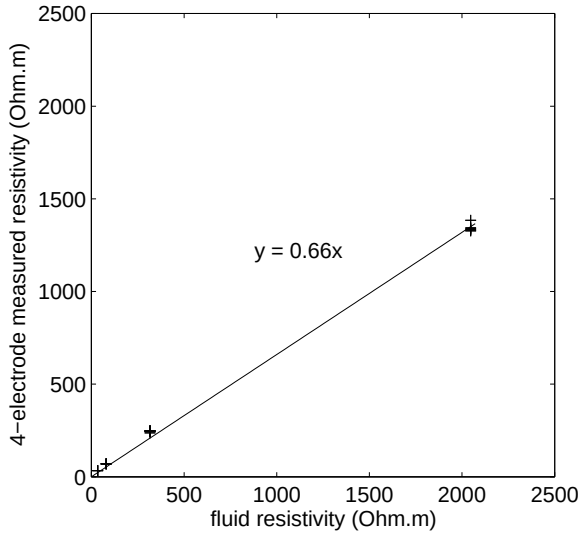

Figure 3.10: Comparison of resistivity measured using the 4-electrode method to the known resistivity of fluid filling the test cell. Resistivity is calculated from the measured resistance using a geometric factor k, which is calculated as a function of sample volume defined in (3.10). Measurement error is within the limits of the marker used to identify discrete data points.

The potential drop is less significant when a soil sample is present due to the larger sample resistance. For a given sample length, the ratio R_s/R_f is on average five times

greater when the test cell houses a soil sample than when the cell is filled entirely with fluid. Figure 3.11 illustrates the difference between 4-electrode and 2-electrode measured potential from resistivity tests performed on a range of soil samples. The linear relation indicates that the potential measured using the Ag-AgCl electrodes underestimates the "true" potential measured at the plate electrodes. Consequently, a 6% correction should be applied to the 4-electrode data if they are to be used to calculate sample resistivity.

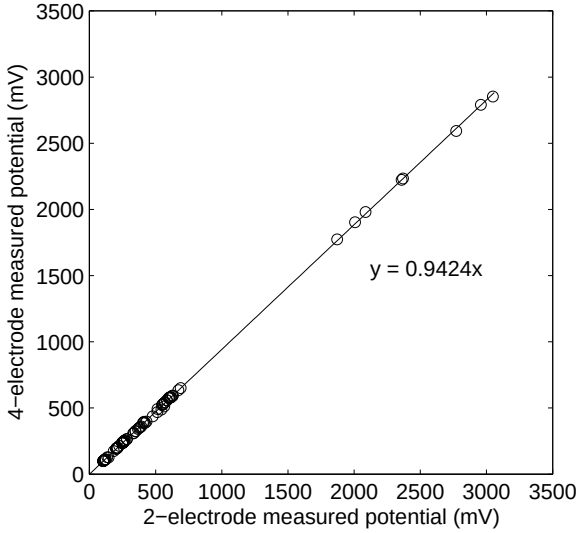

Figure 3.11: Comparison of 4-electrode and 2-electrode potentials measured during resistivity experiments on soil samples (0.117 mA rms current source). Measurement error is within the limits of the marker used to identify discrete data points.

The small discrepancy between 2- and 4-electrode measurements could also be attributed in part to the measurement frequency used to compare the two methods. As discussed in Section 3.4.2, the 4-electrode measured resistivity at 100 Hz may underestimate the true DC resistivity. In oscillatory flow testing, streaming potentials are generated across a soil sample at much lower frequencies (0.1 Hz) and result from a different current source mechanism. Consequently, no correction is applied to streaming potential measurements obtained using the Ag-AgCl electrodes.

3.5 Conclusion

We have developed a laboratory apparatus that allows us to measure the streaming potential coupling coefficient and electrical resistivity on the same saturated soil specimen. These parameters are required to properly characterize the streaming current cross-coupling conductivity of a given material for use in field survey data interpretation. The apparatus enables testing of well-graded soil samples up to a maximum particle size of 9.5 mm, and measurement of relevant sample properties including dry density, porosity and hydraulic conductivity.

The apparatus was designed to measure the streaming potential coupling coefficient using both unidirectional and oscillatory flow methods, in order to validate use of the latter method on unconsolidated samples. The oscillatory flow method was proven to be a valid test method for soils and is the preferred method to achieve sample equilibrium most effectively. Sample resistivity was characterized using a 2-electrode measurement configuration, which was shown to give accurate measurements through a calibration with fluids of known resistivity. A comparison of measured sample resistivity using 2- and 4-electrode configurations at a source frequency of 100 Hz revealed that the 4-electrode method underestimates the 2-electrode value by 6%.

3.6 References

Ahmad, M. U., A laboratory study of streaming potentials, *Geophysical Prospecting*, *12*, 49–64, 1964.

ASTM, D2434-68: Standard test method for permeability of granular soils (constant head), in *Annual Book of ASTM Standards*, vol. 4, American Society of Testing and Materials, 1991.

Corwin, R. F., The self-potential method for environmental and engineering applications, in *Geotechnical and Environmental Geophysics*, vol. 1, edited by S. H. Ward, pp. 127–145, Society of Exploration Geophysicists, Tulsa, 1990.

de Groot, S. R., *Thermodynamics of irreversible processes*, *Selected Topics in Modern Physics*, vol. 3, North Holland Publishing Company, Amsterdam, 1951.

Ishido, T., and H. Mizutani, Experimental and theoretical basis of electrokinetic phenomena in rock-water systems and its application to geophysics, *Journal of Geophysical Research*, *86*(B3), 1763–1775, 1981.

Kuerbis, R., and Y. P. Vaid, Sand sample preparation: The slurry deposition method, *Soils and Foundations*, *28*(4), 107–118, 1988.

Morgan, F. D., Fundamentals of streaming potentials in geophysics: Laboratory methods, in *Detection of Subsurface Flow Phenomena*, *Lecture Notes in Earth Sciences*, vol. 27, edited by G. P. Merkler, H. Militzer, H. Hötzl, H. Armbruster, and J. Brauns, pp. 133–144, Springer-Verlag, Berlin, 1989.

Morgan, F. D., E. R. Williams, and T. R. Madden, Streaming potential properties of Westerly granite with applications, *Journal of Geophysical Research*, *94*(B9), 12,449–12,461, 1989.

Ogilvy, A. A., M. A. Ayed, and V. A. Bogoslovsky, Geophysical studies of water leakages from reservoirs, *Geophysical Prospecting*, *17*, 36–62, 1969.

Olhoeft, G. R., Low-frequency electrical properties, *Geophysics*, *50*(12), 2492–2503, 1985.

Overbeek, J. T. G., Electrokinetic phenomena, in *Colloid Science, Irreversible Systems*, vol. 1, edited by H. R. Kruyt, Elsevier Publishing Company, Amsterdam, 1952.

Packard, R. G., Streaming potentials across glass capillaries for sinusoidal pressure, *Journal of Chemical Physics*, *21*(2), 303–307, 1953.

Pengra, D. B., S. X. Li, and P. Wong, Determination of rock properties by low-frequency AC electrokinetics, *Journal of Geophysical Research*, *104*(B12), 29,485–29,508, 1999.

Reppert, P. M., and F. D. Morgan, Frequency-dependent streaming potentials, *Journal of Colloid and Interface Science*, *234*, 194–203, 2001a.

Reppert, P. M., and F. D. Morgan, Streaming potential collection and data processing techniques, *Journal of Colloid and Interface Science*, *233*, 348–355, 2001b.

Revil, A., H. Schwaeger, L. M. Cathles III, and P. D. Manhardt, Streaming potential in porous media: 2. Theory and application to geothermal systems, *Journal of Geophysical Research*, *104*(B9), 20,033–20,048, 1999.

Sears, A. R., and J. N. Groves, The use of oscillating laminar flow streaming potential measurements to determine the zeta potential of a capillary surface, *Journal of Colloid and Interface Science*, *65*(3), 479–482, 1978.

Telford, W. M., L. P. Geldart, and R. E. Sheriff, *Applied Geophysics*, Cambridge University Press, Cambridge, 1990.

Wurmstich, B., and F. D. Morgan, Modeling of streaming potential responses caused by oil well pumping, *Geophysics*, *59*(1), 46–56, 1994.

Chapter 4

Laboratory measurements of streaming potential and resistivity in well-graded soils [3]

4.1 Introduction

The self-potential method has been used to measure the electrokinetic phenomenon of streaming potential in hydrogeological [*Revil et al.*, 2004; *Titov et al.*, 2005; *Suski et al.*, 2006], earth dam seepage [*Ogilvy et al.*, 1969; *Wurmstich et al.*, 1991], earthquake prediction [*Mizutani et al.*, 1976; *Corwin and Morrison*, 1977], geothermal [*Corwin and Hoover*, 1979; *Revil et al.*, 1999b], and subglacial flow investigations [*Blake and Clarke*, 1999; *Kulessa et al.*, 2003] to garner information about fluid flow in the subsurface. Quantitative interpretation of self-potential data using forward and inverse modelling techniques requires some knowledge of the electrical properties that govern streaming potential to recover information about the hydraulic system.

Electrokinetic processes involve the relative movement between an electrolyte and a charged solid surface. An electrical double layer, which consists of a tightly bound inner layer and a more diffuse outer layer of ions, forms at the solid-fluid interface in a saturated porous medium [*Adamson*, 1990]. The zeta potential is the average electric potential on the surface of shear within the diffuse layer. This parameter is fundamental in describing the solid-fluid interface, as it gives an approximation of the typically negative surface potential of the solid.

[3] A version of this chapter will be submitted for publication. Sheffer, M.R., Reppert, P.M. and Howie, J.A. (2007) Laboratory measurements of streaming potential and resistivity in well-graded soils.

Much of the laboratory work on streaming potentials has focused on measuring the streaming potential coupling coefficient C to study the influence of electrolyte chemistry and temperature on the zeta potential in different materials [e.g., *Ishido and Mizutani*, 1981; *Morgan et al.*, 1989; *Lorne et al.*, 1999; *Revil et al.*, 1999b; *Reppert and Morgan*, 2003]. Other work has focused on examining the link between C and hydraulic permeability [*Jouniaux and Pozzi*, 1995; *Pengra et al.*, 1999], studying the influence of fluid saturation (two-phase flow) on the measured coupling coefficient [*Guichet et al.*, 2003; *Revil and Cerepi*, 2004], and characterizing C for use in SP data interpretation at a specific site [e.g., *Revil et al.*, 2002, 2005]. Although most of these studies report measured values of C along with the saturating fluid properties, measured values of the electrical conductivity of the saturated sample σ are not often included. Both of these properties are fundamental to any mathematical treatment of streaming potential using the theory of coupled flow, and are required to calculate the streaming current cross-coupling conductivity L for a given material.

In this paper we present the results of a laboratory testing program designed to study the influence of soil and fluid parameters on the streaming current cross-coupling conductivity in saturated well-graded soil samples. We are interested in characterizing L to facilitate the quantitative interpretation of streaming potentials using numerical modelling techniques.

Section 4.2.1 describes the streaming potential phenomenon using coupled flow theory and defines L and C for 1-D flow conditions typical of laboratory experiments. Section 4.2.2 describes the properties C, σ and L using empirical and theoretical formulations. The cross-coupling conductivity may be measured directly or derived from the product of C and σ. In the current study we characterize L by measuring C and the electrical resistivity $\rho = 1/\sigma$ on the same saturated soil sample using an apparatus designed specifically for this purpose [*Sheffer et al.*, 2007]. The oscillatory flow method was used to perform streaming potential measurements on well-graded soil samples for the first time using this apparatus. Sections 4.3.1 to 4.3.3 summarize the details of the laboratory apparatus and the testing methods.

Most laboratory studies of geologic materials have focused on uniform samples, such as quartz sand [e.g., *Ahmad*, 1964; *Guichet et al.*, 2003], or crushed rock [e.g., *Morgan et al.*,

1989; *Lorne et al.*, 1999] and intact rock samples [*Jouniaux and Pozzi*, 1995]. Consequently, there is a lack of published streaming potential data for soils, particularly those that exhibit a range of grain sizes. In the present study, we are interested in characterizing well-graded soils for application to hydrogeologic and earth dam seepage investigations. Section 4.3.4 describes the soil samples tested in the current investigation.

Previous laboratory studies report varying timescales of interaction between the sample and the saturating fluid. Section 4.3.5 discusses the importance of sample equilibration and illustrates how fluid properties can vary significantly during the course of ionic exchange with the solid matrix, particularly when resistive fluids are used. This has implications for the use of theoretical estimates that rely on fluid conductivity, as discussed in Section 4.4.3.

Section 4.4 presents the results of tests performed on samples of glass beads, glacial till embankment core material and sand and gravel embankment shell material to study the influence of density, gradation and fluid conductivity on the streaming current cross-coupling conductivity. These results are compared with theoretical estimates of the electrical properties for glass bead samples. Section 4.5 compares the measured values of L in embankment soil samples with published data.

4.2 Theory

4.2.1 Streaming potential

The total flux of electric charge, or current density $\boldsymbol{J}$ [$\mathrm{A\,m^{-2}}$], in a saturated porous medium may be expressed in terms of the sum of primary and secondary potential gradients [*Onsager*, 1931]. In the absence of significant thermal or ionic concentration gradients, electrical current flow is described by

$$\boldsymbol{J} = \boldsymbol{J}_C + \boldsymbol{J}_S, \tag{4.1}$$

where $\boldsymbol{J}_C$ and $\boldsymbol{J}_S$ are respectively the conduction current and streaming current densities. The streaming current is described using a linear flow law [*de Groot*, 1951; *Sheffer and Oldenburg*, 2007]:

$$\boldsymbol{J}_S = -L\nabla h, \tag{4.2}$$

where L [A m^{-2}] is the streaming current cross-coupling conductivity and h [m] is hydraulic head. The conduction current is described using Ohm's law:

$$\boldsymbol{J}_C = -\sigma \nabla \phi, \tag{4.3}$$

where σ [S m^{-1}] is the electrical conductivity and ϕ is the electrical potential [V].

In the absence of any imposed current sources, $\nabla \cdot \boldsymbol{J} = 0$ such that (4.1) reduces to

$$\nabla \cdot \sigma \nabla \phi = -\nabla \cdot L \nabla h. \tag{4.4}$$

By applying the divergence theorem, (4.4) can be expressed as

$$\sigma \int_s \nabla \phi \cdot \hat{n} \, ds = -L \int_s \nabla h \cdot \hat{n} \, ds \tag{4.5}$$

in a homogeneous medium where L and σ are macroscopic properties. For 1-D flow in a porous medium of length l and cross-sectional area A, in which flow occurs along the length of the medium, (4.5) is evaluated to give

$$\sigma \frac{\Delta \phi}{l} A = -L \frac{\Delta h}{l} A \, . \tag{4.6}$$

Equation (4.6) may be further simplified and rearranged to define the cross-coupling conductivity:

$$L = -C \, \sigma \, , \tag{4.7}$$

where

$$C = \frac{\Delta \phi}{\Delta h}. \tag{4.8}$$

The streaming potential coupling coefficient C is typically measured in the laboratory and reported in terms of pressure, such that

$$C = \frac{\Delta \phi}{\Delta P}, \tag{4.9}$$

where $P = \gamma_f h$ and γ_f is the product of fluid density and gravitational acceleration.

4.2.2 Electrical properties

In a saturated and insulating porous matrix, electrolytic conduction dominates and conduction current flows within the interconnected pore space via free ions in solution. Surface

conduction at the solid-fluid interface can contribute significantly to the electrical conductivity of the saturated medium if the solid matrix contains conductive minerals such as clay, or if the saturating fluid exhibits low salinity. [*Ishido and Mizutani*, 1981; *Revil and Glover*, 1998].

Surface conductivity is a function of ionic conductance within the electrical double layer and is attributed to a much smaller extent to proton transfer at the mineral surface [*Revil and Glover*, 1998]. Saturation with a low-conductivity pore fluid increases the thickness of the double layer, such that it becomes a more significant fraction of the total pore diameter [*Hunter*, 1981]. This effect can be quantified by calculating the Debye length Λ_D:

$$\Lambda_D = \left(\frac{\varepsilon k_B T}{2 N_A e_c^2 I} \right)^{1/2} \tag{4.10}$$

where ε is the electric permittivity of the fluid [$\mathrm{F\,m^{-1}}$], k_B is Boltzmann's constant [$\mathrm{J\,K^{-1}}$], T is temperature [K], N_A is Avogadro's number [$\mathrm{mol^{-1}}$] and e_c is the elementary charge [C]. The ionic strength of the fluid I is given by

$$I = \frac{1}{2} \sum_i c_i z_i^2, \tag{4.11}$$

where c_i is the ionic concentration [$\mathrm{mol\,m^{-3}}$] and z_i is the valency of each ion i in solution. The Debye length is referred to as the thickness of the double layer [*Hunter*, 1981]. However, free ions in solution may be considered to exist $> 2\Lambda_D$ from the mineral surface [*Revil et al.*, 1999a]. Surface conductivity effects may be considered to be significant when the pore radius $r < 10\Lambda_D$ [*Morgan et al.*, 1989].

The electrical conductivity of the fluid σ_f [$\mathrm{S\,m^{-1}}$] may be calculated as a function of ionic concentration through the relation

$$\sigma_f = \mathcal{F} \sum_i c_i m_i, \tag{4.12}$$

where $\mathcal{F}$ is Faraday's constant [$\mathrm{C\,eq^{-1}}$], c_i is the ionic concentration stated in terms of equivalents [$\mathrm{eq\,m^{-3}}$] and m_i is the mobility [$\mathrm{m^2\,s^{-1}\,V^{-1}}$] of each ion i in solution [*Keller and Frischknecht*, 1966].

A theoretical description of C is given by the Helmholtz-Smoluchowski equation, which was derived for a capillary subject to laminar fluid flow [*Overbeek*, 1952]:

$$C = \frac{\varepsilon \zeta}{\eta\, \sigma_f}, \tag{4.13}$$

where ζ is the zeta potential [V] and η is fluid viscosity [Pa s]. This equation is valid when the thickness of the electrical double layer is much smaller than the pore radius, and electrical conductivity of the saturated matrix is governed solely by the conductivity of the pore fluid.

In cases where the surface conductivity of the solid cannot be ignored, σ_f in (4.13) can be replaced with an effective fluid conductivity σ_{eff} that accounts for the influence of surface conductivity within the pore:

$$C = \frac{\varepsilon\zeta}{\eta\,\sigma_{\text{eff}}}. \tag{4.14}$$

The effective conductivity of the pore channel may be thought of as the sum of fluid and surface conductivity:

$$\sigma_{\text{eff}} = \sigma_f + \frac{2\lambda_s}{\Lambda_{\text{p}}}, \tag{4.15}$$

where λ_s is the specific surface conductance [S], and $\Lambda_{\text{p}}/2$ is a characteristic length scale of the pore [m], which approximates the ratio of pore volume to pore surface area [*Guéguen and Palciauskas*, 1994]. Some estimates of surface conductance are given in *Ishido and Mizutani* [1981], *Jouniaux and Pozzi* [1995] and *Revil and Glover* [1998]. In a cylindrical pore channel, Λ_{p} is equivalent to the pore radius [e.g., *Overbeek*, 1952]. *Revil and Cathles III* [1999] derived an expression for Λ_{p} based on grain size diameter d in uniform sands:

$$\Lambda_{\text{p}} = \frac{d}{2m(F-1)}, \tag{4.16}$$

where Archie's cementation exponent m and formation factor F are described below.

The effect of surface conductivity can also be estimated by multiplying (4.13) by a ratio of measured formation factors [*Jouniaux and Pozzi*, 1995; *Lorne et al.*, 1999]:

$$C = \frac{\varepsilon\zeta}{\eta\,\sigma_f}\frac{F}{F_o}, \tag{4.17}$$

where $F = \sigma_f/\sigma$ is measured under the same conditions as for C when surface conductivity is present. Formation factor F_o represents the high conductivity limit when surface conductivity is negligible. The formation factor is a function of pore space topology and may be described empirically using Archie's law [*Archie*, 1942]:

$$\frac{\sigma_f}{\sigma} = n^{-m}, \tag{4.18}$$

where n is porosity. This equation is valid in cohesionless materials saturated with a saline pore fluid, such that surface conductivity effects can be neglected. When finite surface conductivity exists but the conductivity of the pore fluid still dominates conduction, the bulk conductivity of the saturated medium may be described by

$$\sigma = \frac{\sigma_{\text{eff}}}{F}, \tag{4.19}$$

where σ_{eff} is as defined in (4.15).

A theoretical description of the cross-coupling conductivity can be derived using (4.7), where C and σ are defined in (4.14) and (4.19), respectively:

$$L = -\frac{\varepsilon\zeta}{\eta F}. \tag{4.20}$$

This expression illustrates that L is a function of the formation factor, or the ratio of the electrical conductivity of the saturated sample and pore space.

4.3 Experimental methods

The laboratory apparatus was designed to enable measurements of the streaming potential coupling coefficient and resistivity on the same saturated soil specimen, as well as relevant sample properties including density, porosity and hydraulic conductivity. A complete description of the design and calibration of the apparatus and the experimental methods used to perform all tests presented in this paper can be found in *Sheffer et al.* [2007].

4.3.1 Apparatus

A schematic of the experimental apparatus is shown in Figure 4.1. The test cell consists of a sample holder and two fluid reservoirs which are fixed above and below the soil specimen. The sample holder is oriented vertically to enable the preparation of fully saturated, homogeneous soil samples. A 10 cm-long sample holder was used for all experiments presented in this paper. The inner diameter of the sample holder is 10 cm, which enables testing of samples exhibiting a maximum particle size of 9.5 mm [*ASTM*, 1991a]. The sample is contained between two pervious acrylic plates, and an external loading assembly is used to apply a nominal vertical seating load of 25 kPa to the top of the sample.

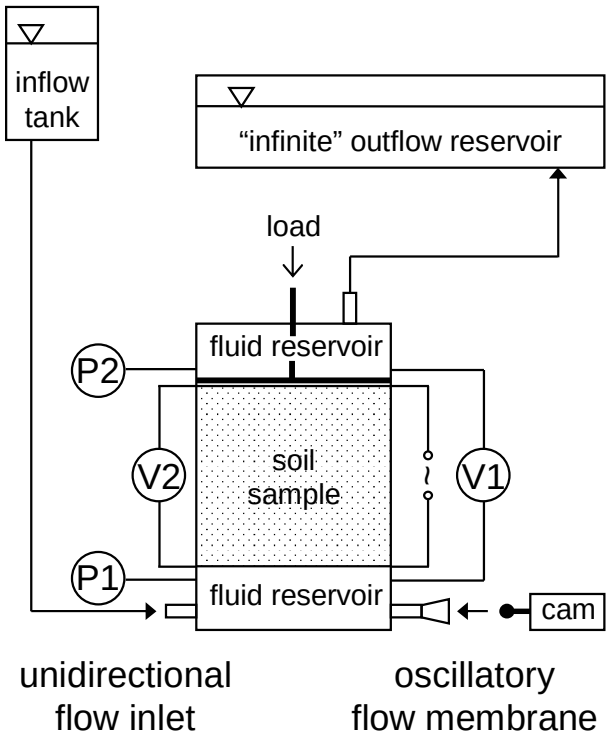

Figure 4.1: Schematic of laboratory apparatus.

The apparatus was designed to enable the use of both unidirectional and oscillatory flow test methods to measure the streaming potential coupling coefficient. These methods are described in Section 4.3.2. An "infinite" reservoir imposes a constant hydraulic head boundary to the top of the soil specimen for the purposes of both testing methods. A constant head reservoir is connected to the base of the test cell to drive fluid flow upwards through the sample for unidirectional flow testing. A sealed rubber membrane is connected to the base of the test cell for the purposes of oscillatory flow testing. Deflection of this membrane using a mechanical actuator generates an oscillating pressure gradient that drives flow through the sample.

Streaming potential measurements (V1 in Figure 4.1) are made using a pair of non-polarizing Ag-AgCl electrodes positioned immediately above and below the sample within the test cell fluid reservoirs. These electrodes are recessed away from the primary flow path to avoid electromotive effects [*Morgan*, 1989]. Pressure measurements (P1 and P2 in Figure

4.1) are made at the same vertical position using a pair of gauge pressure transducers. Resistivity measurements are performed using a pair of pervious stainless steel disk electrodes that are affixed to the acrylic plates in direct contact with both ends of the soil specimen (V2 in Figure 4.1). These electrodes are used to apply current and measure the resultant voltage drop across the sample to characterize the resistivity as a separate experiment. An automated data acquisition and control system with a 100 GΩ input impedance is used to perform all streaming potential and resistivity measurements. Insulating materials were used in the construction of the cell, and grounded shielding surrounds the entire apparatus to reduce the effects of 60 Hz noise from ambient sources.

4.3.2 Streaming potential measurements

Streaming potential measurements were conducted using unidirectional and oscillatory fluid flow techniques to characterize the streaming potential coupling coefficient C. These methods are described in *Reppert and Morgan* [2001b], and *Sheffer et al.* [2007] gives details specific to the apparatus used in this study. Although the oscillatory flow method has been implemented in previous studies of streaming potential on glass capillaries and rock samples [*Packard*, 1953; *Sears and Groves*, 1978; *Pengra et al.*, 1999; *Reppert and Morgan*, 2001a], it had previously not been tested on well-graded soils. Consequently, we adopted a parallel design approach to enable a comparison of the two methods for application to soil samples.

Unidirectional flow testing was performed by measuring the streaming potential response to a series of hydraulic gradients under steady-state flow conditions. The streaming potential coupling coefficient was then calculated from the linear fit between the measured electrical potential and hydraulic head differences for a range of hydraulic gradients. Oscillatory flow testing was carried out by measuring the streaming potential and hydraulic response to a sinusoidal 0.1 Hz pressure pulse applied at the base of the sample. This method takes advantage of the fact that the temporal response of streaming potential and differential head to an applied pressure pulse are identical under laminar flow conditions [*Chandler*, 1981]. The coupling coefficient C was determined through a spectral analysis of the measured signals by calculating the ratio of averaged potential and head amplitudes at the pulsation frequency.

The oscillatory flow method is a more efficient measurement technique as it subjects the sample to a range of hydraulic gradients in a single test. The method facilitates ionic equilibration between the sample and the pore fluid, an issue discussed in detail in Section 4.3.5, since external fluid sources are not required to induce flow through the sample.

The validity of the oscillatory measurement technique for use on soil samples was confirmed through a comparison of C values derived from unidirectional and oscillatory flow testing. Figure 4.2 compares the streaming potential coupling coefficient obtained using each method on the same glass bead or soil sample. Evident in the figure is a strong agreement between C values derived from corresponding flow tests, with the exception of three data points corresponding to samples *gb_a*, *gb_b* and *gbnc_a*. The relatively high percentage of finer grains and resistive fluid ($\sim$500 Ωm) used to saturate these samples led to a rapid change in sample conditions upon termination of steady unidirectional fluid flow. This is confirmed by measured resistivity values, which dropped respectively by 7%, 10% and 13% in these samples between flow tests. The lower sample resistivity translates to a smaller magnitude of C, which is evident in the data shown in Figure 4.2.

4.3.3 Resistivity measurements

Resistivity measurements were conducted using a 2-electrode configuration, where a single pair of stainless steel plate electrodes was used to inject current and measure the potential difference across the length of the soil sample. A 100 Hz AC source current was chosen to characterize the DC limit of resistivity while preventing polarization of the electrodes. Sample resistivity was calculated by multiplying the measured resistance by the ratio of the cross-sectional area and length of the sample.

4.3.4 Sample properties

Sample density and porosity were calculated using measurements of sample volume and values of specific gravity for each material tested. Sample length was measured using a dial gauge. The hydraulic conductivity of each sample was determined using Darcy's law:

$$Q = -K\frac{\partial h}{\partial z}A\,, \tag{4.21}$$

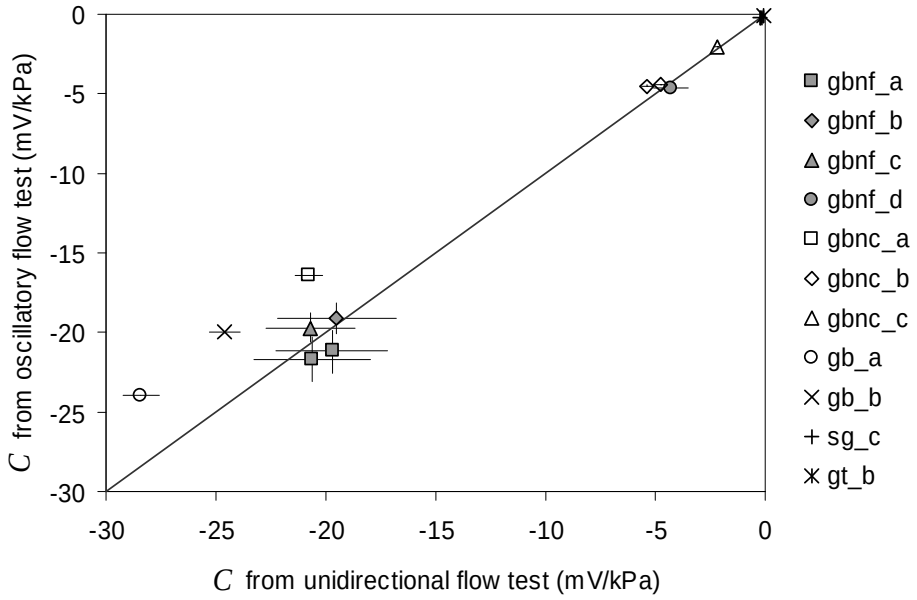

Figure 4.2: Comparison of streaming potential coupling coefficient (C) values measured using unidirectional and oscillatory flow test methods. Soil samples are labelled according to material type (*gb*: glass beads, *sg*: sand and gravel *gt*: glacial till), variations on the gradation (nf: fines removed, *nc*: coarse fraction removed) and the sample identifier (e.g. $\_a$).

where A is the cross-sectional area of the sample and Q [$\mathrm{m^3\,s^{-1}}$] is the volumetric flow rate measured during steady-state unidirectional flow from an applied hydraulic gradient.

Figure 4.3 shows the grain size distribution curves for the glass bead samples tested. The base gradation *gb* represents a well-graded material of uniform mineralogy. Gradations $gbnf$ and *gbnc* represent the same gradation but with fine and coarse fractions removed, respectively. These two gradations serve as bounds on the material for the purposes of studying the influence of gradation on the electrical properties. The average specific gravity for the glass particles is 2.475.

Figure 4.4 shows the grain size distribution curves for soil obtained from the core and inner shell zones of an embankment site in British Columbia. The core material *gt* is a well-graded glacial till with an average clay content of 7%, an average field dry density of 2.11 g/cm^3 and a mean specific gravity of 2.54 [*BC Hydro*, 2002]. Mineralogical analyses

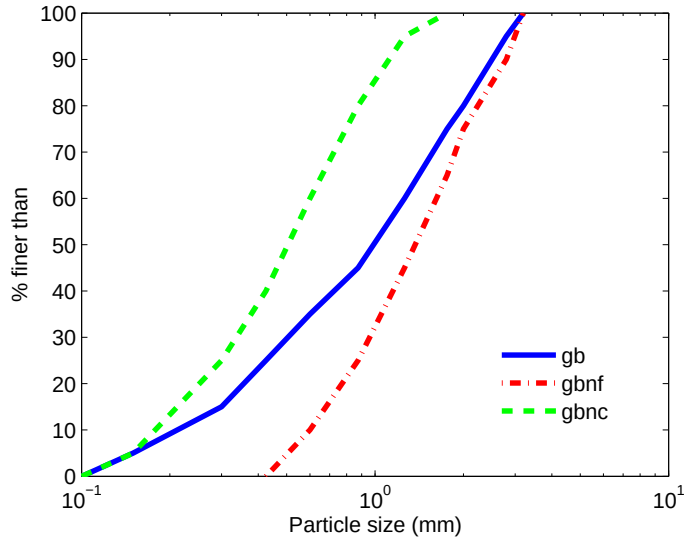

Figure 4.3: Grain-size distribution of glass bead samples.

performed on the fine fraction of the core revealed weight percentages of 30% quartz and over 41% muscovite [*Sheffer*, 2005], where fines are defined as particles < 0.075 mm in diameter. The sand and gravel shell material *sg* consists primarily of sub-angular to sub-rounded particles of quartzite and limestone with approximately 17% mica schist and gneiss, has an average field dry density of 2.34 g/cm^3, and a mean specific gravity of 2.78 [*BC Hydro*, 2002]. The core and shell material was processed using the wet-sieve method [*ASTM*, 1993a] and samples were created to match the average gradations of material placed below a particle size of 9.4 mm, to conform to the capacity of the test cell. The 3% fine fraction was not included in any of the reconstituted shell samples. Gradation *gt* represents core material with the full 40% fine fraction, *gt*25 contains 25% fines and *gt*0 contains none of the fine fraction, as indicated in Figure 4.4.

All soil samples were saturated under vacuum and reconstituted in the cell using a modified slurry deposition technique [*Kuerbis and Vaid*, 1988]. Sample density was increased by tapping on the base of the test cell during sample deposition, for the purposes of studying the influence of density on the electrical properties. The electrical conductivity of the saturating fluid was controlled by adding Na_2SO_4 in solution to de-aired tap water exhibiting a

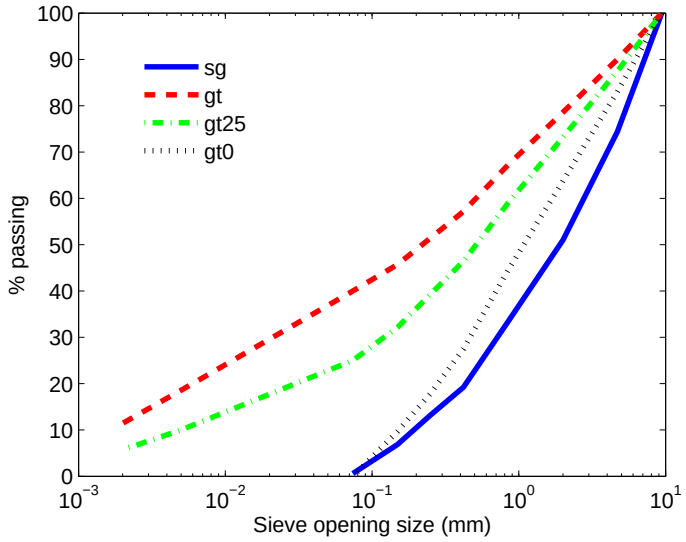

Figure 4.4: Grain-size distribution of embankment soil samples (*sg*: sand and gravel shell, *gt*: glacial till core).

nominal fluid conductivity of 2×10^{-3} S/m. Fluid conductivity, temperature and pH were measured in the external reservoirs using portable electrical conductivity and pH meters. Saturating fluid properties are listed along with the sample data in Table 4.1. Embankment soil samples were saturated with fluid exhibiting a nominal resistivity of 70 Ωm to represent observed fluid properties at site. All samples were subjected to a vertical seating load of 25 kPa following preparation.

4.3.5 Sample equilibration

One main advantage of oscillatory flow testing over unidirectional flow testing is that it allows the soil and pore fluid to reach a state of ionic equilibrium more efficiently since the pore fluid is not completely flushed during testing. This process of equilibration is important to ensure that measured C and ρ values are more representative of the saturated system in its natural state, and to prevent the influence of diffusion potentials on the measured streaming potential.

Figure 4.5 illustrates the influence of soil-fluid equilibration on the measured electrical

properties for glass bead sample *gb_a*. This sample was saturated with a 540 Ωm fluid. Evident in the figure is the rapid change in early time, as the saturated sample starts to equilibrate upon termination of a unidirectional flow test. All subsequent streaming potential measurements were performed using the oscillatory flow method such that no external fluid was introduced to the sample. Resistivity measurements were conducted in between streaming potential measurements. The electrical properties trend towards constant values as the sample approaches equilibrium. Of particular note is the relative change in the amplitude of each parameter with time. Both C and ρ values decrease up to one order of magnitude, whereas L varies by less than half its original value. A fluid resistivity of 327 Ωm was measured within the test cell reservoir following the experiment, and represents a 39% decrease in resistivity of the original saturating fluid. This is attributed to ionic exchange between the solid matrix and saturating fluid, which has been observed by other researchers [*Jouniaux and Pozzi*, 1995; *Guichet et al.*, 2003].

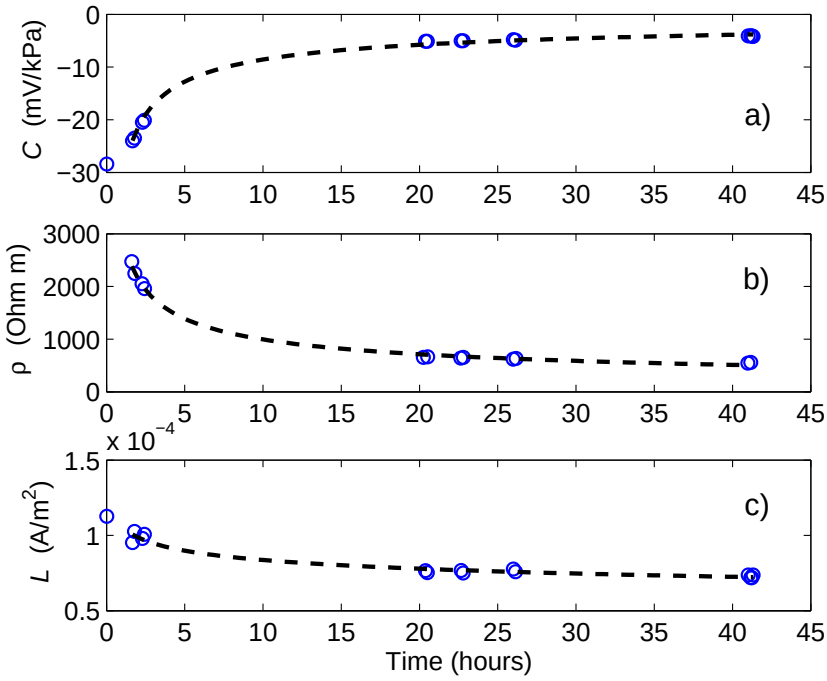

Figure 4.5: Influence of sample equilibration on the electrical properties measured on a sample of glass beads (*gb_a*).

A state of sample equilibrium is marked by measured parameters that are stable over time, and synchronized streaming potential and pressure responses to the onset of fluid flow. A time lag between these responses is indicative of diffusion potential effects caused by ionic imbalances within the system. Gradients in fluid chemistry generate an electrical potential due to the diffusion of ions, which is measured along with the streaming potential.

Unidirectional flow measurements of streaming potential in glass bead samples gave steady, repeatable results if the pore fluid was completely flushed prior to testing. The lower hydraulic conductivity of embankment material precluded reliable unidirectional flow measurements in these samples. In oscillatory flow measurements, diffusion-induced lag was found to be most prevalent in samples of embankment material. Oscillatory flow testing performed in early time revealed up to a 180^{o} phase shift in the streaming potential response. Mineralogical analyses confirmed that this apparent reversal in polarity was not caused by a positive surface potential on the solid grains. However, a long-term experiment was conducted on a sand and gravel sample (sg_c) to confirm that diffusion potential effects were indeed the source of this lag. Fluid was re-circulated through the test cell and external reservoir system over a period of eight weeks to achieve equilibrium conditions, at which time unidirectional flow measurements gave consistent results with oscillatory flow measurements, as shown in Figure 4.2. Fluid resistivity decreased from 82 Ωm at the start of the experiment to 22 Ωm at completion due to ionic exchange with the soil. Any lag evident in oscillatory flow measurements performed at the start of an experiment was found to dissipate as the sample reached equilibrium.

Sample	n	Bulk density g/cm^3	C_u	σ_f (ρ_f) μS/m (Ωm)	Fluid pH
gb_a	0.26	2.08	5.7	18.5 (540) @ 23.1°C	6.40
gb_b	0.26	2.08	5.7	20.4 (489) @ 22.8°C	6.40
gbnf_a	0.32	2.00	2.7	19.7 (508) @ 22.5°C	-
gbnf_b	0.33	1.99	2.7	20.2 (495) @ 22.0°C	-
gbnf_c	0.30	2.03	2.7	23.0 (435) @ 23.5°C	6.40
gbnf_d	0.32	2.00	2.7	100 (100) @ 23.1°C	6.40
gbnc_a	0.32	2.00	3.2	23.4 (428) @ 22.9°C	6.60
gbnc_b	0.32	2.00	3.2	101 (99) @ 23.3°C	6.60
gbnc_c	0.31	2.02	3.2	232 (43) @ 22.8°C	6.80
sg_a	0.22	2.20	15	145 (69) @ 22.2°C	6.64
sg_b	0.22	2.20	15	156 (64) @ 22.1°C	6.38
sg_c	0.14	2.33	15	122 (82) @ 21.7°C	7.46
gt_a	0.28	2.29	417	149 (67) @ 22.8°C	6.36
gt_b	0.29	2.26	417	141 (71) @ 21.5°C	6.46
gt0	0.29	2.27	8	147 (68) @ 21.5°C	6.44
gt25	0.24	2.36	180	154 (65) @ 22.7°C	6.52

Table 4.1: Summary of sample data for tests conducted on glass beads and embankment fill material. Soil samples are labelled according to material type (*gb*: glass beads, *sg*: sand and gravel *gt*: glacial till), variations on the gradation (*nf*: fines removed, *nc*: coarse fraction removed, #: % fines) and the sample identifier (e.g. *_a*). Absolute fluid conductivity (resistivity), temperature and pH characterize the saturating fluid properties and were measured during oscillatory flow testing in the infinite reservoir connected to the apparatus. These values do not necessarily reflect the properties of the pore fluid at ionic equilibrium with the sample.

4.4 Results

Table 4.2 summarizes the experimental results for all glass bead and embankment soil samples studied. The reported electrical properties ρ, C and L represent the saturated sample following a period of soil-fluid equilibration. Measurements of sample resistivity are absolute values with respect to temperature, with all experiments conducted at a nominal ambient temperature of 22.5°C. The quoted uncertainties in the measured properties reflect instrument sensitivity.

In the sections that follow we evaluate the influence of sample density, sample gradation and saturating fluid conductivity on the electrical properties. Data collected for glass bead samples are compared to theoretical estimates of C, ρ and L, which are calculated using (4.14), (4.19) and (4.7), respectively. The average pore radius of each glass bead sample is calculated using (4.16). The mean grain diameter d is approximated using d_{50}, the median particle size for a given gradation. The formation factor is calculated from Archie's law $F = n^{-m}$, using the measured porosity for each sample and $m = 1.3$. To calculate C using (4.14), we assume constant fluid property values of $\varepsilon = 7.08 \times 10^{-10}$ F m^{-1} and $\eta = 8.9 \times 10^{-4}$ Pa s. We calculate σ_{eff} using (4.15), where σ_f is the measured conductivity of the fluid used to saturate the samples in each experiment. Values of surface conductance and zeta potential are taken from *Gu and Li* [2000] who reported $\lambda_s = 2 \times 10^{-7}$ S and $\zeta = -25$ mV for a glass channel saturated with a 2.4×10^{-4} mol L^{-1} NaCl electrolyte, which approximates the dominant ions and nominal fluid resistivity of the natural fluid used in this study. These values lie within the range of those reported for Fontainebleau sandstone, a rock containing 99% quartz, saturated with 10^{-3} to 10^{-4} M NaCl solutions [*Jouniaux and Pozzi*, 1995; *Reppert and Morgan*, 2003].

4.4.1 Influence of density

Samples of glass beads, shell and core material were prepared at different densities to evaluate the influence of this parameter on the electrical properties. The bulk density ϱ of a fully-saturated sample is defined as

$$\varrho = \frac{G_s + e}{1 + e}\,\varrho_f, \tag{4.22}$$

where G_s is the specific gravity of the material, $e = n/(1-n)$ is the void ratio and ϱ_f is fluid density.

Three glass bead samples of the same *gbnf* gradation (*gbnf_a*, *gbnf_b* and *gbnf_c*) were saturated with fluid exhibiting a nominal resistivity of 500 Ωm and prepared at densities ranging from 1.99 to 2.03 g/cm^3, as listed in Table 4.1. These samples exhibit porosities that lie within the maximum range of 0.29 to 0.34 measured for the material [*ASTM*, 1993b, 1991b]. Figure 4.6 compares measured and calculated values of C, ρ and L for each sample.

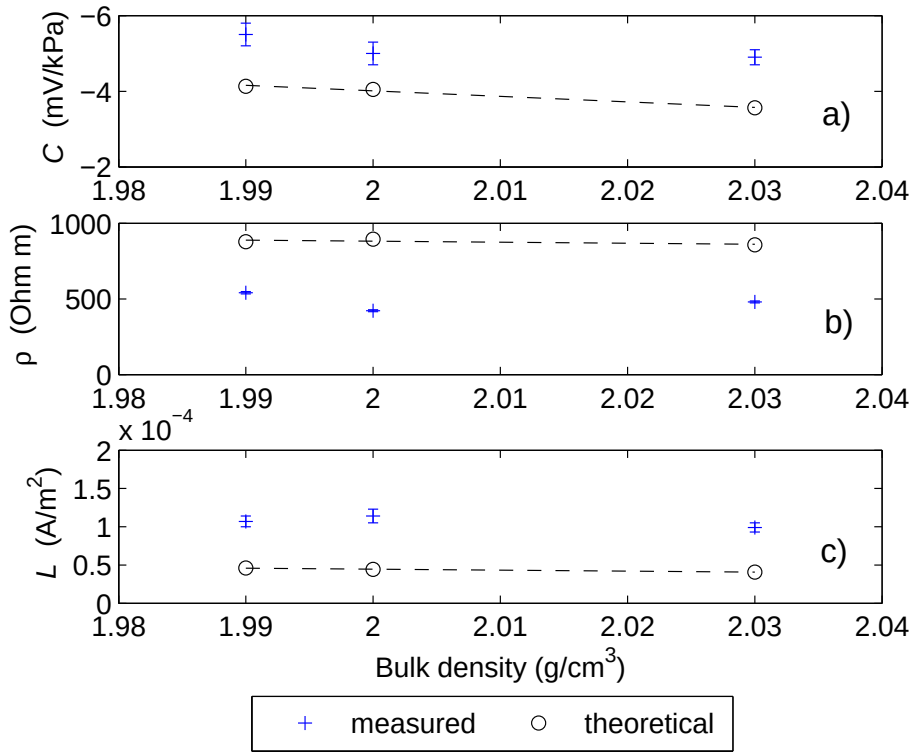

Figure 4.6: Influence of density on the electrical properties in glass bead samples: a) streaming potential coupling coefficient; b) sample resistivity; c) cross-coupling conductivity. Measured data represent samples *gbnf_a*, *gbnf_b* and *gbnf_c*. Open symbols represent calculated theoretical behaviour using parameters described in text. Dashed line is a linear fit to the theoretical data points.

An increase in sample density might be expected to decrease the porosity and average pore radius of a soil. Given the relation shown in (4.15), a smaller pore radius would cause an increase in the effective conductivity of the pore channels due to the larger influence of surface conductivity. The higher effective conductivity would translate to a decrease in the magnitude of both C and sample resistivity, according to (4.14) and (4.19). Figures 4.6(a) and (b) show that both measured and predicted values of the streaming potential coupling coefficient and resistivity exhibit a slight decrease in magnitude with increasing density. However, the relative variation is very small and within the range of error for measured values of C such that no distinct trend may be inferred conclusively. Calculated resistivity values are up to two times larger than measured results, which suggests that the theoretical estimate may not adequately represent true conditions. This issue is discussed further in Section 4.4.3. Figure 4.6(c) shows a slight decrease in measured and predicted values of L. However, the net effect of changing density on the cross-coupling conductivity is insignificant, and suggests an average measured value of $L = 1.1 \pm 0.2 \times 10^{-4}\text{A/m}^2$.

Two samples of glacial till core material (*gt_a* and *gt_b*) were saturated with fluid exhibiting a nominal resistivity of 70 Ωm and prepared at densities of 2.29 and 2.26 g/cm^3, respectively. Figure 4.7 reveals that the change in density has no effect on the measured electrical properties for the conductive core material. Three samples of sand and gravel shell material (*sg_a*, *sg_b* and *sg_c*) were also prepared for the purposes of studying the effect of changing density. The density of sample *sg_b* did not increase following preparation using the method described in Section 4.3.4. Consequently, sample *sg_c* was prepared in layers and densified by tamping the sample with a glass rod to achieve a porosity of 0.14. Figure 4.7 shows a decrease in the magnitude of C, ρ and L with an increase in density. However, conclusive interpretation of these results is complicated by differences in experimental procedure and the much longer timescale of the *sg_c* experiment, as discussed in Section 4.3.5.

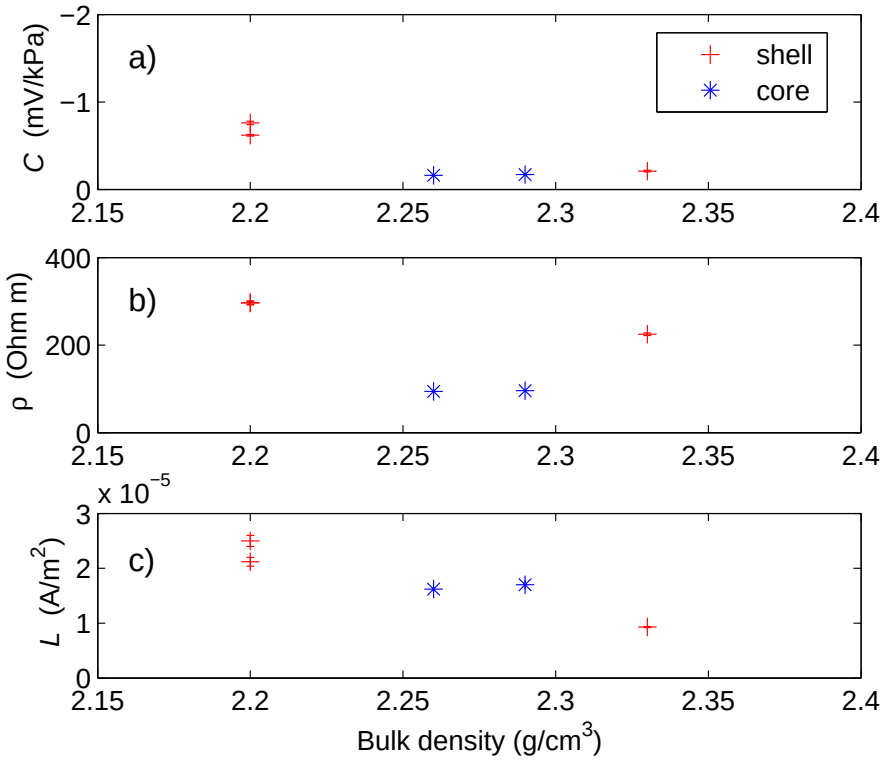

Figure 4.7: Influence of density on the electrical properties of embankment soil samples: a) streaming potential coupling coefficient; b) sample resistivity; c) cross-coupling conductivity. Measured shell data represent samples *sg_a*, *sg_b* and *sg_c*; measured core data represent samples *gt_a* and *gt_b*.

Sample	K	ρ	C	L
	m/s	Ωm	mV/kPa	A/m^2
gb_a	1.3×10^{-3}	552 ± 8	-4.07 ± 0.03	$7.3\,(\pm 0.1) \times 10^{-5}$
gb_b	1.1×10^{-3}	443 ± 7	-3.00 ± 0.02	$6.8\,(\pm 0.1) \times 10^{-5}$
gbnf_a	-	422 ± 6	-5.0 ± 0.3	$1.14\,(\pm 0.09) \times 10^{-4}$
gbnf_b	8.2×10^{-3}	541 ± 8	-5.5 ± 0.3	$1.07\,(\pm 0.07) \times 10^{-4}$
gbnf_c	7.0×10^{-3}	480 ± 7	-4.9 ± 0.2	$9.9\,(\pm 0.6) \times 10^{-5}$
gbnf_d	7.0×10^{-3}	312 ± 5	-2.2 ± 0.1	$7.1\,(\pm 0.4) \times 10^{-5}$
gbnc_a	1.1×10^{-3}	502 ± 8	-4.10 ± 0.02	$8.1\,(\pm 0.2) \times 10^{-5}$
gbnc_b	1.1×10^{-3}	278 ± 4	-2.20 ± 0.01	$7.8\,(\pm 0.2) \times 10^{-5}$
gbnc_c	9.2×10^{-4}	144 ± 2	-1.06 ± 0.01	$7.2\,(\pm 0.1) \times 10^{-5}$
sg_a	3.2×10^{-3}	296 ± 4	-0.76 ± 0.02	$2.5\,(\pm 0.1) \times 10^{-5}$
sg_b	1.1×10^{-3}	297 ± 4	-0.62 ± 0.01	$2.12\,(\pm 0.08) \times 10^{-5}$
sg_c	5.5×10^{-5}	225 ± 3	-0.21 ± 0.01	$9.3\,(\pm 0.1) \times 10^{-6}$
gt_a	-	96 ± 1	-0.17 ± 0.01	$1.70\,(\pm 0.07) \times 10^{-5}$
gt_b	3.2×10^{-7}	94 ± 1	-0.16 ± 0.01	$1.62\,(\pm 0.03 \times 10^{-5}$
gt0	3.4×10^{-4}	228 ± 3	-0.49 ± 0.01	$2.10\,(\pm 0.05) \times 10^{-5}$
gt25	-	133 ± 2	-0.14 ± 0.01	$1.03\,(\pm 0.06) \times 10^{-5}$

Table 4.2: Summary of experimental results for tests conducted on glass beads and embankment fill material. Soil samples are labelled according to material type (*gb*: glass beads, *sg*: sand and gravel *gt*: glacial till), variations on the gradation (*nf*: fines removed, *nc*: coarse fraction removed, #: % fines) and the sample identifier (e.g. *_a*). Values of ρ, C and L characterize the sample following a period of ionic equilibration with the pore fluid. All testing was performed at a nominal ambient temperature of 22.5°C. Uncertainties in the electrical properties were calculated based on instrument sensitivities.

4.4.2 Influence of gradation

Glass bead samples exhibiting different grain size distributions were studied to evaluate the influence of gradation on the electrical properties in a material of uniform mineralogy. Similarly, glacial till samples with varying fines content were studied to examine the effect of gradation accompanied by a change in mineralogy. The change in gradation was quantified using the coefficient of uniformity C_u, which is defined as

$$C_u = \frac{d_{60}}{d_{10}}, \tag{4.23}$$

where d_{60} and d_{10} are representative particle sizes for a given grain size distribution. The subscript represents the percentage of soil grains finer than the stated particle size. A large value of C_u denotes a sample with a wide range of grain sizes, whereas a smaller value denotes a more uniformly graded sample.

Two series of glass bead samples were studied for the purposes of evaluating the effect of gradation. Samples *gb_a*, *gb_b*, *gbnf_a* and *gbnc_a* were saturated with fluid exhibiting a nominal resistivity of 500 Ωm. Samples *gbnf_d* and *gbnc_b* were saturated with fluid exhibiting a nominal resistivity of 100 Ωm. Figure 4.8 presents the measured and theoretical values of C, ρ and L for each set of samples. Although *gbnf* and *gbnc* samples contain dramatically different amounts of fines, as shown in Figure 4.3, the similar shape of the grain size curves results in similar values of C_u, as listed in Table 4.1.

The porosity can be expected to decrease with a wider range of grain sizes, as evidenced by the lower measured porosity of *gb* samples as compared to *gbnf* and *gbnc* samples shown in Table 4.1. Consequently, with larger values of C_u we might expect a decrease in pore radius and an increased influence of surface conductivity on the effective conductivity. An increase in σ_{eff} would decrease the amplitude of C and ρ. Figure 4.8(a) shows a slight decrease in measured values of C in samples saturated with 500 Ωm fluid, with no clear trend visible in the theoretical values. Figure 4.8(b) shows no distinct trend in measured or predicted resistivity values for these samples. However, calculated values of ρ overestimate measured values in *gbnf* (C_u = 2.7) and *gb* (C_u = 5.7) samples saturated with 500 Ωm fluid. This is discussed further in Section 4.4.3. Samples saturated with 100 Ωm fluid display no significant variation in measured or theoretical values of C or ρ with gradation.

Figure 4.8(c) shows that the effect of changing gradation on L is insignificant, and suggests an average measured value of $L = 7 \pm 1 \times 10^{-5}\mathrm{A/m^2}$ independent of the saturating fluid resistivity. The exception to this is the $gbnf\_a$ datum at $\mathrm{C_u} = 2.7$, which exhibits a larger value of L in keeping with the other $gbnf$ samples shown in Figure 4.6.

Figure 4.9 shows the influence of gradation in samples of glacial till core material (gt_a, $gt25$ and $gt0$). In these samples, an increase in $\mathrm{C_u}$ represents an increase in fines content as well as a change in mineralogy. The presence of fine-grained silt and clay material serves to increase the surface conductivity, and leads to a small decrease in the amplitudes of C and ρ as shown in Figures 4.9(a) and (b).

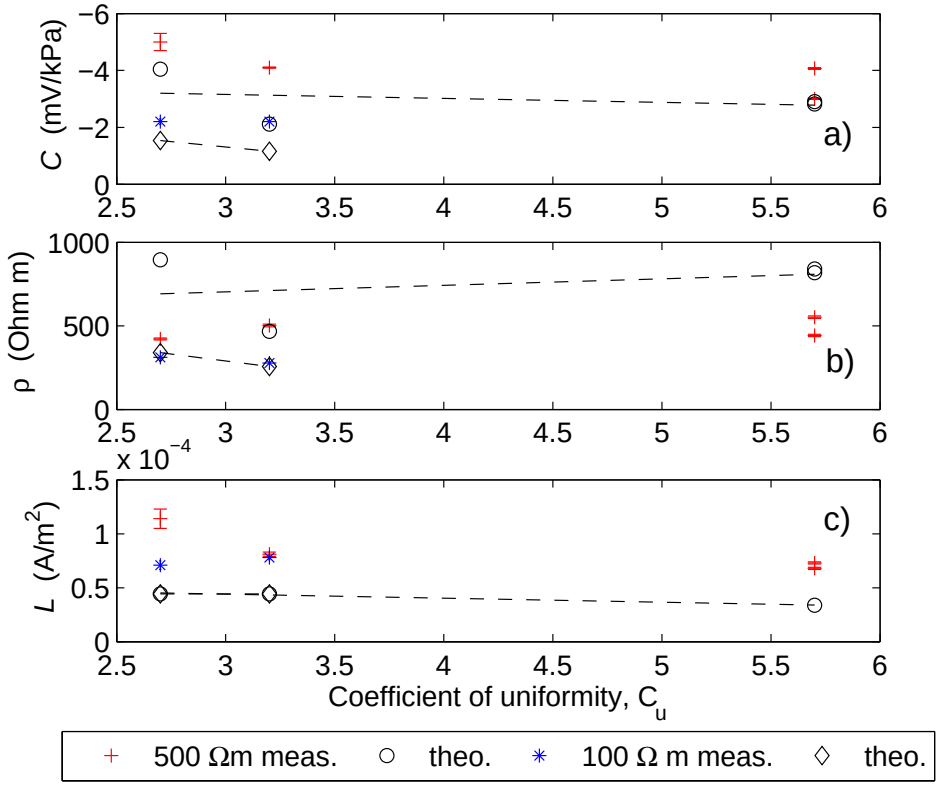

Figure 4.8: Influence of gradation on the electrical properties in glass bead samples: a) streaming potential coupling coefficient; b) sample resistivity; c) cross-coupling conductivity. Measured data represent samples *gb_a*, *gb_b*, *gbnf_a* and *gbnc_a* saturated with fluid exhibiting a nominal fluid resistivity of 500 Ωm; and samples *gbnf_d* and *gbnc_b* saturated with fluid with a nominal resistivity of 100 Ωm. Open symbols represent calculated theoretical behaviour using parameters described in text. Dashed lines represent a linear fit to the theoretical data points.

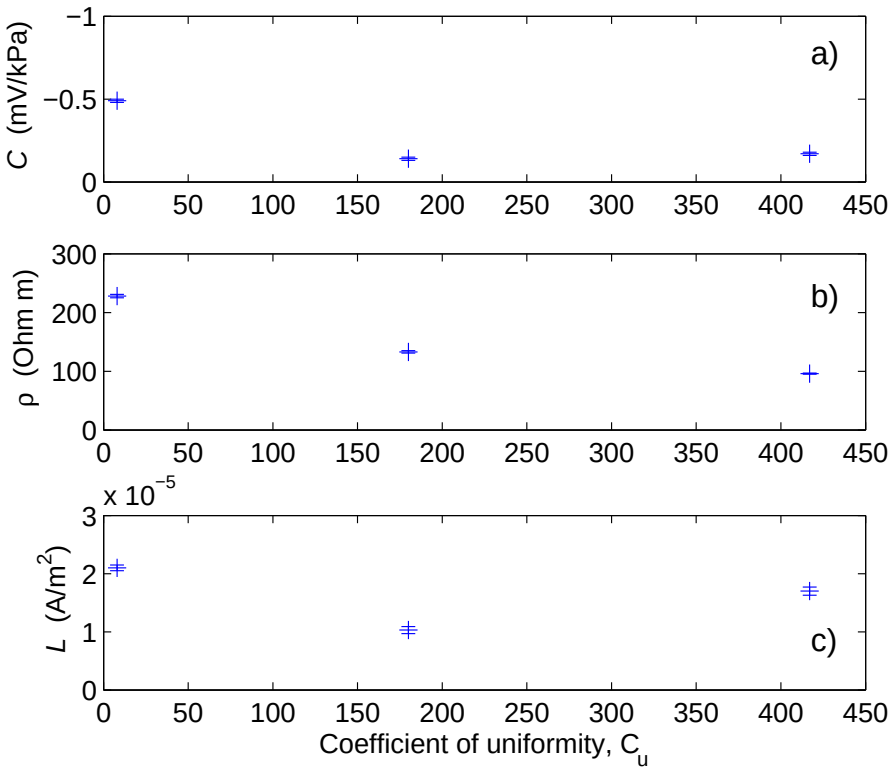

Figure 4.9: Influence of gradation on the electrical properties of embankment soil samples: a) streaming potential coupling coefficient; b) sample resistivity; c) cross-coupling conductivity. Measured data represent samples gt_a, $gt25$ and $gt0$.

4.4.3 Influence of fluid conductivity

The properties of the double layer are influenced by the concentration and type of ions in solution, which exhibit different adsorption properties and mobilities, as illustrated in *Morgan et al.* [1989]. Since natural waters typically contain a range of dissolved ions, we use fluid resistivity as an indicator of the ionic strength of the saturating fluids used in this study.

Three glass bead samples of the same gradation were saturated with fluids exhibiting different resistivities for the purposes of evaluating their effect on the electrical properties. Measured and theoretical values of C, ρ and L are shown in Figure 4.10 for samples *gbnc_a*, *gbnc_b* and *gbnc_c*. As expected from the relations shown in (4.13) and (4.18), both measured and predicted data show an increase in the magnitude of C and ρ with an increase in fluid resistivity. In accordance with (4.20), Figure 4.10(c) shows that measured and predicted values of L show very little variation with fluid resistivity, and suggest an average measured value of $L = 7.7 \pm 0.5 \times 10^{-5}\mathrm{A/m^2}$ for these three samples, which is within range of that reported for the data shown in Figure 4.8(c).

Measured and predicted values of resistivity compare well over the entire range of fluid resistivity for the *gbnc* samples shown in Figure 4.10(b). However, a discrepancy between calculated and measured sample resistivities in *gbnf* and *gb* samples saturated with 500 Ωm fluid was noted in Figures 4.6(b) and 4.8(b). Figure 4.11 compares the measured sample resistivity to that calculated using (4.19) for all glass bead samples, and clearly illustrates this discrepancy. According to (4.19), breakdown of the theory at high fluid resistivities may be caused by too small an estimate of σ_{eff} or too large an estimate of F.

Effective conductivity is a function of both fluid and surface conductivity in the pore space. Surface conductivity is calculated using estimates of surface conductance and average pore radius. The calculation of pore radius using a single representative grain diameter in (4.16) provides a very simple approximation for a well-graded material that exhibits a large range of particle sizes. However, the predicted surface conductivity was found to be of considerable magnitude in resistive samples. Surface conductivity was found to be largest in samples with the most fines (*gbnc*), smallest in the samples with the least fines (*gbnf*), and larger than the saturating fluid conductivity in all cases.

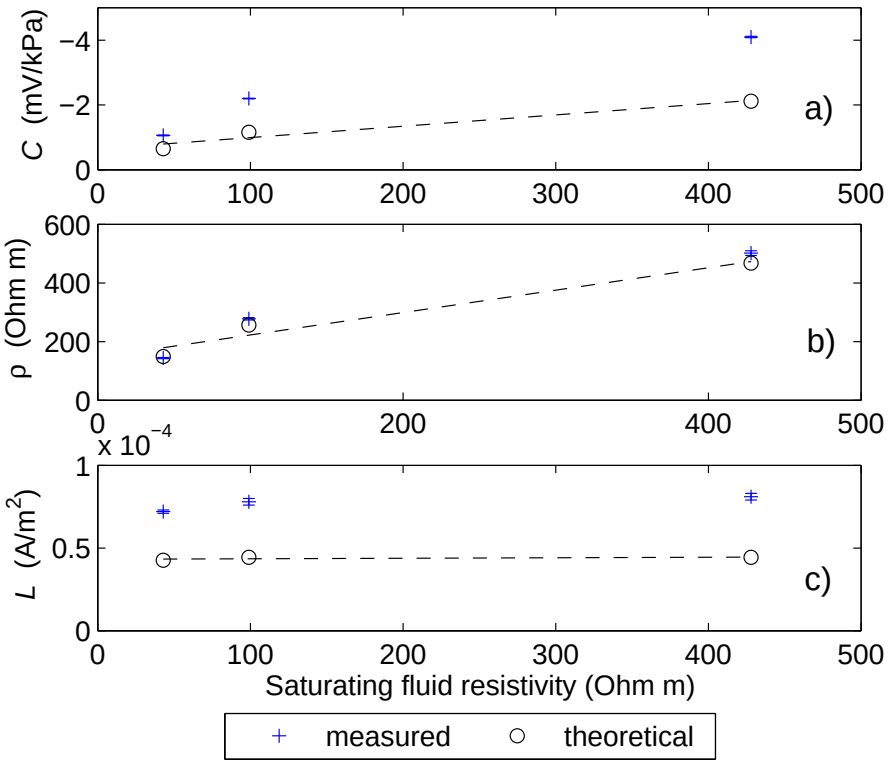

Figure 4.10: Influence of fluid resistivity on the electrical properties in glass bead samples: a) streaming potential coupling coefficient; b) sample resistivity; c) cross-coupling conductivity. Measured data represent samples *gbnc_a*, *gbnc_b* and *gbnc_c*. Open symbols represent calculated theoretical behaviour using parameters described in text. Dashed line is a linear fit to the theoretical data points.

As discussed in Section 4.3.5, very large changes in fluid conductivity of up to 70% were observed for samples *gb_a* and *sg_c* during the course of sample equilibration. This suggests that the measured conductivity of the saturating fluid listed in Table 4.1 may not represent the actual pore fluid. Consequently, calculated values of σ_{eff} using (4.15) will underestimate the true conductivity of the pore channel and result in an overestimate of sample resistivity. Figure 4.11 illustrates the effect of using measured values of pore fluid conductivity to calculate σ_{eff}. Fluid conductivity measurements were made in the upper cell reservoir following testing of samples *gb_a*, *gb_b*, *gbnf_d*, *gbnc_a* and *gbnc_c*. Resistive

samples *gb_a* and *gb_b* show the largest improvement in predicted resistivity, as indicated by the arrows in the figure.

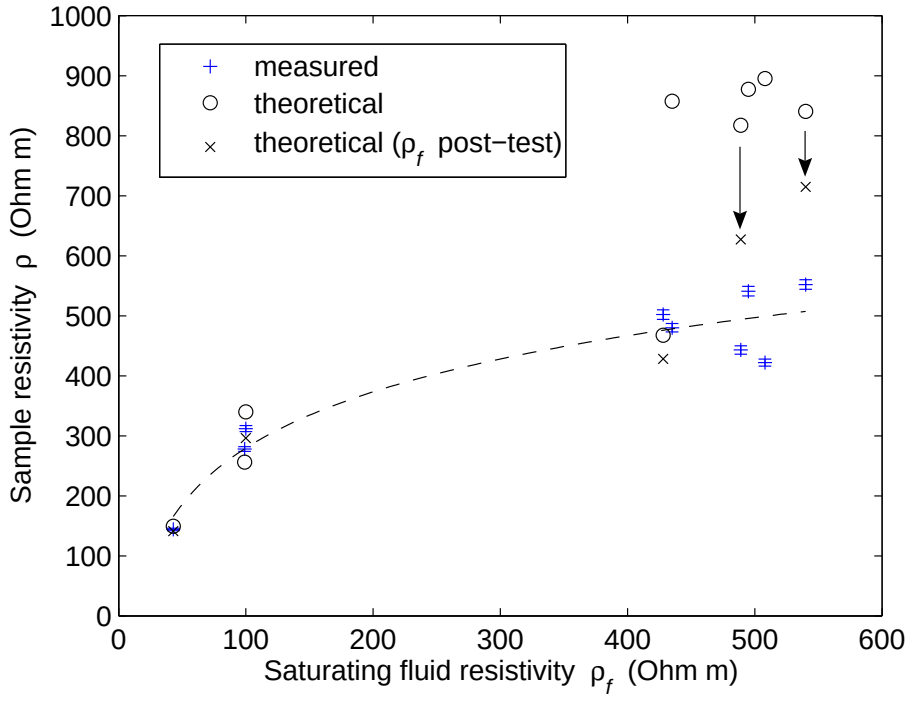

Figure 4.11: Comparison of measured and predicted sample resistivity versus measured saturating fluid resistivity for all samples of glass beads. Theoretical behaviour is calculated using Equation (4.19), where formation factor is estimated from $F = n^{-m}$ and σ_{eff} is calculated using Equation (4.15). Open circles indicate σ_{eff} values calculated using the saturating fluid conductivity; x symbols indicate σ_{eff} values calculated using measured pore fluid conductivity upon completion of the experiment, where available. Arrows denote change in the predicted sample resistivity for samples *gb_a* and *gb_b*

.

Archie's relation $F = n^{-m}$ was used to approximate the formation factor in glass bead samples. However, this relation can not capture the influence of ionic equilibration on sample resistivity. Figure 4.12 compares Archie's law to values of formation factor calculated using measured resistivities. Measured resistivity data acquired upon flushing the sample

with the saturating fluid give formation factors on par with those predicted using Archie's law. However, formation factors calculated from the measured sample resistivity following equilibration are roughly four times smaller at high fluid resistivities.

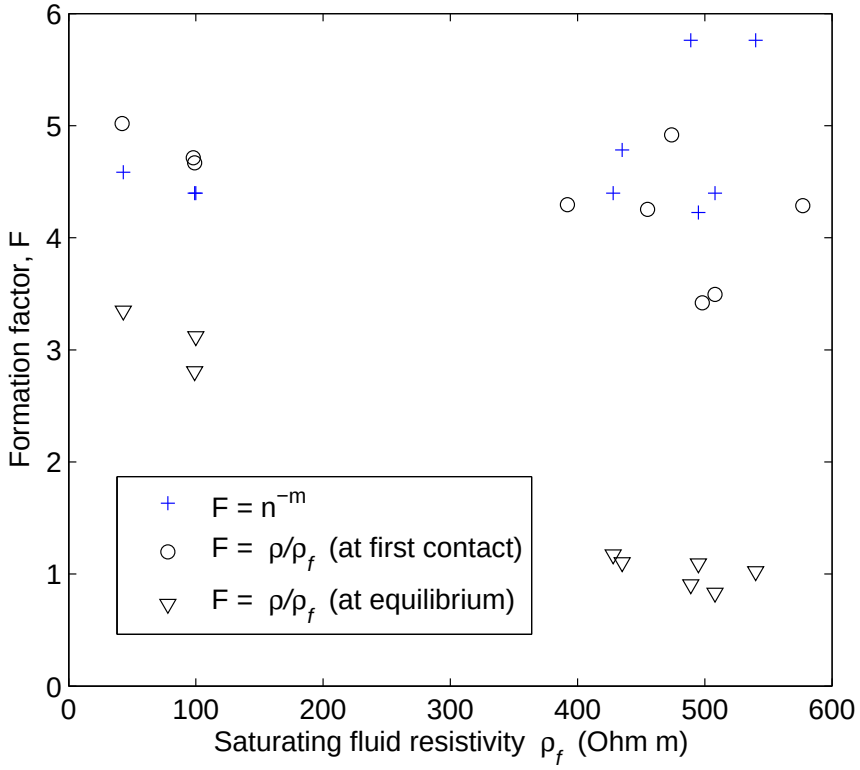

Figure 4.12: Comparison of measured and estimated values of formation factor versus measured saturating fluid resistivity for all samples of glass beads. Theoretical behaviour (+ symbols) is calculated using (4.18). Open circles indicate F values calculated from measured resistivity data acquired upon initial contact between the soil and fluid (not at equilibrium). Open triangles indicate F values calculated from the measured sample resistivity following equilibration and the saturating fluid resistivity.

4.5 Discussion

The experimental results confirm that both C and σ are strongly dependent on fluid conductivity, but that L is relatively independent, as suggested by the equations listed in Section 4.2. Consequently, it is very important to measure C and σ under the same conditions to properly characterize L. Figure 4.13 illustrates the relative change in C and L with sample resistivity measured in glass bead samples at different times during the sample equilibration process. While C can vary over an order of magnitude, L exhibits a much smaller range of variation and appears to be a more constant property of the material.

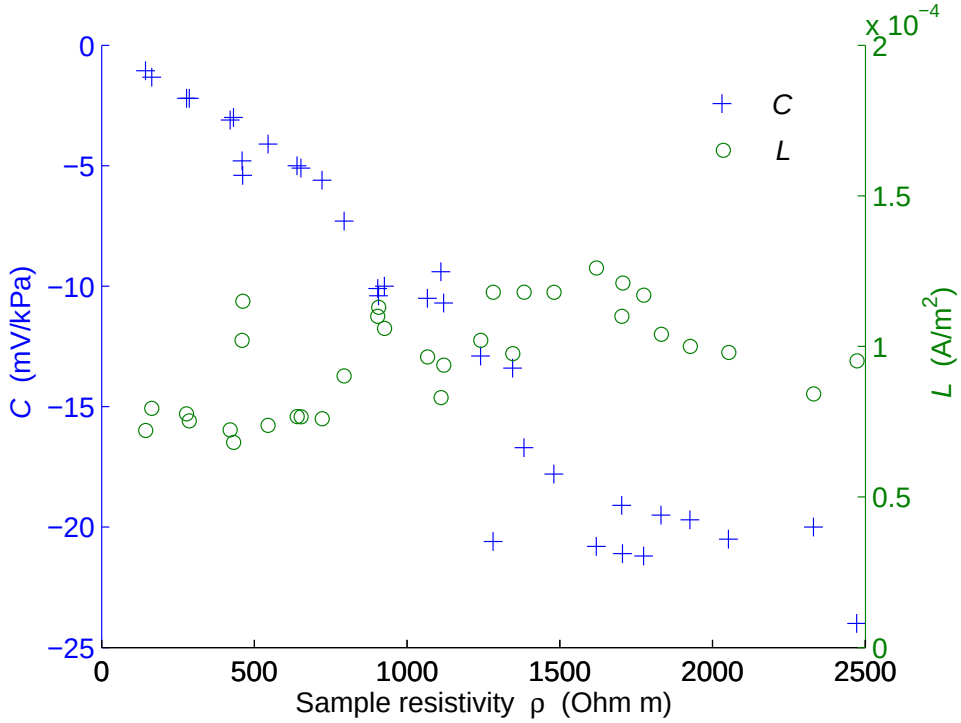

Figure 4.13: Comparison of measured streaming potential coupling coefficient and streaming current cross-coupling conductivity with sample resistivity for samples of glass beads. Data represent different stages of sample equilibrium.

Table 4.3 summarizes the measured electrical properties of embankment soil from the present study along with measured data from *Friborg* [1996], *Gray and Mitchell* [1967], *Pengra et al.* [1999] and *Morgan et al.* [1989] for comparison. These data were chosen for

the similarity of materials studied and, in cases where sample resistivity was not measured directly, for the suitability of estimating sample resistivity using Archie's law due to the high conductivity of the saturating fluid.

Immediately evident in Table 4.3 is that the cross-coupling conductivity varies within only one order of magnitude. The cross-coupling conductivity of $1.7 \times 10^{-5}\mathrm{A/m^2}$ measured for glacial till in the present study compares very well with data collected by *Friborg* [1996], who performed unidirectional flow streaming potential measurements and separate resistivity experiments on till samples. The sand and gravel was found to exhibit an average cross-coupling conductivity of $2.3 \times 10^{-5}\mathrm{A/m^2}$. Although no published data were found to enable a direct comparison, this value is within the range of cross-coupling conductivities measured for rock types listed in the table, which may exhibit similar mineralogy. The sample of glacial till with the fine fraction removed ($gt0$) was found to exhibit a cross-coupling conductivity and resistivity similar to that measured for the sand and gravel shell material. This has implications for the study of internal erosion and fines migration in embankment dams. Although no distinct correlation between L and gradation was observed in the glacial till samples studied, core material that has lost the bulk of the fine fraction may exhibit L and ρ values similar to those of shell material at a given site.

Material	Source	C	ρ_f	ρ	L
		mV/kPa	Ωm	Ωm	A/m^2
well-graded till ($C_u = 417$)	present study (*gt_a*, *gt_b*)	-0.16	68	95	1.7×10^{-5}
sandy till ($C_u = 2.3$)	*Friborg* [1996]	-0.66	100	840	7.7×10^{-6}
well-graded till ($C_u = 22.9$)	*Friborg* [1996]	-0.45	100	340	1.3×10^{-5}
well-graded silty till ($C_u = 7.3$)	*Friborg* [1996]	-0.71 to -0.92	100	541	1.3 to 1.7×10^{-5}
silty clay	*Gray and Mitchell* [1967] †	-0.056 to -0.61	-	333 to 390	1.5 to 3.2×10^{-5}
till with no fines ($C_u = 8$)	present study (*gt0*)	-0.49	68	228	2.1×10^{-5}
sand and gravel	present study (*sg_a*, *sg_b*)	-0.69	66	296	2.3×10^{-5}
sandstone	*Pengra et al.* [1999] ‡	-0.00549 to -0.00948	0.5	-	0.89 to 1.5×10^{-5}
limestone	*Pengra et al.* [1999] ‡	-0.00267 to -0.00483	0.5	-	2.4 to 2.9×10^{-6}
granite	*Morgan et al.* [1989] ‡	-0.198 to -0.217	8.5	-	5.8 to 6.4×10^{-5}

Table 4.3: Comparison of measured results with published data. Measured results for the current study represent average values derived from sample data as noted. † Data derived from electro-osmosis experiments. ‡ Sample resistivity was calculated using Archie's law for the purposes of calculating L.

4.6 Conclusion

A series of streaming potential and resistivity laboratory experiments were conducted to measure the streaming potential coupling coefficient C and resistivity ρ in order to derive the streaming current cross-coupling conductivity L for well-graded soil samples. The main objectives of the study were to assess the influence of sample properties on the cross-coupling conductivity and to characterize this property for two representative embankment dam fill materials.

The oscillatory flow method was shown to be a valid test method for unconsolidated soil samples and was found to be the most efficient technique to acquire streaming potential data and achieve sample equilibrium.

The results of experiments performed on samples of glass beads suggest that changes in density, gradation and saturating fluid conductivity do not significantly influence the streaming current cross-coupling coefficient. The process of ionic equilibration between the soil and saturating fluid was found to significantly affect the measured amplitude of C and ρ, and illustrates the importance of measuring these properties under the same sample conditions to properly characterize L for a given material. The ionic exchange observed in samples saturated with resistive fluids ($\sim 500\Omega$m) precluded reliable theoretical estimates of sample resistivity even when surface conductivity effects were accounted for. This suggests that measurements of pore fluid conductivity are required to estimate sample resistivity using an Archie's law-type formulation in resistive environments.

Measured values of the streaming current cross-coupling conductivity in glacial till and sand and gravel samples compared favorably with published data for similar materials. The compilation of measured results show that L varies within one order of magnitude for typical geologic materials, which is much smaller than the typical range of variation of hydraulic conductivity and electrical resistivity. This suggests that in practice it may not be necessary to measure L with the same rigor as ρ, but that estimates may be sufficient to characterize the subsurface in forward modelling and inversion investigations of streaming potential.

4.7 References

Adamson, A. W., *Physical Chemistry of Surfaces*, John Wiley and Sons, New York, 1990.

Ahmad, M. U., A laboratory study of streaming potentials, *Geophysical Prospecting*, *12*, 49–64, 1964.

Archie, G. E., The electrical resistivity log as an aid in determining some reservoir characteristics, *Transactions of the Society of Petroleum Engineers of the American Institute of Mining, Metallurgical and Petroleum Engineers (AIME)*, *146*, 54–67, 1942.

ASTM, D2434-68: Standard test method for permeability of granular soils (constant head), in *Annual Book of ASTM Standards*, vol. 4, American Society of Testing and Materials, 1991a.

ASTM, D4254-91: Standard test methods for minimum index density and unit weight of soils and calculation of relative density, in *Annual Book of ASTM Standards*, vol. 4, American Society of Testing and Materials, 1991b.

ASTM, D2217-85: Standard practice for wet preparation of soil samples for particle-size analysis and determination of soil constants, in *Annual Book of ASTM Standards*, vol. 4, American Society of Testing and Materials, 1993a.

ASTM, D4253-93: Standard test methods for maximum index density and unit weight of soils using a vibratory table, in *Annual Book of ASTM Standards*, vol. 4, American Society of Testing and Materials, 1993b.

BC Hydro, *Tech. rep.*, British Columbia Hydro and Power Authority, Internal report no. PSE187, Burnaby, 2002.

Blake, E., and G. Clarke, Subglacial electrical phenomena, *Journal of Geophysical Research*, *104*(B4), 7481–7495, 1999.

Chandler, R., Transient streaming potential measurements on fluid-saturated porous structures: An experimental verification of Biot's slow wave in the quasi-static limit, *Journal of the Acoustical Society of America*, *70*(1), 116–121, 1981.

Corwin, R. F., and D. B. Hoover, The self-potential method in geothermal exploration, *Geophysics*, *44*(2), 226–245, 1979.

Corwin, R. F., and H. F. Morrison, Self-potential variations preceding earthquakes in central California, *Geophysical Research Letters*, *4*(4), 171–174, 1977.

de Groot, S. R., *Thermodynamics of irreversible processes*, *Selected Topics in Modern Physics*, vol. 3, North Holland Publishing Company, Amsterdam, 1951.

Friborg, J., Experimental and theoretical investigations into the streaming potential phenomenon with special reference to applications in glaciated terrain, Ph.D. thesis, Luleå University of Technology, Sweden, 1996.

Gray, D. H., and J. K. Mitchell, Fundamental aspects of electro-osmosis in soils, *Tech. rep.*, Soil Mechanics and Bituminous Materials Research Laboratory, University of California, Berkeley, 1967.

Gu, Y., and D. Li, The ζ-potential of glass surface in contact with aqueous solutions, *Journal of Colloid and Interface Science*, *226*, 328–339, 2000.

Guéguen, Y., and V. Palciauskas, *Introduction to the Physics of Rocks*, Princeton University Press, Princeton, 1994.

Guichet, X., L. Jouniaux, and J. P. Pozzi, Streaming potential of a sand column in partial saturation conditions, *Journal of Geophysical Research*, *108*(B3), 2141, doi: 10.1029/2001JB001517, 2003.

Hunter, R. J., *Zeta Potential in Colloid Science: Principles and Applications*, Academic Press, Sydney, 1981.

Ishido, T., and H. Mizutani, Experimental and theoretical basis of electrokinetic phenomena in rock-water systems and its application to geophysics, *Journal of Geophysical Research*, *86*(B3), 1763–1775, 1981.

Jouniaux, L., and J. P. Pozzi, Streaming potential and permeability of saturated sandstones under triaxial stress: Consequences for electrotelluric anomalies prior to earthquakes, *Journal of Geophysical Research*, *100*(B6), 10,197–10,209, 1995.

Keller, G. V., and F. C. Frischknecht, Electrical methods in geophysical prospecting, in *International series of monographs in electromagnetic waves*, vol. 10, edited by A. L. Cullen, V. A. Fock, and J. R. Wait, Pergamon Press, New York, 1966.

Kuerbis, R., and Y. P. Vaid, Sand sample preparation: The slurry deposition method, *Soils and Foundations*, *28*(4), 107–118, 1988.

Kulessa, B., B. Hubbard, and G. H. Brown, Cross-coupled flow modeling of coincident streaming and electrochemical potentials and application to sub-glacial self-potential data, *Journal of Geophysical Research*, *108*(B8), 2381, doi:10.1029/2001JB001167, 2003.

Lorne, B., F. Perrier, and J. P. Avouac, Streaming potential measurements 1. Properties of the electrical double layer from crushed rock samples, *Journal of Geophysical Research*, *104*(B8), 17,857–17,877, 1999.

Mizutani, H., T. Ishido, T. Yokokura, and S. Ohnishi, Electrokinetic phenomena associated with earthquakes, *Geophysical Research Letters*, *3*, 365–368, 1976.

Morgan, F. D., Fundamentals of streaming potentials in geophysics: Laboratory methods, in *Detection of Subsurface Flow Phenomena*, *Lecture Notes in Earth Sciences*, vol. 27, edited by G. P. Merkler, H. Militzer, H. Hötzl, H. Armbruster, and J. Brauns, pp. 133–144, Springer-Verlag, Berlin, 1989.

Morgan, F. D., E. R. Williams, and T. R. Madden, Streaming potential properties of Westerly granite with applications, *Journal of Geophysical Research*, *94*(B9), 12,449–12,461, 1989.

Ogilvy, A. A., M. A. Ayed, and V. A. Bogoslovsky, Geophysical studies of water leakages from reservoirs, *Geophysical Prospecting*, *17*, 36–62, 1969.

Onsager, L., Reciprocal relations in irreversible processes, I, *Physical Review*, *37*, 405–426, 1931.

Overbeek, J. T. G., Electrokinetic phenomena, in *Colloid Science*, *Irreversible Systems*, vol. 1, edited by H. R. Kruyt, Elsevier Publishing Company, Amsterdam, 1952.

Packard, R. G., Streaming potentials across glass capillaries for sinusoidal pressure, *Journal of Chemical Physics*, *21*(2), 303–307, 1953.

Pengra, D. B., S. X. Li, and P. Wong, Determination of rock properties by low-frequency AC electrokinetics, *Journal of Geophysical Research*, *104*(B12), 29,485–29,508, 1999.

Reppert, P. M., and F. D. Morgan, Frequency-dependent streaming potentials, *Journal of Colloid and Interface Science*, *234*, 194–203, 2001a.

Reppert, P. M., and F. D. Morgan, Streaming potential collection and data processing techniques, *Journal of Colloid and Interface Science*, *233*, 348–355, 2001b.

Reppert, P. M., and F. D. Morgan, Temperature-dependent streaming potentials: 2. Laboratory, *Journal of Geophysical Research*, *108*(B11), 2547, doi:10.1029/2002JB001755, 2003.

Revil, A., and L. M. Cathles III, Permeability of shaly sands, *Water Resources Research*, *35*(3), 651–662, 1999.

Revil, A., and A. Cerepi, Streaming potentials in two-phase flow conditions, *Geophysical Research Letters*, *31*, L11605, doi:10.1029/2004GL020140, 2004.

Revil, A., and P. W. J. Glover, Nature of surface electrical conductivity in natural sands, sandstones and clays, *Geophysical Research Letters*, *25*(5), 691–694, 1998.

Revil, A., P. A. Pezard, and P. W. J. Glover, Streaming potential in porous media: 1. Theory of the zeta potential, *Journal of Geophysical Research*, *104*(B9), 20,021–20,031, 1999a.

Revil, A., H. Schwaeger, L. M. Cathles III, and P. D. Manhardt, Streaming potential in porous media: 2. Theory and application to geothermal systems, *Journal of Geophysical Research*, *104*(B9), 20,033–20,048, 1999b.

Revil, A., D. Hermitte, M. Voltz, R. Moussa, J. G. Lacas, G. Bourrie, and F. Trolard, Self-potential signals associated with variations of the hydraulic head during an infiltration experiment, *Geophysical Research Letters*, *29*(7), doi:10.1029/2001GL014294, 2002.

Revil, A., V. Naudet, and J. D. Meunier, The hydroelectric problem of porous rocks: Inversion of the position of the water table from self-potential data, *Geophysical Journal International*, *159*, 435–444, 2004.

Revil, A., L. Cary, Q. Fan, A. Finizola, and F. Trolard, Self-potential signals associated with preferential ground water flow pathways in a buried paleo-channel, *Geophysical Research Letters*, *32*, L07401, 2005.

Sears, A. R., and J. N. Groves, The use of oscillating laminar flow streaming potential measurements to determine the zeta potential of a capillary surface, *Journal of Colloid and Interface Science*, *65*(3), 479–482, 1978.

Sheffer, M. R., Investigation of geophysical methods for assessing seepage and internal erosion in embankment dams: Laboratory testing of the streaming potential phenomenon in soils, *Tech. rep.*, Canadian Electricity Association Technologies Inc. (CEATI), Report T992700-0205B/2, Montreal, 2005.

Sheffer, M. R., and D. W. Oldenburg, Three-dimensional forward modelling of streaming potential, *Geophysical Journal International*, *169*, 839–848, doi:10.1111/j.1365-246X.2007.03397.x, 2007.

Sheffer, M. R., P. M. Reppert, and J. A. Howie, A laboratory apparatus for streaming potential and resistivity measurements on soil samples, *Review of Scientific Instruments*, *78*, 094502, doi:10.1063/1.2782710, 2007.

Suski, B., A. Revil, K. Titov, P. Konosavsky, M. Voltz, C. Dagès, and O. Huttel, Monitoring of an infiltration experiment using the self-potential method, *Water Resources Research*, *42*, W08418, doi:10.1029/2005WR004840, 2006.

Titov, K., A. Revil, P. Konosavsky, S. Straface, and S. Troisi, Numerical modelling of self-potential signals associated with a pumping test experiment, *Geophysical Journal International*, *162*, 641–650, 2005.

Wurmstich, B., F. D. Morgan, G. P. Merkler, and R. L. Lytton, Finite-element modeling of streaming potentials due to seepage: Study of a dam, *Society of Exploration Geophysicists Technical Program Expanded Abstracts*, *10*, 542–544, 1991.

Chapter 5

Evaluating the sensitivity of the self-potential method to detect internal erosion in the core of an embankment [4]

5.1 Introduction

The internal erosion of fine-grained material due to seepage forces can compromise the stability of an earthfill dam and cause its ultimate failure. Monitoring of dam performance has become of critical importance, particularly as structures age and design methods evolve. Conventional monitoring of the hydraulic regime using piezometers and weirs provides sparse sampling, and these methods may not be sufficient to detect the onset of internal erosion. Consequently, a comprehensive investigation tool is needed to complement these methods.

The self-potential (SP) method has been used to successfully delineate anomalous zones that correspond with areas of preferential seepage flow in embankment dams [*Ogilvy et al.*, 1969; *Bogoslovsky and Ogilvy*, 1970; *Black and Corwin*, 1984; *Butler et al.*, 1989]. SP data consist of voltage difference measurements, which are typically collected over the surface of an embankment and in some cases in the impounded reservoir [*Ogilvy et al.*, 1969; *Corwin*, 1990]. Uniform seepage through an embankment gives rise to a background SP response,

[4] A version of this chapter will be submitted for publication. Sheffer, M.R. and Oldenburg, D.W. (2007) Evaluating the sensitivity of the self-potential method to detect internal erosion in the core of an embankment.

which varies in intensity with reservoir level. Areas of preferential seepage flow manifest as deviations from this background response. These deviations, or SP anomalies, may be isolated by differencing repeat SP data sets acquired from single surveys or a continuous monitoring network of electrodes.

The SP method responds to the phenomenon of streaming potential: electrical currents generated by fluid flow through porous media. This electrokinetic process is the complementary phenomenon to electro-osmosis and is explained using coupled flow theory [*de Groot*, 1951; *Overbeek*, 1952]. The streaming potential phenomenon can dominate the SP response in systems where the hydraulic gradient is the driving force (i.e. no externally-imposed electrical current sources exist, and temperature and ionic gradients are negligible).

The current state of practice is to interpret SP data using qualitative and analytical techniques to estimate the location and depth of anomalous sources [*Panthulu et al.*, 2001; *Rozycki et al.*, 2006]. Although these methods enable a spatial interpretation of electrical current sources that explain the geophysical data, they do not give any information about the hydraulic nature of these sources.

Numerical modelling techniques based on coupled flow theory enable a more sophisticated approach to data interpretation, where the SP response can be related to hydraulic parameters. We have developed a three-dimensional forward modelling code that predicts the SP response to laminar fluid flow in the subsurface [*Sheffer and Oldenburg*, 2007]. The algorithm is well-suited to the study of embankment seepage problems, which are three-dimensional in nature due to the irregular topography of the dam and foundation.

The present study uses the numerical code to evaluate the SP response to preferential seepage caused by pipe and construction layer defects within the core of a synthetic model of a field-scale embankment. Section 5.2 provides a description of the streaming potential phenomenon, and Section 5.3 presents the forward modelling methodology. The geometry of the 2-zone synthetic embankment and 24 defect configurations are described in Section 5.4.1. Sections 5.4.2 and 5.4.3 give details on the seepage analysis and SP forward modelling. Sections 5.4.4 and 5.4.5 present the residual SP distributions for each defect case, which are calculated by subtracting the background SP response resulting from seepage through the intact embankment. The influence of the electrical resistivity distribution on the SP

response is discussed in Section 5.4.6. Finally, Section 5.5 discusses practical detection limits for the predicted SP anomalies, and Section 5.6 compares the predicted geophysical response to the predicted hydraulic response to evaluate the sensitivity of the method to physical changes within the embankment.

5.2 The streaming potential phenomenon

Relative movement between the electrically charged surface of a solid particle and free ions in a saturating solution describe different electrokinetic processes, including electro-osmosis and streaming potential. Electro-osmosis is the movement of fluid through a soil matrix in an applied electric field, and has been used in engineering applications to increase the strength of clays and fine-grained soils [*Casagrande*, 1983]. Streaming potential is the complementary phenomenon in which an imposed hydraulic gradient generates an electric field.

Figure 5.1 illustrates a conceptual model of streaming potential in the pore space of a soil. The grain surfaces exhibit a net electrical charge, the magnitude and polarity of which is controlled by surface chemistry. Most geologic materials exhibit a negative surface charge when saturated with natural waters displaying typical pH and ion concentrations. An electrical double layer forms at the solid-fluid interface, which consists of an adsorbed layer of tightly bound positive ions and a more loosely bound diffuse outer layer [*Adamson*, 1990]. Under static conditions, the saturated medium is electrically neutral with adsorbed ions from the fluid completely balancing the negative surface charge of the solid particles. The onset of fluid flow pulls positive ions from the diffuse layer in the direction of flow, which generates a streaming current $\boldsymbol{J}_S$ as illustrated in Figure 5.1. The streaming current may be described mathematically using a linear flow law [*de Groot*, 1951]:

$$\boldsymbol{J}_S = -L\nabla h, \tag{5.1}$$

where L [$\mathrm{A\,m^{-2}}$] is the streaming current cross-coupling conductivity and h [m] is hydraulic head. A charge imbalance results from the movement of ions in the direction of flow, which induces an opposing conduction current $\boldsymbol{J}_C$ that is described using Ohm's law:

$$\boldsymbol{J}_C = -\sigma\nabla\phi, \tag{5.2}$$

where σ [S m^{-1}] is the electrical conductivity of the saturated porous medium and ϕ [V] is the electrical potential. If no significant temperature or ionic gradients exist in the system, the total current $\boldsymbol{J}$ [A m^{-2}] is described using coupled flow theory as the sum of streaming and conduction currents:

$$\boldsymbol{J} = \boldsymbol{J}_C + \boldsymbol{J}_S. \tag{5.3}$$

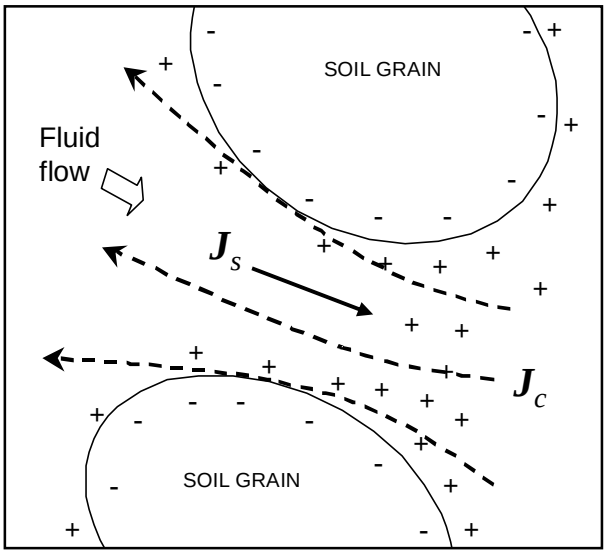

Figure 5.1: Conceptual model of streaming potential, showing streaming current $\boldsymbol{J}_S$ and conduction current $\boldsymbol{J}_C$ flow paths in the pore space of a saturated soil.

The electrical response to a given hydraulic head distribution is considered steady-state, regardless of the nature of the hydraulic system due to the large difference in characteristic times. Consequently, in the absence of any imposed sources of current, the streaming potential mechanism becomes the sole source for conduction current flow:

$$\nabla \cdot \boldsymbol{J}_C = -\nabla \cdot \boldsymbol{J}_S, \tag{5.4}$$

which can be expressed as

$$\nabla \cdot \sigma \nabla \phi = -\nabla \cdot L \nabla h. \tag{5.5}$$

Although the streaming current is strictly limited to the saturated pore channels, the conduction current permeates the entire medium and is quantified through measurements of

ϕ using the self-potential method. The cross-coupling conductivity is defined as $L = -C\,\sigma$, where C is the streaming potential coupling coefficient. Parameters C and L are typically characterized through laboratory measurements.

5.3 Forward modelling of streaming potential

5.3.1 Methodology

A seepage analysis is required to determine the distribution of hydraulic head prior to solving (5.5) for the self-potential distribution. Forward modelling of the streaming potential phenomenon is performed using two independent algorithms to solve the hydraulic and electrical flow problems. The study region is divided into a discrete rectangular mesh, across which distinct material property units are defined based on material type. Hydraulic conductivity (K) values are assigned accordingly to each cell in the mesh. A seepage analysis is performed using established software to facilitate the use of mixed boundary conditions and model calibration. The 3-D finite difference code MODFLOW, developed by the US Geological Survey [*Harbaugh et al.*, 2000], is used for confined or saturated flow problems and MODFLOW-Surfact [*HydroGeoLogic Inc.*, 1996] is used for variably saturated flow problems. Mesh construction, assignment of boundary conditions and the delineation of conductivity units are facilitated with the use of the Visual MODFLOW graphical user interface [*Waterloo Hydrogeologic Inc.*, 2004].

The self-potential distribution is determined using a 3-D forward modelling algorithm described in detail by *Sheffer and Oldenburg* [2007], which is independent of the software used to perform the seepage analysis. The algorithm operates on the same mesh defined in the seepage analysis and requires as input a distribution of hydraulic head and a prescribed distribution of electrical properties, namely streaming current cross-coupling conductivity L, and electrical conductivity σ. A discrete form of Equation (5.5) is solved using the method of finite volumes, where h, ϕ, L, and σ are defined at cell centres.

To solve (5.5), a zero flux boundary is prescribed for conduction current flow at the outer edge of the mesh. This requires that the physical extents of the mesh be expanded with the use of padding cells of prescribed conductivity, in order to remove the influence

of the boundary condition on the solution within the study region. The forward modelling problem is solved using a preconditioned biconjugate gradient stabilized method.

5.3.2 Assessing the influence of unsaturated flow

A variably saturated flow approach is typically required to solve embankment dam seepage problems using the method of finite differences due to the steeply-dipping phreatic surface that separates saturated and unsaturated zones. In order to calculate streaming potential, electrical properties must be prescribed for all soil zones in the model. In a variably saturated flow problem, these properties must be assigned as a function of fluid saturation. The position of the phreatic surface is determined from the hydraulic head solution and is used to distinguish between saturated and unsaturated zones.

Figure 5.2 illustrates the distribution of electrical properties in a homogeneous embankment subject to flow from a reservoir. Contours of hydraulic head are shown as solid lines below the phreatic surface and as dashed lines within the unsaturated zone. Electrical conductivity is expressed in terms of resistivity $\rho = 1/\sigma$ [Ω m], which is the typical parameter used in characterizing geologic systems.

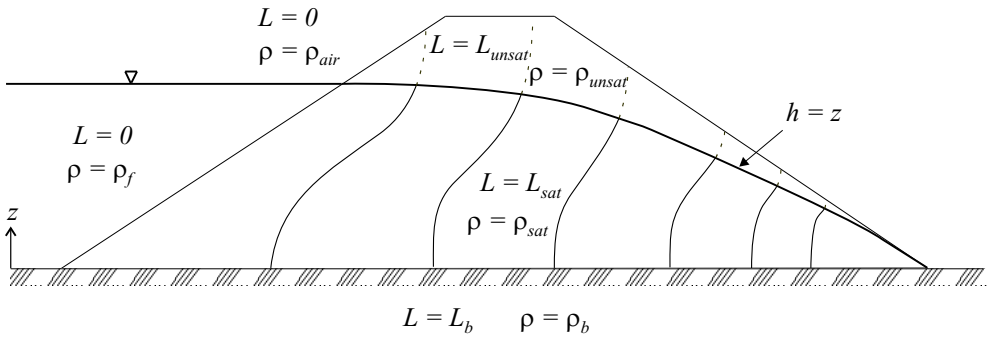

Figure 5.2: Illustration of the distribution of electrical properties in a homogeneous embankment subject to seepage from a reservoir. Hydraulic head contours are indicated in the figure, with dashed lines representing unsaturated head values. Subscripts *sat* and *unsat* respectively refer to the saturated and unsaturated zones. Subscript b refers to the foundation material or bedrock. The value ρ_f represents the electrical resistivity of the reservoir water.

Electrical conduction current flow permeates the entire porous medium and ρ is assigned

a value based on saturation conditions. Streaming current flow may be handled using a saturated or variably saturated approach. In a saturated approach, we consider that the majority of fluid flow and consequently streaming current flow is limited to the saturated zone and assign $L_{unsat} = 0$. In a variably saturated approach, the effect of streaming current flow in the unsaturated zone is included and we must assign a value for L_{unsat} that varies as a function of saturation. Limited data exist on the behaviour of the streaming potential coupling coefficient C in partially saturated conditions, with conflicting reports of a decrease *Guichet et al.* [2003]; *Moore et al.* [2004]; *Revil and Cerepi* [2004] or increase [*Darnet and Marquis*, 2004; *Morgan et al.*, 1989] in the magnitude of C with decreasing fluid saturation. However, it is generally accepted that the streaming potential coupling coefficient reaches a null value at some minimum critical saturation level where the pore fluid becomes immobile [*Revil and Cerepi*, 2004; *Revil et al.*, 1999] and that electrical resistivity increases with decreasing fluid saturation. The net effect is to force the condition $L_{unsat} < L_{sat}$.

A saturated flow approach to modelling streaming current flow is warranted in a typical embankment dam seepage problem due to the nature of the flow regime. The impounded reservoir establishes a large hydraulic gradient that governs seepage through the structure. The influence of the unsaturated flow component of this seepage is dictated by the size of the capillary fringe above the phreatic surface. In free-draining sand and gravel shell or filter materials, saturation levels decay quickly to residual values and unsaturated flow is restricted to a relatively narrow zone. In the finer-grained core, a significant degree of saturation exists above the phreatic surface. However, the contrast in pore pressure between the unsaturated core and downstream shell prevents significant flow from occurring in this zone.

Another component of unsaturated flow is gravity-driven fluid flow from surface recharge. The self-potential response to percolation flow is superimposed on the response to seepage through the embankment. However, the magnitude of the SP response to this vertical flow component is independent of and typically small relative to the response to seepage from the reservoir. We neglect the effect of percolation flow for the purposes of this study, since we are interested in evaluating the change in SP caused by perturbations in the seepage pattern due to internal erosion.

5.4 Two-zone embankment model

5.4.1 Model geometry

The intact embankment model consists of two distinct zones that represent a glacial till core and a sand and gravel shell material. For simplicity, the model exhibits a flat base and vertical abutment contacts. The dam geometry is outlined in Figure 5.3. Defect zones are included in the model to represent areas of elevated hydraulic conductivity caused by the loss of fine-grained material from the core. These defects are located at various depths within the core and extend parallel to the direction of flow. Two main defect configurations were studied: a pipe defect represented by a 1 m^2 zone, and a construction layer defect represented by a 0.5 m-high layer. The width of the layer defect varies between 5 m and 20 m parallel to the crest, such that three distinct layer defect types (labelled A, B and C) are defined. Table 5.1 details the cross-sectional geometry of each of the four defect types. Each defect type is evaluated at depths of 15 m, 45 m and 60 m below the crest, as illustrated in Figure 5.3(a). These defects are modelled both as full defects that extend the full transverse length of the core, and as partial or "half" defects that extend back from the downstream core-shell boundary to beneath the crest of the dam. The full defect models represent breakthrough conditions, while the half defect models represent the progression of internal erosion upstream through the core.

Defect type	Height (m)	Width (m)
Pipe	1	1
Layer A	0.5	5
Layer B	0.5	10
Layer C	0.5	20

Table 5.1: Defect cross-sectional geometry.

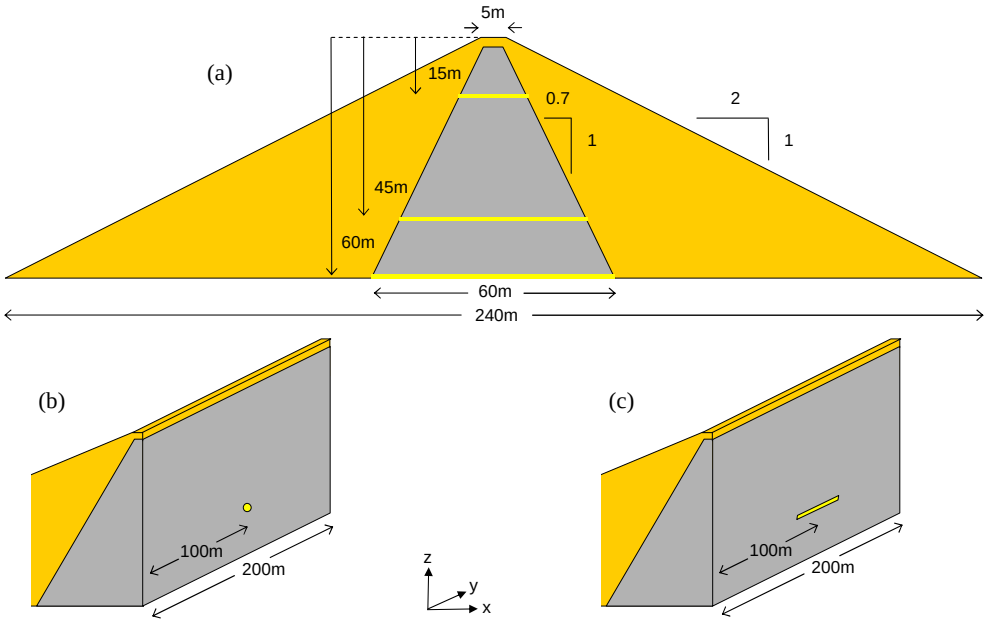

Figure 5.3: Model dam and defect geometry: a) transverse cross-section illustrating the three defect depths; b) cross-section of dam with a pipe defect; c) cross-section of dam with a layer defect.

5.4.2 Seepage analysis

A non-uniform $96 \times 90 \times 51$ cell mesh was generated within Visual MODFLOW to represent the embankment dam model shown in Figure 5.3. Model x and y dimensions respectively represent transverse (parallel to the flow path) and longitudinal (parallel to the crest) dimensions. Distances are stated in metres relative to an origin located at the intersection of the upstream toe with the right abutment. The mesh was refined in the vicinity of the three defect depths, such that cell dimensions range from a maximum of $2.5\text{m} \times 2.5\text{m} \times 2.5\text{m}$ to a minimum of $2.5\text{m} \times 0.5\text{m} \times 0.5\text{m}$.

A variably saturated approach was required to generate a realistic hydraulic head distribution within the saturated zone, and to correctly position the phreatic surface along the downstream face of the core. Hydraulic conductivity values were prescribed for all soil zones in the model and are listed in Table 5.2. These values are assumed isotropic and are within the range of those typically observed for glacially-derived core and shell material.

The relative permeability of all soil zones was defined using van Genuchten parameters $\alpha = 1$ m^{-1}, $\beta = 2$, and a residual saturation $S_{wr} = 0.03$. These values are representative of coarse sand and were chosen to characterize the downstream outer shell material, which was found to remain predominantly unsaturated in the analyses.

Zone	K (m s^{-1})	L (A m^{-2})	ρ (Ω m)
Shell	1×10^{-5}	2.3×10^{-5}	300 (1000)
Core	1×10^{-9}	1.7×10^{-5}	100 (250)
Defect	1×10^{-5}	2.1×10^{-5}	230 (500)
Bedrock	-	-	2500

Table 5.2: Physical properties of 2-zone embankment model. Electrical resistivity values are assigned based on saturation level: fully-saturated resistivity values are listed with unsaturated resistivity values shown in brackets.

Steady-state seepage analyses were performed using the MODFLOW-Surfact numeric engine to generate a variably saturated flow solution. The hydraulic head distribution and total seepage flow were resolved for all embankment defect models subject to an upstream reservoir level of 55 m.

The seepage regime in the intact core model and each of the 24 defect models is characterized by a three-dimensional distribution of hydraulic head. Figures 5.4 and 5.5 display representative transverse cross-sections ($y = 100$ m) through the centre of the B layer defects at each of the three defect depths, corresponding to the full and half defects, respectively. The presence of a full defect results in a small perturbation of the head distribution through the core, which intensifies with the increase in head drop at greater defect depths. The presence of a half defect in the core results in significant variation in the hydraulic head contours, generating large hydraulic gradients immediately upstream of the defect.

Mass-balance calculations of the total volumetric seepage flow through each embankment model enable the computation of anomalous seepage flow resulting from the presence of each defect type. Table 5.3 lists the increase in seepage flow rate for all defect models, which

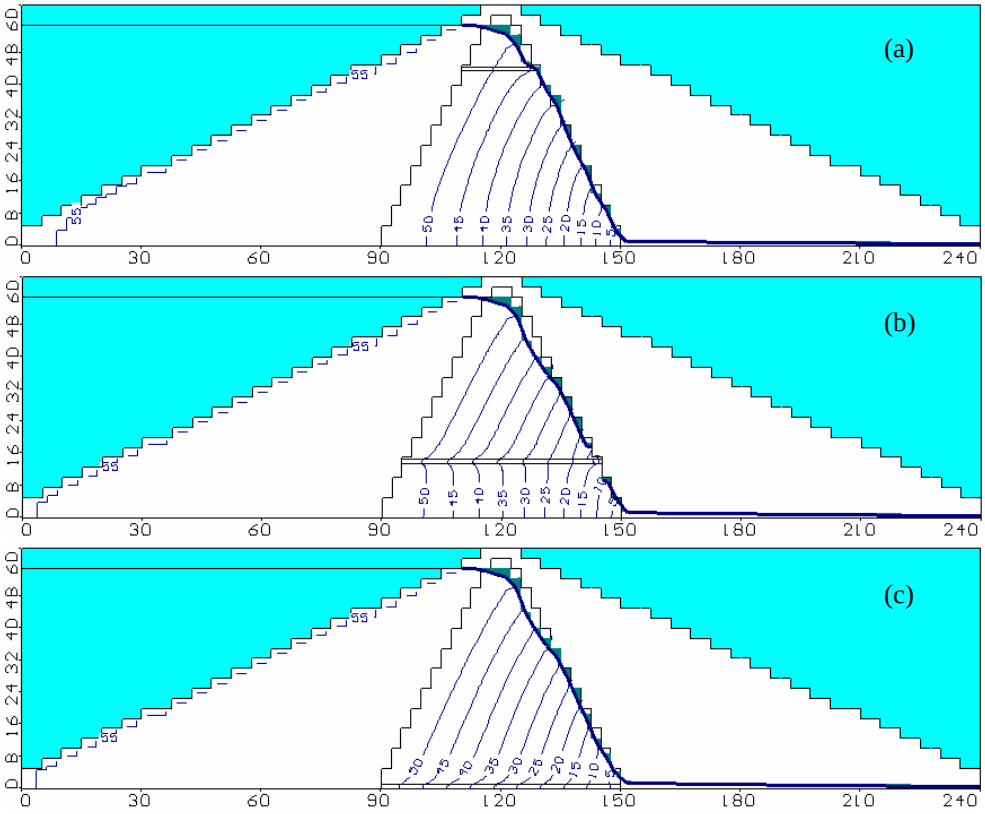

Figure 5.4: Transverse cross-section of hydraulic head distribution in B layer full defect models at defect depths of a) 15 m, b) 45 m, and c) 60 m.

was calculated by subtracting the intact core model seepage flow rate of 0.523 L/minute. Significant incremental seepage was calculated for the full defect models, which provide a pervious path through the entire length of the core. The half defect models result in seepage rates only marginally larger than the intact case.

Of particular note is the behaviour of the phreatic surface downstream of the defects. Figure 5.4 reveals an elevated water level in the downstream shell, which correlates with defect depth. This behaviour is a direct result of the increase in seepage flow, which is shown in Table 5.3 to be quite substantial for breakthrough conditions. Half defect models do not generate the same volume of excess seepage, and consequently the position of the phreatic surface through the core and downstream shell remains essentially unchanged from the intact case. This has implications for the predicted SP response, as discussed in Section

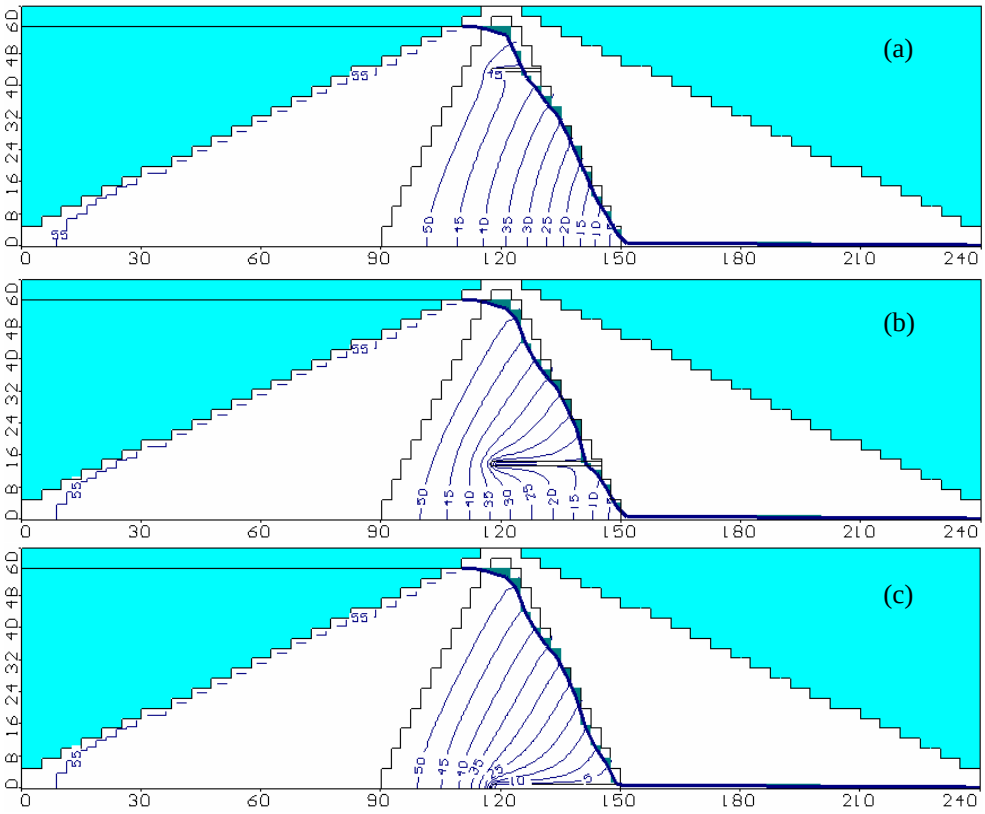

Figure 5.5: Transverse cross-section of hydraulic head distribution in B layer half defect models at defect depths of a) 15 m, b) 45 m, and c) 60 m.

5.4.4.

5.4.3 SP forward modelling

The electrical properties were assigned based on the model grid and material property zones defined in the seepage analysis. Table 5.2 lists the physical property values for each material type. Isotropic properties were assumed for each soil unit, with a distinction made between saturated and unsaturated zones. Measured values of the cross-coupling conductivity L and resistivity ρ were obtained from laboratory experiments conducted on saturated embankment soil specimens, as described in Chapter 4. A saturated approach was used to model streaming current flow and we assigned a null cross-coupling conductivity above the phreatic surface. Resistivity values that characterize the unsaturated zone within each soil

Defect type	15m depth	45m depth	60m depth
full defect - pipe	0.317 (61%)	0.477 (91%)	0.511 (98%)
full defect - layer A	0.772 (148%)	1.18 (226%)	1.26 (240%)
full defect - layer B	1.54 (294%)	2.36 (451%)	2.47 (473%)
full defect - layer C	3.06 (586%)	4.71 (901%)	4.84 (927%)
half defect - pipe	0.005 (1%)	0.015 (3%)	0.013 (2%)
half defect - layer A	0.004 (1%)	0.023 (4%)	0.021 (4%)
half defect - layer B	0.007 (1%)	0.031 (6%)	0.026 (5%)
half defect - layer C	0.011 (2%)	0.046 (9%)	0.041 (8%)

Table 5.3: Predicted volumetric flow rate increase in L/minute. Anomalous seepage rates were obtained by subtracting the total seepage flow rate (0.523 L/min.) through the intact dam. The anomalous increase in seepage is shown as a percentage of the total intact dam seepage in brackets.

unit were assumed based on published values and empirical estimates. The reservoir was included as a distinct unit in the electrical resistivity model and was assigned a value of 70 Ωm. This value represents the saturating fluid used in the laboratory experiments, which corresponds with observed average reservoir water properties at the site from which soil samples were taken.

The original mesh was expanded to apply the zero flux boundary condition required to solve for the SP distribution. This boundary was imposed with the use of padding cells surrounding the original mesh that must be assigned realistic values of electrical resistivity. The embankment was assumed to be flanked by bedrock abutments in the y dimension and underlain by a bedrock foundation, as illustrated in Figure 5.6. An optimum padded mesh size for this problem was determined to be seven times the size of the original grid, as this removes the influence of the boundary on the solution within the dam. The predicted SP values were referenced to a base station coordinate $(120, 0, 60)$ located at the intersection of the crest with the right abutment, since self-potential data are potential differences

measured between two electrodes.

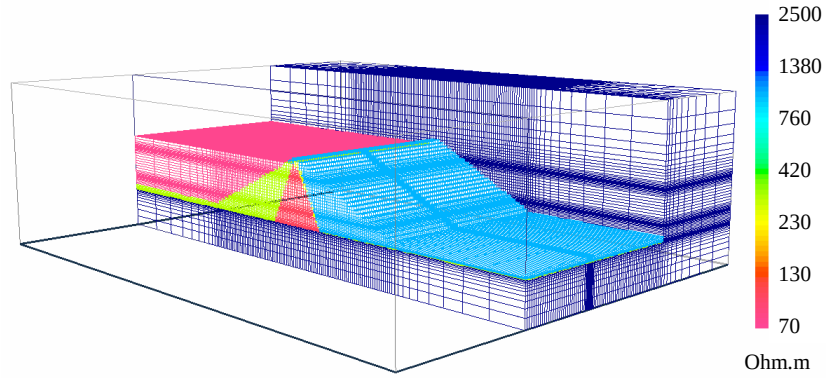

Figure 5.6: Cut-away view of the electrical resistivity model of the embankment, showing padding cells over a portion of the discrete mesh.

A three-dimensional distribution of self-potential was solved for in each embankment model. Figure 5.7 displays a transverse profile intersecting the centre of the crest ($y = 100$ m) of the predicted SP response over the surface of the dam and reservoir for the intact core model. The distribution of surface measurement points is indicated by arrows on the dam schematic in the figure. Similarly, Figure 5.8 presents a longitudinal profile along the crest ($x = 120$ m) for the intact core model. These figures show the characteristic SP signature to uniform seepage through an embankment, which trends from a negative response upstream to a positive response downstream. This is caused by the accumulation of negative and positive charge respectively along the upstream and downstream core-shell interface due to the physical property contrast and the large hydraulic gradient through the core. For this embankment model, the SP response trends from a negative minimum of -8 mV to a maximum of 38 mV over the surface of the downstream shell.

The analysis and interpretation of SP data are aided by some knowledge of the SP response to uniform seepage through the structure. In this synthetic case study, the "true" intact core SP response of the embankment is known. Consequently, we can isolate the residual or anomalous SP response by subtracting the intact core data from the defect model data. In a field situation, repeat SP survey or long-term monitoring data may be compared to isolate seepage-related anomalies.

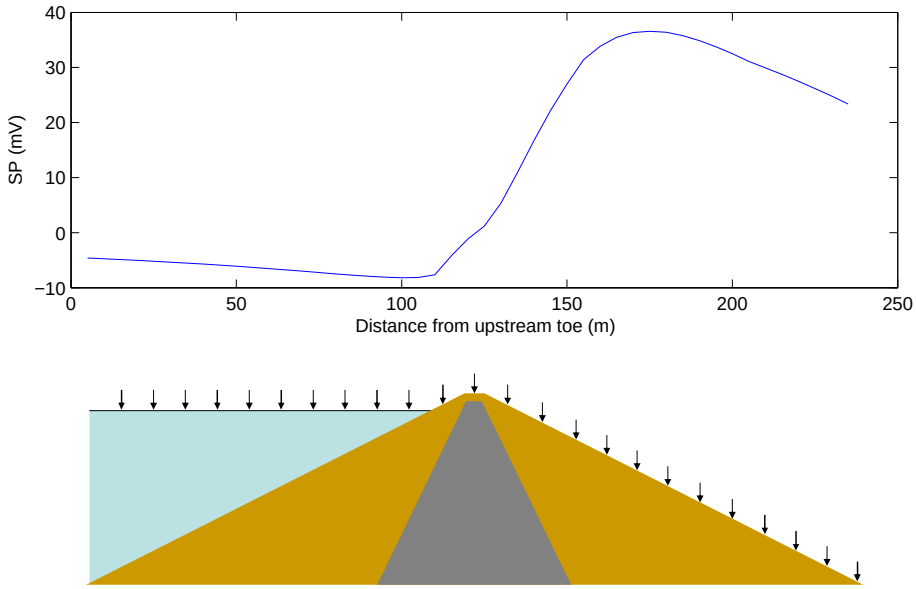

Figure 5.7: Transverse SP data profile over surface of intact embankment ($y = 100$ m).

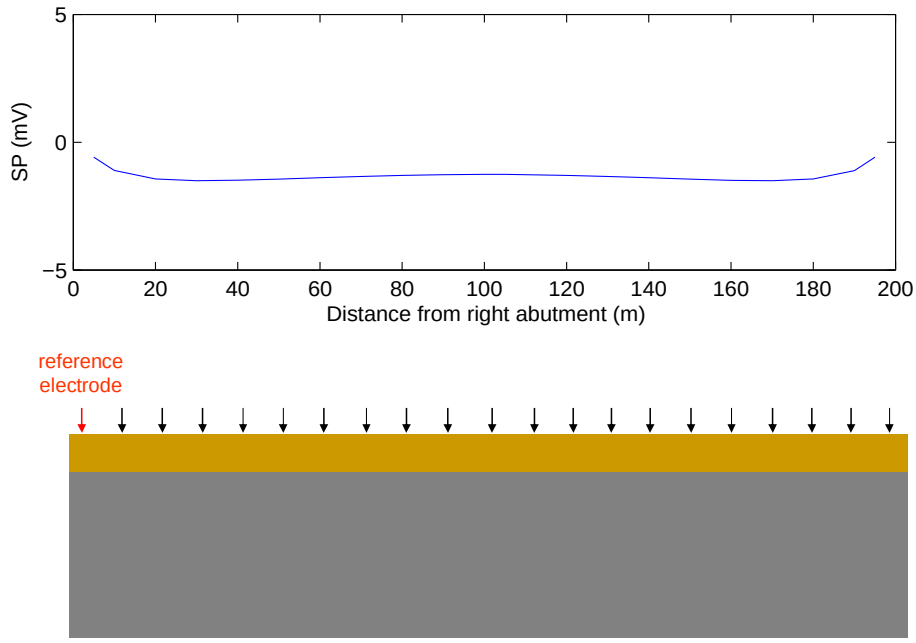

Figure 5.8: Longitudinal SP data profile over surface of crest of intact embankment, looking upstream ($x = 120$ m).

5.4.4 Residual SP response at surface

The residual SP data for full and half defect models are presented in profile form in Figures 5.9 and 5.10, respectively. Model results are identified by defect type at each depth. Transverse and longitudinal profiles display residual data along the same surface measurement points as shown for the intact case.

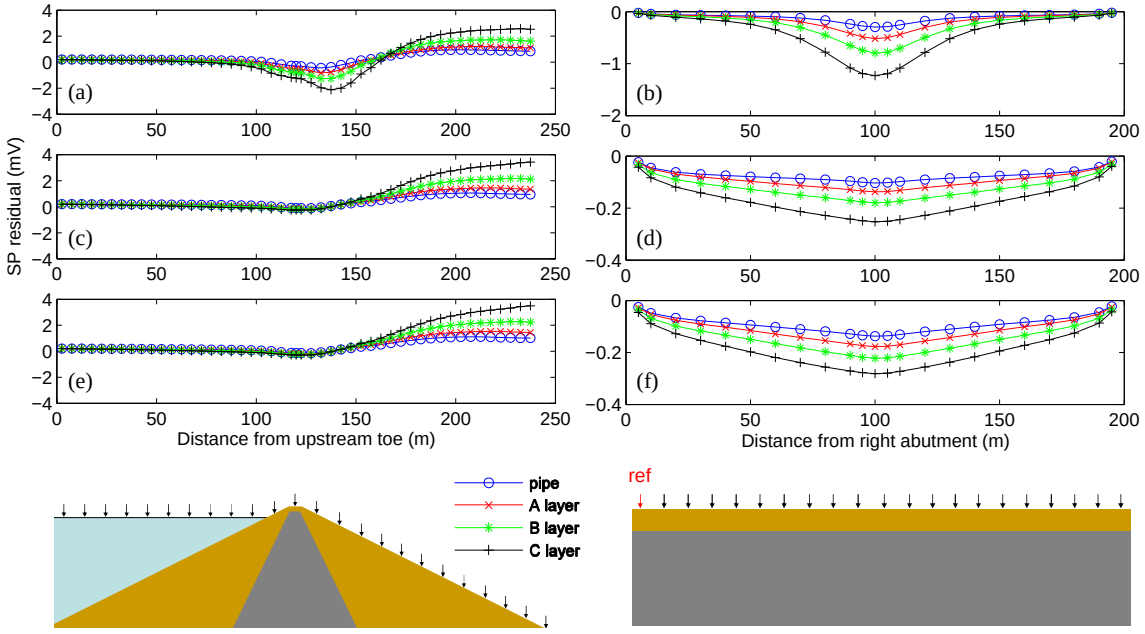

Figure 5.9: Transverse (a, c, e) and longitudinal (b, d, f) profiles of SP residual at the surface of the full defect models at 15 m depth (a, b), 45 m depth (c, d) and 60 m depth (e, f). Residual data are generated by subtracting the intact model response.

The surface SP residual data shown in Figures 5.9(a) and (b) display a small localized negative perturbation centred downstream of the crest for all full defect types at 15 m depth, which is barely visible in the 45 m and 60 m depth models. This is due to the surface proximity of negative sources of electrical charge generated at the defect outlet. Positive charge generated from seepage inflow along the upstream length of the defect does not significantly influence the SP signature at surface due to the high electrical conductivity of the core. This effect is discussed further below in Sections 5.4.5 and 5.4.6. All full defect models display a positive SP residual over the downstream toe, with a maximum residual

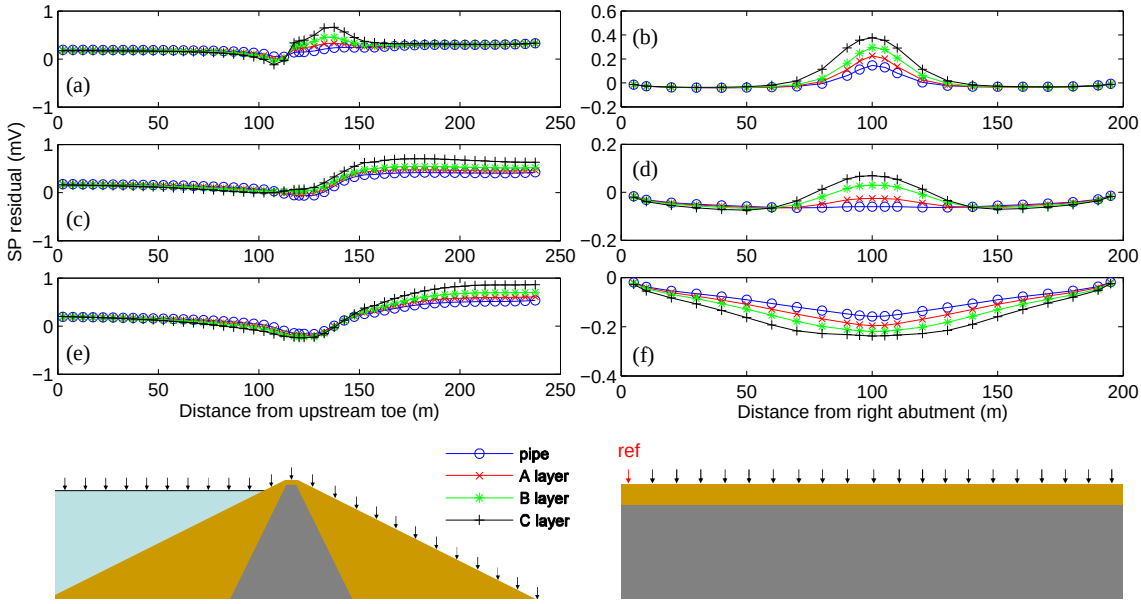

Figure 5.10: Transverse (a, c, e) and longitudinal (b, d, f) profiles of SP residual at the surface of the half defect models at 15 m depth (a, b), 45 m depth (c, d) and 60 m depth (e, f). Residual data are generated by subtracting the intact model response.

anomaly of over 3 mV observed for the C layer defect at 60 m depth. This anomalous SP response is due to positive sources of charge that develop at the phreatic surface in the downstream shell. The SP residual displays a positive correlation with defect size and depth, since these parameters control the increase in seepage flow and consequently the rise in the phreatic surface downstream of the defect.

The half defect models generate residual SP anomalies of smaller amplitude than the full defect models, with a maximum response of < 1 mV at surface, as shown in Figure 5.10(e). This is attributed in part to the negligible change in the position of the phreatic surface downstream of the defects due to the small increase in seepage flow rate. The large hydraulic gradients surrounding the upstream end of the half defects generate significant positive electrical charge within the core, as discussed in Section 5.4.5. The influence of this charge is visible to a slight degree in the 15 m depth profiles due to the proximity of the defects to surface, but is not visible in profiles corresponding to the deeper defect models.

5.4.5 Residual SP response at depth

The small residual anomalies visible at the surface of the embankment suggest that flow through the defects generates a negligible response. However, the residual SP response at depth tells a different story. Figures 5.11 and 5.12 illustrate images of the residual SP distribution in vertical cross-section through the centre of the full and half pipe defects. Evident in the figures is the focused anomalous response surrounding each defect within the core. Flow into the defect generates a positive SP response; outflow from the defect results in a negative SP response. In the full pipe defects shown in Figure 5.11, this translates to positive SP anomalies ranging from 2.5 to 13 mV surrounding the upstream length of the defect, and negative SP anomalies on the order of several mV centred at the defect outlet. For all full layer defect models, maximum anomaly amplitudes range from 13 mV to −7 mV. In general, the residual anomalies surrounding the defects do not propagate to the surface of the embankment due to the low resistivity of the core material. However, as noted in Section 5.4.4, the positive residual anomaly caused by the rise in phreatic surface in the downstream shell does propagate to the surface due to the high resistivity of the unsaturated shell material. These positive responses are evident in the cross-sections shown in Figure 5.11 and the surface profiles shown in Figures 5.9(a), (c) and (e).

The large hydraulic gradients that exist immediately upstream of the half defects generate positive SP anomalies of significant magnitude, as shown in Figure 5.12. Positive SP anomalies ranging from 12 to 65 mV surround the upstream end of the half pipe defects, which are representative for all half layer defects. The magnitude of the hydraulic gradient and resultant SP response are positively correlated with defect depth. These high amplitude SP signals do not propagate to the surface of the embankment due to the high electrical conductivity of the core, as evidenced by the surface profiles shown in Figure 5.10. The influence of the electrical properties of the core is further examined in Section 5.4.6.

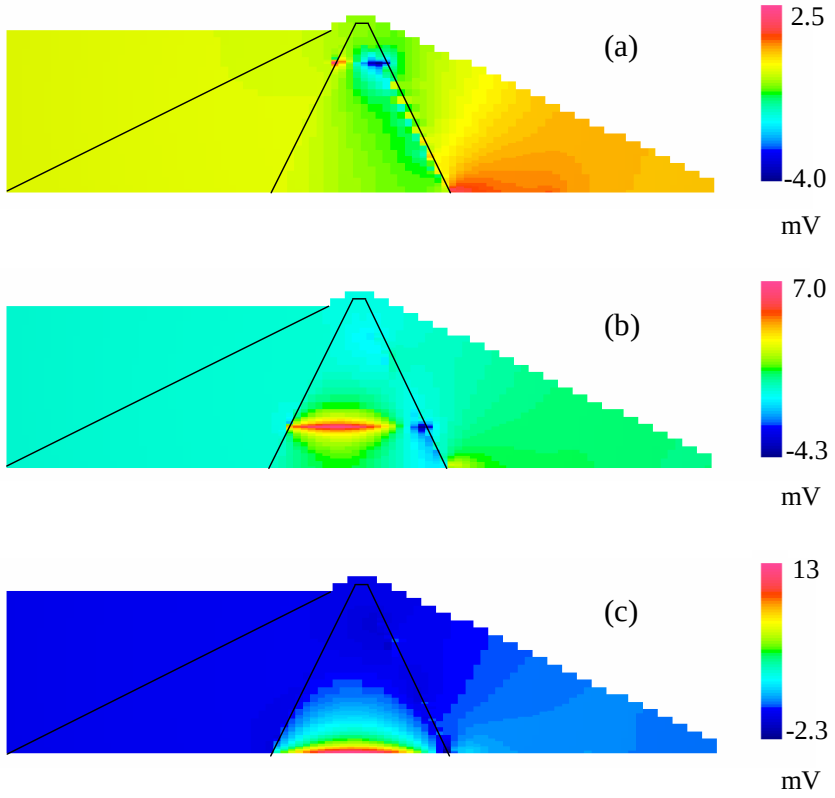

Figure 5.11: SP residual in transverse cross-section intersecting the centre of the full pipe defect: a) 15 m depth; b) 45 m depth; c) 60 m depth.

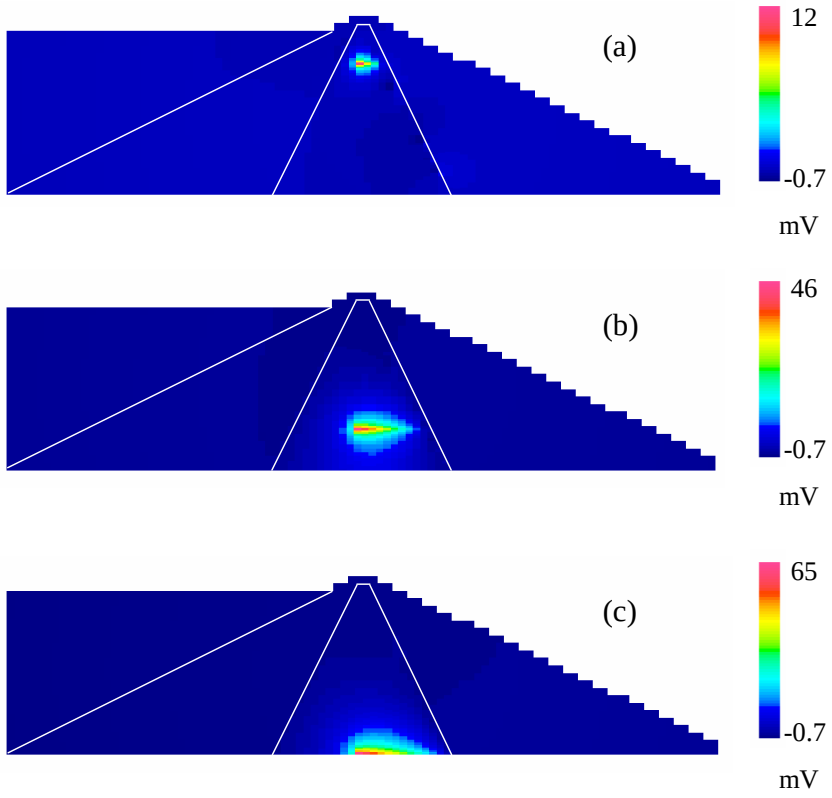

Figure 5.12: SP residual in transverse cross-section intersecting the centre of the half pipe defect: a) 15 m depth; b) 45 m depth; c) 60 m depth.

5.4.6 Influence of the electrical resistivity distribution

The self-potential field is generated by the distribution of streaming current sources, which are concentrated at physical property boundaries within the embankment. The maximum SP residual anomalies are caused by streaming current sources located at the physical boundaries of the defect. The sign and amplitude of these sources are dictated by the direction and magnitude of the gradients in head and physical properties at the boundary. The SP signal decays with inverse distance away from the source. However, the distribution of electrical resistivity in the embankment dictates the amplitude of the electrical potential field. The higher the resistivity, the larger the self-potential signal. The core is the least resistive soil zone within an embankment, since it typically contains electrically conductive silts and clays. Consequently, for a given streaming current source amplitude, the SP residual signal strength is governed to a large extent by the resistivity of this zone.

A twofold increase in the resistivity of the core material is examined to illustrate the resultant effect on the SP response. This change in resistivity is well within the range for glacial till material. It can be seen to represent a minor change in mineralogy, such as a decreased clay content, or a difference in temperature. The electrical properties used in this study were obtained from laboratory measurements made at 22 °C, as presented in Chapter 4. However, below a depth of 10 m, the earth temperature remains constant within one or two degrees of the mean air temperature if we neglect the influence of geothermal effects [*Stevens et al.*, 1975]. An assumed mean air temperature of 10 °C translates to an approximate 30% increase in the resistivity of saturated core material, if we use empirical models [*Archie*, 1942; *Arps*, 1953] to estimate the influence of a decrease in fluid temperature on the bulk resistivity.

Figures 5.13 and 5.14 illustrate the effect of increasing the resistivity of the core material from 100 Ωm to 200 Ωm. As seen in the figures, a twofold increase in core resistivity effectively doubles the residual SP response observed at surface and at depth within the embankment. This has implications for the detection of SP anomalies given typical measurement sensitivities, as discussed in Section 5.5.

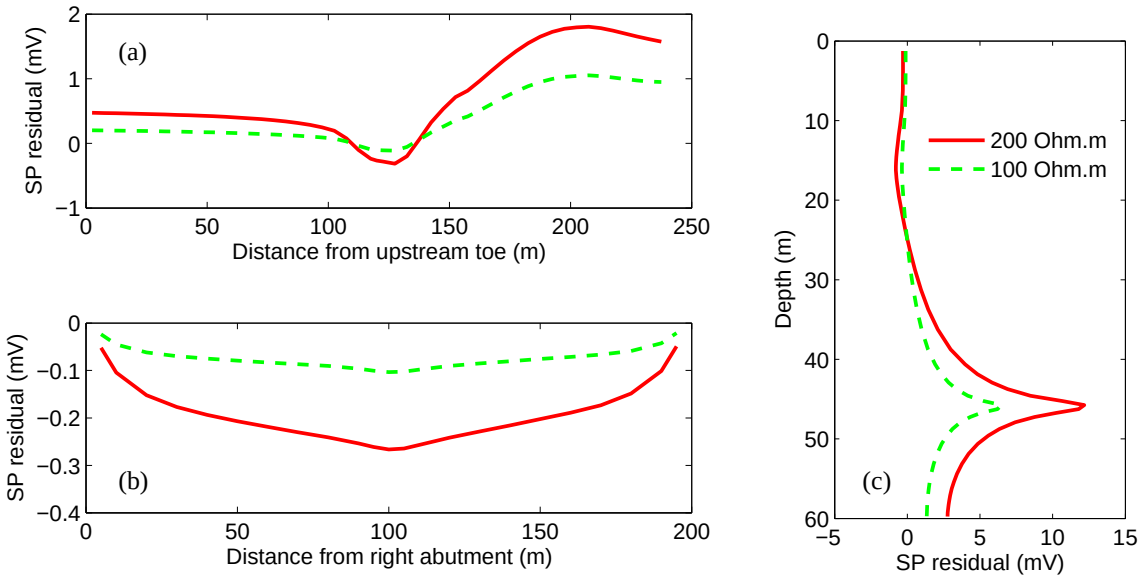

Figure 5.13: Effect of increased resistivity of core on the SP residual resulting from a full pipe defect at 45 m depth: a) surface transverse profile, b) surface longitudinal profile, c) vertical profile beneath centre of crest intersecting defect.

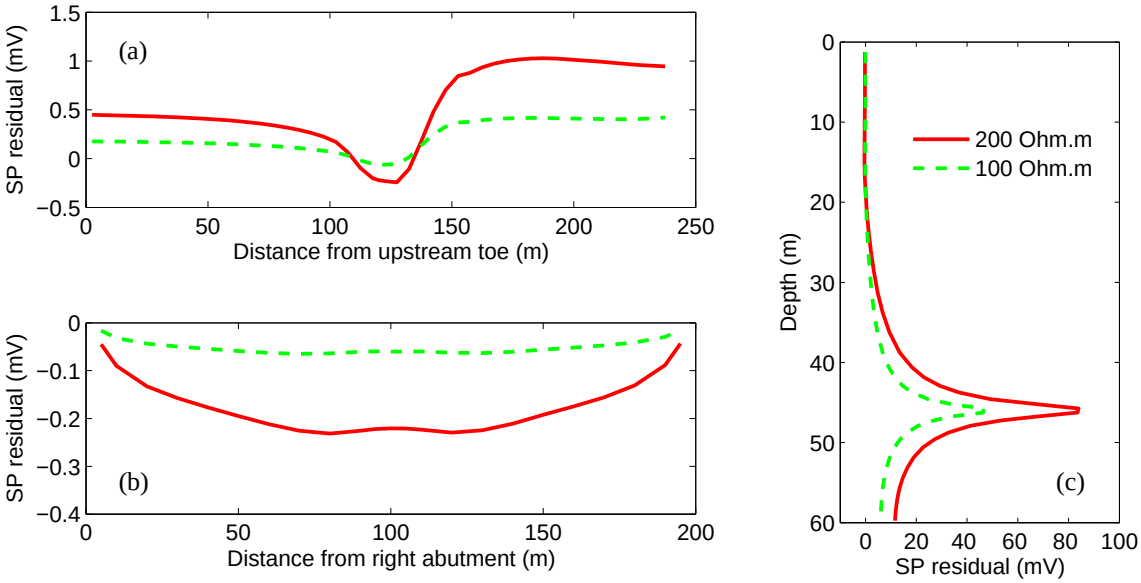

Figure 5.14: Effect of increased resistivity of core on the SP residual resulting from a half pipe defect at 45 m depth: a) surface transverse profile, b) surface longitudinal profile, c) vertical profile beneath centre of crest intersecting defect.

5.5 Practical SP anomaly detection limits

The amplitude of an SP anomaly that can be reasonably detected from field measurements is governed by the ratio of signal strength to noise level at a given site. Sources of noise include telluric currents, spurious currents caused by other operations at site, poor electrical contact between the electrodes and the soil, electrode drift, and the influence of non-streaming potential source mechanisms on the measured self-potential. These noise sources can be minimized with proper field data acquisition procedures [*Corwin*, 2005].

SP data may be acquired in a single survey using a portable pair of electrodes, or through continuous monitoring of a permanently-installed array of electrodes. A single survey typically involves making surface measurements of SP using a fixed base electrode and a roving electrode that is used to occupy survey stations across the site. Single surveys may be performed once or repeated to isolate a residual SP response. Continuous monitoring involves measuring the SP field across multiple electrodes that are installed near surface or at depth within the embankment. Data sets are acquired in a relatively short period of time and may be compared over different time scales to isolate the residual response.

Given that appropriate equipment and acquisition methods are employed, the chosen survey method will influence the measurement sensitivity. The measured self-potential field offers a snapshot of current hydraulic conditions within the embankment. Fluctuations in reservoir level and seasonal variations in water properties generate temporal changes in resistivity and the self-potential field [*Johansson and Dahlin*, 1996; *Johansson et al.*, 2005]. These temporal changes contribute to the total SP response to seepage through the dam. Where single surveys characterize current seepage conditions at the time of measurement, continuous monitoring can more accurately track the temporal response upon which anomalous variations are superimposed. In this way, continuous monitoring can resolve smaller residual changes that develop over time from the background response.

The limit of detection varies between sites depending on the signal to noise ratio. However, as a rough guideline, SP anomalies on the order of 10 mV are generally detectable from single survey data made at the surface of an embankment, while smaller anomalies may be detectable from offshore or borehole measurements. Although steel casing can influence downhole SP measurements [*Darnet et al.*, 2003], these effects are not addressed

here. Detection limits for continuous monitoring data are more difficult to estimate, since the development and application of these systems is in its early stages. However, one might expect that residual anomalies of several milliVolts would be detectable with careful data acquisition and processing procedures. Given these detection limits, the predicted SP residual responses at surface presented in Section 5.4.4 would not typically be detectable using current survey techniques. As discussed in Section 5.4.6, an embankment with a more resistive core would give rise to larger SP anomalies that could be more easily detected from surface measurements. However, the stronger signal levels at depth presented in Section 5.4.5 would surely be detectable by measurements made within the vicinity of the defects. Further examination of the spatial range of detection for anomalies at depth is included in Section 5.6.

5.6 Comparison of SP and hydraulic response to defects

As discussed in Section 5.4.5, the SP anomaly at depth generated by a half defect is of much larger amplitude than that generated by a full defect through the core. This suggests that the SP response actually peaks prior to any significant increase in seepage flow that occurs upon breakthrough of the defect into the upstream shell.

To examine this further we studied the development of a pipe defect at a depth of 45 m within the core. Figure 5.15 illustrates the change in hydraulic head distribution in transverse cross-section through the centre of the dam, as the pipe progresses upstream through the core. Forward modelling was performed for incremental defect lengths of 25%, 50% and 75% of the core and for breakthrough conditions. Figure 5.16 shows the corresponding SP residual in vertical profiles below the crest at each defect length. These profiles may be seen to represent data acquired from a vertical string of electrodes installed permanently within the core or via borehole measurements. Figure 5.16(a) represents a vertical profile that intersects the centre of the defect, while Figures 5.16(b), (c) and (d) respectively represent vertical profiles offset along the crest by distances of 5 m, 10 m and 15 m from the centre of the defect, as illustrated by the schematic shown in the figure.

The SP residual responses clearly show that the maximum SP anomaly occurs prior to

breakthrough of the pipe into the upstream shell. Maximum anomalies range from 46 mV at the defect to over 5 mV a distance of 15 m from the defect, which exceed the expected field sensitivity for measurements made at depth. The maximum SP residual observed at each separation distance from the defect is compared to the total increase in seepage through the dam for each defect length in Figure 5.17. Assuming that a 15% increase in seepage could be detected using an average, manual weir system and as little as a 7% increase could be detected using a more advanced system, we would not detect the presence of the pipe prior to breakthrough with standard seepage flow measurements. As seen in Table 5.3, the increase in seepage flow resulting from any of the partial defects at any depth would typically be undetectable by standard weir measurements. However, the SP response within 10 to 15 m of a partial defect is above a reasonable detection threshold of 5 mV. It is also important to note that weir measurements do not give a clear indication of the location where preferential seepage is occurring. These results demonstrate that the progression of internal erosion through the core should be detectable by SP measurements made at depth, prior to the onset of a significant increase in seepage flow that is detectable at the downstream toe.

The formulation of the coupled flow equation (5.5) and the results shown in Figures 5.15 to 5.17 demonstrate that it is hydraulic gradient, not seepage flow rate, that dictates the amplitude of the streaming current source and resulting streaming potential anomaly. This link suggests that SP measurements may complement pore pressure measurements to alert to changes in seepage patterns within the dam. Figures 5.18 and 5.19 display the residual SP and hydraulic head responses with depth through the core, in the presence of both pipe and B layer full and half defects. Figure 5.18 represents vertical profiles that intersect the centre of the defect, while Figure 5.19 represents vertical profiles offset along the crest by a distance of 10 m from the centre of the defect. Clearly evident in the figures is the correlation between the SP and head responses, where the SP residual profile closely mirrors the residual hydraulic head profile.

The response to the pipe and B layer defects are very similar when the measurement profile intersects the centre of the defect, as shown in Figure 5.18. At a distance of 10 m away from the centre of the defect, the response to the pipe defects is significantly attenuated

whereas the B layer continues to exert a response due to the proximity of the outer edge of the defect to the vertical profile.

Assuming that a 1 m of head variation from background is significant enough to signal an alert, and choosing 5 mV as an alert threshold for a change in SP, we can assess and compare the two measurement methods in terms of detection ability. For a vertical profile intersecting the centre of the defect, both SP and head measurements at depth would signal an alarm for all full and half defects, with the exception of the full defects at 15 m depth, shown in Figure 5.18(a) and (b). For measurements made 10 m away from the centre of the defect, only the half defects at 45 m and 60 m depth would be detectable by both SP and head readings, as shown in Figures 5.19(i) to (l). Given our chosen threshold levels, a full B layer defect at 45 m depth and full pipe and B layer defects at 60 m depth would generate an alert in head but not in SP.

An important consideration in the acquisition and analysis of SP and hydraulic head data is the transient nature of these data sets. Both SP and head respond to fluctuations in reservoir level, tailwater level, as well as regional groundwater patterns. The lag time between the source and the impact of these variations at different locations within the dam will also influence the behaviour of the SP and pore fluid pressure responses. Consequently, a performance history is required to assess normal background behaviour for a given site and the sensitivity of different instrumentation before determining thresholds that alert to anomalous behaviour. However, since SP and pore pressure responses should behave concurrently, SP measurements can be used in conjunction with pressure measurements to substantiate observed behaviour or be used on their own to alert to changes in seepage patterns.

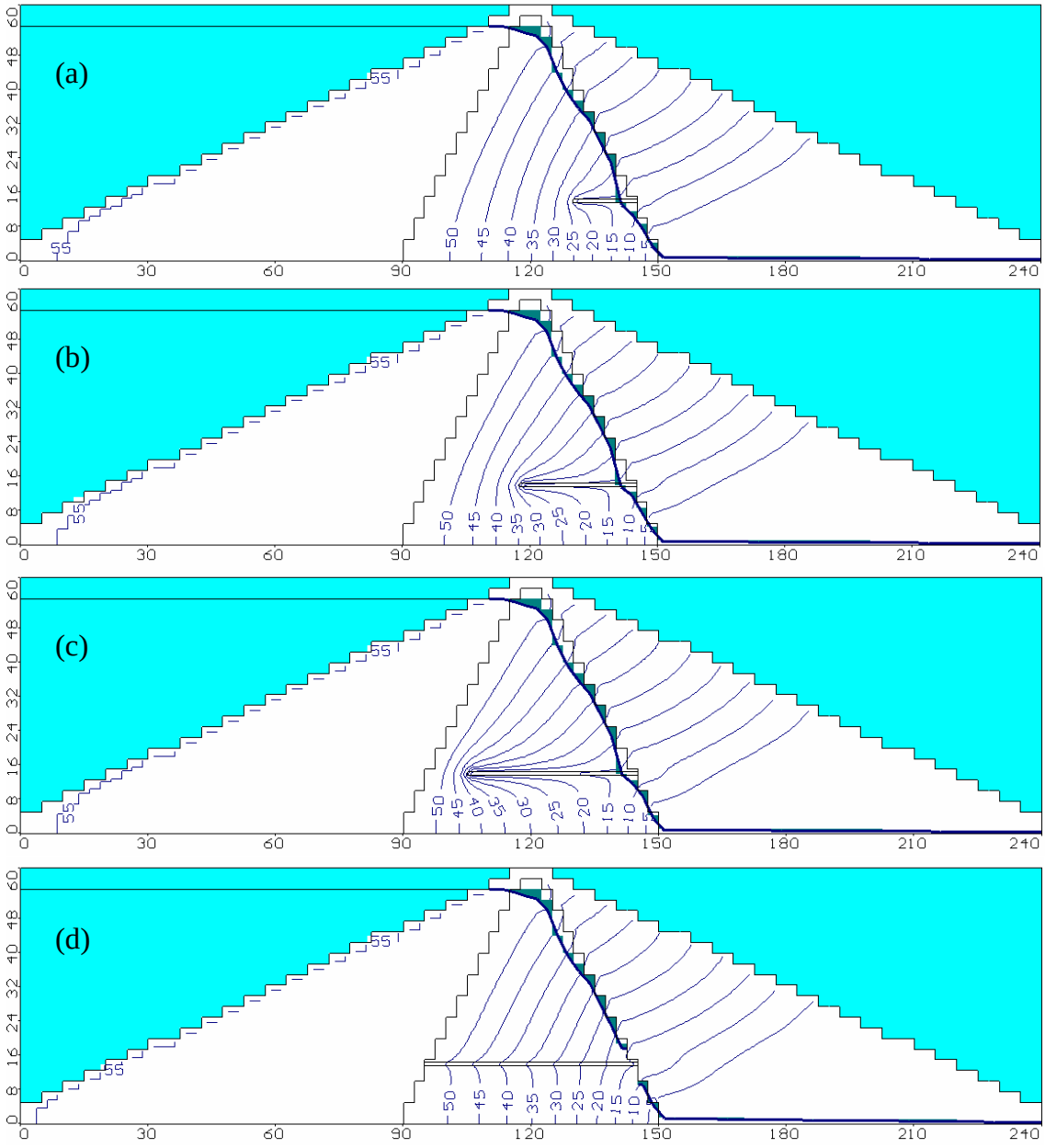

Figure 5.15: Transverse cross-section of hydraulic head distribution for the pipe defect model at 45 m depth, as pipe progresses upstream through the core: a) 25% of core length; b) 50% of core length; c) 75% of core length; d) 100% of core length (breakthrough conditions).

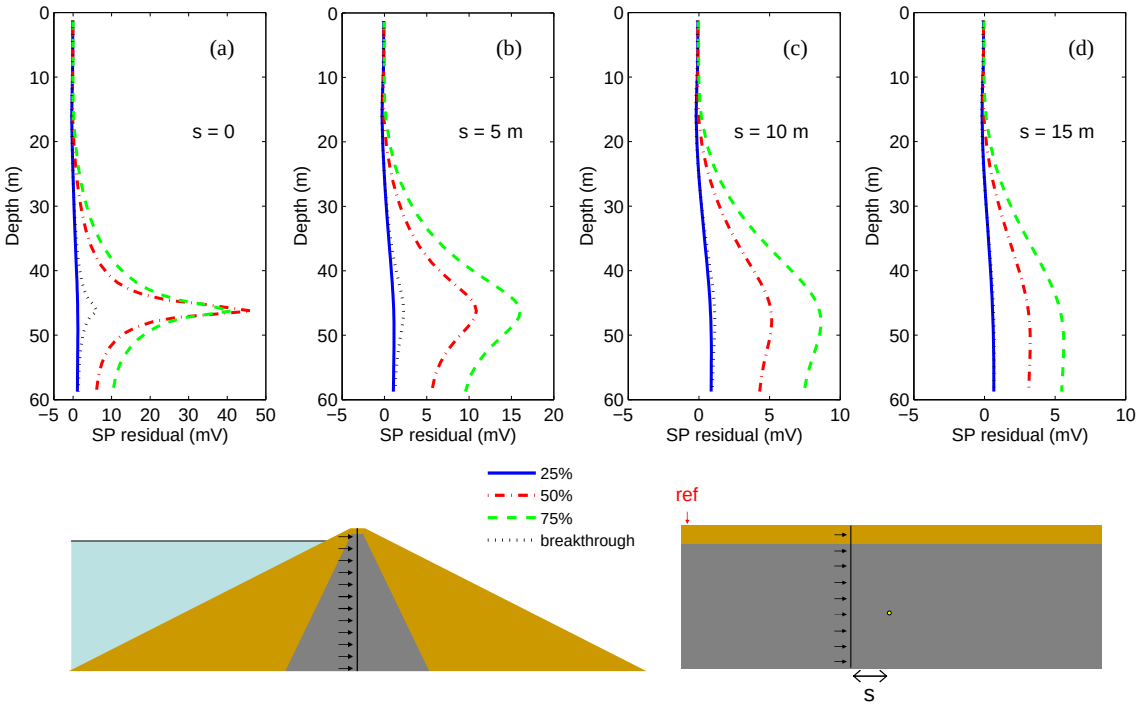

Figure 5.16: Profiles of SP residual with depth beneath the centre of the crest marking the progression of the pipe defect through the core. Vertical profiles are located at incremental offsets (s) from the centre of the defect in a direction parallel to the crest: a) intersecting the defect (s=0); b) 5 m separation; c) 10 m separation; d) 15 m separation.

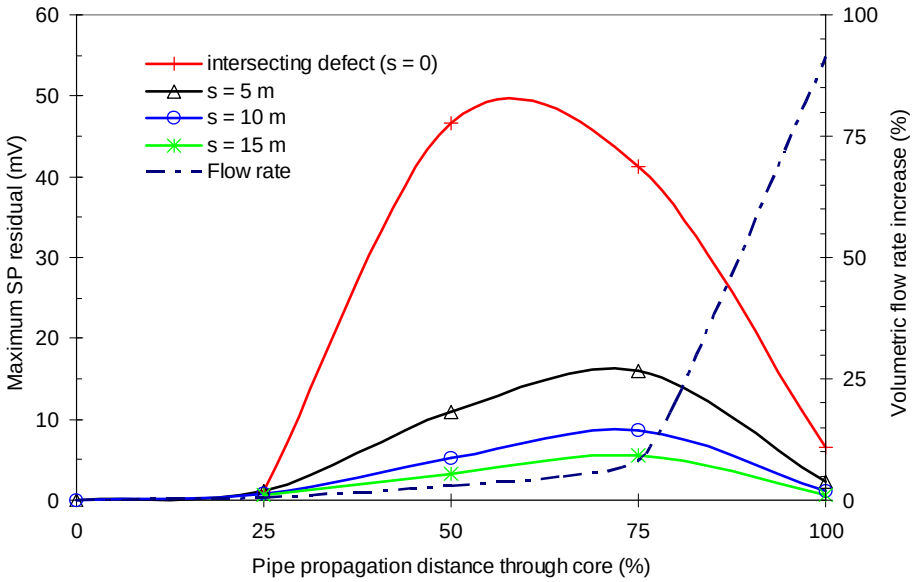

Figure 5.17: Comparison of the maximum SP residual and increase in seepage during the progression of the pipe defect at 45 m depth through the core. SP residual data represent the maximum anomaly measured at depth beneath the centre of the crest, at different offset distances (s) from the centre of the defect in a direction parallel to the crest.

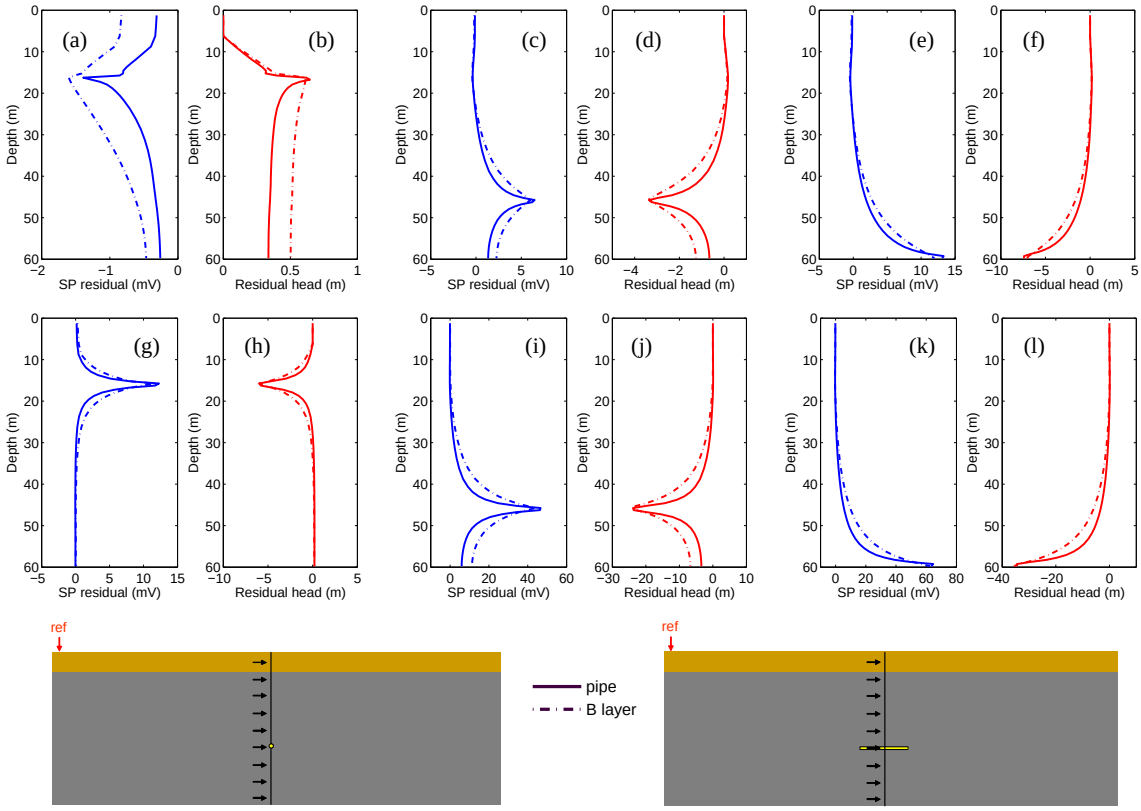

Figure 5.18: Profiles of SP residual and residual hydraulic head with depth beneath the crest for pipe and B layer defect models. Vertical profiles intersect the centre of the defects. Residual data are shown for full defect models at 15 m depth (a, b), 45 m depth (c, d) and 60 m depth (e, f); for half defect models at 15 m depth (g, h), 45 m depth (i, j) and 60 m depth (k, l).

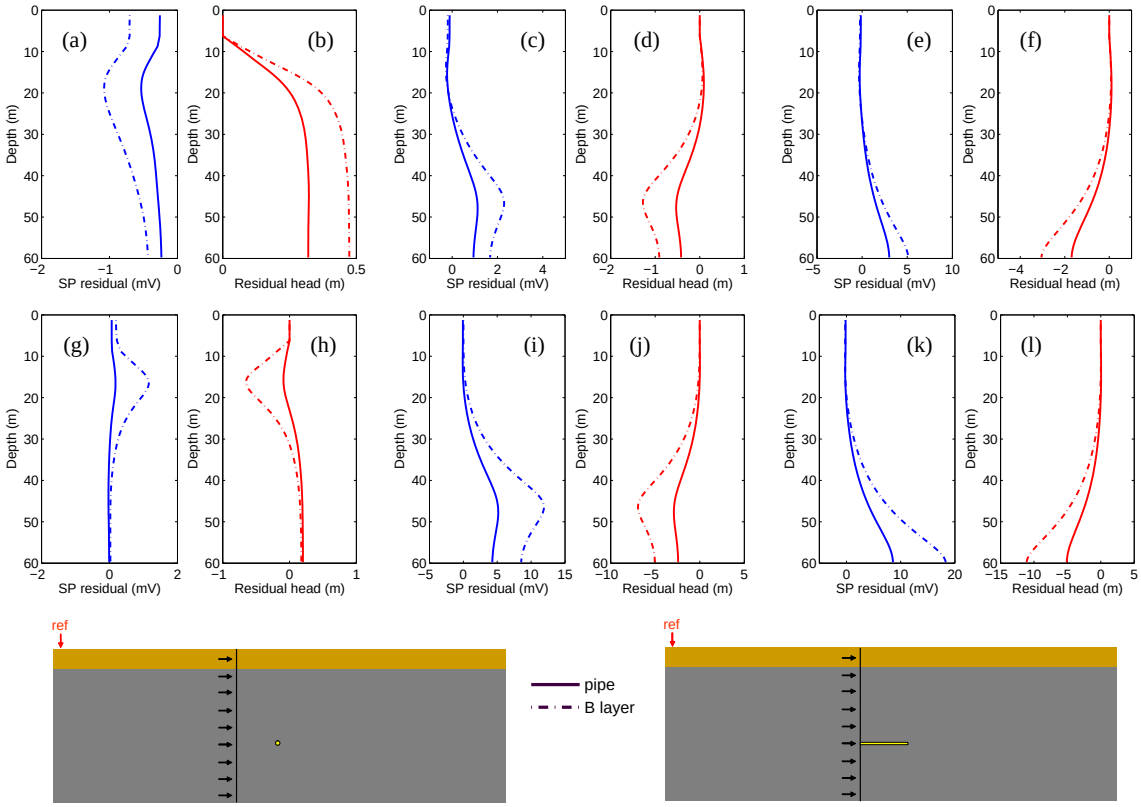

Figure 5.19: Profiles of SP residual and residual hydraulic head with depth beneath the crest for pipe and B layer defect models. Vertical profiles are offset by 10 m along the crest from the centre of the defects. Residual data are shown for full defect models at 15 m depth (a, b), 45 m depth (c, d) and 60 m depth (e, f); for half defect models at 15 m depth (g, h), 45 m depth (i, j) and 60 m depth (k, l).

5.7 Discussion and Conclusion

The streaming potential signal generated by seepage through an embankment was evaluated for a series of synthetic models using a three-dimensional forward modelling algorithm. The purpose of the study was to assess the sensitivity of the self-potential method in detecting preferential flow paths caused by internal erosion.

The current study makes use of an embankment geometry and physical property values assumed to represent a general case. Defect properties were chosen to reflect a realistic approximation of preferential seepage flow paths that could develop in the early stages of internal erosion. However, the self-potential distribution is highly dependent on the embankment geometry and physical property distribution, such that the amplitude and character of a measured SP anomaly may vary significantly from the results presented here.

Pipe and construction layer defects located at three depths within a zoned embankment were studied for different propagation distances through the core. Seepage through an intact core model of the embankment generated a peak-to-peak SP response of 45 mV. The presence of defects within the core resulted in anomalous variations from this background response. Full defect models representing breakthrough conditions generated residual anomalies of up to 3 mV at the surface of the embankment, and a dipolar anomaly at depth exhibiting maximum amplitudes of -7 mV to 13 mV. Half defect models representing the upstream progression of piping through the core generated residual anomalies of less than 1 mV at surface and maximum anomalies ranging from 12 mV to 65 mV at depth.

The numerical modelling results are useful in demonstrating how the SP method may respond to the presence of defect zones within an embankment, and provide guidance for survey design to maximize detection. The studied defects would not be detectable from surface measurements made using portable electrodes in a single or repeat SP survey configuration. Measurements are required at depth in order to detect sufficient signal. The half defect results showed that significant SP anomalies are generated around the upstream end of the defects due to the large hydraulic gradients that develop prior to breakthrough. A comparison of the predicted SP response and fluid flow rate from the upstream migration of a pipe defect in the core clearly showed that the maximum SP anomaly occurs prior to any detectable increase in seepage. The localized SP response mirrors the pressure response

at depth, and shows the capacity of the method to detect changes in hydraulic gradient. Consequently, SP measurements made using buried electrodes could complement existing piezometric measurements, and may provide a cost benefit.

The results have implications for the application of the self-potential method to dam safety investigations. Single or repeat surveying has been successful in delineating preferential seepage paths [e.g., *Butler et al.*, 1989] and is a useful investigative tool that may be used to characterize overall conditions and identify larger-scale anomalies. However, continuous monitoring affords an increased sensitivity to the development of seepage-related anomalies caused by internal erosion, since temporal changes can be tracked more effectively. Ideally, electrodes should be installed beneath the surface to capitalize on larger signal levels. In existing structures, the installation of electrodes at depth can risk damaging the core by drilling, so pre-existing boreholes may prove useful. Electrodes and cabling may be installed during upgrading of existing structures or the construction of new embankments.

Self-potential surveying is a tool to be used in conjunction with standard monitoring methods and other geophysical techniques to help characterize seepage conditions in embankments. Future developments in instrumentation may offer improved measurement sensitivity, but optimizing electrode placement along with data acquisition and processing strategies will improve the effectiveness of the method.

5.8 References

Adamson, A. W., *Physical Chemistry of Surfaces*, John Wiley and Sons, New York, 1990.

Archie, G. E., The electrical resistivity log as an aid in determining some reservoir characteristics, *Transactions of the Society of Petroleum Engineers of the American Institute of Mining, Metallurgical and Petroleum Engineers (AIME)*, *146*, 54–67, 1942.

Arps, J. J., The effect of temperature on the density and electrical resistivity of sodium chloride solutions, *Transactions of the Society of Petroleum Engineers of the American Institute of Mining, Metallurgical and Petroleum Engineers (AIME)*, *198*, 327–330, 1953.

Black, W. E., and R. F. Corwin, Application of self-potential measurements to the delineation of groundwater seepage in earth-fill embankments, *Society of Exploration Geophysicists Technical Program Expanded Abstracts*, *3*, 162–164, doi:10.1190/1.1894185, 1984.

Bogoslovsky, V. A., and A. A. Ogilvy, Application of geophysical methods for studying the technical status of earth dams, *Geophysical Prospecting*, *18*, 758–773, 1970.

Butler, D. K., J. L. Llopis, and C. M. Deaver, Comprehensive geophysical investigation of an existing dam foundation, *The Leading Edge*, *8*(8), 10–18, 1989.

Casagrande, L., Stabilization of soils by means of electro-osmosis: State of the art, *Journal of the Boston Society of Civil Engineers*, *69*(2), 255–302, 1983.

Corwin, R. F., The self-potential method for environmental and engineering applications, in *Geotechnical and Environmental Geophysics*, vol. 1, edited by S. H. Ward, pp. 127–145, Society of Exploration Geophysicists, Tulsa, 1990.

Corwin, R. F., Investigation of geophysical methods for assessing seepage and internal erosion in embankment dams: Self-potential field data acquisition manual, *Tech. rep.*, Canadian Electricity Association Technologies Inc. (CEATI), Report T992700-0205B/1, Montreal, 2005.

Darnet, M., and G. Marquis, Modelling streaming potential (SP) signals induced by water movement in the vadose zone, *Journal of Hydrology*, *285*, 114–124, 2004.

Darnet, M., G. Marquis, and P. Sailhac, Estimating aquifer hydraulic properties from the inversion of surface Streaming Potential (SP) anomalies, *Geophysical Research Letters*, *30*(13), 1679, doi:10.1029/2003GL017631, 2003.

de Groot, S. R., *Thermodynamics of irreversible processes*, *Selected Topics in Modern Physics*, vol. 3, North Holland Publishing Company, Amsterdam, 1951.

Guichet, X., L. Jouniaux, and J. P. Pozzi, Streaming potential of a sand column in partial saturation conditions, *Journal of Geophysical Research*, *108*(B3), 2141, doi: 10.1029/2001JB001517, 2003.

Harbaugh, A. W., E. R. Banta, M. C. Hill, and M. G. McDonald, Modflow-2000, the U.S. Geological Survey Modular Ground-Water Model - User Guide to Modularization Concepts and the Ground-Water Flow Process, *Tech. rep.*, United States Geological Survey, Open-File Report 00-92, Washington, 2000.

HydroGeoLogic Inc., *MODFLOW-SURFACT Version 2.2 Documentation*, HydroGeoLogic Inc., Herndon, 1996.

Johansson, S., and T. Dahlin, Seepage monitoring in an earth embankment dam by repeated resistivity measurements, *European Journal of Environmental and Engineering Geophysics*, *1*, 229–247, 1996.

Johansson, S., J. Friborg, T. Dahlin, and P. Sjödahl, Long term resistivity and self potential monitoring of embankment dams: Experiences from Hällby and Sädva dams, Sweden, *Tech. rep.*, Elforsk/Canadian Electricity Association Dam Safety Interest Group, Report 05:15, Stockholm, 2005.

Moore, J. R., S. D. Glaser, H. F. Morrison, and G. M. Hoversten, The streaming potential of liquid carbon dioxide in Berea sandstone, *Geophysical Research Letters*, *31*, L17610, doi:10.1029/2004GL020774, 2004.

Morgan, F. D., E. R. Williams, and T. R. Madden, Streaming potential properties of Westerly granite with applications, *Journal of Geophysical Research*, *94*(B9), 12,449–12,461, 1989.

Ogilvy, A. A., M. A. Ayed, and V. A. Bogoslovsky, Geophysical studies of water leakages from reservoirs, *Geophysical Prospecting*, *17*, 36–62, 1969.

Overbeek, J. T. G., Electrokinetic phenomena, in *Colloid Science, Irreversible Systems*, vol. 1, edited by H. R. Kruyt, Elsevier Publishing Company, Amsterdam, 1952.

Panthulu, T. V., C. Krishnaiah, and J. M. Shirke, Detection of seepage paths in earth dams using self-potential and electrical resistivity methods, *Engineering Geology*, *59*, 281–295, 2001.

Revil, A., and A. Cerepi, Streaming potentials in two-phase flow conditions, *Geophysical Research Letters*, *31*, L11605, doi:10.1029/2004GL020140, 2004.

Revil, A., H. Schwaeger, L. M. Cathles III, and P. D. Manhardt, Streaming potential in porous media: 2. Theory and application to geothermal systems, *Journal of Geophysical Research*, *104*(B9), 20,033–20,048, 1999.

Rozycki, A., J. M. Ruiz Fonticiella, and A. Cuadra, Detection and evaluation of horizontal fractures in earth dams using the self-potential method, *Engineering Geology*, *82*, 145–153, doi:10.1016/j.enggeo.2005.09.013, 2006.

Sheffer, M. R., and D. W. Oldenburg, Three-dimensional forward modelling of streaming potential, *Geophysical Journal International*, *169*, 839–848, doi:10.1111/j.1365-246X.2007.03397.x, 2007.

Stevens, H. H., J. F. Ficke, and G. F. Smoot, Water temperature: Influencial factors, field measurements, and data presentation, in *Techniques of Water-Resources Investigations Book 1*, United States Geological Survey, Washington, 1975.

Waterloo Hydrogeologic Inc., *Visual MODFLOW version 4.0 User's Manual*, Waterloo Hydrogeologic Inc., 2004.

Chapter 6

Three-dimensional inversion of self-potential data to recover hydraulic head [5]

6.1 Introduction

Self-potential (SP) data resulting from mineral exploration, geothermal and hydrogeological investigations have been interpreted using a number of quantitative techniques. Geometric source methods range from curve-matching [*de Witte*, 1948; *Yüngül*, 1950] and parametric curves [*Paul*, 1965; *Bhattacharya and Roy*, 1981; *Atchuta Rao and Ram Babu*, 1983] to least-squares inversion [*Fitterman and Corwin*, 1982; *Abdelrahman and Sharafeldin*, 1997]. Source imaging [*Di Maio and Patella*, 1994; *Hämmann et al.*, 1997; *Patella*, 1997] and source inversion methods [*Shi*, 1998; *Minsley et al.*, 2007] have also been developed to recover parameters of an electrical current source distribution that explain the measured potentials. Although these methods vary in complexity, they provide a means of interpreting SP data that is essentially independent of the underlying physical source mechanism. This can be beneficial in problems where the source mechanism is unknown or poorly understood.

The SP method may be used to study streaming potentials in order to assess subsurface flow conditions. Fluid flow through porous media generates electrical current flow, and the resultant electrical potentials can be used to evaluate characteristics of the hydraulic regime. To extract information about the hydraulic system, a coupled flow model is required to explain the interaction between the electrical and fluid flow systems.

[5] A version of this chapter will be submitted for publication. Sheffer, M.R. and Oldenburg, D.W. (2007) Three-dimensional inversion of self-potential data to recover hydraulic head.

A number of studies have focused specifically on the inversion of self-potential data to recover parameters related to the hydraulic system, when electrokinetic coupling is the driving mechanism. *Revil et al.* [2003] developed a parametric inversion routine using a weighted least-squares approach to find the depth to the water table. Their method is based on a pseudo-potential formulation of the coupled flow problem [*Nourbehecht*, 1963; *Fitterman*, 1978] and uses an approach first presented by *Fournier* [1989] where electrokinetic sources are represented by a sheet of vertical dipoles at the phreatic surface. *Birch* [1998] and *Revil et al.* [2003] used this same approach to image the position of the water table. *Sailhac and Marquis* [2001] used a wavelet-based technique to invert for electrokinetic source parameters in 2-D assuming a homogeneous conductivity distribution and identical boundary conditions for electrical and hydraulic flow fields.

These techniques assume that any heterogeneities in the electrical conductivity distribution have a negligible effect, particularly between saturated and unsaturated zones. The assumption of a homogeneous conductivity distribution in a truly heterogeneous system can have ramifications on the recovered model [*Minsley et al.*, 2007; *Sheffer and Oldenburg*, 2007]. *Revil et al.* [2004] included the effect of an electrical conductivity contrast between saturated and unsaturated zones into their parametric inversion routine to recover the depth to the water table. *Darnet et al.* [2003] used a weighted least-squares approach to invert for the hydraulic conductivity, cross-coupling conductivity and thickness of a homogeneous aquifer subject to flow from a pumping well. Their approach accounts for the electrical conductivity contrast between the aquifer and well casing, and shows that this can have a significant effect on the resulting potential field distribution at surface.

In this paper we present an inverse method to recover a three-dimensional hydraulic head distribution from measured self-potential data. Our approach enables us to extract pertinent information about the underlying hydraulic regime from the geophysical data, and permits us to include the effect of heterogeneous conductivity distributions. The method is for particular application to systems where streaming potential is the dominant mechanism giving rise to the SP response. The recovered head distribution may be interpreted directly to identify zones of preferential flow caused by subsurface heterogeneity, or used as input to an inversion routine to recover other hydraulic parameters, such as hydraulic conductivity.

As a first step, we have developed an efficient 3-D forward modelling algorithm that enables us to determine the SP distribution resulting from a saturated or variably saturated flow model and a known distribution of electrical properties, namely the electrical conductivity and cross-coupling conductivity [*Sheffer and Oldenburg*, 2007]. The study region is divided into a discrete rectangular mesh, in which hydraulic head and electrical properties are defined for each cell. Discrete equations are formulated using the method of finite volumes and the forward problem, which is a linear relationship between the electrical potentials and hydraulic head, is solved using a preconditioned biconjugate gradient stabilized method.

In the inverse problem we are supplied with measured electrical potentials and our goal is to estimate the causative 3-D model of hydraulic head. We assume that electrical properties are not a function of hydraulic head, i.e. the medium is fully-saturated or the position of the phreatic surface is known a priori. The earth model is divided into rectangular cells, each of which is assigned constant values of the electrical properties. In practice, these must be obtained through additional analysis, but the cross-coupling coefficient may usually be estimated since it varies over a small range, and the electrical conductivity may be characterized using DC resistivity survey techniques. Since the number of available SP data is usually less than the number of grid cells we are faced with a typical underdetermined inverse problem. We solve the inverse problem by minimizing an objective function that consists of a data misfit and a model objective function. The data misfit is weighted according to the measurement error. A priori information is incorporated into the solution via the model objective function. We use a Tichonov-type regularization technique to balance fitting the data with fitting a chosen reference head model.

Section 6.2 gives an overview of the streaming potential phenomenon and coupled flow theory. Section 6.3 describes the formulation of the inverse problem, including a discussion of boundary conditions, physical properties, and an active cell approach used to isolate relevant regions in the problem domain. Finally, Section 6.4 presents the inversion of measured SP data from a laboratory tank model of seepage under a cut-off wall, and illustrates how the solution is improved by incorporating prior information about the problem.

6.2 Coupled flow model of streaming potential

Streaming potential is a function of the properties of the solid-fluid interface in a saturated porous medium. An electrical double layer forms at the surface of the solid grains, which consists of a tightly adsorbed inner layer and a weakly-bound diffuse outer layer of ions. These act together to balance the surface charge of the solid. Fluid flow through the pore space drags ions from the diffuse layer in the direction of flow and generates a streaming current. This movement of ions causes a charge imbalance within the pore space, which drives an opposing conduction current that permeates the porous medium.

The total charge flux, or current density $\boldsymbol{J}$ [$\mathrm{A\,m^{-2}}$], can be expressed in terms of the sum of primary and secondary potential gradients in a system [*Onsager*, 1931]. In the absence of significant thermal or ionic concentration gradients, electrical current flow is described by:

$$\boldsymbol{J} = \boldsymbol{J}_C + \boldsymbol{J}_S = -\sigma\nabla\phi - L\nabla h, \tag{6.1}$$

where $\boldsymbol{J}_C$ and $\boldsymbol{J}_S$ are respectively the conduction current and the streaming current densities [*Sill*, 1983]. The flow of conduction current is governed by the distribution of electrical conductivity σ [$\mathrm{S\,m^{-1}}$] and electrical potential ϕ [V] in the subsurface. The streaming current is governed by the distribution of cross-coupling conductivity L [$\mathrm{A\,m^{-2}}$] and hydraulic head h [m].

The electrical response to a given hydraulic head distribution is considered a steady-state process, regardless of whether the hydraulic system exhibits steady-state or transient behaviour. In the absence of any imposed current sources on the volume, ϕ is referred to as the self-potential and is described by:

$$\nabla \cdot \sigma\nabla\phi = -\nabla \cdot L\nabla h. \tag{6.2}$$

6.3 Inversion Methodology

6.3.1 Discrete formulation

We wish to analyze observed self-potential data to recover a subsurface distribution of hydraulic head in systems where streaming potential is the driving mechanism for the self-

potential field. We represent the study region using a discrete mesh of rectilinear grid cells, in which values of ϕ, h, σ and L are defined at cell centres. Each self-potential datum corresponds to an observed potential difference at a given coordinate with respect to a reference position. The self-potential data at surface or at points within the subsurface are related to the subsurface distribution of hydraulic head through the relation:

$$\mathbf{d} = \boldsymbol{\mathcal{G}}\mathbf{h}\,, \tag{6.3}$$

where $\mathbf{h}$ is a vector of hydraulic head values corresponding to each cell, and $\mathbf{d}$ is a vector of self-potential data. The matrix $\boldsymbol{\mathcal{G}}$ is the discrete representation of (6.2) and is defined as:

$$\boldsymbol{\mathcal{G}} = -\mathbf{Q}\{\mathbf{DSG}\}^{-1}\{\mathbf{DLG}\}\,, \tag{6.4}$$

where $\mathbf{S}$ and $\mathbf{L}$ are matrices that respectively describe the distribution of electrical conductivity and cross-coupling conductivity using a finite volume approximation. Matrices $\mathbf{D}$ and $\mathbf{G}$ are respectively the divergence and gradient operators, and $\mathbf{Q}$ is a linear operator that relates each datum to the self-potential ϕ according to:

$$\mathbf{d} = \mathbf{Q}\boldsymbol{\phi}\,. \tag{6.5}$$

Self-potential data yield information on the hydraulic gradient. To recover a unique solution for $\mathbf{h}$, we choose to specify zero mean potential in formulating the discrete equations. The forward problem defined in (6.3) is linear provided that L and σ do not vary as a function of h. The implications of this assumption are further discussed in Section 6.3.3.

We are faced with solving an underdetermined inverse problem in which an infinite number of solutions exist, since the number of data is typically much smaller than the number of discrete model cells that define the study region. Consequently, we define a model objective function in which we can include prior information about the hydraulic head distribution. We seek to minimize the model objective function ψ_m to recover the simplest hydraulic head model that leads to an acceptable fit with the observed self-potential data. The model objective function is defined as:

$$\begin{aligned}\psi_m = \alpha_s \int_V w_s(h - h_{ref})^2 dV \;+\; \alpha_x \int_V w_x \left(\frac{\partial h}{\partial x}\right)^2 dV \;+ \\ \alpha_y \int_V w_y \left(\frac{\partial h}{\partial y}\right)^2 dV \;+\; \alpha_z \int_V w_z \left(\frac{\partial h}{\partial z}\right)^2 dV\,,\end{aligned} \tag{6.6}$$

where the first term works to minimize the difference between the recovered solution h and a reference model of hydraulic head h_{ref}, and the remaining three terms seek to minimize the recovered hydraulic head gradient in each spatial dimension. The functions w_s, w_x, w_y and w_z are spatially-dependent weighting functions that regulate the minimization on a cell-by-cell basis. The scalar coefficients α_s, α_x, α_y and α_z govern the relative weighting of each term in the objective function. These values are determined through a dimensional analysis. The discrete form of (6.6) is defined on the mesh described above and is expressed as:

$$\psi_m = \|\mathbf{W_s}(\mathbf{h} - \mathbf{h_{ref}})\|_2^2 + \|\mathbf{W_x}(\mathbf{h})\|_2^2 + \|\mathbf{W_y}(\mathbf{h})\|_2^2 + \|\mathbf{W_z}(\mathbf{h})\|_2^2 \,, \tag{6.7}$$

or more simply as

$$\psi_m = \|\mathbf{W_s}(\mathbf{h} - \mathbf{h_{ref}})\|_2^2 + \|\mathbf{W}(\mathbf{h})\|_2^2 \,, \tag{6.8}$$

where $\mathbf{W_s}$ and $\mathbf{W}$ are matrices that contain discrete approximations of the functions operating on the model.

The chosen formulation of the model objective function enables us to incorporate discrete hydraulic head observations and information about the nature of the subsurface flow regime to help constrain the solution. Observed head values obtained through point measurements or associated with boundary conditions for the problem can be incorporated into the reference model. In areas where we have confidence in our reference model, we can penalize discrepancies between the recovered model and the reference model by choosing appropriately large w_s values. Prior knowledge of the orientation of hydraulic gradients can be included by preferentially weighting the appropriate spatial term. For example, in low-topography groundwater flow problems where the preferential flow direction lies in a plane approximately parallel to the ground surface, we can encourage a head model with a minimum vertical gradient below the phreatic surface by choosing a relatively large value for α_z.

We must estimate the noise present in the observed self-potential data in order to achieve an acceptable fit between the observed data and the predicted data from our model. This noise originates from measurement errors, which include instrument sensitivity and positional errors, as well as from spurious SP signals caused by telluric currents or other subsurface source mechanisms. Our discrete approximation of the earth can also lead to

errors between the observed and predicted data. Since the noise is typically unknown, we assume it exhibits a Gaussian distribution and choose to fit the data within a noise envelope characterized by a standard deviation ϵ defined for each datum d^{obs}:

$$\psi_d = \sum_{j=1}^{N} \left(\frac{\boldsymbol{\mathcal{G}} h - d_j^{obs}}{\epsilon_j} \right)^2 , \tag{6.9}$$

where N is the number of data points and ψ_d is the data misfit. The discrete form of the data misfit is expressed as:

$$\psi_d = \|\mathbf{W_d}(\boldsymbol{\mathcal{G}}\mathbf{h} - \mathbf{d^{obs}})\|_2^2 , \tag{6.10}$$

where diagonal elements of the matrix operator $\mathbf{W_d}$ are equal to $1/\epsilon_j$. Since ψ_d is a chi-squared variable, we seek a target data misfit $\psi_d = \psi_d^*$, where $\psi_d^* \sim N$.

The inverse problem is solved by finding a hydraulic head model that minimizes our model objective function and satisfies our data misfit criterion. The inverse problem is posed as an unconstrained optimization problem, where we seek to minimize a global objective function:

$$\psi = \psi_d + \beta\psi_m , \tag{6.11}$$

where β is a regularization or "trade-off" parameter. The discrete form of the global objective function ψ is expressed as:

$$\psi = \|\mathbf{W_d}(\boldsymbol{\mathcal{G}}\mathbf{h} - \mathbf{d^{obs}})\|_2^2 + \beta\{\|\mathbf{W_s}(\mathbf{h} - \mathbf{h_{ref}})\|_2^2 + \|\mathbf{W}(\mathbf{h})\|_2^2\} . \tag{6.12}$$

Calculating the gradient of (6.12) with respect to head and setting $\nabla_h \psi = 0$ results in:

$$\begin{aligned} \left\{\boldsymbol{\mathcal{G}}^T {\mathbf{W_d}}^T \mathbf{W_d} \boldsymbol{\mathcal{G}} + \beta \left[{\mathbf{W_s}}^T \mathbf{W_s} + \mathbf{W}^T \mathbf{W}\right]\right\} \mathbf{h} = \\ \boldsymbol{\mathcal{G}}^T {\mathbf{W_d}}^T \mathbf{W_d} \mathbf{d^{obs}} + \beta {\mathbf{W_s}}^T \mathbf{W_s} \mathbf{h_{ref}} . \end{aligned} \tag{6.13}$$

Equation 6.13 is of the form $\mathbf{Ax} = \mathbf{b}$ and is solved using a preconditioned method of conjugate gradients. A cooling method is used to determine the optimum value β^* that results in $\psi_d = \psi_d^*$.

6.3.2 Boundary conditions

The problem domain is represented by a discrete 3-D mesh of grid cells. The outer edge of the mesh is specified as a zero flux boundary for conduction current flow ($\nabla\phi \cdot \hat{\mathbf{n}} = 0$).

Consequently, the mesh must be large enough to impose the zero flux boundary condition far from areas in which significant hydraulic head gradients are expected to occur. Problems of irregular topography are handled by specifying null values of electrical conductivity in air cells. This effectively propagates the no-flow boundary at the limit of the rectilinear mesh down to the earth's surface.

Unlike conduction current flow, which propagates through any electrically conductive medium, convection current flow is restricted to the limits of the porous medium in which fluid flows. Null values of the cross-coupling conductivity are specified in grid cells that do not correspond to the porous medium, such as air, external bodies of water, or infrastructure such as well casings.

6.3.3 Physical property models

To solve (6.13), the distribution of cross-coupling conductivity and electrical conductivity must be prescribed in the problem domain. The conductivity distributions are represented mathematically by piecewise constant functions, which can vary significantly from one cell to the next.

The electrical conductivity of the subsurface may be characterized using a geophysical field survey technique such as DC resistivity. This approach is preferable, particularly if we have limited prior information about subsurface structural features. Empirical estimates [e.g. *Archie*, 1942] or laboratory-measured values may be assigned to a given material unit if we have some lithologic or stratigraphic information.

The cross-coupling conductivity is a function of the electrical conductivity of the saturated medium and a streaming potential coupling coefficient C through the relation $L = -C\sigma$, where C is typically characterized through laboratory measurements [e.g. *Ishido and Mizutani*, 1981; *Morgan et al.*, 1989; *Jouniaux and Pozzi*, 1995]. The streaming potential coupling coefficient may also be estimated using different forms of the Helmholtz-Smoluchowski equation [e.g *Overbeek*, 1952], which note the dependence of this parameter on the saturating fluid conductivity and in some cases surface conductivity. Consequently, care must be taken in estimating L using independent measurements of C and σ, to ensure that these values correspond to similar saturating fluid properties for a given material

[*Sheffer et al.*, 2007].

As stated in Section 6.3.1, the inverse problem is linear assuming that L and σ do not vary as a function of h. This condition is satisfied in confined or fully-saturated flow problems. In unconfined flow problems, a phreatic surface delineates the boundary between saturated and unsaturated zones, as shown in Figure 6.1. This surface defines where pore fluid pressure is atmospheric and hydraulic head is equal to the elevation z above some datum. Since L and σ vary with the degree of saturation S_w, we must know the position of the phreatic surface a priori to prescribe values for $L(S_w)$ and $\sigma(S_w)$.

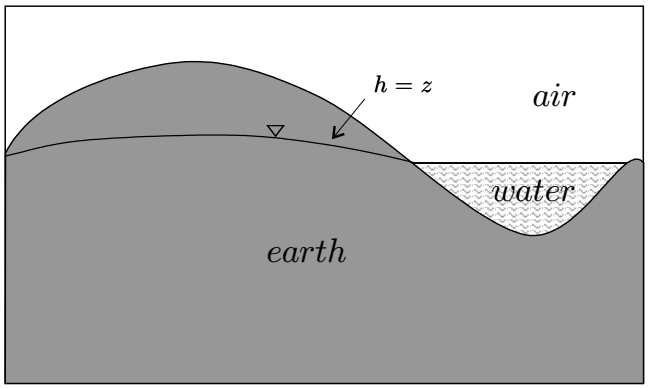

Figure 6.1: Schematic of the spatial flow domain.

Electrical conduction current flow permeates the entire medium and σ is assigned a value representative of average unsaturated or partially saturated conditions above the phreatic surface. Streaming current flow may be treated using a saturated or variably saturated approach. In a saturated approach, we consider streaming current flow to be limited to the saturated zone and L is assigned a null value above the phreatic surface. In a variably saturated approach, the influence of streaming current flow in the unsaturated zone is included. The behaviour of the streaming potential coupling coefficient has been studied for partially saturated conditions [*Guichet et al.*, 2003; *Revil and Cerepi*, 2004; *Moore et al.*, 2004] and tends to decrease in magnitude with saturation level. However, the behaviour of streaming current flow in the unsaturated zone is not fully understood. In this paper we assume that the phreatic surface acts as a zero flux boundary for streaming current flow.

6.3.4 Active cell approach

It is not reasonable to recover a hydraulic head model in regions of the mesh where it is not physically realistic to do so. Examples of this include air cells in problems of irregular geometry, and cells corresponding to impervious non-porous structures such as well-casings. Similarly, it is not reasonable to recover a hydraulic head model above the phreatic surface in problems where we are only concerned with flow in the saturated zone. Consequently, we separate the domain into active and inactive regions for the purposes of solving the inverse problem. We solve for the active component of the hydraulic head vector and specify a null head value in inactive regions.

Considering only active model components, (6.13) becomes:

$$\left\{\boldsymbol{\mathcal{G}}_{\mathbf{A}}{}^{T}\mathbf{W}_{\mathbf{d}}{}^{T}\mathbf{W}_{\mathbf{d}}\boldsymbol{\mathcal{G}}_{\mathbf{A}} + \beta\left[\mathbf{W}_{\mathbf{sA}}{}^{T}\mathbf{W}_{\mathbf{sA}} + \mathbf{W}_{\mathbf{A}}{}^{T}\mathbf{W}_{\mathbf{A}}\right]\right\}\mathbf{h}_{\mathbf{A}} = \boldsymbol{\mathcal{G}}_{\mathbf{A}}{}^{T}\mathbf{W}_{\mathbf{d}}{}^{T}\mathbf{W}_{\mathbf{d}}\mathbf{d}^{\mathbf{obs}} + \beta\mathbf{W}_{\mathbf{sA}}{}^{T}\mathbf{W}_{\mathbf{sA}}\mathbf{h}_{\mathbf{refA}}\ , \tag{6.14}$$

where the subscript $\mathbf{A}$ denotes the active vector or matrix. Solving this equation effectively reduces the size of the problem, and ensures that head is only recovered in cells where it is physically reasonable to do so.

The active component $\mathbf{h_A}$ of the head vector is isolated using the expression:

$$\mathbf{h_A} = \mathbf{R_A}{}^{T}\mathbf{h}\ , \tag{6.15}$$

where $\mathbf{R_A}$ is a matrix operator that specifies active cells in the mesh. The complete head vector is reconstructed for the purposes of evaluating the data misfit using:

$$\mathbf{h} = \mathbf{R_A}\mathbf{h_A} + \mathbf{R_I}\mathbf{h_I}\ , \tag{6.16}$$

where $\mathbf{h_I}$ is the inactive head vector component and $\mathbf{R_I}$ identifies inactive cells in the mesh. Similarly, the active columns of matrix $\boldsymbol{\mathcal{G}}$ are isolated using the expression:

$$\boldsymbol{\mathcal{G}}_{\mathbf{A}} = \boldsymbol{\mathcal{G}}\mathbf{R_A}\ , \tag{6.17}$$

and the complete matrix is defined by:

$$\boldsymbol{\mathcal{G}} = \boldsymbol{\mathcal{G}}_{\mathbf{A}}\mathbf{R_A}{}^{T} + \boldsymbol{\mathcal{G}}_{\mathbf{I}}\mathbf{R_I}{}^{T}. \tag{6.18}$$

A zero flux boundary imposed by null conductivity values in $\mathcal{G}$ is upheld even when inactive cells are removed from the matrix. This is a result of the finite volume approximation, which implements harmonic averaging to calculate the conductivity at cell faces. The boundary condition is therefore applied at the interface between active and inactive regions, and is not affected by the removal of inactive cells.

Special consideration must be given to the construction of $\mathbf{W_A}$, since this matrix contains a discrete approximation of the first derivative. We do not wish to minimize the model gradient across boundaries between active and inactive cells. Therefore, we must remove the influence of inactive cells on adjacent cells in addition to removing inactive columns of the matrix.

6.4 Flow under a cut-off wall

The example of seepage under a cut-off wall is used to demonstrate a successful application of the inversion algorithm using data acquired under controlled conditions. We use this example to illustrate how the solution is improved by incorporating prior information about the problem into the model objective function, and by including data acquired at depth below the ground surface.

Following a discussion of the laboratory measurements and details of the discrete model, we present the results of inverse modelling as four progressive case studies. Each case incorporates additional information about the problem. The recovered head models obtained by inverting SP data collected at the earth surface and at depth are evaluated for each case. In addition, we compare the recovered head models to observed hydraulic head values to evaluate the quality of the result.

6.4.1 Laboratory measurements

A laboratory-scale model of a cut-off wall was constructed to measure self-potential and hydraulic head in a saturated homogeneous system subject to steady-state seepage. Figure 6.2 presents a schematic of the acrylic tank showing tank dimensions, the position of the cut-off wall, and manometer port locations. The acrylic tank was filled with uniform quartz

sand compacted in layers up to a height of 38 cm. Steady-state seepage was initiated by maintaining constant surface water levels of 70.8 cm and 40 cm respectively upstream and downstream of the cut-off wall.

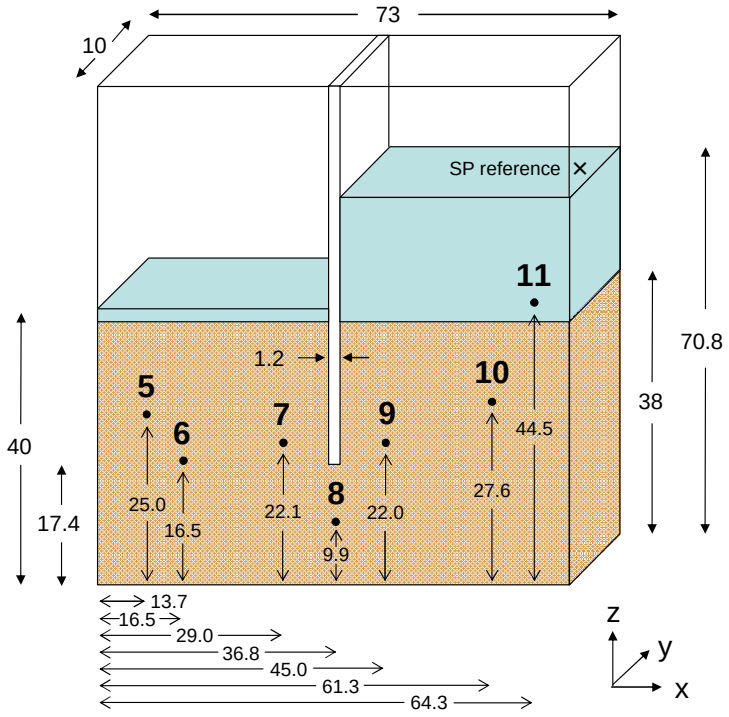

Figure 6.2: Schematic of the laboratory cut-off wall model, indicating tank dimensions and the position of manometer measurement ports, labelled as 5 to 11 (all dimensions in cm).

Self-potential data were acquired using a high-impedance voltmeter and a pair of non-polarizing Ag-AgCl electrodes. One electrode served as a fixed reference and was positioned near the upstream edge of the tank at the surface of the upstream water column, as indicated in Figure 6.2. The second electrode was used to occupy survey stations along the surface of each water column, and within seven fluid-filled manometer tubes located along the front face of the tank. Data were collected with a measurement sensitivity of 0.01 mV.

Hydraulic head measurements were obtained by manually recording water levels in the seven manometers. These readings were compared with the recovered head model to help evaluate the quality of inversion result, as discussed in the sections that follow.

Water was circulated through the system until a state of ionic equilibrium was reached

between the soil and fluid, to ensure that streaming potential was the primary coupled flow mechanism in the system. A state of chemical equilibrium was confirmed by fluid resistivity and self-potential measurements that were stable with time.

The streaming potential coupling coefficient and resistivity were measured directly in the tank to derive a cross-coupling conductivity of $L = 7 \times 10^{-5}\text{A/m}^2$ for the saturated quartz sand using the relation $L = -C/\rho$. A streaming potential coupling coefficient of $C = 9$ mV/m (0.9 mV/kPa) was obtained by calculating the linear fit between the measured self-potential and hydraulic head values under steady-state flow conditions. The resistivity of the saturated sand was characterized as $\rho = 130$ Ωm through DC resistivity measurements using a Wenner array configuration. A fluid resistivity of 40 Ωm was measured using a portable conductivity meter. These quantities were used to build the discrete physical property models described in the next section.

6.4.2 Discrete model development

Solution of the inverse problem requires that we approximate the study region using a discrete model and prescribe electrical property values to each cell in the mesh. The tank was modelled using a $37 \times 5 \times 35$ cell mesh with a uniform cell dimension of 2 cm. The limits of the mesh were chosen to correspond with the tank dimensions, since the sides of the acrylic tank impose a no-flow boundary for both conduction and convection current flow.

The upper surface of the sand acts as a no-flow boundary for convection current flow, since the porous medium is completely saturated. Consequently, all air and surface water cells were assigned a null cross-coupling conductivity, and the sand cells were assigned the measured value noted above. Cells used to represent the acrylic cut-off wall were assigned a null cross-coupling value. The air-water interface serves as a no-flow boundary for conduction current flow and air cells were therefore assigned a null electrical conductivity. Water and sand cells were assigned the measured values noted above. Cells representing the acrylic cut-off wall were assigned a null conductivity.

In all inversion models, the relative spatial weighting term α_y was set 3 orders of magnitude higher than α_x and α_z in the model objective function to reflect the planar nature

of seepage flow under the cut-off wall. The data misfit was calculated using a standard deviation of $\epsilon = 0.05$mV to represent observed noise levels for this experiment. A solution to the inverse problem was achieved by minimizing the model objective function subject to the data misfit being equal to the number of data points used in the inversion. Table 6.1 lists the optimum regularization parameter and corresponding data misfit and model norm for each inverse solution. In cases 1, 2 and 3 where no prior head information is supplied (i.e. $\alpha_s = 0$), the solutions are referenced to a known head at a single point on the surface of the upstream water column to enable a comparison between recovered and observed heads. In case 4, prior head information is included by setting w_s to be 4 orders of magnitude higher in cells where the hydraulic head is known.

Case	Data set	β_o	β^*	ψ_d	ψ_m	$\|h - h_{obs}\|$
1	surface	200,000	21,868	8	0.01107	0.00113
	subsurface	200,000	22,968	7	0.00702	0.00072
	all	200,000	28,145	15	0.01149	0.00150
2	surface	200,000	29,225	8	0.00801	0.00194
	subsurface	200,000	25,863	7	0.00589	0.00012
	all	200,000	35,330	15	0.00843	0.00030
3	surface	200,000	85,317	8	0.00322	0.00199
	subsurface	200,000	60,437	7	0.00290	0.00050
	all	200,000	122,830	15	0.00329	0.00042
4	surface	200,000	n/a	0.88	0.00396	0.00029
	subsurface	1,500,000	207,110	7	0.00399	0.00027
	all	1,500,000	494,630	15	0.00397	0.00024

Table 6.1: Parameters that characterize the inversion results for each case of modelling flow under a cut-off wall, listed according to input data set: initial (β_o) and optimum (β^*) regularization parameters, data misfit (ψ_d) and model norm (ψ_m). The difference between observed and recovered head values at the seven manometer ports is quantified using an l-1 norm measure. Note: $\psi_d < \psi_d^*$ for all values of β in case 4 using only surface data.

6.4.3 Case 1: Homogeneous subsurface approximation

As a first pass at interpreting the SP data, we consider that we have no prior information about the head distribution and no knowledge of the vertical extent or integrity of the cut-off wall below the ground surface. In this case we assume a homogeneous subsurface. Figure 6.3 illustrates the distribution of the various input parameters specified in the inverse problem. Active and inactive regions of the model are identified in Figure 6.3(a). Cells representing air and the acrylic cut-off wall above the surface of the sand were set as inactive for the purposes of the inversion, since it is unrealistic to solve for head in these cells. The prescribed cross-coupling conductivity and electrical resistivity distributions reflect the homogeneous subsurface assumption and are shown in Figures 6.3(b) and (c).

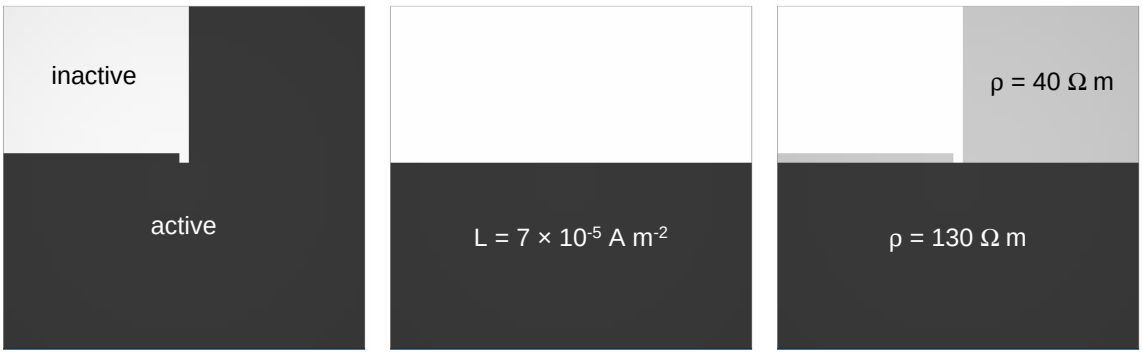

Figure 6.3: Cut-off wall model input - homogeneous subsurface approximation: a) active model cells; b) cross-coupling conductivity distribution; c) electrical resistivity distribution.

Three separate inversions were performed using data collected along the surface of the water columns, at points below surface corresponding to manometer locations, and the combination of surface and subsurface data sets. Figures 6.4, 6.5 and 6.6 present the observed data locations and the results of each inversion.

Figure 6.4 presents the inversion results for the self-potential data set collected only at surface. Figure 6.4(a) denotes the eight SP data locations along the surface of upstream and downstream water columns. Figure 6.4(b) shows a vertical cross-section through the

recovered hydraulic head model, which is smoothly-varying and ranges from 72 cm in the upstream water column to 40 cm downstream. A hydraulic head equipotential coincides with the known location of the cut-off wall below surface. The fit between observed and predicted SP data is reasonable, as shown in Figure 6.4(c). However, a comparison between observed and recovered head values at each of the manometer ports in Figure 6.4(d) reveals that a relatively poor fit exists at manometer ports 7 and 9, positioned immediately upstream and downstream of the known location of the wall.

The inversion results for self-potential data collected at points below surface are presented in Figure 6.5. Figure 6.5(a) denotes the seven SP data locations, which correspond to the position of manometer ports along the side of the tank. The recovered model result shown in Figure 6.5(b) displays significantly different behaviour than that obtained using the surface data, with more structure in the vicinity of observed data locations. Although a good SP data fit exists, Figure 6.5(d) shows that the recovered model underpredicts the observed head in manometers 5, 6 and 7 downstream of the known location of the wall.

Figure 6.6 presents the inversion results for the complete SP data set consisting of both surface and subsurface data points. Figure 6.6(b) displays the recovered head model obtained by including all 15 data points as indicated in Figure 6.6(a). The recovered head model is smoothly varying and comparable to that from the inversion of surface data. However, small head perturbations in the vicinity of manometer ports 7 and 9 may indicate a tendency for the head contours to curve inwards toward the known location of the wall. Figure 6.6(c) shows a good SP data fit, but Figure 6.6(d) shows that the recovered model underpredicts the observed head downstream of the known location of the wall.

Inconsistencies between the recovered models suggest that the homogeneous subsurface approximation is inadequate. The inversion of surface data and all data points result in similar hydraulic head models, where a head equipotential coincides with the known location of the cut-off wall (Figures 6.4(b) and 6.6(b)). These models are plausible only if the barrier is pervious with a hydraulic conductivity essentially equivalent to that of the soil.

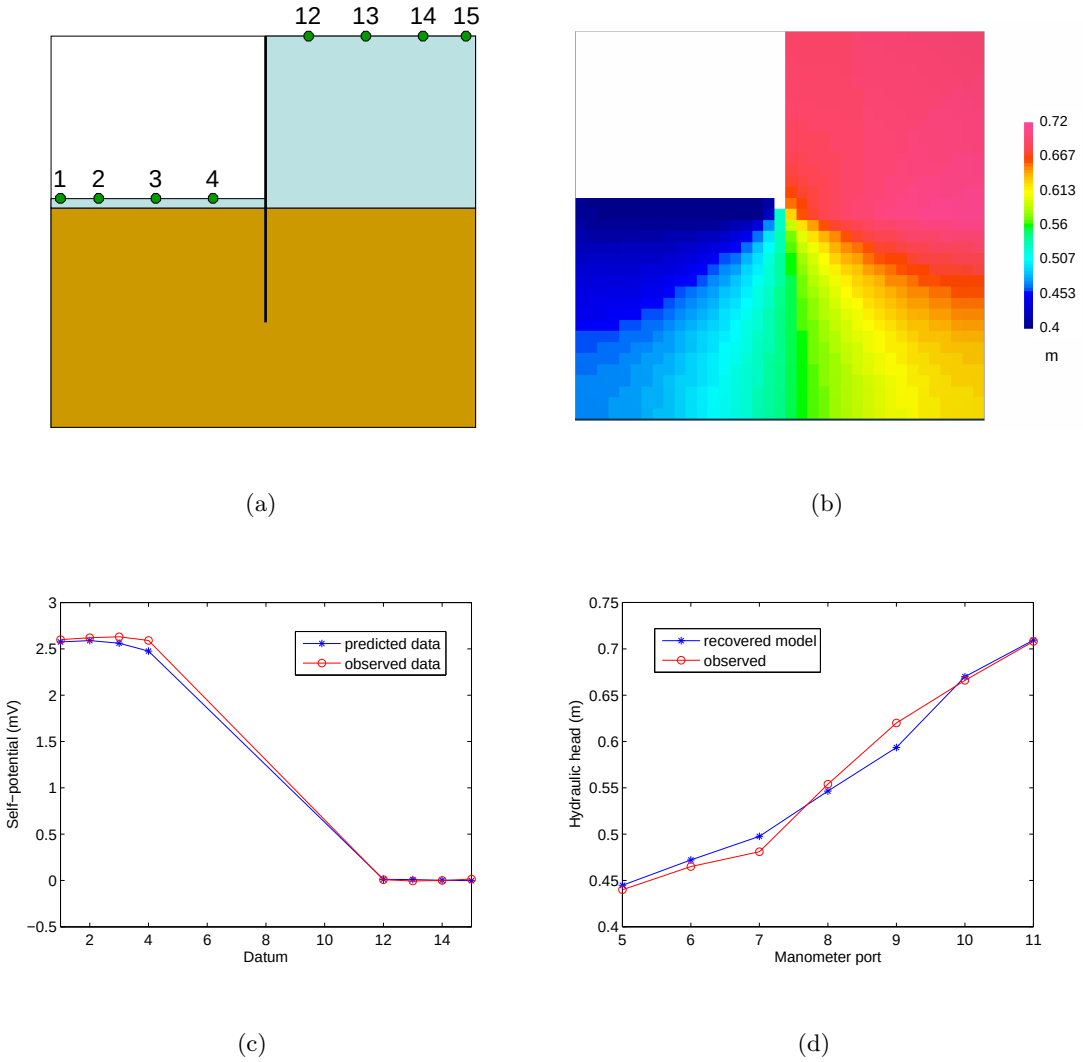

Figure 6.4: Cut-off wall model results - homogeneous subsurface approximation - surface data: a) observation locations; b) vertical cross-section of recovered head model; c) comparison of observed and predicted SP data at each measurement location; d) comparison of observed and recovered model head values in each manometer.

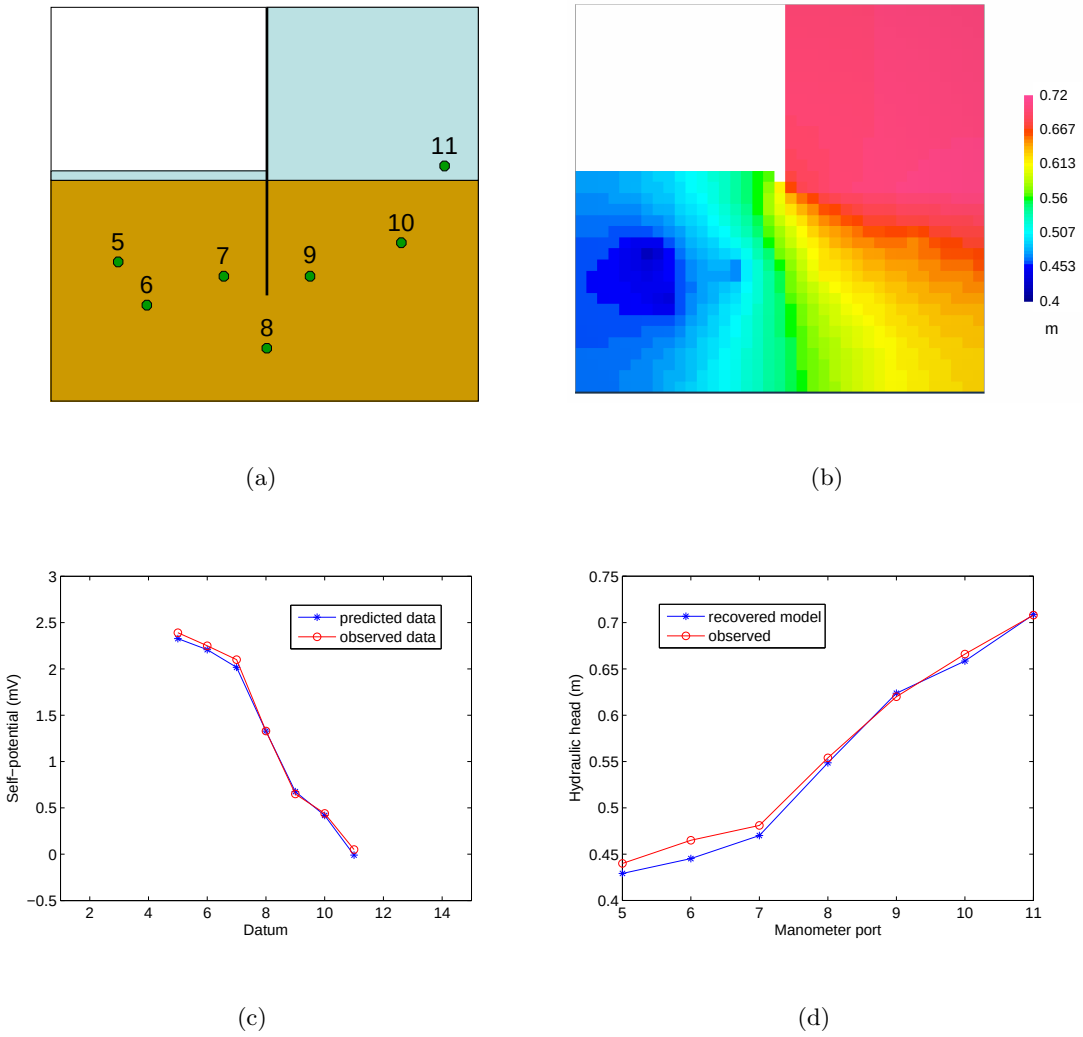

Figure 6.5: Cut-off wall model results - homogeneous subsurface approximation - subsurface data: a) observation locations; b) vertical cross-section of recovered head model; c) comparison of observed and predicted SP data at each measurement location; d) comparison of observed and recovered model head values in each manometer.

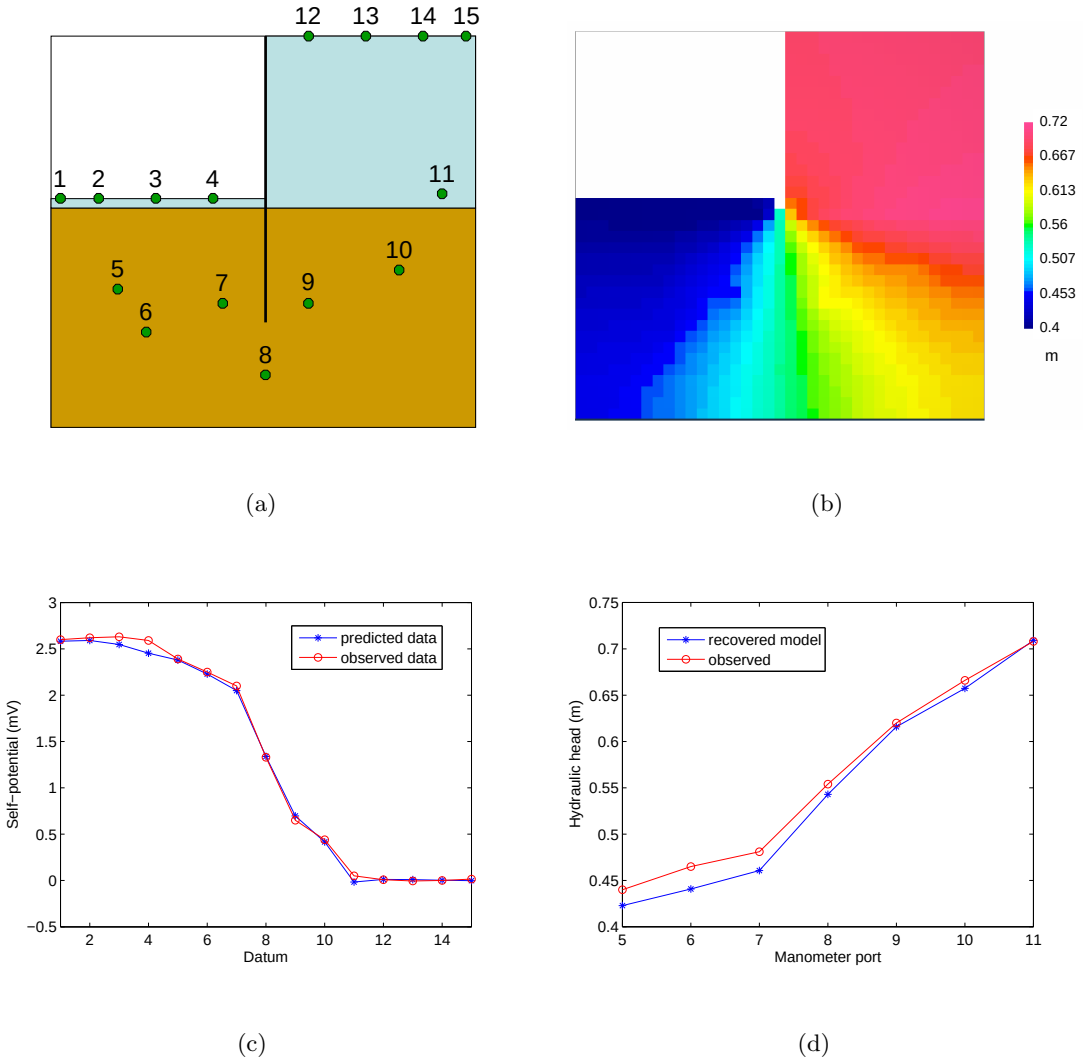

Figure 6.6: Cut-off wall model results - homogeneous subsurface approximation - all data: a) observation locations; b) vertical cross-section of recovered head model; c) comparison of observed and predicted SP data at each measurement location; d) comparison of observed and recovered model head values in each manometer.

6.4.4 Case 2: Heterogeneous subsurface approximation

We will now incorporate a priori information about the existence and depth of the cut-off wall. Without any prior information about the geometry of this structure, we assume a vertical barrier exhibiting the same electrical properties as the segment of the cut-off wall that exists above ground. In this instance, the material is acrylic and so we assume null values of cross-coupling conductivity and electrical conductivity in subsurface cells that represent the barrier, as illustrated in Figures 6.7(b) and (c). The chosen electrical properties of the barrier make this structure impervious to electrical current flow. However, by setting these cells active for the purposes of the inversion, as indicated in Figure 6.7(a), we are assuming that the wall is hydraulically pervious to some degree.

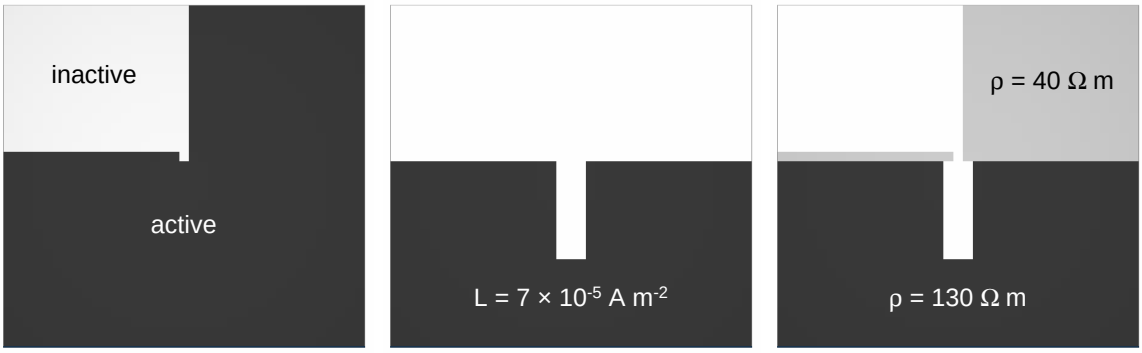

Figure 6.7: Cut-off wall model input - heterogeneous subsurface approximation: a) active model cells; b) cross-coupling conductivity distribution; c) electrical resistivity distribution.

Figures 6.8, 6.9 and 6.10 present the inversion results respectively for surface data, subsurface data, and the complete data set. The recovered models exhibit similar characteristics to those presented in Figures 6.4 to 6.6 for the homogeneous subsurface approximation. However, as in Case 1, the recovered model resulting from the inversion of subsurface data points is not consistent with those resulting from the inclusion of surface data. The lack of any significant head gradient across the known location of the wall suggests that the wall does not impede fluid flow, which we know not to be true.

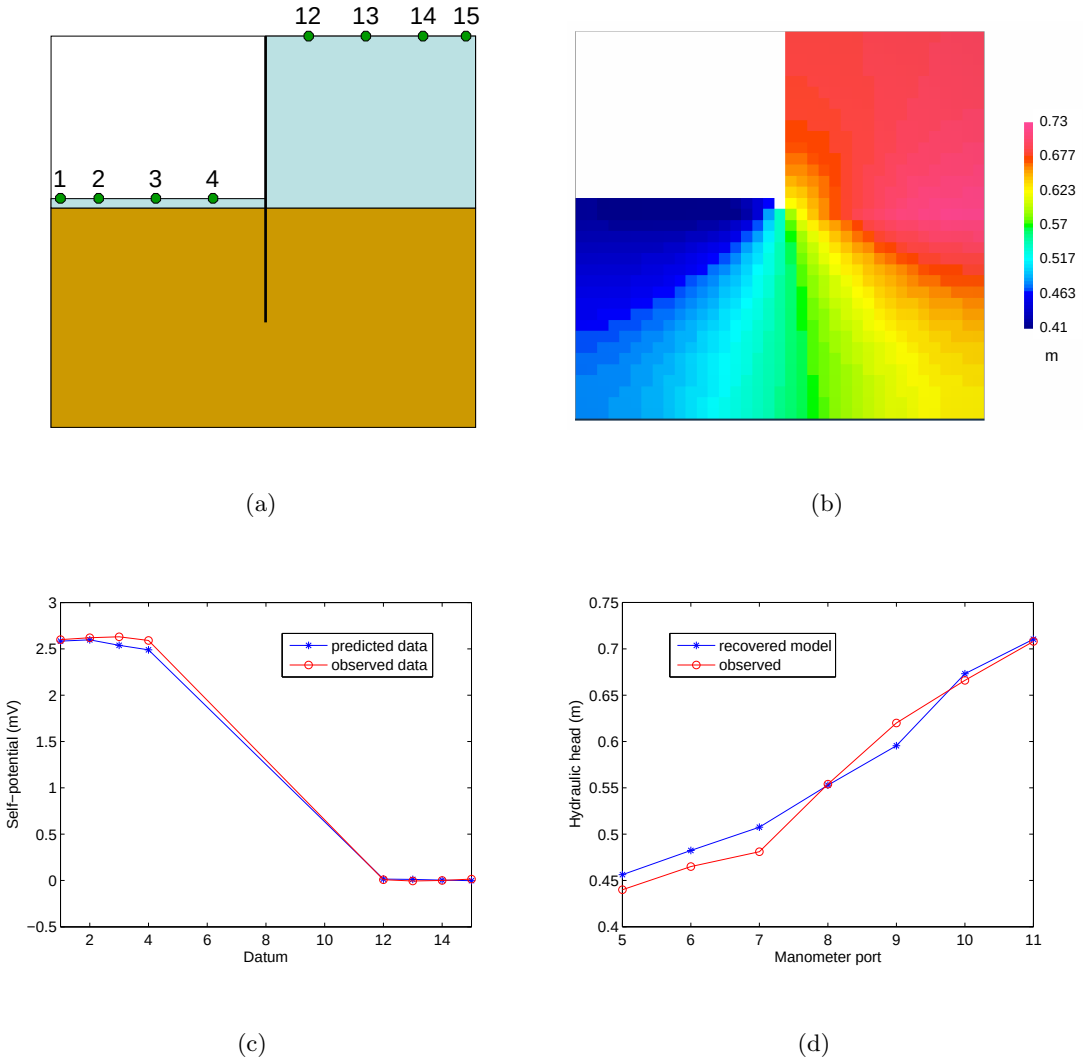

(a) (b)

(c) (d)

Figure 6.8: Cut-off wall model results - heterogeneous subsurface approximation - surface data: a) observation locations; b) vertical cross-section of recovered head model; c) comparison of observed and predicted SP data at each measurement location; d) comparison of observed and recovered model head values in each manometer.

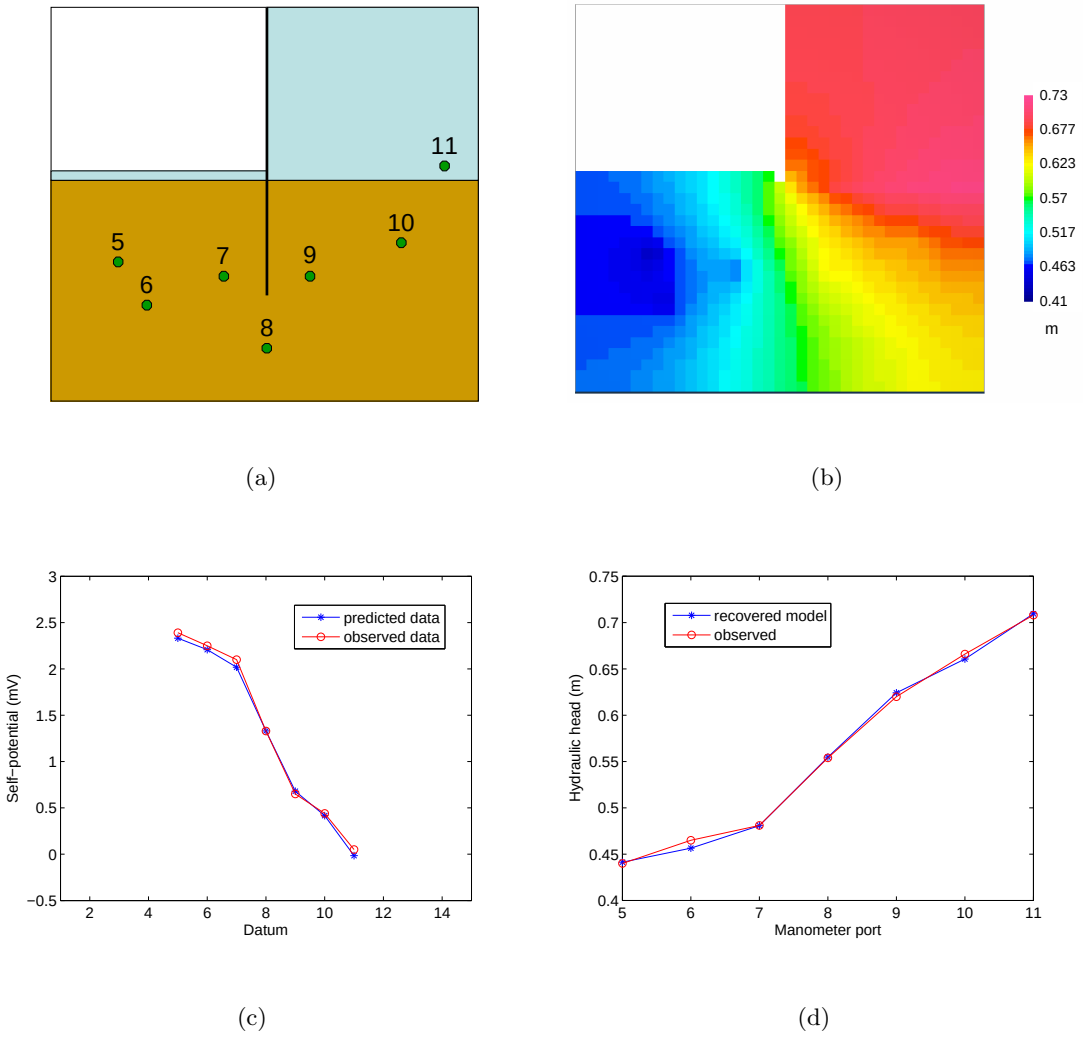

(a) (b)

(c) (d)

Figure 6.9: Cut-off wall model results - heterogeneous subsurface approximation - subsurface data: a) observation locations; b) vertical cross-section of recovered head model; c) comparison of observed and predicted SP data at each measurement location; d) comparison of observed and recovered model head values in each manometer.

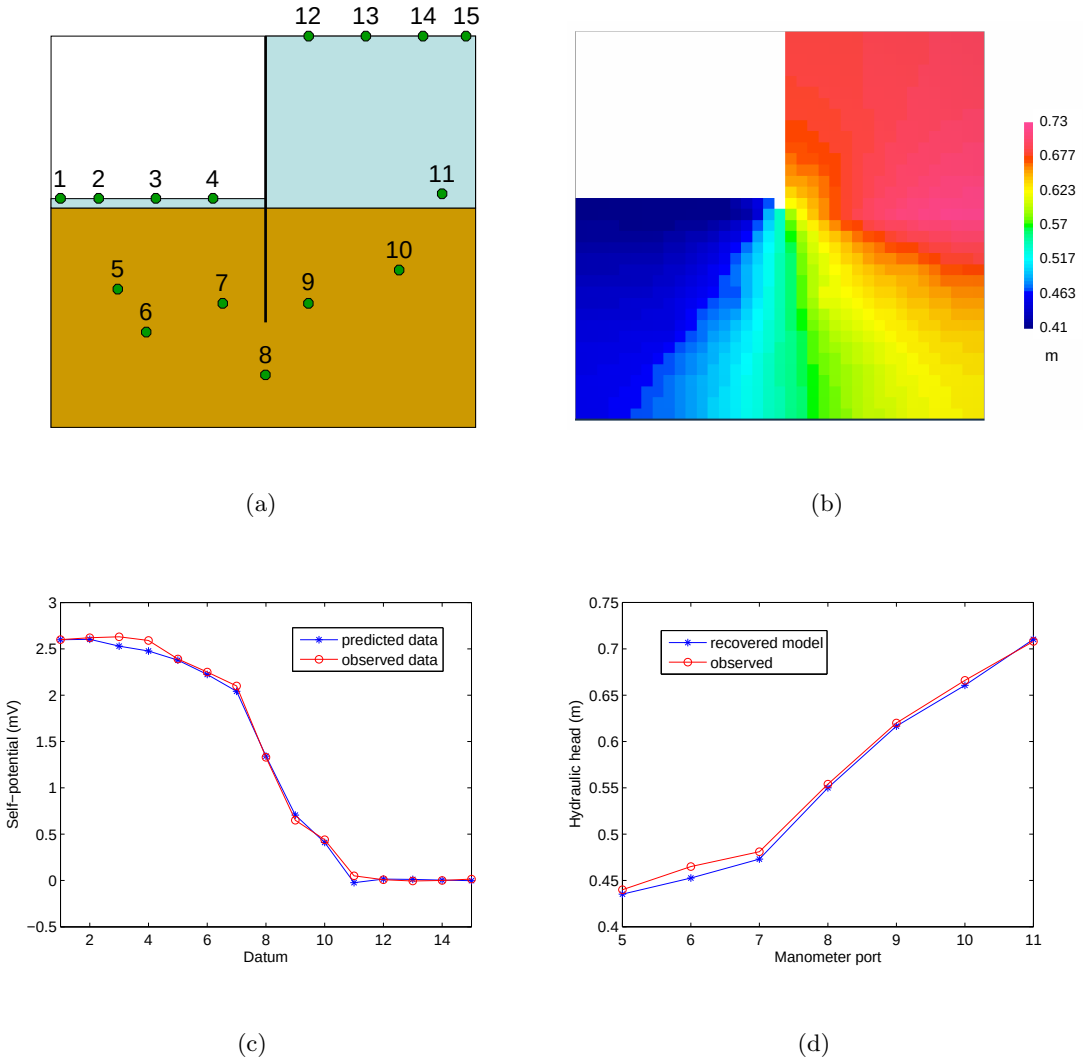

Figure 6.10: Cut-off wall model results - heterogeneous subsurface approximation - all data: a) observation locations; b) vertical cross-section of recovered head model; c) comparison of observed and predicted SP data at each measurement location; d) comparison of observed and recovered model head values in each manometer.

6.4.5 Case 3: Inactive wall approximation

If the cut-off wall acts as a ideal no-flow barrier below surface, then it is not physically realistic to solve for head in these grid cells. Consequently, we now set the wall cells as inactive for the purposes of the inversion, as shown in Figure 6.11(a). We choose to incorporate additional information about the geometry of the wall by specifying a wall thickness consistent with that observed above surface. In a field investigation, prior information about the geometry and material properties of the cut-off wall could be garnered from design drawings.

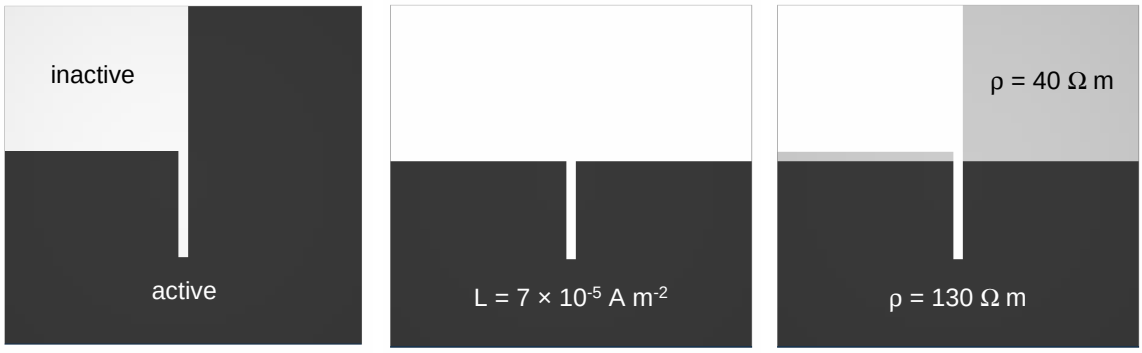

(a) (b) (c)

Figure 6.11: Cut-off wall model input - inactive wall approximation: a) active model cells; b) cross-coupling conductivity distribution; c) electrical resistivity distribution.

Figure 6.12 presents the inversion results obtained using surface data. The presence of the impervious cut-off wall imposes a no-flow boundary that is clearly represented in the recovered head distribution shown in Figure 6.12(b). Observed and recovered heads correlate well, but Figure 6.12(d) suggests that the recovered head model may exhibit a smaller dynamic range. The inversion of subsurface data and all data points shown in Figures 6.13 and 6.14 results in head models that are consistent with Figure 6.12(b). This gives confidence that the inactive wall approximation is a valid representation of the cut-off wall. However, the dynamic range of these models is over 2 cm smaller than the known head distribution. This suggests that including known head data may improve the solution.

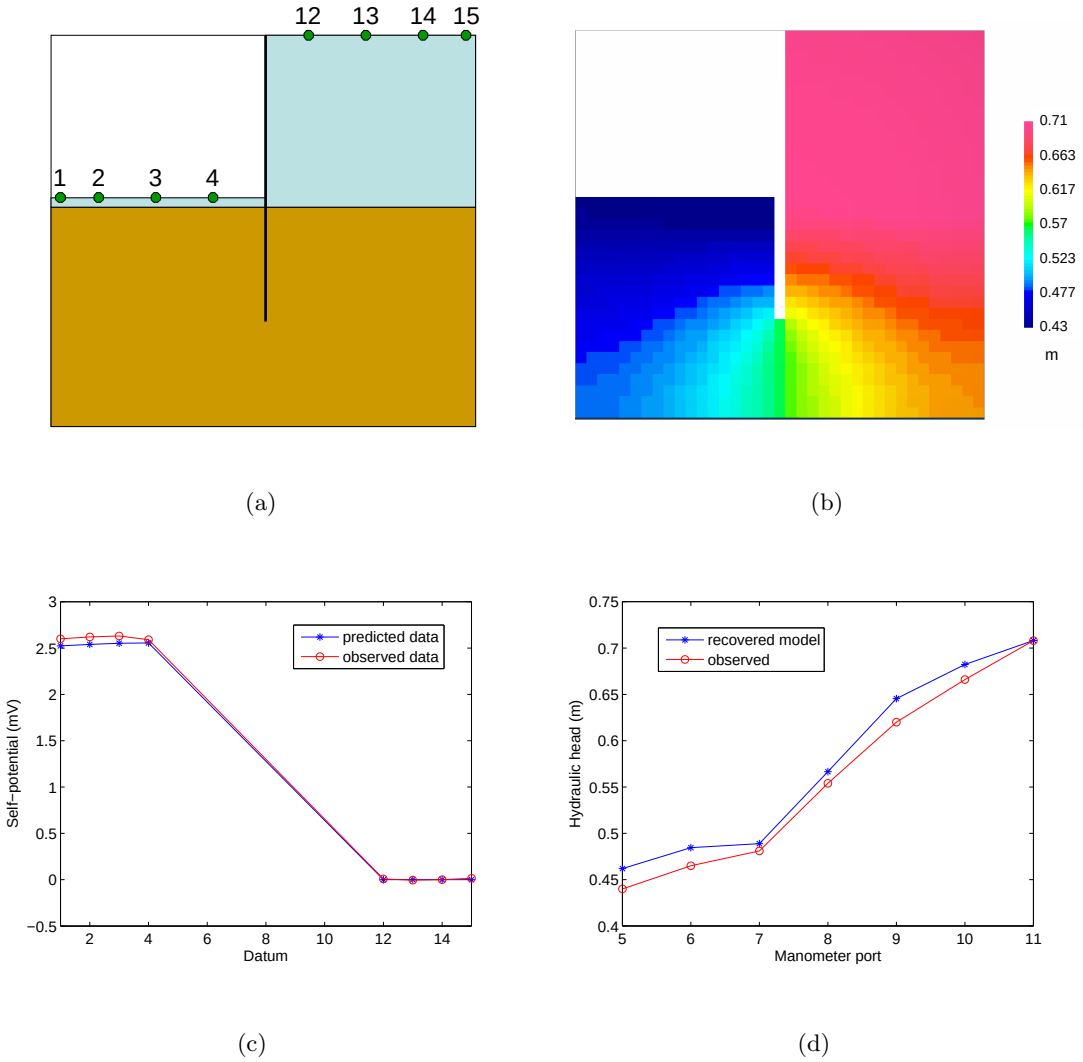

(a) (b)

(c) (d)

Figure 6.12: Cut-off wall model results - inactive wall approximation - surface data: a) observation locations; b) vertical cross-section of recovered head model; c) comparison of observed and predicted SP data at each measurement location; d) comparison of observed and recovered model head values in each manometer.

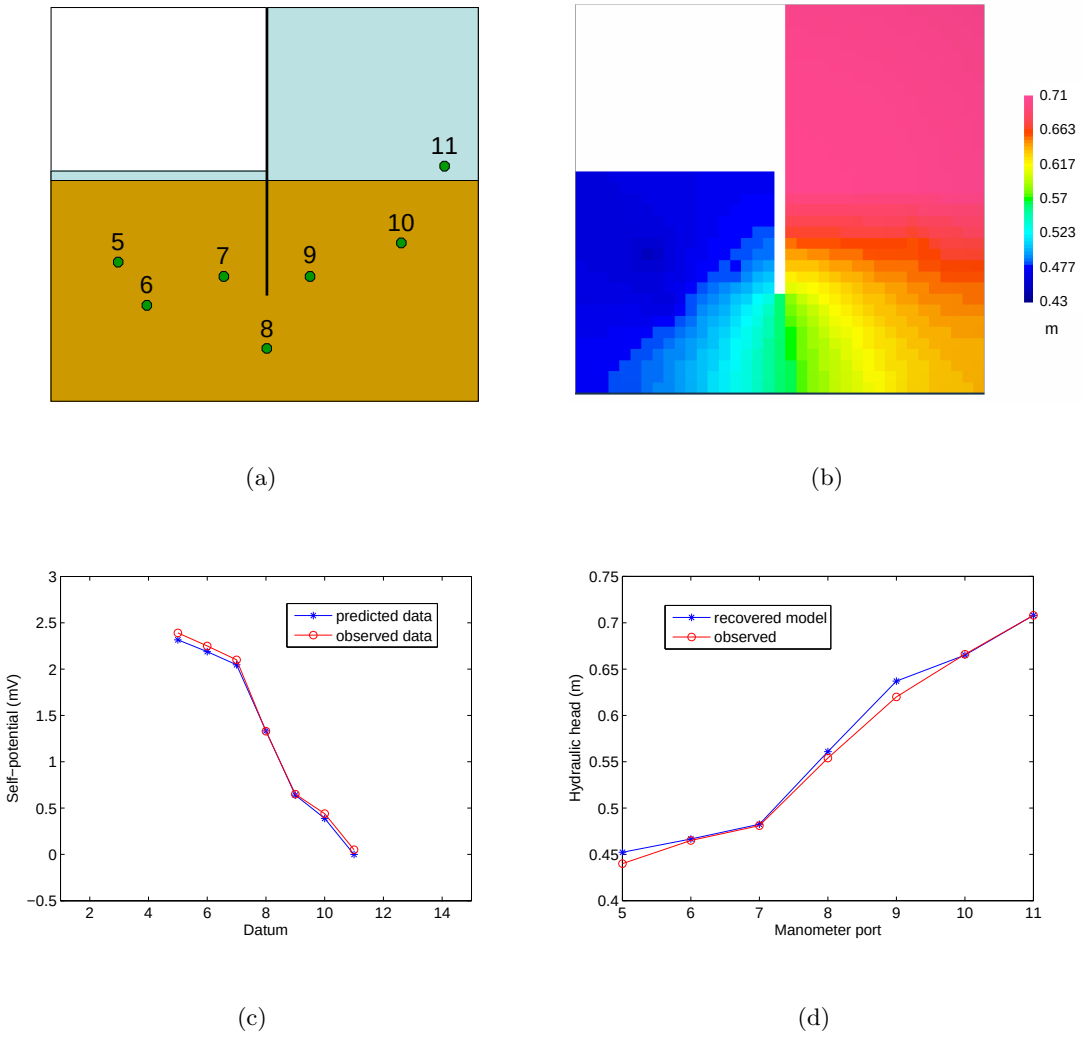

Figure 6.13: Cut-off wall model results - inactive wall approximation - subsurface data: a) observation locations; b) vertical cross-section of recovered head model; c) comparison of observed and predicted SP data at each measurement location; d) comparison of observed and recovered model head values in each manometer.

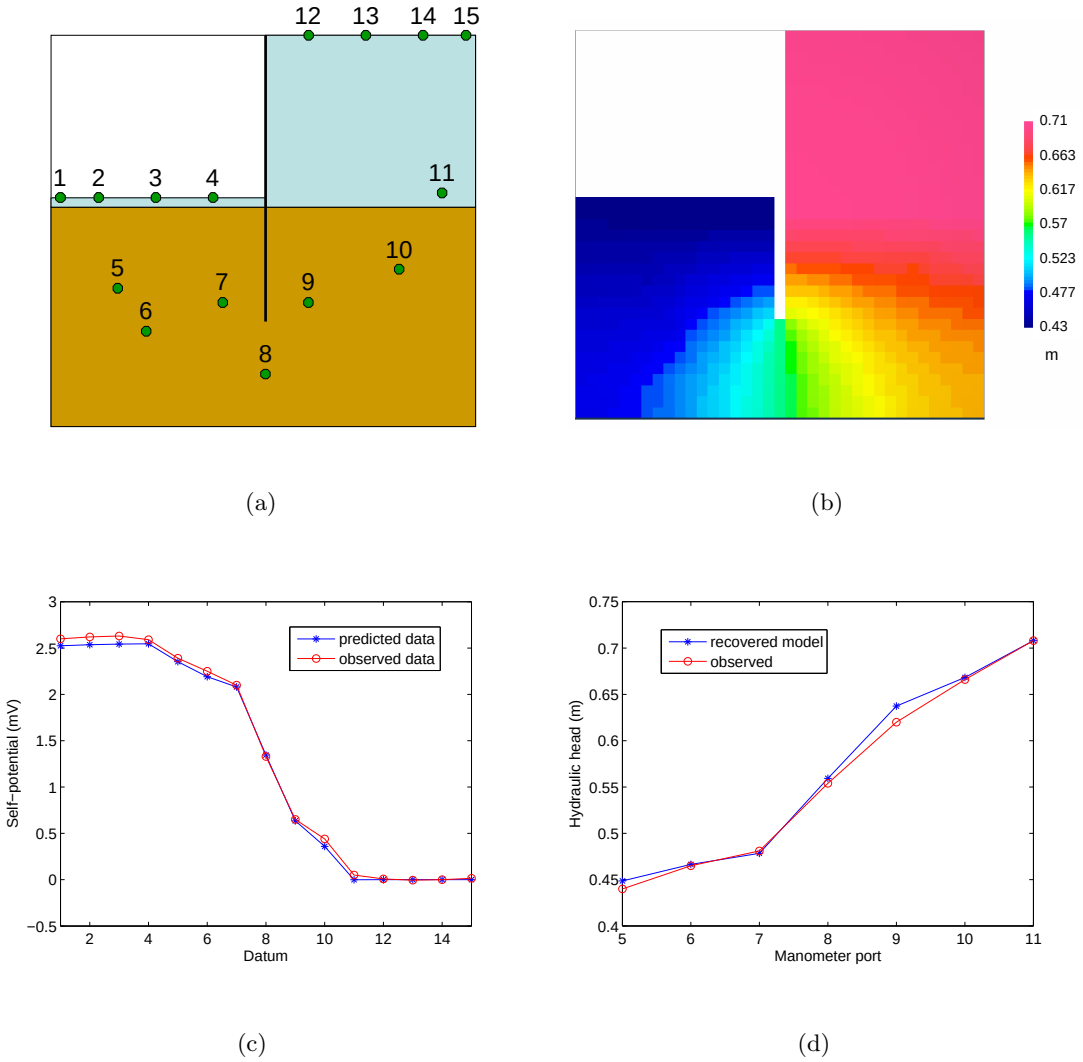

(a) (b)

(c) (d)

Figure 6.14: Cut-off wall model results - inactive wall approximation - all data: a) observation locations; b) vertical cross-section of recovered head model; c) comparison of observed and predicted SP data at each measurement location; d) comparison of observed and recovered model head values in each manometer.

6.4.6 Case 4: Incorporating known head values

The subsurface representation of the cut-off wall using inactive cells discussed in Section 6.4.5 significantly improves the inversion result. We now seek to further improve the solution by incorporating observed values of hydraulic head as a constraint.

The observed water levels in the upstream and downstream water columns were included in the reference model h_{ref}, as shown in Figure 6.15(a). In a field situation, these observations could be obtained from water depth measurements made from surface. In water cells, the relative weighting parameter w_s was set 4 orders of magnitude higher than in adjoining cells to encourage a close fit between the recovered and reference head values in the water columns.

Figure 6.16 presents the inversion results using surface data. The recovered model exhibits a very similar character to that shown in Figure 6.12(b), except that the dynamic range of head is consistent with that observed. This is evidenced by the close fit between observed and recovered head values, as shown in Figure 6.16(d). The combination of correct model geometry, stipulated reference head values at surface, and a lack of SP data at depth serve to limit the solution such that the SP surface data are essentially not required to recover a model that satisfies the constraints. A very small data misfit is achieved regardless of the chosen regularization parameter, as indicated in Table 6.1. This was not the case when the inversion was performed using subsurface data. Figures 6.17 and 6.18 respectively show the inversion results from subsurface and all data points. The recovered head models are nearly identical and similar to that obtained using surface data alone. The close fit between recovered and observed head values at manometer locations make 6.18(b) the preferred solution to represent the hydraulic head distribution around the cut-off wall.

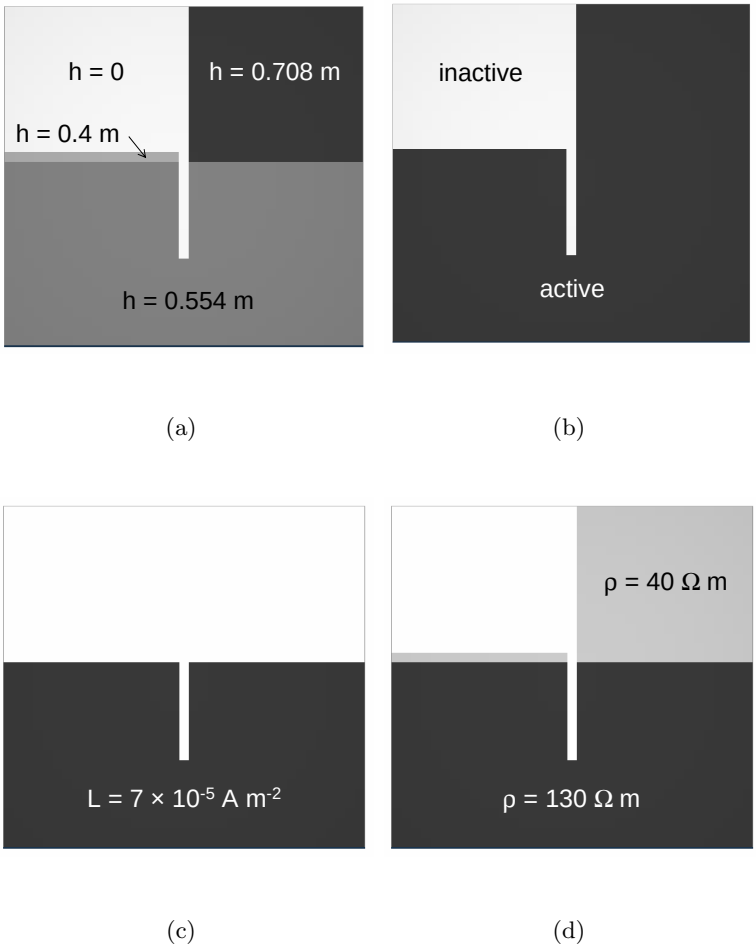

(a) (b)

(c) (d)

Figure 6.15: Cut-off wall model input - reference head in water column: a) reference hydraulic head model; b) active model cells; c) cross-coupling conductivity distribution; d) electrical resistivity distribution.

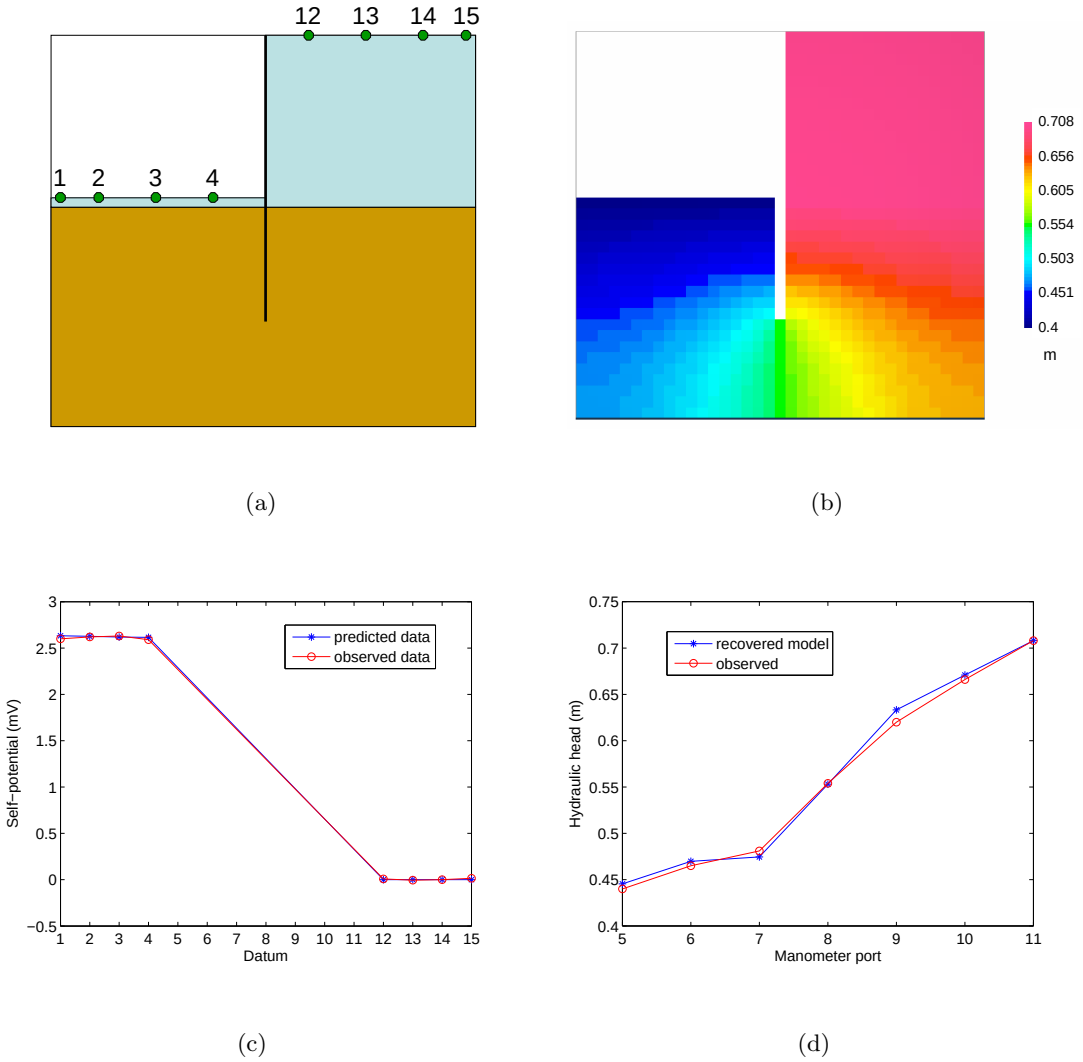

(a) (b)

(c) (d)

Figure 6.16: Cut-off wall model results - reference head in water column - surface data: a) observation locations; b) vertical cross-section of recovered head model; c) comparison of observed and predicted SP data at each measurement location; d) comparison of observed and recovered model head values in each manometer.

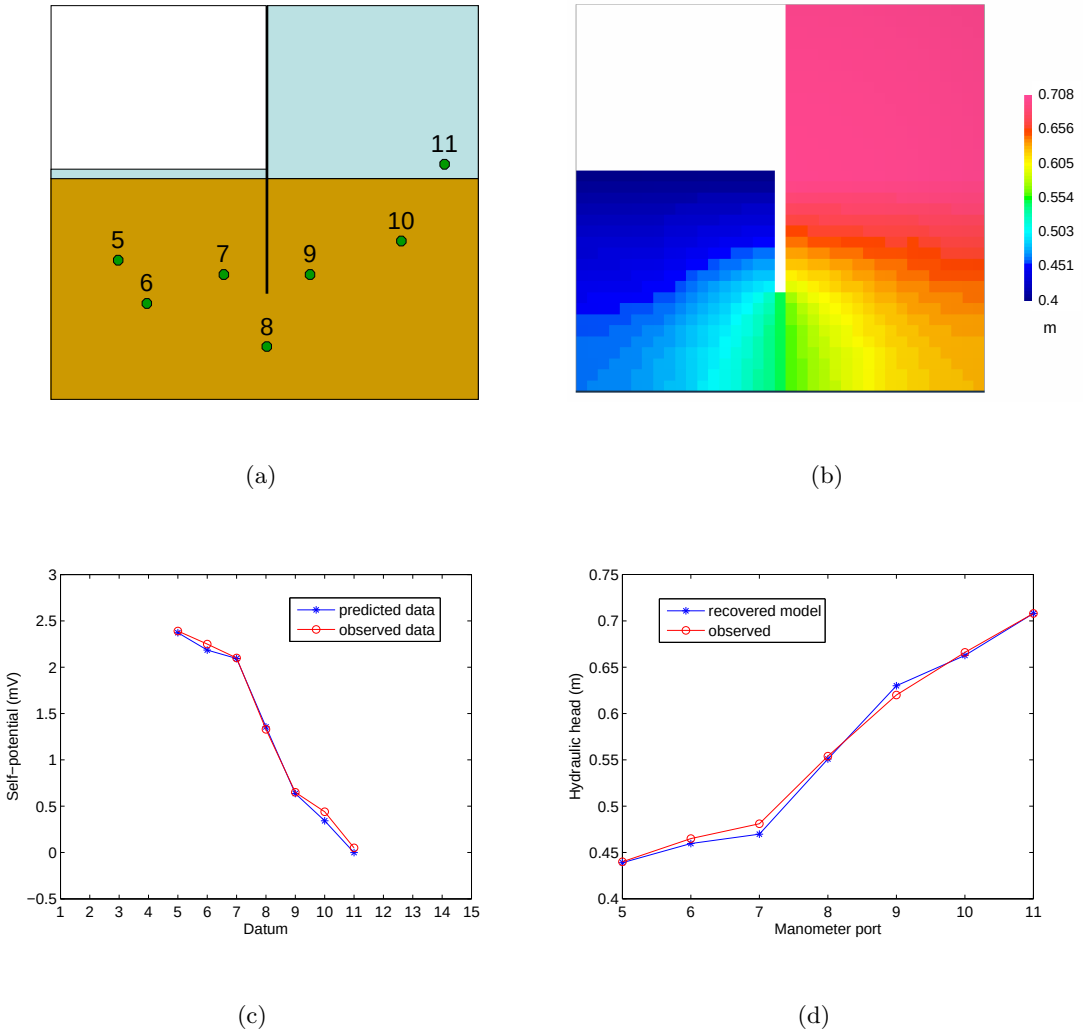

Figure 6.17: Cut-off wall model results - reference head in water column - subsurface data: a) observation locations; b) vertical cross-section of recovered head model; c) comparison of observed and predicted SP data at each measurement location; d) comparison of observed and recovered model head values in each manometer.

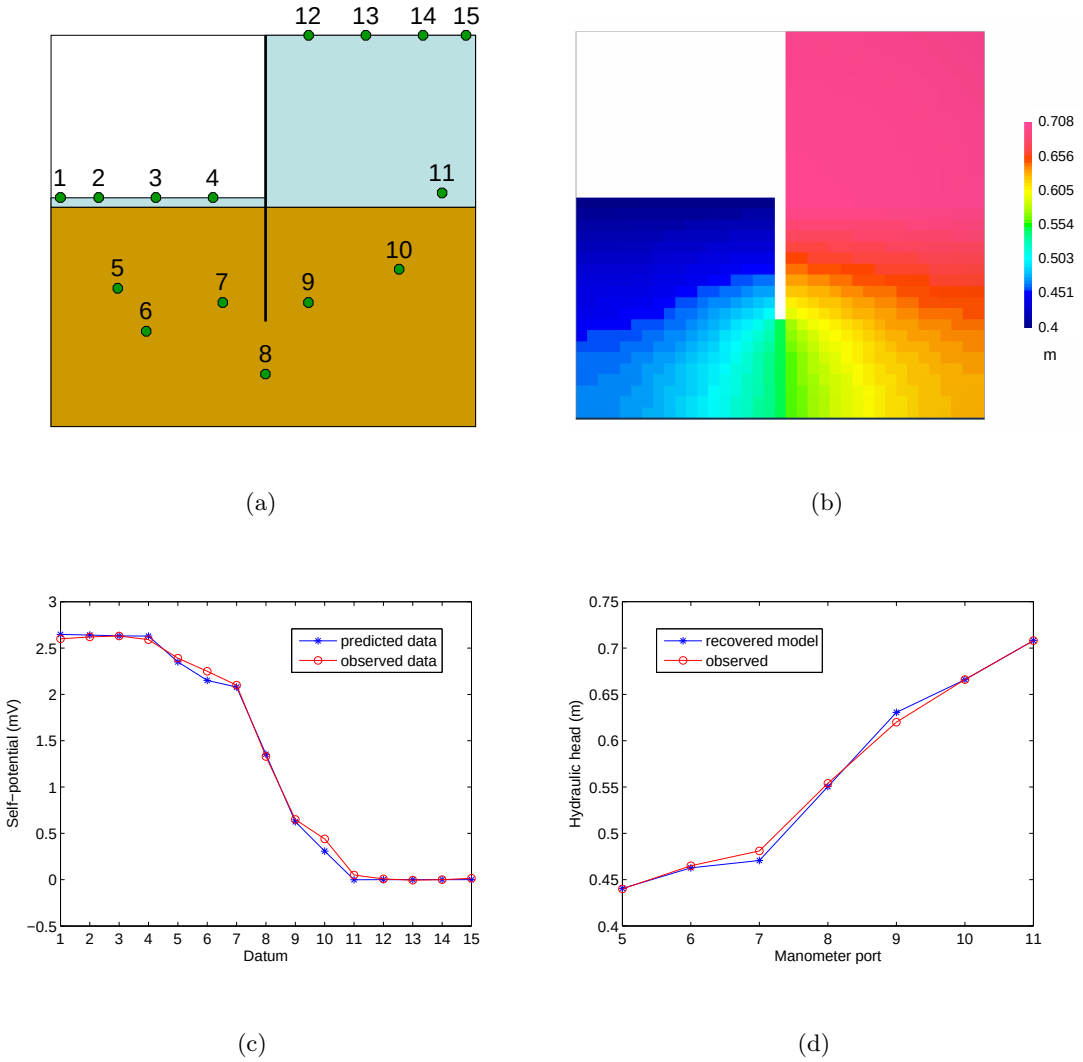

Figure 6.18: Cut-off wall model results - reference head in water column - all data: a) observation locations; b) vertical cross-section of recovered head model; c) comparison of observed and predicted SP data at each measurement location; d) comparison of observed and recovered model head values in each manometer.

6.5 Conclusion

We have developed an inversion method that recovers a 3-D model of hydraulic head from measured self-potential data in systems where streaming potential is the dominant signal. Our approach permits an interpretation of subsurface flow patterns directly from the geophysical data. The recovered hydraulic head model may be studied on its own to identify subsurface flow patterns, or used as input to a subsequent inversion to recover other hydraulic parameters, such as hydraulic conductivity.

The inverse problem was formulated as an unconstrained optimization in which we minimize a model objective function subject to fitting the measured data. This approach enables us to cope with the inherent non-uniqueness of the underdetermined problem. The ability to account for heterogeneous cross-coupling conductivity and electrical conductivity distributions was included as these can impact the quality of the solution. The model objective function was designed to allow the inclusion of prior information about the nature of the hydraulic head distribution and observed head values by means of a reference model and 3-D weighting functions. This additional information can help to constrain the solution and improve the quality of the recovered model.

The inversion algorithm was successfully applied to study flow under a cut-off wall in a laboratory tank model, where the recovered head distribution was found to be consistent with observed head values. This example served to illustrate how prior information is incorporated into the inverse problem and how it can improve the solution.

6.6 References

Abdelrahman, E. M., and S. M. Sharafeldin, A least-squares approach to depth determination from self-potential anomalies caused by horizontal cylinders and spheres, *Geophysics*, *62*(1), 44–48, 1997.

Archie, G. E., The electrical resistivity log as an aid in determining some reservoir characteristics, *Transactions of the Society of Petroleum Engineers of the American Institute of Mining, Metallurgical and Petroleum Engineers (AIME)*, *146*, 54–67, 1942.

Atchuta Rao, D., and H. V. Ram Babu, Quantitative interpretation of self-potential anomalies due to two-dimensional sheet-like bodies, *Geophysics*, *48*(12), 1659–1664, 1983.

Bhattacharya, B. B., and N. Roy, A note on the use of a nomogram for self-potential anomalies, *Geophysical Prospecting*, *29*, 102–107, 1981.

Birch, F. S., Imaging the water table by filtering self-potential profiles, *Ground Water*, *36*(5), 779–782, 1998.

Darnet, M., G. Marquis, and P. Sailhac, Estimating aquifer hydraulic properties from the inversion of surface Streaming Potential (SP) anomalies, *Geophysical Research Letters*, *30*(13), 1679, doi:10.1029/2003GL017631, 2003.

de Witte, L., A new method of interpretation of self-potential field data, *Geophysics*, *13*(4), 600–608, 1948.

Di Maio, R., and D. Patella, Self-potential anomaly in volcanic areas: The Mt. Etna case history, *Acta Vulcanologica*, *4*, 119–124, 1994.

Fitterman, D. V., Electrokinetic and magnetic anomalies associated with dilatant regions in a layered earth, *Journal of Geophysical Research*, *83*(B12), 5923–5928, 1978.

Fitterman, D. V., and R. F. Corwin, Inversion of self-potential data from the Cerro Prieto geothermal field, Mexico, *Geophysics*, *47*(6), 938–945, 1982.

Fournier, C., Spontaneous potentials and resistivity surveys applied to hydrogeology in a volcanic area: Case history of the Chaîne des Puys (Puy-de-Dôme, France), *Geophysical Prospecting*, *37*, 647–668, 1989.

Guichet, X., L. Jouniaux, and J. P. Pozzi, Streaming potential of a sand column in partial saturation conditions, *Journal of Geophysical Research*, *108*(B3), 2141, doi: 10.1029/2001JB001517, 2003.

Hämmann, M., H. R. Maurer, A. G. Green, and H. Horstmeyer, Self-potential image reconstruction: Capabilities and limitations, *Journal of Environmental and Engineering Geophysics*, *2*(1), 21–35, 1997.

Ishido, T., and H. Mizutani, Experimental and theoretical basis of electrokinetic phenomena in rock-water systems and its application to geophysics, *Journal of Geophysical Research*, *86*(B3), 1763–1775, 1981.

Jouniaux, L., and J. P. Pozzi, Streaming potential and permeability of saturated sandstones under triaxial stress: Consequences for electrotelluric anomalies prior to earthquakes, *Journal of Geophysical Research*, *100*(B6), 10,197–10,209, 1995.

Minsley, B. J., J. Sogade, and F. D. Morgan, Three-dimensional source inversion of self-potential data, *Journal of Geophysical Research*, *112*, B02202, doi:10.1029/2006JB004262, 2007.

Moore, J. R., S. D. Glaser, H. F. Morrison, and G. M. Hoversten, The streaming potential of liquid carbon dioxide in Berea sandstone, *Geophysical Research Letters*, *31*, L17610, doi:10.1029/2004GL020774, 2004.

Morgan, F. D., E. R. Williams, and T. R. Madden, Streaming potential properties of Westerly granite with applications, *Journal of Geophysical Research*, *94*(B9), 12,449–12,461, 1989.

Nourbehecht, B., Irreversible thermodynamic effects in inhomogeneous media and their applications in certain geoelectric problems, Ph.D. thesis, Massachusetts Institute of Technology, Cambridge, 1963.

Onsager, L., Reciprocal relations in irreversible processes, I, *Physical Review*, *37*, 405–426, 1931.

Overbeek, J. T. G., Electrokinetic phenomena, in *Colloid Science*, *Irreversible Systems*, vol. 1, edited by H. R. Kruyt, Elsevier Publishing Company, Amsterdam, 1952.

Patella, D., Introduction to ground surface self-potential tomography, *Geophysical Prospecting*, *45*(4), 653–681, 1997.

Paul, M. K., Direct interpretation of self-potential anomalies caused by inclined sheets of infinite horizontal extensions, *Geophysics*, *30*(3), 418–423, 1965.

Revil, A., and A. Cerepi, Streaming potentials in two-phase flow conditions, *Geophysical Research Letters*, *31*, L11605, doi:10.1029/2004GL020140, 2004.

Revil, A., V. Naudet, J. Nouzaret, and M. Pessel, Principles of electrography applied to self-potential electrokinetic sources and hydrogeological applications, *Water Resources Research*, *39*(5), 1114, doi:10.1029/2001WR000916, 2003.

Revil, A., V. Naudet, and J. D. Meunier, The hydroelectric problem of porous rocks: Inversion of the position of the water table from self-potential data, *Geophysical Journal International*, *159*, 435–444, 2004.

Sailhac, P., and G. Marquis, Analytic potentials for the forward and inverse modeling of SP anomalies caused by subsurface flow, *Geophysical Research Letters*, *28*(9), 1851–1854, 2001.

Sheffer, M. R., and D. W. Oldenburg, Three-dimensional forward modelling of streaming potential, *Geophysical Journal International*, *169*, 839–848, doi:10.1111/j.1365-246X.2007.03397.x, 2007.

Sheffer, M. R., J. A. Howie, and P. M. Reppert, Laboratory measurements of the streaming potential coupling coefficient and resistivity in well-graded soils, 2007.

Shi, W., Advanced modeling and inversion techniques for three-dimensional geoelectrical surveys, Ph.D. thesis, Massachusetts Institute of Technology, Cambridge, 1998.

Sill, W. R., Self-potential modeling from primary flows, *Geophysics*, *48*(1), 76–86, 1983.

Yüngül, S., Interpretation of spontaneous polarization anomalies caused by spheroidal orebodies, *Geophysics*, *15*(2), 237–246, 1950.

Chapter 7

Conclusion

The main objective of the research presented in this thesis was to investigate what useful information about hydraulic parameters and embankment integrity could be garnered from self-potential data in systems where streaming potential is the driving mechanism. This objective was fulfilled through the development and application of forward and inverse modelling algorithms, and a laboratory investigation of the electrical properties that govern the streaming potential phenomenon. Figure 7.1 highlights the key contributions of the thesis research and illustrates how they combine to advance the current state of self-potential data interpretation. The motivation for this work stems from the application to embankment dam seepage monitoring and detection, which demands a quantitative interpretation of hydraulic parameters from the geophysical data.

A three-dimensional forward modelling algorithm was developed using a coupled flow model of streaming potential to study variably saturated flow problems of complicated geometry. This approach is necessary for the study of practical embankment seepage problems. The forward model enables us to study the self-potential response to a given seepage regime, and serves as a basis for the inverse problem.

The practical interpretation of measured SP data requires an inverse methodology. An inversion algorithm was developed to recover a three-dimensional distribution of hydraulic head from self-potential data. This was the first documentation of such an approach, and it enables us to extract pertinent hydraulic information from the geophysical data. The recovered head model may be used on its own to interpret flow patterns, or used as input to another inversion routine to recover other hydraulic parameters such as hydraulic conductivity or flow rate.

Realistic estimates of the electrical properties are required for an effective SP data interpretation using the numerical modelling techniques. A lack of available data on the

electrical properties of soils prompted a laboratory study to measure these parameters. A new laboratory apparatus was designed and developed to perform measurements of the streaming potential coupling coefficient C and electrical resistivity ρ on the same specimen in order to characterize the streaming current cross-coupling coefficient L for well-graded soils. This apparatus was used in a laboratory investigation to study the influence of soil and fluid properties on L and to characterize this property for typical embankment soils. The results of this investigation showed that L does not vary considerably for typical geologic materials. This suggests that we may not have to characterize L with the same rigor as ρ at a given site when interpretating SP data using the forward and inverse modelling techniques.

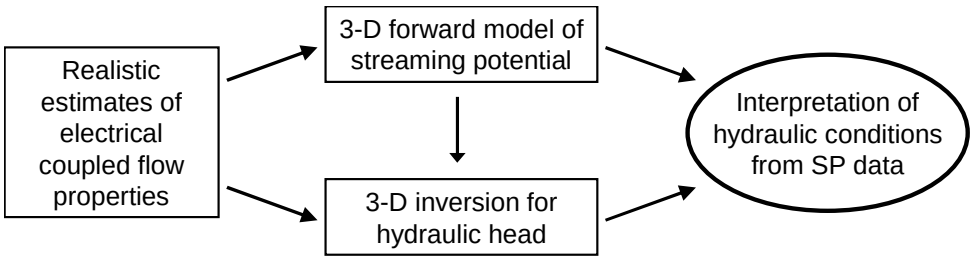

Figure 7.1: Key contributions to the quantitative interpretation of hydraulic conditions from SP data.

The following sections discuss the practical contributions of the research to SP survey design and data interpretation, and comment on areas of future work, with specific focus on the study of embankment dams.

7.1 Practical contributions

7.1.1 Survey design

Self-potential surveys can be conducted as single or repeat surveys, where a field crew is deployed to re-occupy survey stations, or in an automated monitoring framework using a permanently-installed array of electrodes. Practical field survey design for single or repeat surveys is often guided by soil conditions and access on the upstream and downstream faces

of the dam. Most often, the dam crest offers the easiest access for SP data collection. However, as shown by the examples in Chapters 2 and 5, SP data at the crest often show the least amount of variation in response to changing hydraulic conditions. The results of Chapter 5 showed that SP measurements at depth are most favourable for detecting small variations in seepage patterns caused by internal erosion. However, the specific hydraulic boundary conditions, structure and physical properties will dictate the seepage regime and resulting SP distribution at a given site.

Effective placement of electrodes in the design of a field survey or monitoring network will maximize the ability of the method to detect changes that are of particular interest. A mathematical description of primary and secondary sources of charge was derived in Chapter 2 to facilitate a conceptual understanding of the polarity and accumulation pattern of charge caused by fluid flow and physical property boundaries in the subsurface. This equation can be used to give a first pass estimate of the polarity and distribution of charge for a given system in a practical field setting. The forward modelling algorithm enables a thorough examination of the self-potential distribution resulting from a comprehensive seepage analysis in 3-D. This code can be used to evaluate the suitability of self-potential measurements for a given site, and to design optimum electrode placement and survey configurations.

7.1.2 SP data interpretation

The forward and inverse modelling routines developed in Chapters 2 and 6 can be applied to interpret hydraulic conditions from SP data, given some knowledge of the structure and electrical properties of the subsurface.

The cross-coupling coefficient is a fundamental parameter required in numerical modelling, which had not been studied previously for well-graded soils. The results of the laboratory investigation described in Chapter 4 concluded that the streaming current cross-coupling coefficient does not vary over a wide range based on the results of testing and published data in the literature. However, a limited number of soil types were studied and the reported values and trends may not apply to every site. The lab apparatus and testing methods described in Chapter 3 and documented in detail in a report by *Sheffer*

[2005] provide both guidance and a means with which to measure the streaming current cross-coupling coefficient. If laboratory measurements are not possible, theoretical relations may be used to estimate values of L. Special considerations for the practical application of theoretical estimates, particularly in resistive environments, are discussed in Chapter 4.

The interpretation of SP data acquired from a conventional survey provides a snapshot of hydraulic conditions, and is most useful for characterizing global or background seepage conditions at a given site. A comparison of data acquired from repeat surveys can help to identify seepage-related anomalies. However, the interpretation of SP anomalies from data acquired in a conventional survey at an embankment site can be very challenging. The surface expression of SP anomalies caused by preferential seepage within the dam may be very small, as suggested by the results of Chapter 5. Noise in the data can further hinder detection. Furthermore, it is difficult to characterize and assign physical property distributions that reflect actual conditions. Fluctuations in the reservoir level lead to transient hydraulic conditions within the core of the embankment. Seasonal variations in temperature and reservoir properties can lead to variations in the electrical properties. The boundary conditions at the time of a conventional survey may not reflect current conditions inside the dam.

These difficulties suggest that a monitoring approach to SP data collection and interpretation is required. Chapter 5 illustrated that the localized hydraulic head and SP responses to the development of a pervious defect peak prior to any detectable increase in seepage flow from the dam body. This suggests that SP electrodes installed in conjunction with or in place of piezometers could support or provide evidence of a problem prior to failure of the core. This is one example of how SP measurements could be integrated into a dam seepage monitoring system. Long-term monitoring affords an increased sensitivity to the development of localized gradients caused by internal erosion, since temporal changes can be tracked more effectively. Deviations from an established background response can then be evaluated using numerical methods to determine their hydraulic significance. Acquiring data in a monitoring framework also affords the opportunity to study the temporal SP response to transient hydraulic behaviour and seasonal variations, and to determine whether these factors assist or hinder the detection of anomalous behaviour.

The simplest means of interpreting SP data acquired from a monitoring network would be to track the SP signals with time, much like pressure measurements are typically monitored. A range of variation typical of normal operating conditions could be established from observations over time and predictive modelling. A steady deviation in the SP signal level outside of this normal range would then trigger a warning that conditions inside the dam may be changing.

A more comprehensive picture of changing hydraulic conditions could be obtained by integrating inverse modelling into the interpretation methodology. Recovered head models from successive inversions could be used to identify areas where localized gradients may be developing. These models could be used to evaluate the location and severity of the anomalous region in conjunction with other investigative tools.

7.2 Future work

The ultimate goal of this research is to investigate how SP measurements can be incorporated into an embankment dam seepage monitoring and detection methodology to extract pertinent information about hydraulic conditions. A first step is to interpret an SP data set to infer the hydraulic conditions within an embankment. Of particular interest is the application of the inversion algorithm to a field-scale problem.

A sensitivity analysis must be conducted using the inversion algorithm to evaluate the influence of the prescribed electrical property distributions on the recovered hydraulic head model. The sensitivity of the solution to the electrical conductivity and the cross-coupling conductivity, in particular, will determine how much effort should be put towards characterizing these properties.

The main challenge limiting the development of SP interpretation strategies in embankment dam problems is a lack of comprehensive field data sets. Conventional surveys have been performed at a number of sites, but to date SP monitoring has only been performed on a handful of sites using a single line array of electrodes along the crest. This suggests a strong need for carefully designed, site-specific monitoring array installations to establish baseline readings and enable further research into the effectiveness of SP for dam seepage

applications.

The capability of the SP method to detect small streaming potential signals is governed in a large part by the measurement sensitivity. An evaluation of SP field data acquisition and processing methods must be performed to determine if improvements can be made to reduce noise levels in the data, particularly for monitoring applications.

The contribution of the unsaturated flow component to the measured SP signal may be significant in certain problems. Consequently, it is of interest to examine how best to incorporate this flow contribution in the forward modelling algorithm by assigning values of L as a function of saturation. In the inverse problem, allowing the electrical properties to vary with saturation renders the problem non-linear. The benefit of solving the non-linear problem would have to be evaluated following further application of the linear algorithm.

In some cases, streaming potential may not be the sole source mechanism, as is assumed in the present research, and other sources will have to be accounted for. External sources of current, due to cathodic protection devices or other infrastructure, will have a significant effect on measured SP data and should be stopped or minimized prior to data collection. Other natural source mechanisms are a function of mineralogy, fluid properties and site conditions. Consequently, the relative importance of each mechanism must be weighed on a site-by-site basis. Since the measured SP signal results from the superposition of sources in the subsurface, other source mechanisms could be studied by removing the streaming potential component from the data, assuming the primary flows are decoupled. The forward modelling algorithm can be used to predict the streaming potential component or other individual coupled flow mechanisms to aid in the interpretation.

Temperature and resistivity measurements have been implemented to monitor and detect anomalous seepage in embankments [*Johansson and Dahlin*, 1996; *Sjödahl*, 2006; *Johansson*, 1997]. Estimates of anomalous seepage flow rates may be interpreted from temperature data, temporal variations in the electrical resistivity of the core may be interpreted from the inversion of resistivity data, and the current research showed that hydraulic head may be interpreted from the inversion of self-potential data. It is of great interest to investigate the joint interpretation of these data to give a more comprehensive picture of subsurface conditions.

7.3 References

Johansson, S., Seepage monitoring in embankment dams, Ph.D. thesis, Royal Institute of Technology, Sweden, 1997.

Johansson, S., and T. Dahlin, Seepage monitoring in an earth embankment dam by repeated resistivity measurements, *European Journal of Environmental and Engineering Geophysics*, *1*, 229–247, 1996.

Sheffer, M. R., Investigation of geophysical methods for assessing seepage and internal erosion in embankment dams: Laboratory testing of the streaming potential phenomenon in soils, *Tech. rep.*, Canadian Electricity Association Technologies Inc. (CEATI), Report T992700-0205B/2, Montreal, 2005.

Sjödahl, P., Resistivity investigation and monitoring for detection of internal erosion and anomalous seepage in embankment dams, Ph.D. thesis, Lund University, Sweden, 2006.

Appendix A

Discrete approximation using the finite-volume method

Poisson's equation for the self-potential distribution with no imposed external sources of current flow is defined as:

$$\nabla \cdot \sigma \nabla \phi = -\nabla \cdot L \nabla h \; . \tag{A.1}$$

To avoid having to evaluate the derivative of conductivity at discontinuous boundaries, we restate (A.1) as two first-order equations with unknown variables $\boldsymbol{J}$ and ϕ:

$$\nabla \cdot \boldsymbol{J} = f \tag{A.2}$$

and

$$\sigma^{-1} \boldsymbol{J} - \nabla \phi = 0 \; , \tag{A.3}$$

where $\boldsymbol{J}$ is the conduction current density. The source term f describes sources of streaming current:

$$f = -\nabla \cdot L \nabla h \; . \tag{A.4}$$

The weak forms of (A.2) and (A.3) are:

$$\int_V (\nabla \cdot \boldsymbol{J}) \; dV = \int_V f \; dV, \tag{A.5}$$

and

$$\int_V (\sigma^{-1} \boldsymbol{J} - \nabla \phi) \; dV = 0. \tag{A.6}$$

The discrete forms of (A.5) and (A.6) are derived using a cell-centred finite-volume method on a staggered grid. The self-potential ϕ is defined at cell centres, with normal components of current density $\boldsymbol{J}$ defined at cell faces, as shown in Figure A.1.

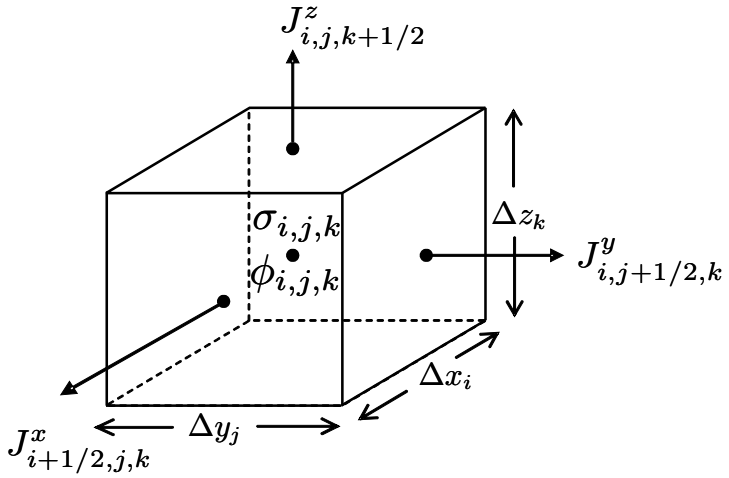

Figure A.1: Discrete grid cell showing cell dimensions, location of components of current density **J** at cell faces, and location of potential ϕ and conductivity σ at the cell centre.

The 3-D volume is divided into rectangular cells with nx rows, ny columns and nz layers respectively in the x, y and z directions. Each cell is defined by the coordinate at its centre (x_i, y_j, z_k), where the position of cell boundaries in each dimension are denoted as $\{x_{i-1/2} \quad x_{i+1/2}\}, \{y_{j-1/2} \quad y_{j+1/2}\}$ and $\{z_{k-1/2} \quad z_{k+1/2}\}$. The length of the cell in each dimension is denoted as $\Delta x_i, \Delta y_j$ and Δz_k, respectively. This arrangement corresponds to $nx * ny * nz$ cells with a total of $(nx+1)(ny+1)(nz+1)$ cell faces. Consequently, quantities may be identified by their location in terms of grid coordinates (e.g. $\phi_{i,j,k}$, $J^y_{i,j-1/2,k}$).

To solve (A.5) and (A.6) on the staggered grid, values of σ and L must be determined at cell faces. Integrating (A.6) over a cell volume shows that it is the harmonic average of conductivity that is needed. This is also consistent with our physical understanding that the overall conductivity of two conductors in series is quantified by their harmonic average.

A.1 Discrete approximation of equation (A.5)

Invoking the divergence theorem, (A.5) becomes

$$\oint_S \boldsymbol{J} \cdot \hat{\mathbf{n}} \; dS = \int_V f \; dV, \tag{A.7}$$

which may be expressed in discrete form for the cell at (x_i, y_j, z_k) as

$$(J^x_{i+1/2,j,k} - J^x_{i-1/2,j,k})\,\Delta y_j\,\Delta z_k \;+ (J^y_{i,j+1/2,k} - J^y_{i,j-1/2,k})\,\Delta x_i\,\Delta z_k \;+ (J^z_{i,j,k+1/2} - J^z_{i,j,k-1/2})\,\Delta x_i\,\Delta y_j \;=\; \bar{f}_{i,j,k}\,\Delta x_i\,\Delta y_j\,\Delta z_k \tag{A.8}$$

or

$$\frac{(J^x_{i+1/2,j,k} - J^x_{i-1/2,j,k})}{\Delta x_i} + \frac{(J^y_{i,j+1/2,k} - J^y_{i,j-1/2,k})}{\Delta y_j} + \frac{(J^z_{i,j,k+1/2} - J^z_{i,j,k-1/2})}{\Delta z_k} \;=\; \bar{f}_{i,j,k}\,, \tag{A.9}$$

where $\bar{f}_{i,j,k}$ is the volume-averaged value of f represented at the cell centre. This discrete equation may be written in matrix form as

$$\begin{pmatrix} -\frac{1}{\Delta x_i} & \frac{1}{\Delta x_i} \end{pmatrix} \begin{pmatrix} J^x_{i-1/2,j,k} \\ J^x_{i+1/2,j,k} \end{pmatrix} + \begin{pmatrix} -\frac{1}{\Delta y_j} & \frac{1}{\Delta y_j} \end{pmatrix} \begin{pmatrix} J^y_{i,j-1/2,k} \\ J^y_{i,j+1/2,k} \end{pmatrix} + \begin{pmatrix} -\frac{1}{\Delta z_k} & \frac{1}{\Delta z_k} \end{pmatrix} \begin{pmatrix} J^z_{i,j,k-1/2} \\ J^z_{i,j,k+1/2} \end{pmatrix} = \bar{f}_{i,j,k}\,. \tag{A.10}$$

At the outermost edge of the mesh, we assume Neumann boundary conditions for $\boldsymbol{J}$:

$$\boldsymbol{J} \cdot \hat{\mathbf{n}}|_{\partial\Omega} = 0.$$

This condition eliminates $\boldsymbol{J}$ on the outer boundaries, reducing the number of unknown values to $(nx-1)(ny-1)(nz-1)$. Consequently, the numbering scheme for components of $\boldsymbol{J}$ may be rewritten in terms of cell number. Cells are numbered consecutively starting at cell 1 and increasing in x then y then z directions. J^x_1 corresponds to the cell face at $(x_{1+1/2}\,, y_1\,, z_1)$, J^x_{nx-1} is at $(x_{nx-1/2}\,, y_1\,, z_1)$. J^x_{nx} is in the second row of cells at $(x_{1+1/2}\,, y_2\,, z_2)$, and $J^x_{(nx-1)\,ny\,nz}$ is the final element of J^x at $(x_{nx-1/2}\,, y_{ny}\,, z_{nz})$. A similar pattern describes J^y and J^z.

Based on this numbering scheme, we can expand (A.10) to include all cells from 1 to $nx * ny * nz$, and write the matrix equation as

$$\mathbf{D_x J_x} + \mathbf{D_y J_y} + \mathbf{D_z J_z} = \mathbf{f}, \tag{A.11}$$

where the matrices $\mathbf{D_x}$, $\mathbf{D_y}$ and $\mathbf{D_z}$ are finite difference operators, and vectors $\mathbf{J_x}$, $\mathbf{J_y}$ and $\mathbf{J_z}$ contain components of current density. Considering the first term of (A.11), non-zero

elements of $\mathbf{D_x}$ are of the form $\pm 1/\Delta x_1$, and the matrix has dimensions $\{nx * ny * nz\} \times \{(nx-1) * ny * nz\}$. Matrices $\mathbf{D}_y$, $\mathbf{D}_z$ show similar characteristics in y and z dimensions, respectively. Vector $\mathbf{J_x}$ takes the form

$$\mathbf{J_x} = \begin{pmatrix} J_1^x \\ J_2^x \\ \vdots \\ \\ \\ \vdots \\ J^x_{(nx-1)\,ny\,nz} \end{pmatrix},$$

and similarly for $\mathbf{J_y}$ and $\mathbf{J_z}$. The source vector is described by

$$\mathbf{f} = \begin{pmatrix} \bar{f}_1 \\ \bar{f}_2 \\ \vdots \\ \\ \\ \vdots \\ \bar{f}_{nx\,ny\,nz} \end{pmatrix}.$$

Equation (A.11) may be more simply written as

$$\mathbf{D}\,\mathbf{J} = \mathbf{f}, \tag{A.12}$$

where the matrix $\mathbf{D}$ is the discrete form of the divergence operator $\nabla\cdot$, consisting of $[\mathbf{D_x}\ \mathbf{D_y}\ \mathbf{D_z}]$. Its dimension is $\{nx * ny * nz\} \times \{(nx-1) * ny * nz\ +\ nx * (ny-1) * nz\ +\ nx * ny * (nz-1)\}$. The vector $\mathbf{J}$ is the concatenation of vectors $\mathbf{J_x}$, $\mathbf{J_y}$ and $\mathbf{J_z}$.

A.2 Discrete approximation of equation (A.6)

Equation (A.6) may be split into three integral equations:

$$\int_V (\sigma^{-1} J^x - \tfrac{\partial \phi}{\partial x})\ dV = 0, \tag{A.13}$$

$$\int_V (\sigma^{-1} J^y - \tfrac{\partial \phi}{\partial y})\ dV = 0, \tag{A.14}$$

$$\text{and} \qquad \int_V (\sigma^{-1} J^z - \tfrac{\partial \phi}{\partial z})\ dV = 0. \tag{A.15}$$

Since components of $\boldsymbol{J}$ are located at the boundaries between adjacent cells, the volume integration is carried out over a new volume. This volume is defined between cell centres in a given dimension, as shown in Figure A.2 for the x-dimension. The expanded integral form of (A.13) defined on this new volume is

$$\int_{x_i}^{x_{i+1}} \int_{y_j-1/2}^{y_j+1/2} \int_{z_k-1/2}^{z_k+1/2} \sigma^{-1}\, J^x \;\, dx\, dy\, dz = \int_{x_i}^{x_{i+1}} \int_{y_j-1/2}^{y_j+1/2} \int_{z_k-1/2}^{z_k+1/2} \frac{\partial \phi}{\partial x} \;\, dx\, dy\, dz \;, \tag{A.16}$$

which may be written in discrete form as

$$(\bar{\sigma}_{i+1/2,j,k})^{-1} J^x_{i+1/2,j,k} = \begin{pmatrix} -\frac{1}{\Delta \bar{x}_{i+1/2}} & \frac{1}{\Delta \bar{x}_{i+1/2}} \end{pmatrix} \begin{pmatrix} \phi_{i,j,k} \\ \phi_{i+1,j,k} \end{pmatrix}. \tag{A.17}$$

The length of the new volume in the x direction is defined by

$$\Delta \bar{x}_{i+1/2} = x_{i+1} - x_i.$$

The quantity $\bar{\sigma}_{i+1/2,j,k}$ is the harmonic average of conductivity located at the interface between cells centred at (x_i, y_j, z_k) and (x_{i+1}, y_j, z_k). It is defined as

$$\bar{\sigma}_{i+1/2,j,k} = \frac{2\, \sigma_{i,j,k}\, \sigma_{i+1,j,k}}{\sigma_{i,j,k} + \sigma_{i+1,j,k}}. \tag{A.18}$$

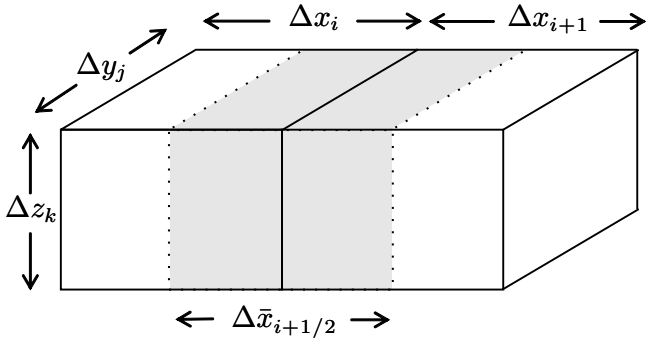

Figure A.2: Dimensions of the new cell volume over which (A.6) is solved in the x direction. Shaded area indicates the new volume that straddles the interface between cell centres.

Assembling (A.17) for all cells and adopting the revised numbering scheme that accounts for the grid boundary conditions, we can write the matrix equation as

$$\mathbf{S}_\mathbf{x}^{-1} \mathbf{J}_\mathbf{x} = \mathbf{G}_\mathbf{x} \boldsymbol{\phi}. \tag{A.19}$$

The inverse conductivity matrix takes the form

$$\mathbf{S}_x^{-1} = \begin{pmatrix} 1/\bar{\sigma}_1^x & \cdots & & 0 \\ \vdots & 1/\bar{\sigma}_2^x & & \vdots \\ & & \ddots & \\ 0 & \cdots & & 1/\bar{\sigma}^x_{(nx-1)\,ny\,nz} \end{pmatrix},$$

where $\bar{\sigma}^x$ denotes the harmonic average value of σ in the x direction. Matrix $\mathbf{G_x}$ is a finite difference operator of dimension $\{(nx-1)*ny*nz\} \times \{nx*ny*nz\}$, whose non-zero elements are of the form $\pm 1/\Delta\bar{x}_{i+1/2}$.

Similarly, the discrete forms of (A.14) and (A.15) may be written as

$$\mathbf{S_y^{-1}J_y} = \mathbf{G_y}\boldsymbol{\phi}, \tag{A.20}$$

$$\text{and} \qquad \mathbf{S_z^{-1}J_z} = \mathbf{G_z}\boldsymbol{\phi}. \tag{A.21}$$

Equations (A.19), (A.20) and (A.21) are joined to form the matrix system

$$\begin{pmatrix} \mathbf{S_x^{-1}} & & \\ & \mathbf{S_y^{-1}} & \\ & & \mathbf{S_z^{-1}} \end{pmatrix} \begin{pmatrix} \mathbf{J_x} \\ \mathbf{J_y} \\ \mathbf{J_z} \end{pmatrix} = \begin{pmatrix} \mathbf{G_x} \\ \mathbf{G_y} \\ \mathbf{G_z} \end{pmatrix} \boldsymbol{\phi}, \tag{A.22}$$

which may be simplified and expressed as

$$\mathbf{S^{-1}J} = \mathbf{G}\boldsymbol{\phi}. \tag{A.23}$$

The matrix $\mathbf{G}$ is the discrete form of the gradient operator ∇, with a dimension of $\{(nx-1)*ny*nz \;+\; nx*(ny-1)*nz \;+\; nx*ny*(nz-1)\} \times \{nx*ny*nz\}$. The matrix $\mathbf{S}^{-1}$ corresponds to the inverse of the harmonic average of conductivity, with a dimension of $\{(nx-1)*ny*nz \;+\; nx*(ny-1)*nz \;+\; nx*ny*(nz-1)\}^2$.

Since matrix $\mathbf{S^{-1}}$ is invertible, we can multiply both sides of (A.23) by $\mathbf{S}$ to obtain an explicit algebraic equation for $\mathbf{J}$:

$$\mathbf{J} = \mathbf{SG}\boldsymbol{\phi}. \tag{A.24}$$

To solve for $\boldsymbol{\phi}$, (A.24) is substituted into (A.12) to give the discrete form of Poisson's equation:

$$\mathbf{DSG}\boldsymbol{\phi} = \mathbf{f}, \tag{A.25}$$

where

$$\mathbf{f} = -\mathbf{DLGh}. \tag{A.26}$$

The matrix $\mathbf{L}$ in (A.26) represents the harmonic average of cross-coupling conductivity.